Characterization and Bioanalysis of Protein-Based Biopharmaceuticals, Peptides and Amino Acids by Liquid Chromatography and Mass Spectrometry

Dissertation

der Mathematisch-Naturwissenschaftlichen Fakultät

der Eberhard Karls Universität Tübingen

zur Erlangung des Grades eines

Doktors der Naturwissenschaften

(Dr. rer. nat.)

vorgelegt von

Simon Jonas Jaag

aus

Künzelsau

Tübingen

2023

Gedruckt mit Genehmigung der Mathematisch-Naturwissenschaftlichen Fakultät der Eberhard Karls Universität Tübingen.

Tag der mündlichen Qualifikation: 12.01.2024

Dekan: Prof. Dr. Thilo Stehle

1. Berichterstatter/-in: Prof. Dr. Michael Lämmerhofer

2. Berichterstatter/-in: Jun.-Prof. Dr. Matthias Gehringer

Table of contents

I. Summary

Biopharmaceuticals have become an essential class of therapeutics and are used for different medical indications such as diabetes, cancer, inflammatory diseases, and infectious diseases. Monoclonal antibodies (mAbs) have the biggest share within the biopharmaceuticals regarding the drug approval numbers. However, the benefits in terms of high specificity and efficacy come with the drawback of higher cost and higher complexity. This complexity arises from the high molecular weight on the one hand and high structural heterogeneity on the other hand, making the analytical characterization and quality control of mAbs and other biopharmaceuticals a significant challenge. In addition to these protein-based biopharmaceuticals, the elucidation of the absolute configuration of therapeutic peptides and natural (lipo)peptides is also of particular interest for drug discovery.

To address these challenges, different liquid chromatography (LC) and mass spectrometric (MS) methods were used for the more comprehensive analysis in the presented work. The first publication of this dissertation was dedicated to the analysis of charge variants of mAbs, which is an important quality attribute that might affect safety and efficacy of the drug product. To characterize the charge variants, the mAbs were analysed at the intact protein level and the subunit level after limited digestion and disulphide reduction using strong cation-exchange chromatography (SCX). The SCX method was systematically optimized to enable the separation of the maximum number of charge variants using a design of experiments (DoE) approach. The optimized SCX mobile phase, however, contains high concentrations of non-volatile salt in the mobile phase, which is incompatible with MS detection. On the other hand, MS analysis is essential for the identification of the charge variants. To overcome this limitation, an online two-dimensional liquid chromatographic (2D-LC) method was successfully developed, which uses SCX in the first separation dimension and reversed-phase (RP) LC in the second separation dimension, which can be used for de-salting prior MS analysis. An ultra-short analysis time (≤ 1 min) of the second dimension RP method was essential to establish a full comprehensive 2D-LC analysis. For this purpose, a column comparison study was performed using a set of monolithic and superficially porous particle (SPP) columns, and the separation efficiency and analysis speed were investigated.

An even more comprehensive column comparison study focusing on the kinetic performance was done for the second work presented in this dissertation. A set of 13 RP protein separation columns including monolithic, SPP, and fully porous particle (FPP) columns was investigated regarding their capability to separate peaks in the shortest possible time. It could be demonstrated that SPP columns with a pore size of 400 Å and a thin, porous shell provided the best performance especially for large proteins such as mAbs.

Proteins themselves can also be the potential targets of drug products such as the tumour suppressor protein p53 studied in publication III. Intact protein LC-MS was successfully used to investigate the binding efficiency and specificity of covalent inhibitors.

Amino acids are the building blocks of proteins and peptides and most of these amino acids are chiral. As the biological activity is usually dependent on the absolute configuration of the amino acids, the enantioselective analysis is of utmost importance for structural elucidation and quality control. Therefore, one goal of the presented work was to develop a fast and comprehensive method to separate amino acids, their enantiomers, diastereomers, and constitutional isomers. This was achieved by derivatization using 6-aminoquinolyl-*N*-hydroxysuccinimidyl carbamate (AQC) and subsequent analysis by enantioselective liquid chromatography ion mobility-mass spectrometry (LC-IM-MS). A very fast three minutes short analysis method could be developed and was applied for the successful structure elucidation of a therapeutic peptide and a natural lipopeptide.

The absolute configuration of a tetrapeptide originating from the natural antimicrobial peptide-polyene epifadin could be determined using chiral LC-MS, which was crucial for the structure elucidation. In this work, all eight enantiomer peak pairs could be successfully separated and the separation of the diastereomers was optimized.

II. Zusammenfassung

Biopharmazeutika sind zu einer essenziellen Klasse von Therapeutika geworden und werden für verschiedene medizinische Indikationen wie Diabetes, Krebs, entzündliche Erkrankungen und Infektionskrankheiten eingesetzt. Monoklonale Antikörper (mAbs) haben innerhalb der Biopharmazeutika den größten Anteil bezogen auf die Zulassungszahlen. Den Vorteilen bezüglich hoher Spezifität und Effektivität stehen jedoch Nachteile durch hohe Kosten und erhöhter Komplexität gegenüber. Die Komplexität ergibt sich einerseits aufgrund des hohen Molekulargewichts und anderseits aufgrund der strukturellen Heterogenität, wodurch die analytische Charakterisierung und Qualitätskontrolle von mAbs und anderer Biopharmazeutika zu einer Herausforderung wird. Neben diesen protein-basierten Biopharmazeutika ist auch die Aufklärung der absoluten Konfiguration von therapeutischen und natürlichen (Lipo)peptiden von besonderem Interesse für die Wirkstoffforschung.

Zur Bewältigung dieser Herausforderungen wurden in der hier präsentierten Arbeit flüssigchromatographische (LC) und massenspektrometrische (MS) Methoden für die umfassende Analyse eingesetzt. Die erste Publikation dieser Dissertation bezog sich auf die Analyse von Ladungsvarianten von mAbs, welche wichtige Qualitätsmerkmale darstellen und die Sicherheit und Wirksamkeit des Arzneimittels beeinflussen können. Zur Charakterisierung der Ladungsvarianten wurden die mAbs auf Ebene des intakten Proteins als auch auf Fragmentebene nach begrenztem Verdau und Reduzierung der Disulfidbrücken mittels starker Kationenaustauschflüssigkeitschromatographie (SCX) analysiert. Die SCX-Methode wurde systematisch mittels statistischer Versuchsplanung (DoE) dahingehend optimiert, die höchstmögliche Anzahl an Ladungsvarianten zu trennen. Die mobile Phase der optimierten SCX-Methode enthielt jedoch eine hohe Konzentration an nicht-flüchtigen Salzen, wodurch sie nicht mit MS Detektion kompatibel ist, welche wiederum entscheidend für die Identifikation der Ladungsvarianten ist. Um dieser Herausforderung zu begegnen, wurde erfolgreich eine online zweidimensionale flüssigchromatographische (2D-LC) Methode entwickelt, bei der SCX in der ersten Trenndimension und Umkehrphasenflüssigchromatographie (RP-LC) in der zweiten Trenndimension zur Entsalzung vor der MS Detektion verwendet wurde. Die Entwicklung einer extrem kurzen (≤ 1 min) RP-LC Methode war unabdingbar zur Etablierung einer umfassenden 2D-LC Methode. Dazu wurde eine

Säulenvergleichsstudie mit monolithischen und oberflächlich porösen Partikelsäulen (SPP-Säulen) durchgeführt und die Trenneffizienz sowie die Analysengeschwindigkeit untersucht.

Eine noch umfassendere Säulenvergleichsstudie mit Fokus auf das kinetische Leistungsvermögen wurde in der zweiten Arbeit dieser Dissertation durchgeführt. Eine Auswahl von 13 RP-Proteintrennsäulen inklusive monolithischer, SPP und vollporöser Partikelsäulen (FPP-Säulen) wurde hinsichtlich ihrer Fähigkeit, Peaks in der kürzest möglichen Zeit zu trennen, untersucht. Es konnte gezeigt werden, dass SPP-Säulen mit einer Porengröße von etwa 400 Å und einer dünnen, porösen Schicht die beste Performance insbesondere für größere Proteinen besitzen.

Proteine selbst können auch potenzielle Ziele für Arzneistoffe sein, wie z.B. das Tumorsuppressorprotein p53, welches in der dritten Publikation dieser Arbeit untersucht wurde. Intakte Protein LC-MS wurde erfolgreich verwendet, um die Bindungseffizienz und -spezifität des kovalenten Inhibitors an p53 nachzuweisen.

Aminosäuren sind die Bausteine von Proteinen und Peptiden und die Mehrheit dieser Aminosäuren sind chiral. Die biologische Aktivität ist in der Regel abhängig von der absoluten Konfiguration der Aminosäuren, wodurch die enantiomerenselektive Analyse von höchster Wichtigkeit für die Strukturaufklärung und zur Qualitätskontrolle ist. Daher war die Entwicklung schneller und umfassender Trennmethoden zur Analyse von Aminosäuren, deren Enantiomeren, Diastereomeren und konstitutionellen Isomeren ein Ziel dieser Arbeit. Dieses konnte durch Derivatisierung mittels 6-Aminochinolyl-*N*-hydroxysuccinimidylcarbamat (AQC) und anschließender Analyse durch enantioselektiver flüssigchromatographischer Ionenmobilitäts-Massenspektrometrie (LC-IM-MS) erreicht werden. Eine sehr schnelle dreiminütige Analysenmethode konnte entwickelt und zur Strukturaufklärung von therapeutischen Peptiden und eines natürlichen Lipopeptides eingesetzt werden.

Die absolute Konfiguration eines Tetrapeptides als Bestandteil des natürlichen, antimikrobiellen Peptidpolyens‘ Epifadin konnte mittels chiraler LC-MS bestimmt werden, was wiederum entscheidend für die Strukturaufklärung war. In dieser Arbeit konnten alle acht Enantiomerenpaare erfolgreich getrennt werden und die Diastereomerentrennung wurde optimiert.

III. List of Publications

Publications included in this dissertation

Publication I

S. Jaag, M. Shirokikh, M. Lämmerhofer, Charge variant analysis of protein-based biopharmaceuticals using two-dimensional liquid chromatography hyphenated to mass spectrometry, J. Chromatogr. A 1636 (2021) 461786.

DOI: 10.1016/j.chrom.2020.461786

Publication II

S. Jaag, C. Wen, B. Peters, M. Lämmerhofer, Kinetic performance comparison of superficially porous, fully porous and monolithic reversed-phase columns by gradient kinetic plots for the separation of protein biopharmaceuticals, J. Chromatogr. A 1676 (2022) 463251.

DOI: 10.1016/j.chroma.2022.463251

Publication III

J. Stahlecker, T. Klett, M. Schwer, S. Jaag, M. Dammann, L.N. Ernst, M.B. Braun, M.O. Zimmermann, M. Kramer, M. Lämmerhofer, T. Stehle, M. Coles, F.M. Boeckler, Revisiting a challenging p53 binding site: a diversity-optimized HEFLib reveals diverse binding modes in T-p53C-Y220C, RSC Med Chem 13(12) (2022) 1575-1586.

DOI: 10.1039/d2md00246a

Publication IV

S. Jaag, Y. Valadbeigi, T. Causon, H. Gross, M. Lämmerhofer; Three-Minute Enantioselective Amino Acid Analysis by Ultra-High Performance Liquid Chromatography Drift Tube Ion Mobility-Mass Spectrometry Using a Chiral Core-Shell Tandem Column Approach, Anal. Chem. (2024).

DOI: 10.1021/acs.analchem.3c05426

Publications not included in this dissertation

Publication V

B.O. Torres Salazar, T. Dema, N.A. Schilling, D. Janek, J. Bornikoel, A. Berscheid, A.M.A. Elsherbini, S. Krauss, S.J. Jaag, M. Lammerhofer, M. Li, N. Alqahtani, M.J. Horsburgh, T. Weber, J.M. Beltran-Belena, H. Brotz-Oesterhelt, S. Grond, B. Krismer, A. Peschel, Commensal production of a broad-spectrum and short-lived antimicrobial peptide polyene eliminates nasal *Staphylococcus aureus*, Nat Microbiol, 9 (1) (2024) 200-213.

DOI: 10.1038/s41564-023-01544-2

IV. Author Contributions

Publication I:

Charge variant analysis of protein-based biopharmaceuticals using two-dimensional liquid chromatography hyphenated to mass spectrometry

Simon Jaag

Conceptualization and investigation

Sample preparation

Method development and sample analysis

Data analysis and interpretation

Main writing of the manuscript

Marina Shirokikh

Investigation

Michael Lämmerhofer

Conceptualization

Methodology

Supervision

Writing and review of manuscript

Financing of the project

Corresponding author

Publication II:

Kinetic performance comparison of superficially porous, fully porous and monolithic reversed-phase columns by gradient kinetic plots for the separation of protein biopharmaceuticals

Simon Jaag

Conceptualization and investigation

Sample preparation

Method development and sample analysis

Data analysis and interpretation

Main writing of the manuscript

Chunmei Wen

Investigation

Sample preparation

Method development and sample analysis

Data analysis and interpretation

Review of manuscript

Benjamin Peters

Methodology

Data curation

Review of manuscript

Michael Lämmerhofer

Conceptualization

Methodology

Supervision

Writing and review of manuscript

Financing of the project

Corresponding author

Publication III:

Revisiting a challenging p53 binding site: a diversity-optimized HEFLib reveals diverse binding modes in T-p53C-Y220C

Jason Stahlecker

Analysis of samples with ^{1}H,^{15}N-HSQC NMR

Data analysis of STD NMR data

Crystallographic data reduction and refinement

Writing of final manuscript

Theresa Klett

Performance and analysis of DSF studies

Writing of final manuscript

Martin Schwer

Performance and analysis of GSH assays

Writing of final manuscript

Simon Jaag

Performance and analysis of ESI-MS experiments

Marcel Dammann

STD NMR experiments performance and data analysis

Larissa N. Ernst

Mutagenesis

Michael B. Braun

Crystallographic data reduction and refinement

Markus O. Zimmermann

Adduct formation calculations and electrostatic potential (ESP) plots

Markus Kramer

STD NMR experiments

Michael Lämmerhofer

Supervision and manuscript reviewing

Thilo Stehle

Crystallographic data reduction and refinement

Murray Coles

Analysis of samples with $^{1}H,^{15}N$-HSQC NMR

Frank M. Boeckler

Conceptualization

Writing of final manuscript

Publication IV:

Three-Minute Enantioselective Amino Acid Analysis by Ultra-High Performance Liquid Chromatography Drift Tube Ion Mobility-Mass Spectrometry Using a Chiral Core-Shell Tandem Column Approach

Simon Jaag

Conceptualization and investigation

Sample preparation

Method development and sample analysis including LC-MS and LC-IM-MS

Data analysis and interpretation

Main writing of the manuscript

Younes Valadbeigi

LC-IM-MS experiments

Density functional theory (DFT) and collision cross-sections (CCS) calculations

Data analysis and interpretation

Tim Causon

LC-IM-MS experiments

Data analysis and interpretation

Conceptualization

Methodology

Supervision

Writing and review of manuscript

Financing of the project

Corresponding author

Harald Gross

NMR analysis

Bioinformatic studies

Supply of lipopeptide sample

Writing and review of manuscript

Michael Lämmerhofer

Conceptualization

Methodology

Supervision

Writing and review of manuscript

Financing of the project

Corresponding author

Publication V

Commensal production of a broad-spectrum and short-lived antimicrobial peptide polyene eliminates nasal *Staphylococcus aureus*

Benjamin O. Torres Salazar

Performance and Analysis of most bacteriological, molecular, and compound isolation experiments

Animal experiments

Taulant Dema

Elucidation of epifadin structure

Total synthesis of all tetrapeptides including their purification and chemical analyses

Nadine A. Schilling

Elucidation of epifadin structure

Daniela Janek

Helped with performance and Analysis of most bacteriological, molecular, and compound isolation experiments and isolation of strain IVK83

Jan Bornikoel

Microscopic experiments

Anne Berscheid

Analysis of epifadin toxicity and membrane potential effects

Ahmed M. A. Elsherbini

Performance of the bioinformatic search for epifadin-like BGCs

Sophia Krauss

Helped with performance and Analysis of most bacteriological, molecular, and compound isolation experiments and isolation of strain IVK83

Identification and provision epifadin-producing S. epidermidis strains

Simon J. Jaag

Confirmation the absolute configuration of the tetrapeptide via chiral HPLC

Michael Lämmerhofer

Supervision and manuscript reviewing

Min Li

Identification and provision epifadin-producing S. epidermidis strains

Norah Alqahtani

Performance of the experimental evolution and analysis the epifadin-resistant mutants

Malcolm J. Horsburgh

Identification and provision epifadin-producing S. epidermidis strains

Performance of the experimental evolution and analysis the epifadin-resistant mutants

Tilmann Weber

Analysis of the potential epifadin biosynthesis enzymes

José Manuel Beltrán-Beleña

Helped with elucidation of epifadin structure

Heike Brötz-Oesterhelt

Supervision of the experiments and writing of the manuscript

Stephanie Grond

Elucidation of epifadin structure

Supervision of the experiments and writing of the manuscript

Bernhard Krismer

Helped with performance and Analysis of most bacteriological, molecular, and compound isolation experiments and isolation of strain IVK83

animal experiments

Supervision of the experiments and writing of the manuscript

Andreas Peschel

Supervision of the experiments and writing of the manuscript

V. List of Poster Presentations

36th International Symposium on Microscale Separations and Bioanalysis (MSB) 2020

Virtual edition, September 27th to 30th,

Charge Variant Analysis of Monoclonal Antibodies by SCX x RP Online 2D-LC-ESI-QTOF-MS

Simon Jaag, Marina Shirokikh, Michael Lämmerhofer

17th International Symposium on Hyphenated techniques in Chromatography and Separation Technology (HTC-17), 2022

Ghent, Belgium, May 18th to 20th

Evaluation of Different Reversed-Phase Columns for the Separation of Proteins Using the Gradient Kinetic Plot Model

Simon Jaag, Chunmei Wen, Michael Lämmerhofer

50th International Symposium on High Performance Liquid Phase Separations and Related Techniques (HPLC), 2022

San Diego, California, United States of America, June 18th to 23rd

Performance Comparison of Superficially Porous, Fully Porous and Monolithic Reversed-Phase Columns by Gradient Kinetic Plots for the Separation of Protein Biopharmaceuticals

Simon Jaag, Chunmei Wen, Michael Lämmerhofer

51st International Symposium on High Performance Liquid Phase Separations and Related Techniques (HPLC), 2023

Düsseldorf, Germany, June 18th to 22nd

Ultra-Fast Enantioselective LC-IM-MS Separation of Derivatized Amino Acids Using a Tandem-Column Approach"

Simon Jaag, Ryan. Karonga, Younes Valadbeigi, Tim Causon, Michael Lämmerhofer

VI. List of Oral Presentations

33rd PhD students meeting of the German Chemical Society (GDCh), AK Separation Science, 2023

Hohenroda, Germany, January 8th to 10th

Evaluation of the Kinetic Performance of Reversed Phase Columns for Protein Separation

Simon Jaag, Chunmei Wen, Benjamin Peters, Michael Lämmerhofer

Anakon 2023

Vienna, Austria, April 11th to 14th

Comparison of Reversed-Phase Columns by Gradient Kinetic Plots for the Separation of Proteins

Simon Jaag, Chunmei Wen, Benjamin Peters, Michael Lämmerhofer

VII. Abbreviations

^{1}D	First dimension
1D-LC	One-dimensional liquid chromatography
^{2}D	Second dimension
2D-LC	Two-dimensional liquid chromatography
ACN	Acetonitrile
AEX	Anion exchange
AQC	6-aminoquinolyl-*N*-hydroxysuccinimidyl carbamate
ASM	Active solvent modulation
CAD	Collisionally-activated fragmentation
CCS	Collision cross-section
CDA	Chiral derivatizing agent
CE	Collision energy
CEX	Cation exchange
CID	Collision induced dissociation
cps	Counts per seconds
CQA	Critical quality attribute
CSP	Chiral stationary phase
DAD	Diode array detector
DBU	1,8-Diazabicyclo [5.4.0]undec-7-ene
DCM	Dichloromethane
DFT	Density functional theory
DMA	Differential mobility analyzer
DMF	Dimethylformamide
DNB-F	1-Fluoro-2,4-dinitrobenzene
Dns-Cl	Dansyl chloride
DoE	Design of experiments
DP	Declustering potential
DSF	Differential scanning fluorimetry
DTIM-MS	Drift tube ion mobility mass spectrometry
DTIMS	Drift tube IMS
DTT	Dithiothreitol

ECD	Electron capture dissociation
EIC	Extracted ion chromatogram
ELSD	Evaporative light scattering detector
EMA	European medicines agency
ESI	Electrospray ionization
ESP	Electrostatic potential
ETD	Electron transfer dissociation
FA	Formic acid
FAIMS	Field asymmetric IMS
FDA	Food and Drug Administration
FDAA	*N*-(2,4-dinitro-5-fluorophenyl)-L-alaninamide
Fig.	Figure
FLEC	(+)-1-(9-Fluorenyl)ethyl chloroformate
Fmoc-Cl	9-Fluorenylmethyl-chloroformate
FPP	Fully porous particle
FT-ICR	Fourier-transform ion cyclotron resonance
FWHM	Full width at half maximum
GRAVY	Grand average of hydropathy
HATU	O-(7-azabenzotriazol-1-yl)-N,N,N',N'-tetramethyluronium hexafluorophosphate
HCD	Higher energy collisional dissociation
HIC	Hydrophobic interaction chromatography
HILIC	Hydrophilic interaction chromatography
HOBt	1-Hydroxybenzotriazole
HPLC	High performance liquid chromatography
HRdm	High resolution demultiplexing
HSQC	Heteronuclear single quantum coherence
IAA	2-Iodoacetamide
ICH	International Council for Harmonization of Technical Requirements for Pharmaceuticals for Human Use
ID	Inner diameter
IdeS	Immunoglobulin G-degrading enzyme of *Streptococcus pyrogens*

IEF	Isoelectric focusing
IEX	Ion exchange
IgG	Immunoglobulin G
IM	Ion mobility
IMS	Ion mobility spectrometry
IPA	Isopropanol
IS	Internal standard
LC	Liquid chromatography
LC-LC	Single heart-cutting 2D-LC
LC-MS	Liquid chromatography mass spectrometry
LCxLC	Full comprehensive 2D-LC
LOD	Limit of detection
LOQ	Limit of quantification
m/z	Mass-to-charge
mAb	Monoclonal antibody
MALDI	Matrix-assisted laser desorption/ionization
MeOH	Methanol
mLC-LC	Multiple heart-cutting 2D-LC
MS	Mass Spectrometry
MS/MS	Tandem mass spectrometry
NBD-F	4-fluoro-7-nitrobenzofurazan
NH_4Ac	Ammonium acetate
NH_4FA	Ammonium formate
NIST	National Institute of Standards and Technologies
NMDA	*N*-methyl-D-aspartate
NMM	*N*-Methylmorpholine
NMR	Nuclear magnetic resonance
NPP	Non-porous particle
PEEK	Polyether ether ketone
pH	Potentia hydrogenii
Ph. Eur.	European Pharmacopoeia
p*I*	Isoelectric point

ppm	Parts per million
PTM	Post-translational modification
QC	Quality control
QN-AX	Quinidine-derived chiral anion exchanger
qTOF	Quadrupole time-of-flight
RP	Reversed phase
RP-LC	Reversed phase liquid chromatography
RT	Retention time
SAX	Strong anion exchange
SCX	Strong cation exchange
SEC	Size-exclusion chromatography
SFC	Supercritical fluid chromatography
sLCxLC	Selective comprehensive 2D-LC
SPAM	Stationary phase assisted modulation
SPE	Solid phase extraction
SPP	Superficially porous particle
SPPS	Solid-phase peptide synthesis
STD	Saturation transfer difference
SWATH	Sequential window acquisition of all theoretical mass spectra
t_0	Void time or dead-time
TFA	Trifluoroacetic acid
t_G	Gradient time
TIM-MS	Trapped ion mobility-MS
TIMS	Trapped IMS
TIPS	Triisopropyl-silane
TOF	Time of flight
t_R	Retention time
TWIMS	Traveling wave IMS
UHPLC	Ultra high performance liquid chromatography
USA	United States of America
USP	United States Pharmacopeia
UV	Ultraviolet

WAX	Weak anion exchange
XIC	Extracted ion chromatogram
ZWIX	Zwitterionic ion exchange

1 Introduction

1.1 Pharmaceutical Background

Pharmaceutical products must meet high requirements in terms of efficacy, safety and quality and are therefore strictly regulated. Comprehensive national and international laws and guidelines, established by regulatory agencies like the Food and Drug Administration (FDA) from the United States of America (USA) or the European Medicines Agency (EMA), ensure that the drug products meet these requirements. The quality control of pharmaceutical products involves a multitude of different analytical methods ensuring all requirements regarding identity, content and purity can be checked [1]. Identity testing is used to confirm that the correct drug substance(s) is in the drug product. Content testing is used to verify that the correct amount of drug substance is present. Purity testing ensures that impurities are present in the drug only up to the tolerated limits [2, 3]. Impurities can originate from the raw materials or can be formed during the manufacturing process. Furthermore, impurities can result from degradation during storage. Stability studies can be performed to monitor the impurity levels and investigate the influence of different degradation pathways like oxidation, hydrolysis, light exposure, and temperature. A plethora of different analytical methods is used to characterize the drug products and many of them are described in pharmacopoeias like the European pharmacopoeia (Ph. Eur.) or the United States Pharmacopeia (USP).

1.1.1 Protein-Based Biopharmaceuticals

In recent decades, biopharmaceuticals became more important due to their higher target specificity and potency compared to the low molecular weight drugs [4, 5]. The number of new biopharmaceutical drug approvals significantly increased during the period of 2015-2019 compared to earlier periods, proofing the trend towards this product group (see **Fig. 1**). It is essential to have suitable analytical methods to meet the high-quality requirements. On the other hand biopharmaceuticals possess some disadvantages like very high cost, which limits their access to poor population groups [6]. In 2017, biopharmaceutical products accounted for 37% of net drug spending in the USA, despite making up only 2% of total prescriptions [6]. Another disadvantage is poor bioavailability, which often limits administration to parenteral routes [4, 5].

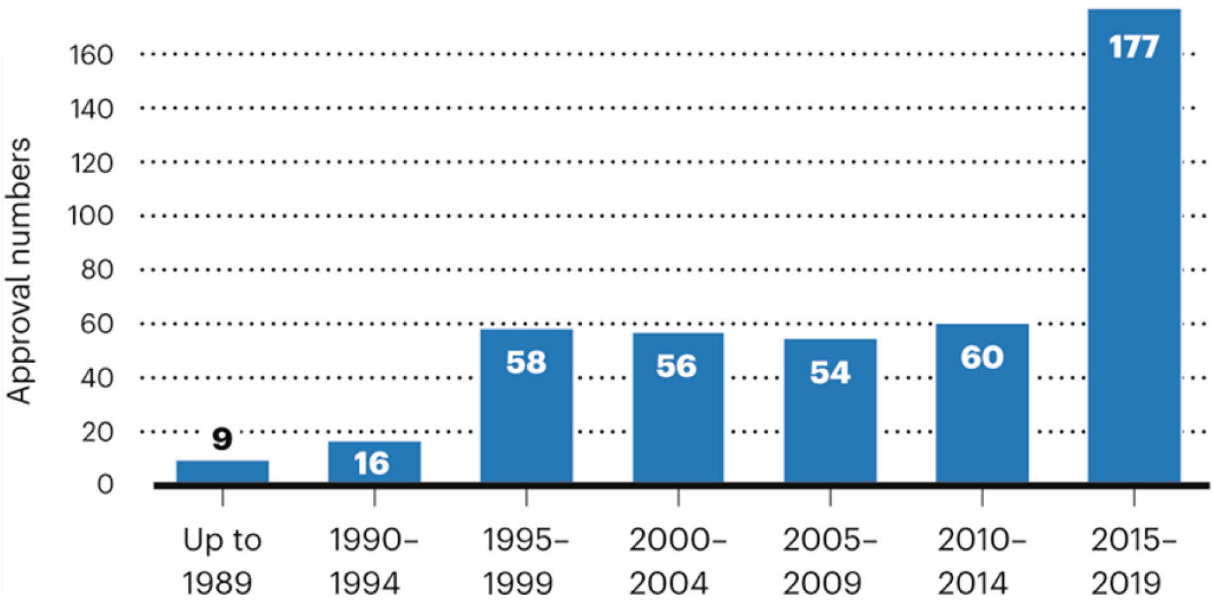

Fig. 1: Number of biopharmaceutical approvals in US and/or EU over the indicated period. Reprinted with permission from Walsh et al., Biopharmaceutical benchmarks 2022, Nat. Biotechnol., 40 (12) (2022) 1722-1760. Ref. [7]. Copyright 2022 Springer Nature America.

Monoclonal antibodies (mAbs) within the class of biopharmaceutical drug products account for the highest number of new drug approvals [7]. mAbs dominate the numbers of new biopharmaceuticals approvals with a ratio of 49 % (see **Table 1**). Even more impressive is that mAbs accounted for 80.2% of total biopharmaceutical sales in 2021 [7]. Monoclonal antibodies are used for a variety of different purposes including therapeutic and diagnostic applications. They play a crucial role within fields such as oncology, inflammatory diseases, infections, neutropenia and immunosuppression [7].

Table 1: Drug approval numbers from January 2018 to June 2022 in the USA and/or the EU. Data reused with permission from Walsh et al., Biopharmaceutical benchmarks 2022, Nat. Biotechnol., 40 (12) (2022) 1722-1760. Ref. [7]. Copyright 2022 Springer Nature America.

Category	Number of Approvals	[%]
Monoclonal Antibodies	**97**	**49.2**
Hormones	19	9.6
Clotting factors	6	3
Enzymes	8	4.1
Vaccines	16	8.1
Nucleic acid-based/ gene therapy	16	8.1
cell-based	9	4.6
colony-stimulating factors	12	6.1
fusion products	7	3.6
other	7	3.6
total	**197**	**100**

1.1.2 Therapeutic Peptides

Already in the 1920s, insulin was the first isolated and used therapeutic peptide which was administrated as replacement therapy to diabetics who did not produce sufficient amount of this peptide hormone [8]. Progress in purification techniques, synthesis, amino acid sequencing and structure elucidation made the development and production of synthetic peptides like oxytocin [9] and vasopressin possible [10, 11]. Most therapeutic peptides have a molecular weight between 500 and 5,000 Da which is in between the typical molecular weights of small molecules and protein-based biopharmaceuticals [11, 12]. Therapeutic peptides can also contain D-amino acids, uncommon amino acids, or hydroxy (amino) acids to enhance their therapeutic properties. Replacing L-amino acids with D-amino acids in therapeutic peptides is an important method to improve their stability against proteolytic enzymes, thereby increasing their half-life time in the blood [13]. Two examples of therapeutic peptides which have been used in the presented dissertation are octreotide and aureobasidin A (see **Fig. 2**).

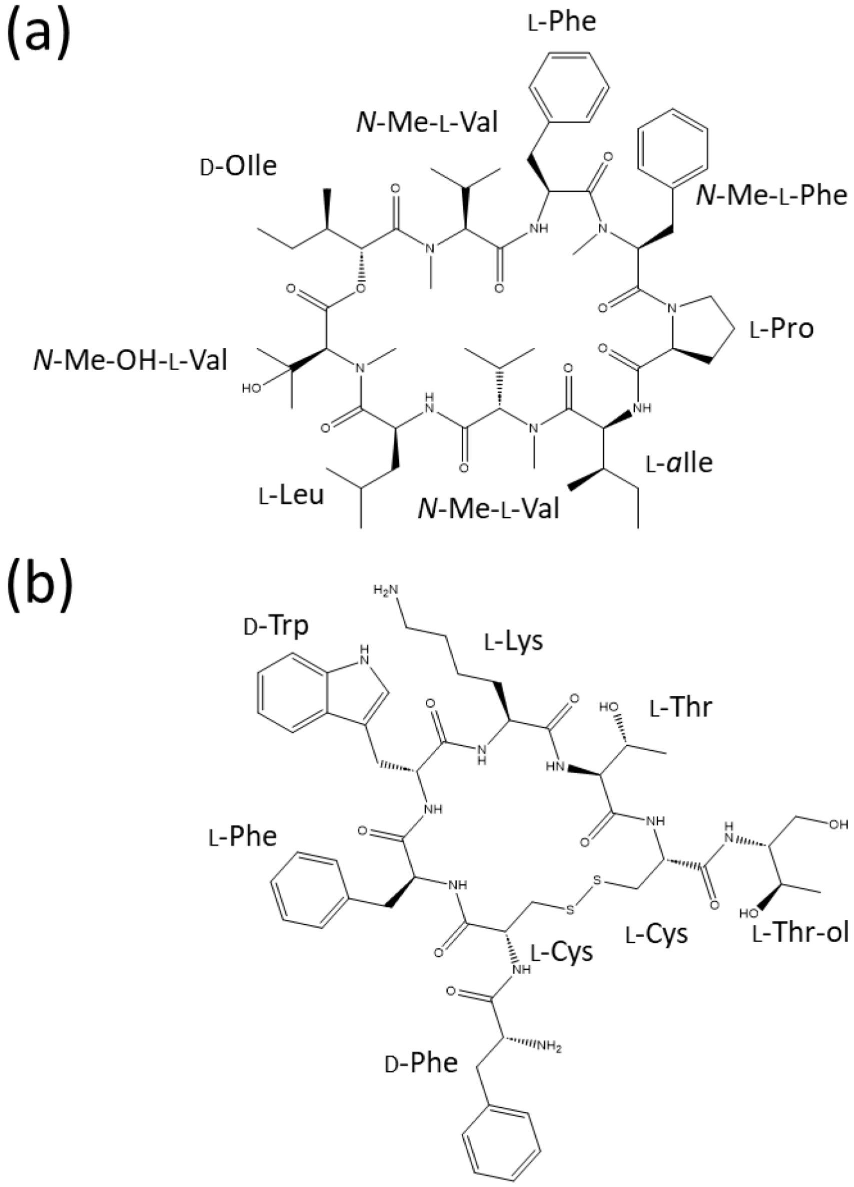

Fig. 2: Structures of the therapeutic peptides (a) aureobasidin A and (b) octreotide.

Aureobasidin A (see **Fig. 2a**) is a fungicidal antibiotic naturally produced by *Aureobasidium pullulans* with activity against *Saccharomyces cerevisiae* and contains proteinogenic amino acids (L-Phe, L-Pro, L-Leu), special amino acids (*N*-methyl-L-valine, *N*-methyl-L-phenylalanine, L-*allo*-isoleucine) as well as hydroxy (amino) acids [2-(*R*)-hydroxy-3-(*R*)-methylpentanoic acid and *β*-hydroxy-*N*-methyl-L-valine] [14].

Octreotide (see **Fig. 2b**) is an example of a synthetic therapeutic peptide that acts as somatostatin analogue. It is used for the treatment of acromegaly, diarrhoea associated with metastatic carcinoid tumours and tumours producing vasoactive intestinal peptides [15]. It consists of D-Phe-L-Cys-L-Phe-D-Trp-L-Lys-L-Thr-L-Cys-L-Thr(ol) with a disulphide bond between the two cysteines [16, 17]. In contrast to the natural somatostatin, which has a half-life of 2-3 minutes, octreotide possesses a half-life of 90-120 min [18], making it much more suitable for medical treatment. The longer half-life originates from the use of D-Phe at the *N*-terminus and L-threoninol on the *C*-terminus of the peptide, which enhances its stability against degradation [19].

These two examples of therapeutic peptides highlight the importance of distinguishing between different proteinogenic L-amino acids, their D-enantiomers, isomeric amino acids, and other special amino acids, which can be challenging from an analytical perspective.

1.1.3 Amino Acids

Peptides and proteins are oligomers and polymers, respectively, composed of amino acids as their monomeric building blocks. Moreover, amino acids can have diverse biological functions, such as serving as precursors for neurotransmitters like *N*-methyl-D-aspartate (NMDA) [20]. The predominant configuration of amino acids in biological systems is the L-enantiomer. But there are several examples where the D-enantiomer is present (like in NMDA) and plays a crucial role for the biological activity [21]. Another example is D-Ser, which acts as coagonist of NMDA and is associated with the Alzheimer’s disease [22]. Furthermore, the presence of D-amino acids in food can be used as quality indicator. A higher D-amino acid content is associated with lower food quality, as they can originate from thermal and alkaline treatment or microbial contamination [21]. These examples highlight the importance of analytical methods which can distinguish between amino acid enantiomers.

1.2 Structure and Structural Heterogeneity of Proteins

Proteins, including protein-based biopharmaceuticals, pose a significant analytical challenge due to their huge size and structural heterogeneity. In contrast to small molecules, which are typically under 1,000 Da in size, proteins have molecular weights that range from a few kDa to ~150 kDa for IgG1 antibodies, and can even exceed 3

MDa in case of the titin protein [23, 24]. This enormous size has a significant impact on analytical techniques such as chromatography and mass spectrometry, which will be discussed more thoroughly in the subsequent chapters. The protein structure depends not only on its amino acid sequence, referred to as the primary structure, but also on higher order structures, including secondary, tertiary, and in some cases, quaternary structures, where separate amino acid chains are cross-linked via disulphide bonds and non-covalent interactions [25, 26]. For example, an IgG1 antibody consists of two light and two heavy chains which are cross-linked via four interchain disulphide bonds, and it also possesses twelve additional intrachain disulphide bonds (see **Fig. 3**) [25].

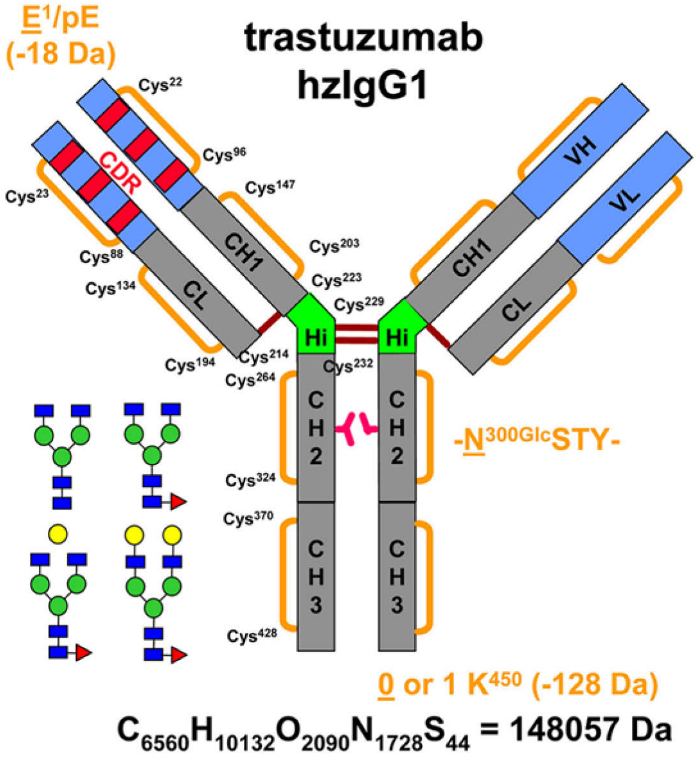

Fig. 3: The structure of an IgG1 antibody, using trastuzumab as an example. The structure shows the disulphide structure, *N*-glycosylation, *C*-terminal Lys-clipping, *N*-terminal pyro-glutamate formation and includes example glycans. Reprinted with permission from Beck et al., Characterization of Therapeutic Antibodies and Related Products, Anal. Chem., 85 (2) (2013) 715-736. Ref. [25]. Copyright 2013 American Chemical Society.

Even in therapeutic monoclonal antibodies, where the amino acid sequence is well defined, there are a variety of modifications that can impact efficacy and safety. Important modifications include changes in charge, size, disulphide bonds, glycosylation patterns, oxidation states, and even low level point mutations [25]. The superimposition of all these variants can result in thousands of unique structures for a single monoclonal antibody, posing a great challenge for analytical methods [27].

Charge variants can potentially influence the stability and biological activity of an antibody, resulting from modifications that change the protein's isoelectric point [28]. An example of a charge variant is the deamidation of asparagine (Asn) or glutamine (Gln) to aspartic acid (Asp) and glutamic acid (Glu), respectively [29]. Deamidation leads to acidic charge variants as the more acidic amino acids Asp and Glu are formed. In the case of Asp, isomerization to isoaspartic acid (isoAsp) can also lead to charge variants [29, 30]. Deamidation causes only a mass shift of 1 Da, thus its identification through mass spectrometry requires very high resolving powers [25]. *C*-terminal clipping of lysine (Lys) results in the formation of acidic variants as one basic Lys residue is removed [28]. Cyclic pyroglutamatic acid (pyroGlu) can be formed from glutamine (through loss of NH_3) and leads to an acidic charge variant at the *N*-terminus [31, 32]. Formation of PyroGlu from glutamic acid (through the loss of H_2O), on the other hand, results in a basic charge variant [32]. Glycation of the lysine side chain can occur in the presence of reducing sugars such as glucose or lactose, which may be an ingredient in cell culture media or in the drug product formulation buffers [28]. Sialylation at the glycosylation sites introduces additional carboxylate groups (sialic acid), thereby forming acidic charge variants [28].

Alongside charge variants, various other post-translational modifications (PTMs) significantly contribute to the microheterogeneity of proteins. These PTMs include phosphorylation, acetylation, *O/N*-linked glycosylation, methylation, ubiquitination and several more [33]. The correct glycosylation pattern of mAbs is of utmost importance for their efficacy, pharmacokinetics and safety [34]. *N*-glycosylation is the most frequently observed type of glycosylation, typically located on an asparagine residue on the constant heavy chain domain 2 (CH2) of the Fc-part (see **Fig. 3**). Therapeutic mAbs typically have the *N*-glycosylation at the consensus sequence (Asn)-X-Ser/Thr, where X is any amino acid except Pro [34]. The glycosylation can differ between both heavy chains, therefore, glycosylation alone can result in multiple variants of the mAb [35].

The current dissertation contains work dedicated to the characterisation of charge variants and glycovariants of mAbs.

1.3 Liquid Chromatography of Proteins

Protein analysis by liquid chromatography (LC) requires consideration of various factors including protein adsorption onto LC material, the influence of temperature, column morphologies, and many more.

The requirements for LC systems vary significantly depending on the type of analyte being analysed. Proteins tend to adsorb onto standard LC materials such as stainless steel [36]. Therefore, stainless steel-free systems use alternative materials such as polyether ether ketone (PEEK) [37], titanium (Ti) [38] or nickel alloys like MP35N [39]. Dedicated LC systems for bioanalysis are often referred to bio-inert or biocompatible systems [39]. An alternative approach to reduce adsorption of proteins is to graft polymers onto the stainless steel surface [40].

1.3.1 Performance Parameters for Chromatographic Separations

The final goal of a chromatographic separation is to successfully separate the sample components from each other. One measure to evaluate the separation success is the resolution R_s, which can be calculated as follows [41]:

$$R_s = \frac{\Delta t}{W_{avg}} = \frac{t_{R_2} - t_{R_1}}{0.5 \cdot (W_{4\sigma,1} + W_{4\sigma,2})}$$

(eq. 1.1)

Where Δt is the retention time difference between two peaks, t_{R1} and t_{R2} are the retention times of the first and second eluting peak, respectively. Often the peak width at 4σ ($W_{4\sigma}$) is used which represents 95 % of the peak area. However, it can be difficult to accurately determine this peak width manually or using software. Therefore, the more robust peak width at half height ($W_{1/2}$, 2.354σ) [41] can be used and transformed mathematically to the peak width at 4σ resulting finally in (eq. 1.2):

$$R_S = 1.18 \cdot \frac{t_{R_2} - t_{R_1}}{W_{1/2_1} + W_{1/2_2}}$$

(eq. 1.2)

The selectivity is a measure of the relative retention of two peaks and can be calculated as follows [42]:

$$\alpha = \frac{k_2}{k_1}$$

(eq. 1.3)

Here, k_1 and k_2 are the retention factors of the first and second eluting peak, respectively.

The selectivity must be greater than 1.0, otherwise, no separation would be possible at all. The selectivity in a reversed-phased separation is influenced by factors including the stationary phase, type of mobile phase (e.g. ACN vs. MeOH), mobile phase pH, mobile phase buffer type and concentration, ion-pair reagent, column temperature and gradient design [42, 43]

The performance of an LC separation can be evaluated using various performance parameters such as the plate number, peak capacity, and analysis time. The plate number *N* is a widely accepted performance parameter for isocratic LC separations, but it is not commonly used in gradient elution. This is because the determination of the retention factor at the point of elution requires additional experiments [42, 44]. Instead, the performance of gradient separation can be evaluated using the peak capacity, which is the theoretical number of peaks, that can be separated within a certain gradient time and a fixed resolution [45].

The peak capacity n_p can be calculated as follows [46]:

$$n_p = 1 + \frac{t_G - t_0}{W_{4\sigma}} = 1 + \frac{t_G - t_0}{1.7 \cdot W_{1/2}}$$

(eq. 1.4)

Where t_G is the gradient time and t_0 is the LC systems' void time (sometimes also called dead time). A more practical performance parameter of LC separations is the analysis time. The shorter the analysis time, the more samples can be analysed, and the higher is the sample throughput.

1.3.2 Column Morphologies

In general, four main types of column morphologies are used for LC separations: (i) fully porous particle (FPP) columns (see **Fig. 4a**), (ii) superficially porous particle (SPP) columns (see **Fig. 4b**), (iii) non-porous particle (NPP) columns and (iv) monolithic columns (see **Fig. 4c**).

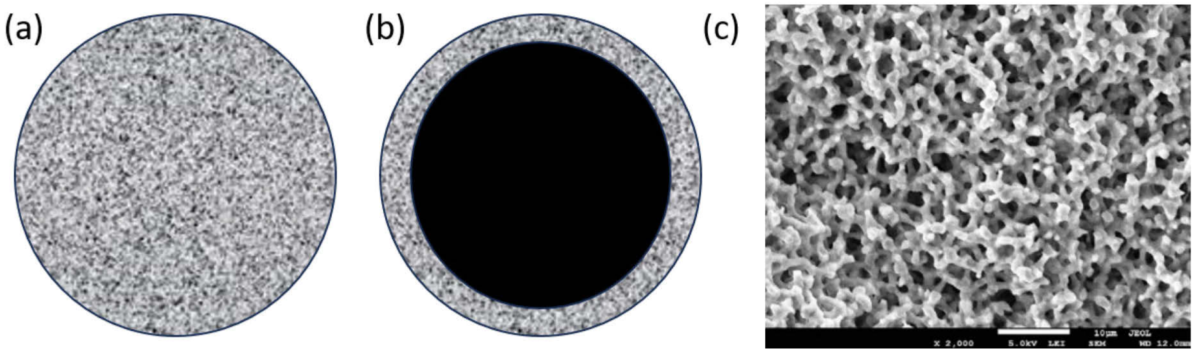

Fig. 4: Illustration of different column morphologies. (a) fully porous particle, (b) focused ion beam scanning electron micrographs of a wide-pore superficially porous particle, (c) scanning electron microscopy (SEM) of a bare-silica monolithic column. Subfigure (c) is reprinted with permission from Hormann et al., Morphology and separation efficiency of a new generation of analytical silica monoliths, J. Chromatogr. A, 1222 (2012) 46-58. Ref. [47]. Copyright 2011 Elsevier.

The first three (i-iii) columns are all particle-based columns and consist of distinct spherical particles inside a column housing. One characteristic parameter for each column type is the accessible surface area, where the interaction between the analyte and the stationary phase takes place [48]. The stationary phase consists either of the unmodified column support, as in the case of pure silica or polymeric columns, or the column support can carry specific ligands such as a C_{18} alkyl (octadecyl) ligand [49, 50]. The larger the accessible surface area, the higher the retention onto the stationary phase and the higher is the columns' sample capacity [51]. The sample capacity is a measure of how much analyte can be injected onto a column before breakthrough occurs, indicating that all interactions sites on the column are already occupied by analyte molecules [42].

FPP columns (i) consist of porous spherical particles, with more than 99% of the total surface area is inside the porous particles, while only a minor fraction is allocated to the outer particle surface [42]. The particles of SPP columns (ii), also known as core shell columns, have a solid core and a porous outer shell [52]. The surface area is smaller compared to FPP columns as only the porous shell contributes to the total surface area whereas the solid core does not contribute to the surface area [48]. NPP columns (iii) consist of solid particles, which do not possess any porous structure, therefore, they have only a very low total surface area compared to the porous column types [53]. Monolithic columns (iv) are not composed of spherical particles but rather form a continuous interconnected sponge-like chromatographic bed [54]. Silica-based monolithic columns consist of larger macropores, responsible for the low backpressure, and smaller mesopores where the analyte-stationary phase interaction takes place [55].

The unhindered diffusion of the analyte into the stationary phase pores is essential for a proper interaction [51]. In case of partial or total pore exclusion, only a small part of the theoretically available surface area of the stationary phase can be used. Consequently, there is much less interaction causing bad column performance or even lack of any retention [56]. The pore size should be at least four to ten times larger than the hydrodynamic diameter of the analyte [42, 51]. On the other hand, an increase in the pore size leads to a decrease in the total surface area what is accompanied with a decrease in analyte retention and sample capacity [51]. Typical pore sizes for small molecules range between 80 and 120 Angstroms (Å) [56, 57]. Columns dedicated for peptide analysis typically have a pore size of 160 Å [58], whereas protein columns have pore sizes between 200 and 1,500 Å [56, 59-61]. The appropriate pore size depends on the analyte's hydrodynamic diameter, which, in case of proteins, is influenced by the amino acid sequence and the protein's conformation. A denatured protein has a bigger hydrodynamic diameter than the protein in its native conformation, thus the choice of experimental conditions (native vs. denaturing) must be carefully considered [62].

1.3.3 Reversed-Phase Liquid Chromatography

Reversed-phase liquid chromatography (RP-LC) separates proteins according to their hydrophobicity, which correlates with the protein's molecular weight but is primarily dependent on the amino acid composition [63]. In the RP-LC separation, the protein is adsorbed onto the hydrophobic stationary phase at a high aqueous mobile phase composition and is eluted by applying an organic modifier gradient [42]. The hydrophobicity of a protein can be estimated using the grand average of hydropathy (GRAVY), which assigns to each amino acid side chain a hydropathy index in the range of +4.5 (isoleucine, most hydrophobic) and -4.5 (arginine, least hydrophobic) [64]. The hydropathy indexes of all amino acids are summed up and divided by the number of all amino acids to obtain the final GRAVY score. The higher the score, the more hydrophobic the protein is, and the more it should be retained in RP-LC.

A water-acetonitrile gradient is the most frequently used mobile phase composition for RP-LC of proteins. The application of such an organic modifier gradient might lead to poor recovery of the proteins due to solubility problems at high organic composition in the mobile phase. The recovery can be increased by using a higher mobile phase temperature, but this comes with the potential problem of on-column protein degradation [65]. Another benefit of higher mobile phase temperatures is sharper peaks due to accelerated diffusion rates [66] and maintaining higher protein solubility during acetonitrile gradients [60]. The use of ancillary additives like *n*-propanol or *n*-butanol can significantly increase recovery, allowing for the use of lower temperatures [65, 67]. The stationary phase typically consists of alkyl ligands such as octadecyl (C_{18}) or butyl (C_4), with the latter historically preferred due to the assumption of better recovery compared to C_{18} columns [68]. The recovery depends on a multitude of stationary phase properties including carbon load, ligand density, ligand surface coverage, flexibility of ligand, relative hydrophobicity, and the presence of free silanols

[65, 68, 69]. The detrimental effect of secondary interactions by free silanols can be reduced by end-capping [70].

Mobile phase additives can be used to tune selectivity of protein separations. Trifluoroacetic acid (TFA) provides very sharp peaks and increases protein solubility, which is why the protein's recovery becomes higher [71, 72]. Formic acid (FA) is used in LC-MS experiments as mobile phase additive because of its better MS-sensitivity than TFA but suffers from broader peaks and stronger peak tailing [71, 73].

Column temperature has a significant influence on the LC separation of proteins. It has been demonstrated that the protein recovery increases at elevated temperatures, typically ranging from 80-90°C, especially for mAbs [73]. The recovery is a measure of how much of the injected analyte elutes from the LC system and can be determined by the peak area [42]. The addition of 5 % *n*-butanol as an ancillary solvent to the mobile phase decreases the minimal required column temperature for sufficient recovery, thereby reducing the risk of heat-induced degradation of the column and protein [73].

RP-LC of proteins is considered a denaturing technique due to the common usage of organic modifiers, acidic additives and elevated temperature [74] in contrast to other LC methods like ion-exchange chromatography (IEX) [75], size-exclusion chromatography (SEC) [76] and hydrophobic interaction chromatography (HIC) [77]. Denaturation of proteins comes with some advantages like sharper peaks due to restriction of secondary interactions between the protein and the stationary phase [78]. On the other hand, there are applications where it is necessary to keep the protein in its native structure e.g. for enzyme activity [79] or drug protein interactions [80].

The retention behaviour of proteins differs significantly from smaller molecules and is described as an on/off-like retention mechanism, where the protein is completely retained until a specific organic modifier concentration has been reached, and above this concentration, there is no retention at all [81-83]. In other words, the protein's retention and elution behaviour is very sensitive to even small changes (< 3 %) of the organic modifier concentration what can be expressed by the analyte's *S*-value. The *S*-value is the slope of the logarithmic retention factor *k* and the change in the organic modifier concentration (see **Fig. 5**).

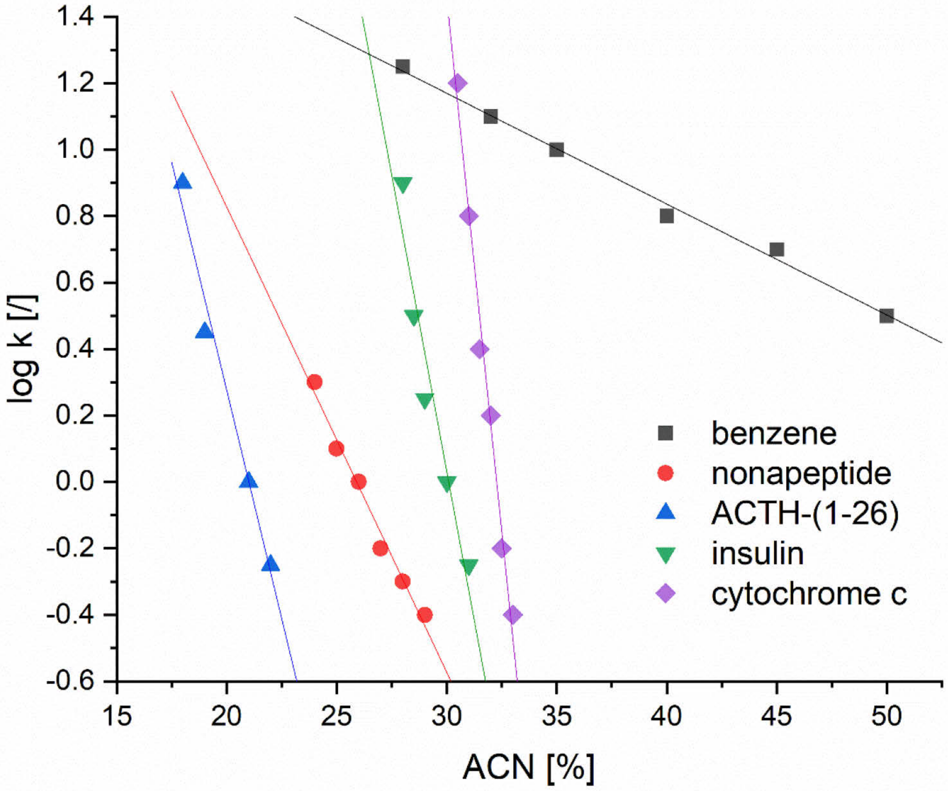

Fig. 5: Plot of the logarithmic retention factor *k* vs. the concentration of the organic modifier acetonitrile (ACN). The slope of the regression lines is equivalent to the analyte's *S*-value. Adapted with permission from Terabe et al., Separation of cytochromes c by reversed-phase high-performance liquid chromatography, J. Chromatogr. A, 212 (3) (1981) 295-304. Ref. [84]. Copyright 1981 Elsevier.

Small molecules like benzene have a very shallow slope, therefore, the corresponding *S*-value is small [*S*(benzene) = 3)]. The larger the analyte's molar mass becomes, the steeper the slope, and the higher the respective *S*-value. A protein like cytochrome c, with a molar mass of approximately 13,000 g/mol, has an *S*-value of 64. One consequence of the on/off-like retention mechanism is that only a small part of the column length is effectively used for the separation, while the rest of the column's length acts more like an inert void volume, potentially leading to undesired band broadening [83].

The gradient steepness *b* is an important factor and can be calculated as follows [83]:

$$b = \frac{S\Delta\phi\, t_0}{t_G}$$

(eq. 1.5)

Where $\Delta\phi$ is the change of the organic modifier concentration, t_0 is the void time and t_G is the gradient time.

If the same gradient time and flow rate is used, the gradient steepness *b* is shallower for shorter columns (smaller t_0, see (eq. 1.5), which overcompensates for the lower plate number *N* and increases the peak capacity for the shorter columns [85]. Therefore, the use of shorter columns is deemed more promising for future applications and comes with some additional benefits like shorter analysis time, lower sample consumption, faster re-equilibration and less on-column degradation because of shorter on-column residence time [83].

At very high organic concentrations, the RP-LC separation mode can change into a hydrophilic interaction liquid chromatographic mode (HILIC) [86]. In HILIC, a reversed gradient elution compared to RP-LC is applied (i.e., from high organic to high aqueous eluent composition).

1.3.4 Ion-Exchange Chromatography

In ion-exchange chromatography (IEX), proteins are separated according to their charge. The analysis of the protein's charge variants is a critical quality attribute in the quality control of protein-based biopharmaceuticals [87]. The protein's charge depends on its isoelectric point (p*I*). The p*I* of a protein can be experimentally determined by isoelectric focusing (IEF), where the protein moves under the influence of an electric field inside a gel, which exhibits a pH-gradient [88]. The protein's charge changes in the gel depending on the respective pH-segment of the gel and stops moving when its net charge reaches zero [89]. The pH-value at which the protein's net charge is zero is the p*I* of the protein. Alternatively, the protein's theoretical p*I* can be calculated based on its amino acid composition by software tools like ProtParam [90]. The significant difference between IEX and IEF is that IEX interacts only with the charged protein surface, while IEF separates proteins based on their total net charge [91]. Therefore, the separation order between IEX and IEF can be different.

The stationary phase of an IEX column consists of ionizable groups of either positive charge in case of anion exchange chromatography (AEX) or of negative charge in case of cation-exchange chromatography (CEX) [42]. CEX is used for the separation of basic proteins, which exhibit a positive charge if the pH is below their p*I* and are therefore retained on the negatively charged surface of the stationary phase by ionic interactions. The proteins can be either eluted by the application of a (i) salt-gradient, (ii) pH-gradient or (iii) a combined of salt- and pH-gradient, called a salt-mediated pH-gradient [91]. A salt-gradient simply displaces the protein ion by a salt-ion of the same polarity, e.g., a positively charged protein can be displaced by a sodium cation (Na^+) using a sodium chloride (NaCl) gradient. The application of a mobile phase pH-gradient leads to a change of the protein's charge. In case of CEX, a gradient from low to high pH is applied. As a result, the proteins become protonated, exhibit a positive charge, and are retained on the stationary phase. During the gradient the pH becomes higher, and the protein deprotonates until it possesses a neutral or even negative charge and is therefore not retained on the stationary phase anymore.

CEX is regarded as the gold standard for monoclonal antibody separations, as their p*I* values usually range between 6 and 9.5, which falls withing the slightly basic range [74, 88, 92]. In CEX, the acidic charge variants elute before the main charge variant, and the basic variants elute last. IEX stationary phases can be classified into four groups depending on their stationary phase [42]:

(i) Weak cation exchange (WCX) chromatography stationary phases have a weakly acidic group like carboxy groups, which exhibit a negative charge depending on the mobile phase pH-value [42]. If the pH value is above the pK_a-value of the carboxylate groups, they are negatively charged. At a pH-value below the pK_a, the carboxylate group is protonated and possesses no charge. Without a negative charge, the positively charged proteins are no longer retained and elute. Thus, the mobile phase pH influences the elution behaviour based both on the protein's charge and the stationary phase charge in the case of weak ion exchange stationary phases.

(ii) Weak-anion exchange (WAX) columns consist of a weakly basic group like tertiary amines [42]. The same principles apply as for the WCX columns, just with a reversal of the charge and an opposite pH-gradient design (from high pH to low pH).

(iii) Strong-cation exchange (SCX) columns have a strongly acidic group like sulfonate, which has a low pKa-value, resulting in a nearly pH-independent, permanent negative charge [42].

(iv) The last class of IEX columns is the strong anion exchangers (SAX), which have a permanent positive charge, usually in the form of a quaternary ammonium group [42].

Most IEX columns have non-porous particles that consist of a co-polymer as hydrophobic core and are grafted with a hydrophilic layer to minimize undesired hydrophobic interactions [74]. The polymeric base material allows the use of the entire pH range, in contrast to the more limited range of silica material (typically pH 2-8) [49, 92, 93]. The ionic ligands are only on the outer surface of the particle. A minimum buffer concentration is required to prevent the column from swelling, which is caused by the repulsion of the equally charged ionic groups [92, 94, 95]. In absence of any buffer salts, the column resin swells and increases the column backpressure, whereas with a minimum recommended buffer strength of 20 mM, the stationary phase is de-swelled and has a lower column backpressure [92].

The selectivity in IEX is not only determined by the stationary phase but also by the type of the buffer salts in the mobile phase. The mobile phase strength for different cations used in SCX can be sorted according to the retention factor *k* (in descending order from high values of *k* to smaller values) [42]:

$Li^+ < H^+ < Na^+ < NH_4^+ < K^+ < Rb^+ < Cs^+ < Ag^+ < Mg^{2+} < Zn^{2+} < Co^{2+} < Cu^{2+} < Cd^{2+} < Ni^{2+} < Ca^{2+} < Pb^{2+} < Ba^{2+}$

Some challenges arise from the usage of high salt concentrations. The use of halides like chloride (Cl^-) is corrosive for stainless steel instruments [96]. This can be addressed by the usage of bio-inert instruments where stainless steel is replaced by alternative materials like titanium [39]. High salt concentrations and the frequent use of non-volatile salts are detrimental for the hyphenation of IEX with MS [74, 97, 98]. The mobile phase incompatibility can be overcome by using two-dimensional liquid chromatography (chapter 1.3.6) which removes non-volatile salts prior MS analysis

[74]. An alternative approach is to use volatile salts at lower concentrations and application of a pH-gradient to directly couple IEX with MS [74, 75].

In IEX, the proteins remain in their native structure, which is crucial for preserving their biological activity [74]. In addition to its use for charge variant analysis, IEX is also employed for the purification of biopharmaceutical proteins [99].

1.3.5 Chiral Chromatography

The chirality of amino acids in peptides and proteins is crucial for their biological activity. The L-enantiomer of amino acids is the dominant configuration in biological systems, but there are several examples where the presence of D- amino acids is found in proteins in diseases like Alzheimer's disease [100]. The analysis of isomeric impurities in protein- or peptide-based drug products is of utmost importance, as the amino acid configuration is responsible for the therapeutic effects as well as of possible toxic side effects [101]. Consequently, there is a high demand for enantioselective analysis methods to determine the absolute configuration of amino acids in biological products, as well as for quality control for synthetic therapeutic peptides. The chiral analysis can be performed at both the peptide level and the amino acid level. The latter requires full hydrolysis of the protein or peptide [102]. If acidic hydrolysis is used, care must be taken to avoid the influence of hydrolysis-induced racemization [103]. Deuterated chloric acid (DCl) and deuterium oxide (D_2O, heavy water) can be used to distinguish between the original configuration of the amino acids and hydrolysis-induced racemisation [102]. The incorporation of deuterium at the alpha carbon atom during the racemisation causes a +1 Da mass shift between non-racemised (contains ^1H) and the racemised amino acids (contains D) which can be differentiated using mass spectrometry [103]. The chiral analysis of the amino acids can be carried out directly on the free amino acids or after their derivatization. Different chiral stationary phases (CSP) are used to separate peptide and amino acid enantiomers including cinchona alkaloid-based ion exchanger [104], crown ether [105-107], polysaccharide [102, 108], macrocyclic antibiotic and steroid-based columns [102]. The ZWIX(+) and ZWIX(-) columns (**Fig. 6**) belong to the cinchona alkaloid-based columns, and their CSPs are diastereomeric to each other but behave like enantiomers, therefore called pseudo-enantiomers. Consequently, they provide opposite enantiomer elution order in enantiomer separations.

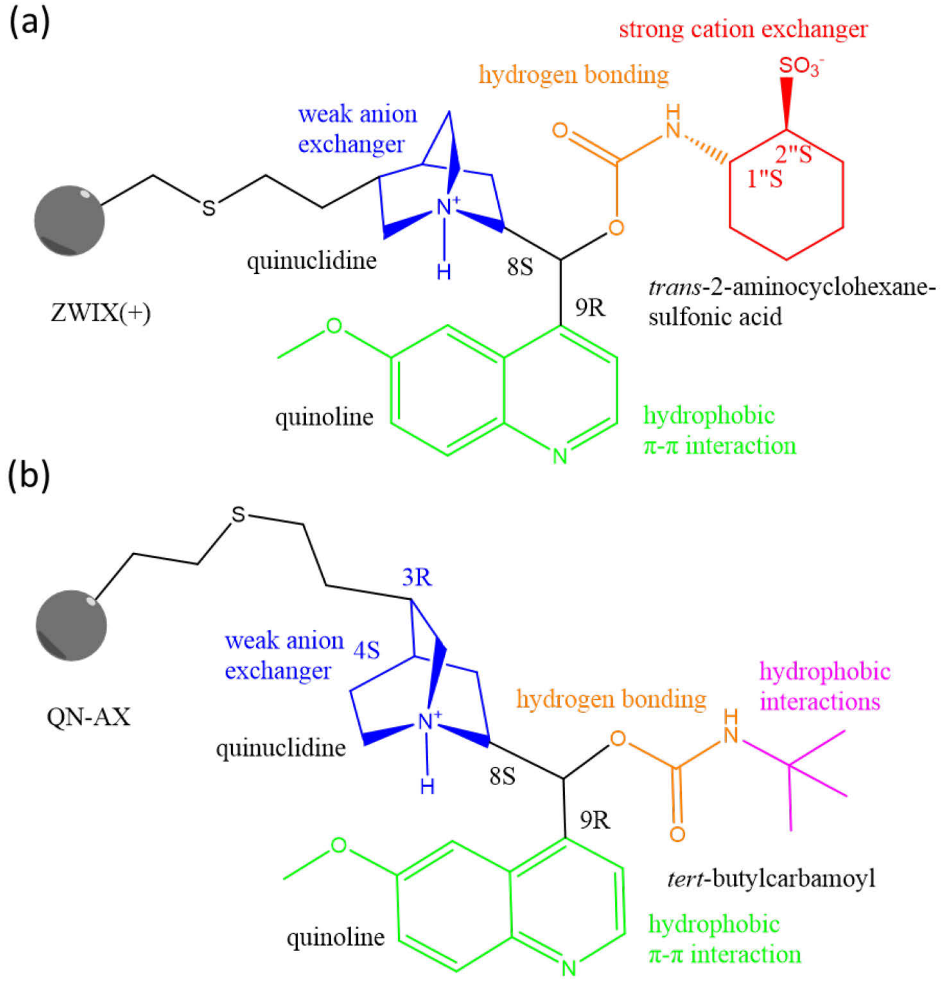

Fig. 6: Structures of the chiral stationary phases of the (a) ZWIX(+) column and (b) the QN-AX columns. The molecule parts contributing to the main interactions such as the weak anion exchange (blue), strong cation exchange (red), hydrophobic π-π (green), hydrogen bonding (orange) and hydrophobic van der Waals forces (purple) are highlighted.

The ligand on the ZWIX column consists of a weak anion exchange quinuclidine moity, a strong cation exchanger group (*trans*-2-amino-1-cyclohexanesulfonic acid) and the quinoline ring with hydrophobic π-π interactions. The ZWIX columns have been used for the separation of free, non-derivatized amino acids [104]. The performance of superficially porous particle columns is better compared to fully porous particle columns [109].

The QN-AX and QD-AX columns also belong to the cinchona alkaloid-based columns and are pseudo-enantiomeric, actually diastereomeric to each other [110]. In contrast to the ZWIX columns, these two columns do not have a strong cation exchange group but instead a *tert*-butylcarbamoyl moiety with hydrophobic interactions. A combination of the QN-AX column and the ZWIX(+) column as a tandem column, where the two columns are connected in series, could be used to separate AQC-derivatized amino acids [111].

1.3.6 Two-Dimensional Liquid Chromatography

The combination of two or more chromatographic dimensions is called two-dimensional (2D-LC) or multi-dimensional liquid chromatography, respectively. A very simple application of 2D-LC is paper chromatography, where the paper only needs to be dried and rotated by 90° before a second mobile phase with different selectivity is used to obtain a two-dimensional separation [112].

2D-LC can be done either offline or online [113, 114]. In the offline mode, fractions of the first dimension (^{1}D) are collected and stored until they are later injected onto the second dimension (^{2}D). Offline 2D-LC can be performed using a standard 1D-LC instrument without any special technical requirements [114]. Indeed, the same instrument can be used for both dimensions by changing the respective mobile and stationary phases. Some advantages of the offline 2D-LC include the possibility to aliquot the fractions, to concentrate the fractions, and to exchange the solvent prior further analysis. Furthermore, there is no time limit for the ^{2}D separation in contrast to some online 2D-LC modes. However, offline 2D-LC analysis can be very time consuming, requires more manual interventions like pipetting of the ^{1}D fractions and suffers from poor reproducibility [114].

Online 2D-LC, however, requires specific instruments und software. In between the two dimensions, a modulation valve, along with several capillaries, is needed to collect, store, and transfer fractions from the ^{1}D separation [115]. The modulation valve acts as an injector for the ^{2}D.

Different modes of operation can be used for online 2D-LC to address specific analytical requirements (see **Fig. 7**).

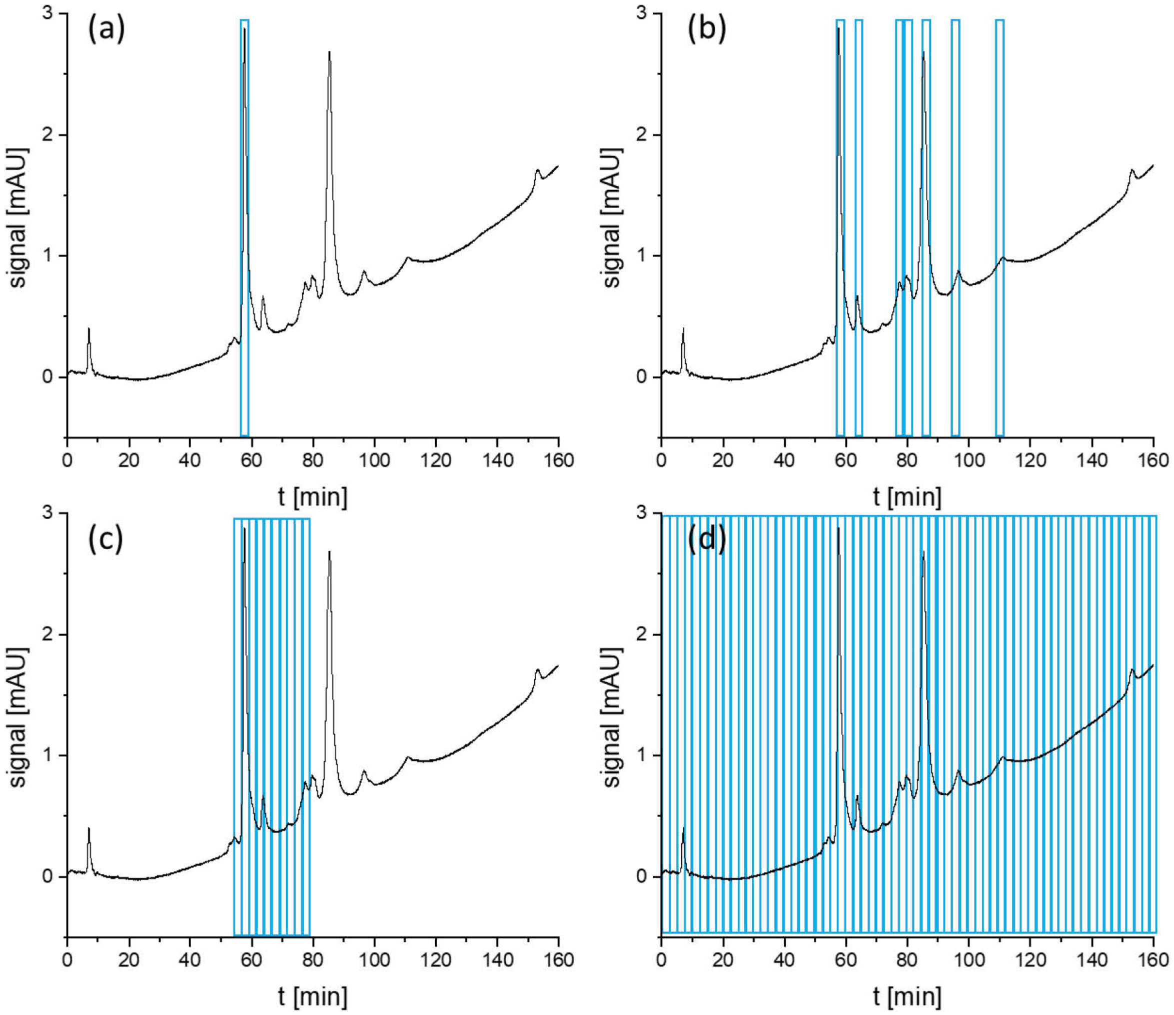

Fig. 7: Illustration of different 2D-LC operation modes showing the chromatogram of the first dimension (^{1}D) separation and fractions (cuts), which are transferred to the second dimension (^{2}D) separation (blue boxes). (a) Single heart-cutting (LC-LC) mode, (b) multiple heart-cutting (mLC-LC) mode, (c) selective comprehensive (sLCxLC) mode, and (d) full comprehensive (LCxLC) mode.

The most straight forward operation mode is the single heart-cutting mode (LC-LC, see **Fig. 7a**), where only a single fraction of the ^{1}D is transferred to the ^{2}D [115, 116]. The ^{2}D analysis time is independent of the ^{1}D analysis time, as is the case for offline 2D-LC as well.

The extension of the LC-LC mode is the more frequently used multiple heart cutting mode (mLC-LC), where several fractions of the ^{1}D are transferred to the ^{2}D (see **Fig.**

7b) [115, 117]. The Agilent Infinity II 2D-LC system uses two loop decks (deck A and B), each consisting of six capillaries. There is a constant flow from both dimensions, therefore, one capillary in each deck acts as a flow-through capillary and cannot be used for sample storage. Thus, only five capillaries of each deck (a total of ten loops) can be used to store fractions from the ^{1}D. Consequently, a minimum of ten fractions can be collected and stored during the ^{1}D separation time. Depending on the ^{2}D run time, one or several loops can be injected and already analysed during the ^{1}D separation time. Loops with fraction that have already been analysed can be used again for additional fraction collections during the same 2D-LC run. The more fractions there are to be analysed, the shorter the runtime of the ^{2}D must be.

The transfer of the entire effluent of the ^{1}D into the ^{2}D is called full-comprehensive 2D-LC (LCxLC, see **Fig. 7d**) [115, 118]. In this mode, the entire effluent of the ^{1}D is analysed, eliminating the risk of missing an important fraction of the ^{1}D. In this setup the modulation valve is only equipped with two loop capillaries for deck A and B, respectively. One capillary is used to collect a fraction of the ^{1}D effluent, while the second one is used for the ^{2}D analysis. The ^{2}D run time needs to be very fast to enable the full analysis in the ^{2}D before the second loop is completely filled to avoid sample loss.

A special case of LCxLC is when only one or several parts of the ^{1}D effluent are transferred to the ^{2}D. This approach is called selective comprehensive liquid chromatography (sLCxLC, see **Fig. 7c**) [115, 119]. In this mode, the same valve and loop configuration as in mLC-LC is used, but the ^{2}D method can be slower because the ^{1}D-fractions are stored in the storage loops until they are analysed. However, if several parts of the ^{1}D-chromatogram are to be analysed in sLCxLC mode, the ^{2}D analysis time must be fast enough to ensure that the storage loops have been analysed and can be used for new sample collection.

1D-LC has some limitations regarding its peak capacity. As a rule of thumb, 1D-LC can separate samples containing 10 or 20 compounds within one or two hours, or up to 50 compounds in about 10 h [115, 120, 121]. The addition of a second dimension in 2D-LC not only adds the peak capacity of the second dimension but even multiplies it [120]. An example from Sarrut et al. showed a 4-fold increase in the peak capacity at an analysis time of 60 min using 2D-LC compared to 1D-LC [122]. The performance can also be compared in terms of the peak production rate, which is the peak capacity dived by the analysis time [115]. 1D-LC has peak production rate of around one peak per minute, while 2D-LC separations can achieve a peak production rate of one peak per second [115].

1.3.6.1 Orthogonality

One of the most critical requirements for efficient 2D-LC separation is the orthogonality of the two separation dimensions, meaning a sufficiently different selectivity for both dimensions [123]. The orthogonality can be estimated and visualized by plotting the normalized ^{1}D and ^{2}D retention times [123]. In case the two dimensions have identical selectivities, no additional separation through the ^{2}D can be achieved, and data points are located on a straight diagonal line (**Fig. 8A**) [120]. In this case, the ^{2}D does not bring any advantage at all. The ideal case is when the selectivity is completely different, and the entire possible 2D separation space is used (**Fig. 8B**). The more realistic case for achieving sufficient orthogonality is shown in **Fig. 8C**, where the peaks are distributed randomly and overlap in several cases. Different classes of analytes can be grouped in a certain area of the 2D separation space, which might help with the classification of unknown compounds (**Fig. 8D**) [120]. The degree of orthogonality can be expressed numerically, for example, by dividing the 2D separation space into bins and determining which bins contain a peak and which do not contain any peak [123].

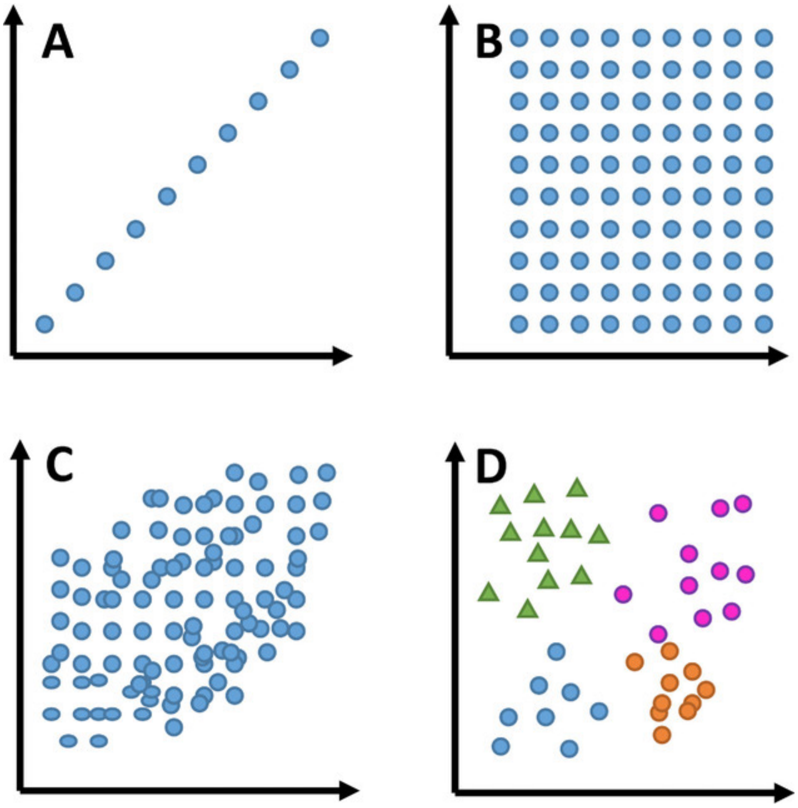

Fig. 8: Examples of the theoretical peak distributions for different degrees of orthogonality between both dimensions. (A) The selectivities in both dimensions are identical resulting in no orthogonality. (B) The ideal case if the orthogonality is maximal and (C) the more realistic case of high orthogonality. (D) Peak distribution of different classes of analytes. Usage granted by CC BY, Pirok et al., Optimizing separations in online comprehensive two-dimensional liquid chromatography, J. Sep. Sci., 41 (1) (2018) 68-98. Ref. [120]. Copyright 2017 WILEY.

1.3.6.2 Modulation

Depending on the two selected separation dimensions, there might be incompatibility issues between the two mobile phase systems. Therefore, different modulation strategies were developed to overcome these incompatibility issues. Incompatibility can arise from miscibility problems when the eluent of the ^{1}D is immiscible with the mobile phase of the ^{2}D [120]. For example, a normal-phase chromatography mobile phase composed of *n*-hexane cannot be mixed with an aqueous mobile phase from ion-exchange chromatography. Mixing of high salt containing mobile phases, such as those used in IEX chromatography, with mobile phases with high organic concentration, like in HILIC, can result in precipitation issues [123]. Mixing two mobile phases with different viscosities can lead to flow instabilities and an effect called viscous fingering, which can result in poor peak shapes or even peak splitting [115, 124]. Furthermore, the eluent of the ^{1}D, which is also the injection solvent for the ^{2}D, can have a strong elution strength on the ^{2}D separation, leading to peak broadening or peak shape distortion [125]. For example, using pure aqueous mobile phases from IEX as ^{1}D in HILIC separations as ^{2}D, where water is the strong eluent, can result in these issues [120]. The ^{1}D effluent can also cause problems with ^{2}D detectors like MS or evaporative light scattering detector (ELSD), which do not tolerate high amounts of non-volatile salts [97, 126, 127]. The ^{2}D stationary phase might degrade through the ^{1}D effluent plug e.g., silica-based columns are unstable at high pH, which might be the elution condition of IEX separations [128]. These incompatibility issues can be overcome using different modulation techniques.

The Agilent Infinity II 2D-LC system used for the presented works in this dissertation implemented the so-called active solvent modulation (ASM, refer to **Fig. 9**) [129]. The ASM valve splits the flow of the ^{2}D pump into two flow paths (**Fig. 9B**). One fraction of the flow still goes through the sample loop to inject the sample onto the ^{2}D column. The second fraction goes through a bypass capillary and joins the flow leaving the sample loop to mix and dilute the solvent prior entering the ^{2}D column. This dilution by the ^{2}D mobile phase decreases the potential high elution strength from the ^{1}D mobile phase in the sample loop, reducing problems such as break-through or peak shape deterioration [130].

An alternative modulation mode is the stationary-phase assisted modulation (SPAM) where, instead of capillary loops, small-volume trapping columns are used [131]. The ^{1}D effluent flows through the trap columns, and the analytes of interest are retained onto the column, while the mobile phase passes unretained. If necessary, the elution strength of the ^{1}D effluent can be reduced by mixing with a low elution strength diluent prior entering the trap columns [131]. The ^{1}D effluent is efficiently removed, and the analyte is focused onto the trap column. The ^{2}D injection volume of SPAM can be much lower compared to ASM allowing the use of shorter columns without a loss of efficiency and thus reducing the total analysis time [115].

Important prerequisites for the use of SPAM are that all the trapping columns must have identical properties, and the analytes are sufficiently retained onto the columns [132].

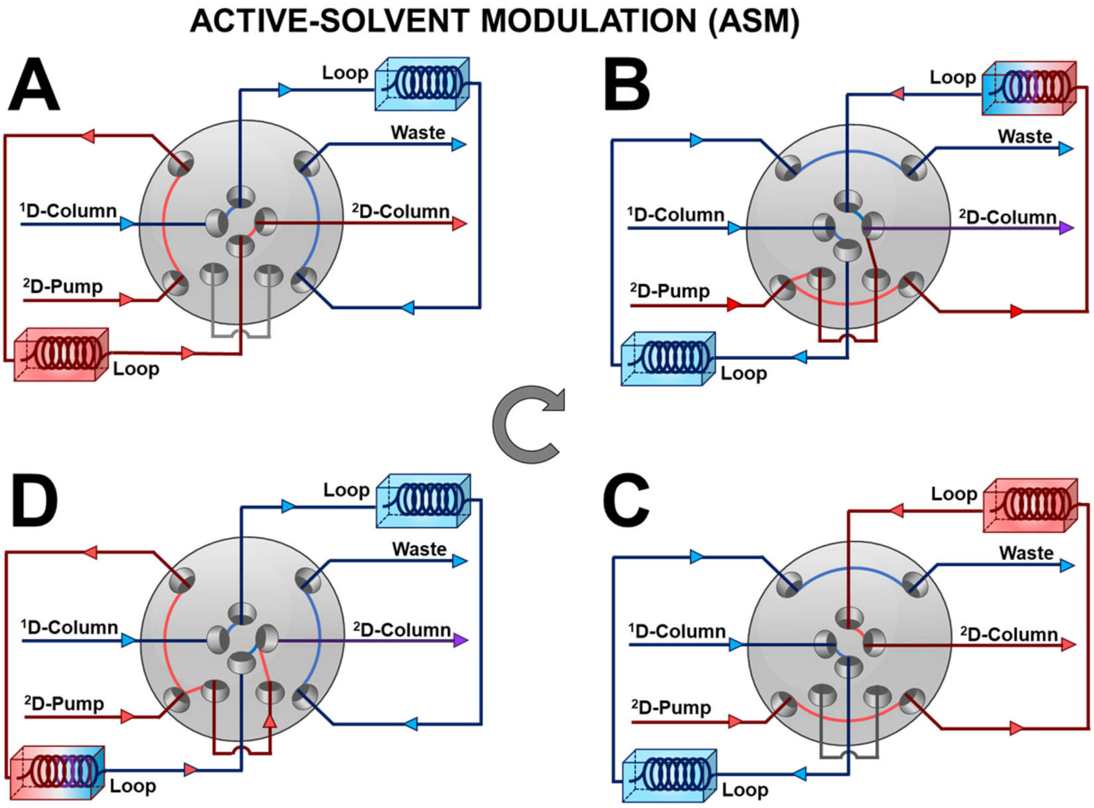

Fig. 9: Illustration of the working principle of the active solvent modulation valve. Positions A and C are equivalent to the standard 2D-LC valve positions. Position B and D show the positions where the eluent coming from the sample loop is diluted by a portion of the ²D pumps flow prior entering the ²D column. Usage granted by CC-BY-NC-ND, Pirok et al., Recent Developments in Two-Dimensional Liquid Chromatography: Fundamental Improvements for Practical Applications, Anal. Chem., 91 (1) (2019) 240-263. Ref. [115]. Copyright 2018 American Chemical Society.

Chromatographic separations are always accompanied by sample dilution effects due to band broadening effects during the separation. This dilution can be detrimental for the sensitivity and should therefore be minimized. In 2D-LC the second dimension further increases this dilution effect [133]. Moreover, since in most cases not an entire ^{1}D-peak is collected in the storage loops, there is an additional dilution effect [134]. Therefore, the sensitivity in 2D-LC can be lower compared to 1D-LC method. On the other hand, the two-fold separation in two dimensions can decrease the noise level, and the final signal-to-noise level can be higher compared to 1D-LC method. Thus, depending on the analytical problem, either 1D-LC or 2D-LC can have a better sensitivity.

1.4 Mass Spectrometry of Proteins

An important performance parameter for mass spectrometry instruments is their mass resolving power R_p based on a single mass peak [135]:

$$R_p = \frac{m}{\Delta m}$$

(eq. 1.6)

Where m is the m/z value of the ion and Δm its full width of the peak at half maximum (FWHM).

The ionization for LC-MS of proteins is mostly based on electrospray ionisation (ESI) [25].

1.4.1 Fragmentation

Tandem mass spectrometry (MS/MS) allows the controlled fragmentation of selected precursor ions in the gas phase. The gas phase fragmentation of ions using mass spectrometers is called tandem mass spectrometry (MS/MS). It helps both to identify analytes with higher certainty and can increase the sensitivity in quantitative experiments. Some instruments, like ion traps, allow to fragment isolated product ions again (MS^n), which can increase the selectivity for qualitative experiments. One standard fragmentation technique is the so-called collision induced dissociation (CID) or collisionally-activated dissociation (CAD), which uses a neutral gas such as nitrogen (N_2) as a collision gas for fragmentation [136]. The neutral gas molecule has an inelastic collision with a precursor ion, transferring the collision energy to the ion's internal energy [137]. This vibrational energy is rapidly redistributed throughout the precursor ion, leading to the cleavage of its weakest bond(s) [138]. Rearrangements of the precursor ion prior to fragmentation is often observed. In case of peptides, the amide bond in the peptide backbone is typically cleaved, resulting in b- and y-type fragments (refer to **Fig. 10**) [139]. Furthermore, the loss of carbon dioxide, water, and ammonia was found frequently [138]. Some labile bonds, such as post-translational modifications (PTM), might break even faster than the peptide bond, making PTM characterisation considerably more challenging using CID methods [138]. Another collision-induced fragmentation technique available for Orbitrap MS instruments is the so-called higher energy collisional dissociation (HCD), which can increase sequence coverage because of longer b/y-series [140, 141].

A different type of gas phase fragmentation is electron-based and provides c- and z-type fragments, making it a good choice for PTM-characterisation [142]. Electron capture dissociation (ECD) and electron-transfer dissociation (ETD) are two major electron-based fragmentation techniques [138]. ECD is usually used with Fourier-transform ion cyclotron resonance (FT-ICR) instruments because the electromagnetic field stabilizes the electron’s motion [138]. Paul trap type MS instruments suffer from a low mass cut-off limitation of the radiofrequency field, making it difficult to trap the electrons [138]. ETD can be implemented with ion trap type MS instruments like Orbitraps [138]. In contrast to the CID techniques, there is no rearrangement step prior the fragmentation for the electron-based fragmentation techniques, thus not only labile bonds are cleaved. Therefore, fragments still containing PTMs can be observed, which makes their identification and location possible [138]. According to the Utah-Washington mechanism the electron is first captured by the π-orbital of the positive charge site of the peptide followed by an intra-molecular electron transfer to the amide π* or S-S* orbitals and finally the N-Cα bond is cleaved [138, 143]. ETD uses anions to transfer electrons to the multiply charged-peptide cations and enables the implementation in low-cost ion trap instruments [144].

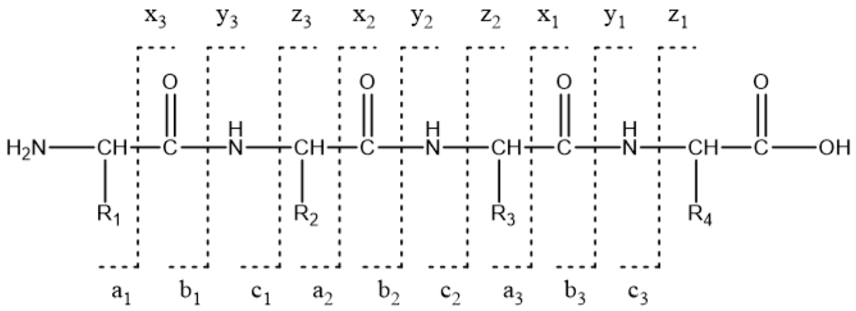

Fig. 10: Peptide fragmentation scheme with the nomenclature of Roepstorff [145] and Biemann [146].

One way to assess the performance of the different fragmentation techniques is to compare the sequence coverage, representing how many amino acids can be identified and their position assigned within the protein using tandem MS. The frequently used CID has a lower sequence coverage compared to ETD and ECD fragmentation. Furthermore, these electron-based techniques cleave disulphide bonds without the need for disulphide reduction and alkylation prior MS analysis [138].

1.4.2 Intact Protein Mass Spectrometry

The mass spectrometric measurement of proteins is significantly different compared to small molecules due to the higher mass and the vast structural heterogeneity of the proteins. One major difference is the absence of a monoisotopic peak for large proteins. The stable isotopes of carbon have an abundance of 98.9 % for ^{12}C and 1.1 % for ^{13}C, respectively [147]. A typical monoclonal antibody has around 6,600 carbon atoms [148]. The isotope abundance can be calculated using software tools like IDCalc – Isotope Distribution Calculator [149, 150]. The most abundant carbon isotope composition is $^{12}C_{6529}{}^{13}C_{71}$, with a fraction abundance of 4.75 % when only carbon atoms are considered. The abundance of the monoisotopic peak containing only ^{12}C ($^{12}C_{6600}$) is close to zero and cannot be observed by MS measurements. The broad isotope distribution is one reason why the MS sensitivity for intact proteins is lower compared to small molecules (see **Fig. 11**). This is because the signal of one molecule is distributed across many isotope peaks, in contrast to only a few isotope peaks for small molecules. Large proteins such as mAbs have an isotopic envelope which is about 25 Da broad [151]. Consequently, small mass changes, such as those resulting from deamidation (+ 1 Da), dehydration (-18 Da), and oxidation (+ 16 Da) pose challenges in terms of mass resolution and necessitate the use of mass spectrometers with very high resolving power [25, 148].

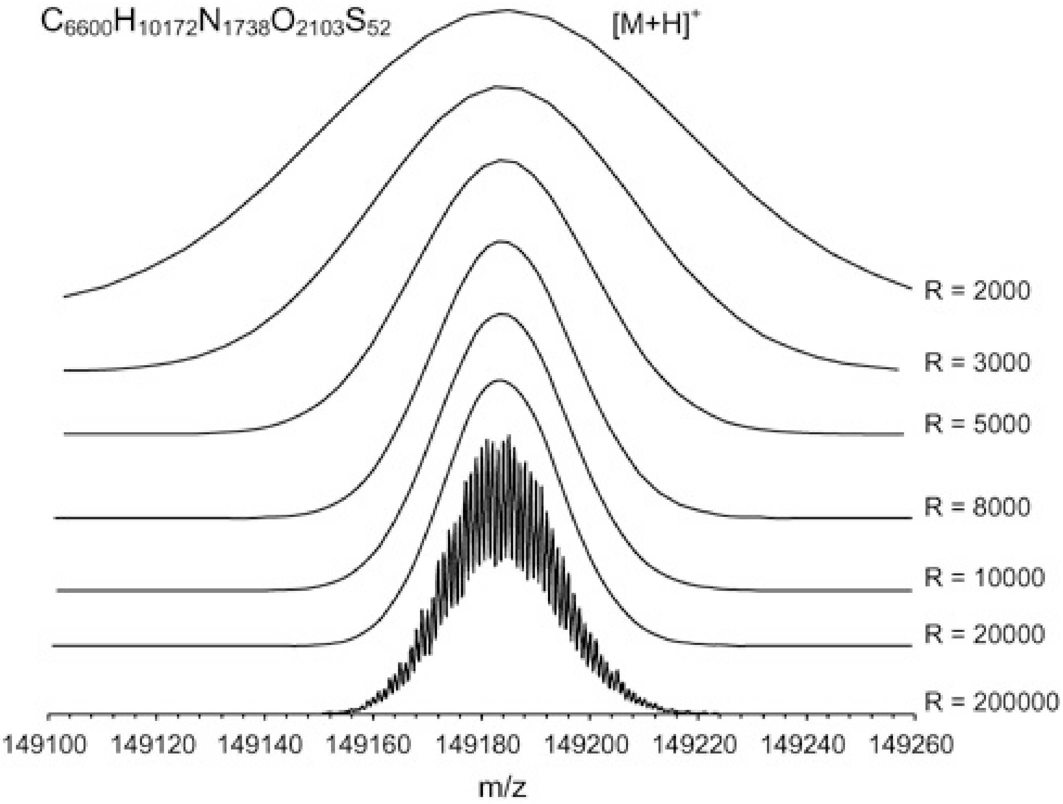

Fig. 11: Simulated isotopic distribution, at different mass resolving powers (see(eq. 1.6), of a typical mAb with an elemental composition of $C_{6600}H_{10172}N_{1738}O_{2103}S_{52}$. The simulation was performed on a custom developed program (MassAnalyzer) by randomly determining what isotope each atom in a molecule will be, using the natural isotopic abundance of each isotope as the probability of occurrence of the corresponding isotope. Distributions shown here were generated by simulating 200,000 molecules. Molecules with same total nominal mass were combined and the peak was represented by a Gaussian profile with a width Δm (FWHM) determined by the mass resolving power. Reprinted with permission from Zhang et al., Mass spectrometry for structural characterization of therapeutic antibodies, Mass Spectrom. Rev., 28 (1) (2009) 147-76. Ref. [148]. Copyright 2008 WILEY.

The ionization of proteins using positive electrospray ionization (ESI) under denaturing condition results in several charge states, typically ranging between +40 to +60 while small molecules often have only one or a few charge states [25]. The presence of multiple charge states, often referred to as the protein's charge envelope, results in a signal distribution across multiple MS peaks with varying charges, consequently reducing MS sensitivity. Both the isotope distribution and the charge envelope result in lower MS signal intensity compared to small molecules [152]. The charge state can be calculated based on the *m/z* difference between the MS peaks, and the intact protein mass can be calculated by mass spectra deconvolution using software tools [153]. One example for an intact mAb and its main glycoforms is shown in **Fig. 12**.

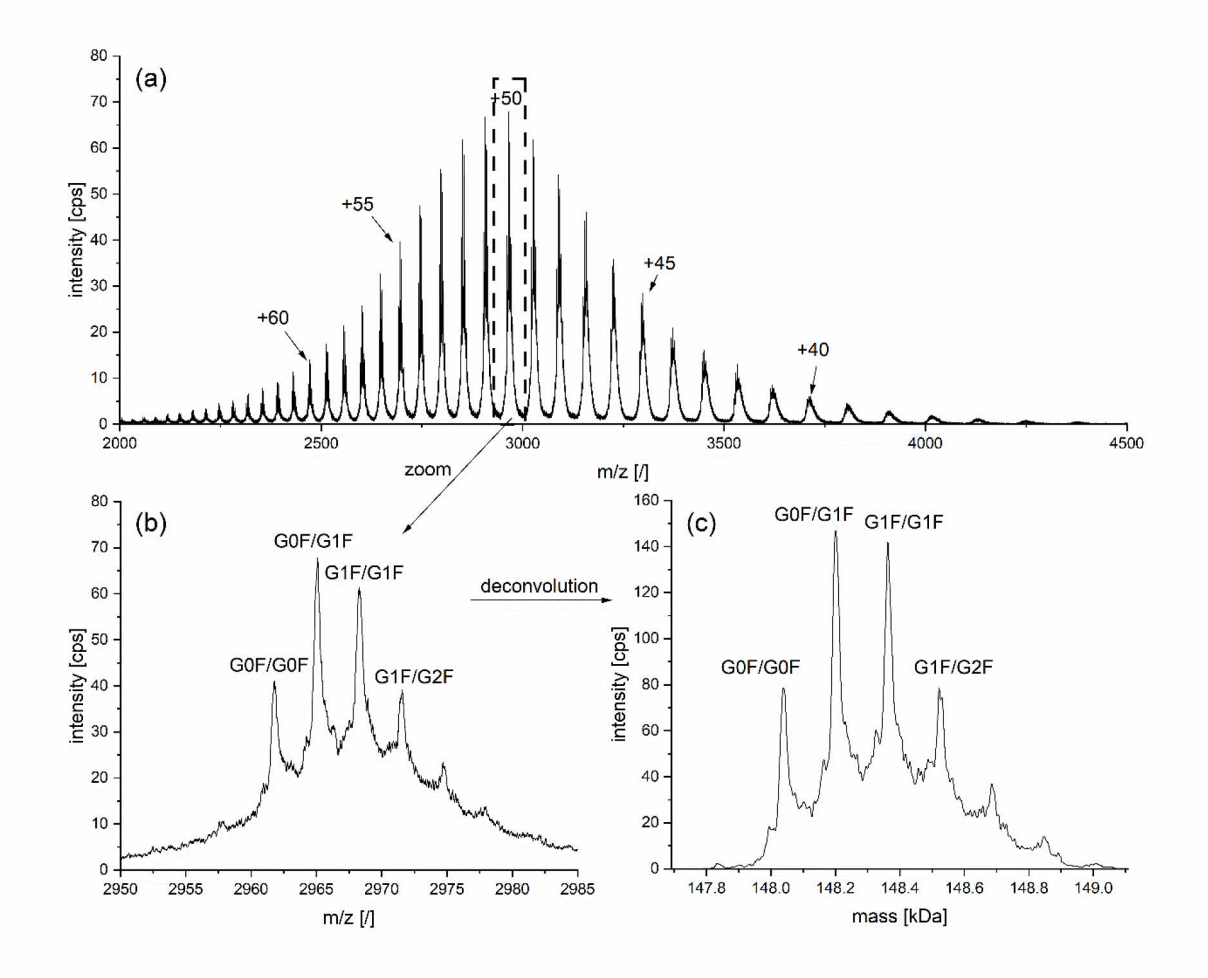

Fig. 12: Intact protein MS spectra of the NISTmAb. (a) Raw MS spectrum with charge envelope, (b) zoom-in of the +50 charge state and (c) deconvoluted mass. G0F, G1F and G2F refer to different *N*-glycosylations of the two heavy chains.

The number of charge states can be reduced using alternative ionization methods, such as matrix assisted laser desorption/ionization mass spectrometry (MALDI-MS), but the latter cannot be easily hyphenated to LC [25]. A different option is to use native MS, where the protein is kept close to its original folding structure [152]. ESI of native proteins leads to lower charge states and a lower number of different charge states (**Fig. 13**). As the number of charges decreases, the *m/z* value increases, necessitating extended *m/z* ranges for MS instruments. Native MS can enhance the signal-to-noise (S/N) ratio for a 100 kDa protein by 17 times compared to denaturing MS conditions [152].

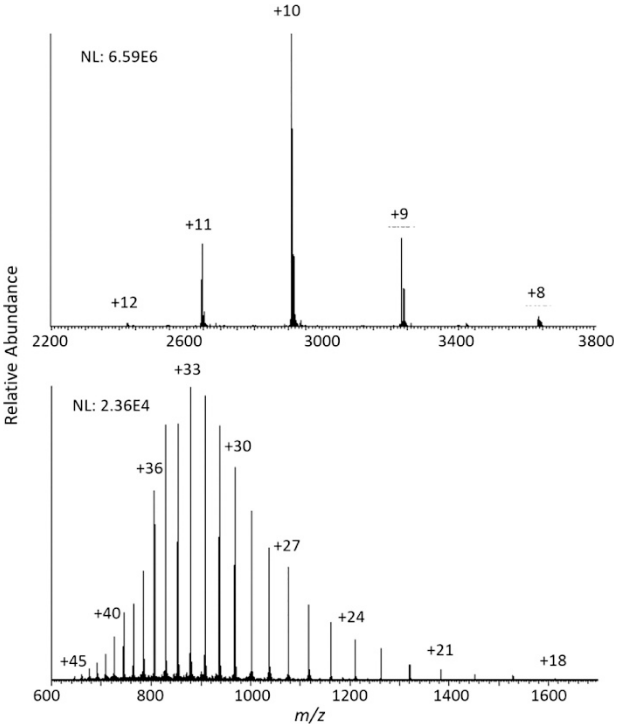

Fig. 13: Charge state distributions of carbonic anhydrase under native (top) and denaturing (bottom) electrospray ionization conditions. Reprinted with permission from Kafader et. al., Native vs Denatured: An in Depth Investigation of Charge State and Isotope Distributions, J. Am. Soc. Mass. Spectrom., 31 (3) (2020) 574-581. Ref. [152]. Copyright 2020 American Chemical Society.

The most frequently used high-resolution instruments for proteomics analysis are FT-ICR, quadrupole time-of-flight (qTOF) and Orbitrap mass spectrometers [154]. Among these MS-instruments, the FT-ICR offers the highest mass resolving power (~1,000,000) but suffers from high instrument and operational costs, a large footprint in the lab, and is difficult to operate [154]. qTOF instruments have resolutions around 10,000 to 30,000 and provide fast scanning speed, which is important for high-throughput methods such as fast chromatography [135]. Furthermore, it covers a wide *m/z* range and can perform sequential window acquisition of all theoretical mass spectra (SWATH-MS) [155]. However, the resolution of qTOF instruments strongly depends on operating conditions such as high vacuum requirements and room temperature [156]. The Orbitrap mass spectrometer offers higher mass resolution (100,000) compared to the qTOF instrument if slow data acquisition mode is used [135]. Higher acquisition speeds come at the cost of lower resolution.

1.4.3 Top-Down and Middle-Down Protein Mass Spectrometry

Gas-phase fragmentation of intact proteins using MS is called top-down MS, while the gas phase fragmentation of antibody fragments obtained through limited proteolysis or reduction is called middle-down analysis [25]. These techniques are valuable for confirming protein sequences, locating, and identifying post-translational modifications [25, 157, 158]. One significant advantage of both top-down and middle down MS is the minimal sample preparation required before analysis, reducing the risk of artifacts [25, 158].

Intact proteins are highly charged and have much higher *m/z* values than small molecules [159]. Due to overlapping charge states and multiple isotopic mass peaks, only high-resolution MS instruments are suitable for top-down and middle-down applications [148]. The bigger the molecular weight of the analytes is, the more important is the resolution of the MS instrument. The middle-down approach is a compromise to top-down MS lowering the molecular weight of an antibody into a better measurable *m/z* range. For example, digesting an antibody with the Immunoglobulin G-degrading enzyme of *Streptococcus pyogenes* (IdeS) and subsequent disulphide reduction can reduce the molecular weight from around 150 kDa to around 25 kDa [25].

In addition to the high resolution, the fragmentation technology of the MS devices also plays a crucial role (see chapter 1.4.1).

1.4.4 Bottom-Up Protein Mass Spectrometry

In bottom-up proteomics the proteins are denatured, cysteine disulphide bonds are reduced and alkylated before the protein undergoes digestion by proteolytic enzymes such as trypsin, endoproteinase Asp-N, or Lys-C [160]. The obtained peptide mixture is then subjected to LC-MS/MS analysis, in which, in most cases, either CID, HCD, ECD or ETD fragmentation is employed [160].

Bottom-up proteomics is more sensitive compared to intact protein MS or top/middle-down MS due to a smaller number of charge states, resulting in less signal distribution across multiple mass peaks [161]. Moreover, in bottom-up proteomics, the monoisotopic mass of peptides can be measured, while for intact protein MS, often only the average mass can be measured, depending on the mass resolving power of the MS instrument [148]. There is a lower signal distribution across multiple isotope peaks in bottom-up proteomics compared to intact protein MS, which also increases sensitivity [162]. Consequently, bottom-up proteomics allows the identification of a higher number of proteins for a limited sample amount compared to the other approaches. Localization of post-translational modifications is possible with both bottom-up and top/middle-down techniques, while intact protein MS can only be used to obtain information about the quantity of a certain modification present [25]. A disadvantage of bottom-up proteomics is the limited sequence coverage [163]. If the peptides are too long, they might fall outside of the measuring range of the MS instrument. For example, the Sciex qTOF 5600+ system used for the current work can only isolate precursor ions up to a *m/z* value of 1250. Precursor ions above this limit cannot be submitted for MS/MS experiments. On the other hand, if peptides are too short or single amino acids are generated, they are more likely to be not unique for a certain protein or might occur several times within the same protein [163]. Therefore, these parts of the protein sequence cannot be assigned with absolute certainty, and the sequence coverage is lower. Peptides with a length ranging from 7 to 35 amino acids are typically observable experimentally by MS [163]. Conventional sample preparation for bottom-up proteomics is often tedious and involves overnight digestion, whereas top-down MS requires minimal sample preparation. Furthermore, lengthy and extensive sample preparation can introduce artifacts such as deamidation and must therefore be carefully controlled [25].

1.5 Ion Mobility Mass Spectrometry

Ion mobility spectrometry (IMS) is a separation technique where ions are separated in an electric field in the gas phase [164]. It is very similar to gel electrophoresis, with the main difference being that in gel electrophoresis, ions are separated within the gel, whereas in IMS, ions are separated in the gas phase within an inert buffer gas like nitrogen [165]. The electric field moves the ions through a buffer gas, and the analyte ions collide with buffer gas molecules, which slows down the analyte ions [164]. The larger the three-dimensional structure, the more collisions occur with the buffer gas molecules, resulting in slower ion movement. An IM-instrument, such as a drift-tube IM spectrometer, measures the arrival time of ions. With knowledge of the drift tube length L and the arrival time t_A of the ion, the velocity v_d can be calculated as follows:

$$\mathrm{v_d} = \frac{\mathrm{L}}{\mathrm{t_A}}$$

(eq. 1.7)

The analyte's mobility K can be calculated as follows [164]:

$$K = \frac{v_d}{E}$$

(eq. 1.8)

Where E is the applied electric field.

The mobility K of each ion depends on experimental conditions such as pressure (p) and temperature (T). Therefore, normalization to standard conditions is used to calculate a reduced mobility K_0 [164]:

$$K_0 = K\frac{pT_0}{p_0T}$$

(eq. 1.9)

Here, p and p_0 represent the pressures at the experimental and standardized conditions, while T and T_0 represent the temperatures under those conditions. The ion mobility instrument directly provides the arrival time as result, which is typically converted either into the mobility K or the more commonly used and better comparable collision cross-section value (CCS or Ω). The CCS value can be calculated using the Mason-Schamp equation [166, 167]:

$$CCS = \frac{\frac{3}{16}\left(\frac{1}{m} + \frac{1}{M}\right)^{1/2}\left(\frac{2\pi}{k_bT}\right)^{1/2} ze}{N_0K_0}$$

(eq. 1.10)

The CCS value depends on various factors, including the ion mass m, the neutral molecule mass M, the Boltzmann's constant k_b, the temperature T in the drift region, the ion charge z, the charge of an electron e, the buffer gas density N_0, and the reduced mobility K_0 [164]. In principle, the separation is governed by the gas phase size of the ion, and thus, the unit of the CCS is typically square Angstroms (Å²) [168, 169].

IMS devices can be used as standalone instruments and play a crucial role in areas such as the detection of explosives and chemical warfare, where portable devices are often used [170, 171]. There are different instrument platforms for measuring IMS such as drift tube IMS (DTIMS), trapped IMS (TIMS), traveling wave IMS (TWIMS), field asymmetric IMS (FAIMS), and differential mobility analyzer (DMA) spectrometers [164].

A typical drift tube ion mobility mass spectrometry (DT-IM-MS) instrument (**Fig. 14**) possesses an ion source, such as an electro spray ionisation (ESI) source, for ionizing the analytes [172]. Ions are then directed to a front funnel, where excess gas is removed, and ions are focused before entering the trapping funnel, which accumulates and releases ions into the drift tube [172, 173]. Inside the drift tube, ions are subjected to a constant electric field and a constant buffer gas pressure, where the separation of the ions occurs based on their mobilities. The ions then exit the drift tube and enter the rear funnel, where they are refocused before being transferred to the mass spectrometer for detection. The result obtained from the drift tube ion mobility separation is the arrival time in milliseconds, which can be converted into a mobility or CCS value.

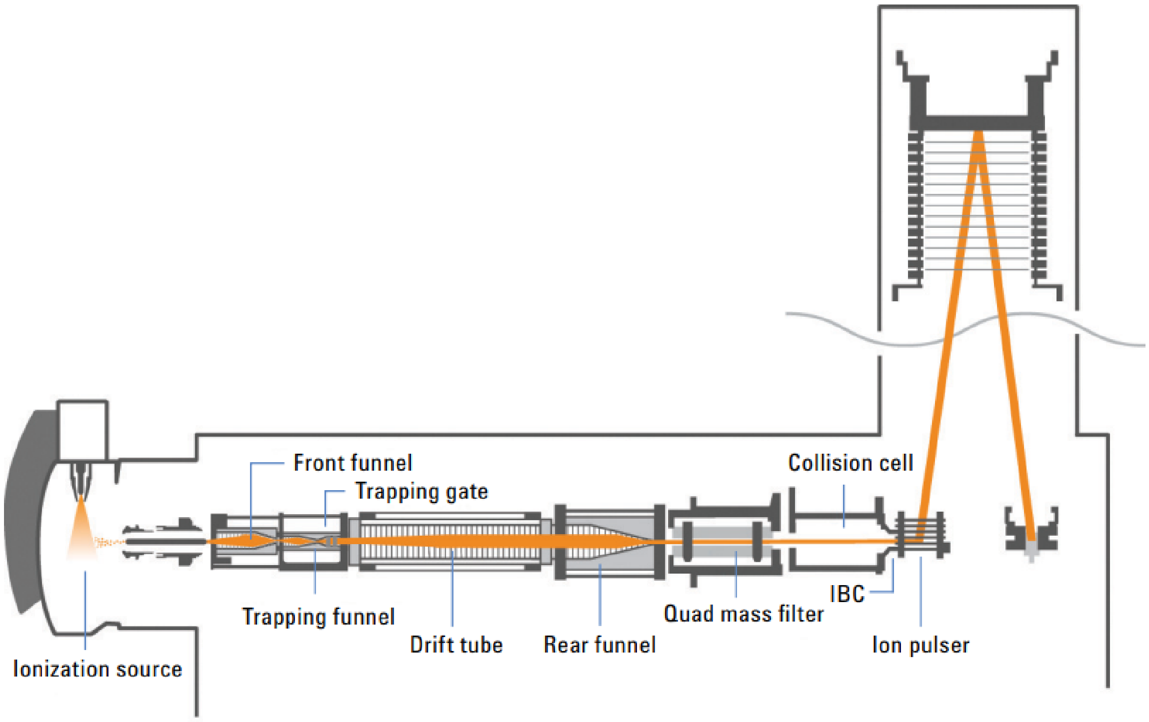

Fig. 14: Schematic of the Agilent ion mobility QTOF instrument. Reproduced with permission from Kurulugama et al., Evaluation of drift gas selection in complex sample analyses using a high performance drift tube ion mobility-QTOF mass spectrometer, Analyst, 140 (20) (2015) 6834-6844. Ref. [172]. Copyright 2015 Royal Society of Chemistry.

In comparison to MS, where the ions are separated according to the *m/z* ratio, IMS separates the ions according to their mobility, which is dependent on the analyte's shape [164]. Thus, the three-dimensional structure of the analyte ions governs the separation process. Consequently, MS and IMS separation techniques exhibit some orthogonality to each other, although this orthogonality is limited by the correlation between an analyte's mass and its shape (see (eq. 1.10) [174]. As a rule of thumb, the bigger the ion's mass, the lower its mobility and the higher its CCS-value. In some cases, the orthogonality of IMS and MS can be strong enough to separate isomeric compounds, which are isobaric. One significant advantage of IMS is its speed, as the separation occurs on a millisecond (ms) time scale. Thus, IMS can be easily coupled to both LC, which operates typically on the hour to minute time scale, and MS, which operates on the microseconds (µs) time scale. However, IMS comes with some limitations in terms of reduced sensitivity and the need for more complex data processing [30, 164]. Sensitivity decreases as only a fraction of the ions are transferred into the IM-MS instrument. In a typical example experiment, ions are trapped only for

4 ms, followed by a subsequent separation in the drift tube that takes 60 ms. As a result, a duty cycle of only 6.7 % (4 ms/60 ms) is used, and a significant loss in sensitivity occurs as most of the ions are not transferred to the MS [164]. To increase the duty cycle, multiplexing strategies have been invented, where several ion packages are pulsed into the drift tube at defined times, while the first ion package is still travelling through the drift tube. Using advanced data analysis algorithms and defined pulsing times, the correct arrival times of the ions can be deconvoluted. Thus, the duty cycle can be increased to 50 %, compared to the initial 6.7 % [164, 175]. As consequence of the multiplexing, data processing becomes more challenging, requiring software algorithms to deconvolute the correct arrival times. The resolving power of ion mobility instruments (R_p = 50-300) is several orders of magnitude lower compared to the resolving power of high-resolution MS instruments (R_p = 10,000-1,000,000), which makes MS instruments the more powerful separation platform (**Fig. 15**) [135].

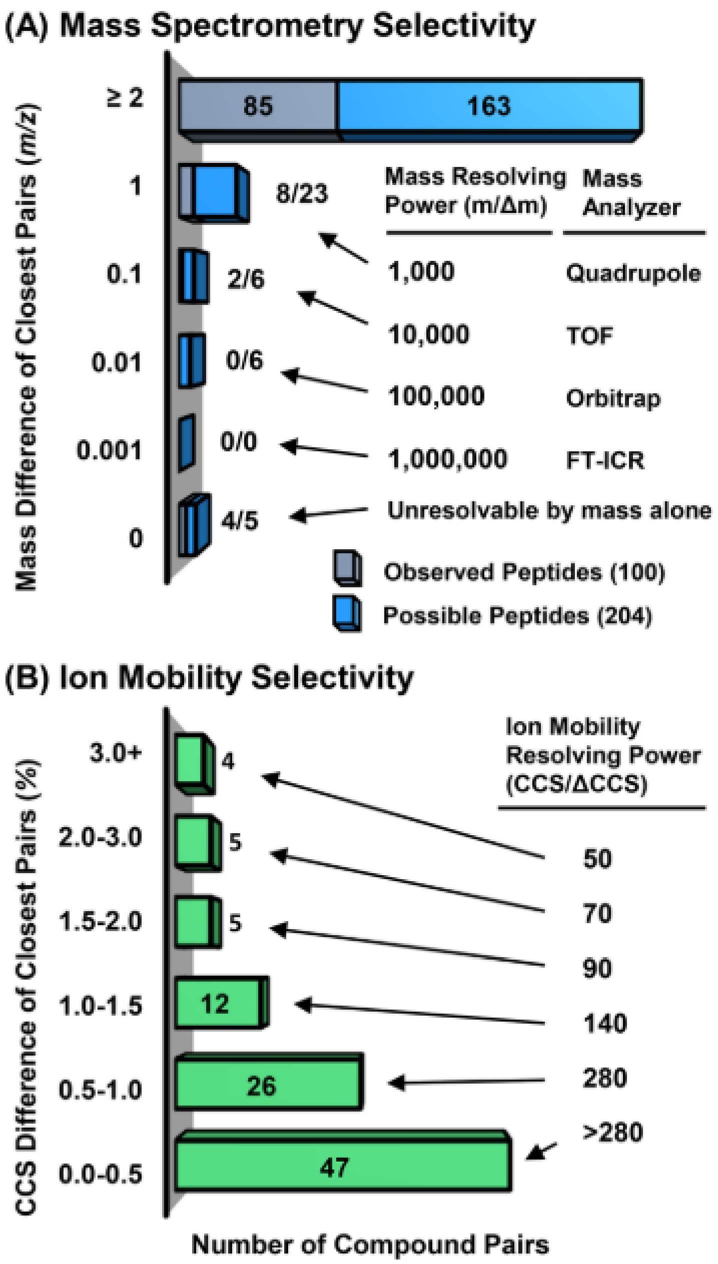

Fig. 15: Comparison of mass spectrometry and ion mobility data collected from a tryptic peptide mixture originating from four proteins. (A) Difference in *m/z* between nearest neighbours for all possible peptides in the digest mixture (blue) and from those peptides observed experimentally in this study (gray). (B) Bar graph of the percent difference in CCS between nearest neighbour peptides for the 99 analyte pairs observed. (C) Separation of two doubly charged peptides by mass spectrometry and suspected conformers of each peptide noted through ion mobility. Reprinted with permission from Dodds et al., Correlating Resolving Power, Resolution, and Collision Cross Section: Unifying Cross-Platform Assessment of Separation Efficiency in Ion Mobility Spectrometry, Anal. Chem., 89 (22) (2017) 12176-12184. Ref. [135]. Copyright 2017 American Chemical Society.

1.6 References

[1] ICH, ICH Harmonised Tripartite Guideline - Validation of Analytical Procedures: Text and Methodology Q2(R1), 2005, p. 13.

[2] ICH, ICH Harmonised Tripartite Guideline - Impurities in New Drug Substances Q3a(R2), (2006).

[3] ICH, ICH Harmonised Tripartite Guideline - Impurities in New Drug Products Q3B(R2), (2006).

[4] D.J. Craik, D.P. Fairlie, S. Liras, D. Price, The Future of Peptide-based Drugs, Chemical Biology & Drug Design, 81 (1) (2013) 136-147.

[5] S. Mitragotri, P.A. Burke, R. Langer, Overcoming the challenges in administering biopharmaceuticals: formulation and delivery strategies, Nature Reviews Drug Discovery, 13 (9) (2014) 655-672.

[6] F.D. Makurvet, Biologics vs. small molecules: Drug costs and patient access, Medicine in Drug Discovery, 9 (2021) 100075.

[7] G. Walsh, E. Walsh, Biopharmaceutical benchmarks 2022, Nat. Biotechnol., 40 (12) (2022) 1722-1760.

[8] F.G. Banting, C.H. Best, J.B. Collip, W.R. Campbell, A.A. Fletcher, Pancreatic Extracts in the Treatment of Diabetes Mellitus, Can Med Assoc J, 12 (3) (1922) 141-6.

[9] V. du Vigneaud, C. Ressler, J.M. Swan, C.W. Roberts, P.G. Katsoyannis, The Synthesis of Oxytocin, Journal of the American Chemical Society, 76 (12) (1954) 3115-3121.

[10] V. Du Vigneaud, D.T. Gish, P.G. Katsoyannis, G.P. Hess, Synthesis of the Pressor-Antidiuretic Hormone, Arginine-Vasopressin, Journal of the American Chemical Society, 80 (13) (1958) 3355-3358.

[11] L. Wang, N. Wang, W. Zhang, X. Cheng, Z. Yan, G. Shao, X. Wang, R. Wang, C. Fu, Therapeutic peptides: current applications and future directions, Signal Transduction and Targeted Therapy, 7 (1) (2022) 48.

[12] S. Rastogi, S. Shukla, M. Kalaivani, G.N. Singh, Peptide-based therapeutics: quality specifications, regulatory considerations, and prospects, Drug Discovery Today, 24 (1) (2019) 148-162.

[13] H.M. Werner, C.C. Cabalteja, W.S. Horne, Peptide Backbone Composition and Protease Susceptibility: Impact of Modification Type, Position, and Tandem Substitution, ChemBioChem, 17 (8) (2016) 712-718.

[14] M. Endo, K. Takesako, I. Kato, H. Yamaguchi, Fungicidal action of aureobasidin A, a cyclic depsipeptide antifungal antibiotic, against Saccharomyces cerevisiae, Antimicrob. Agents Chemother., 41 (3) (1997) 672-676.

[15] P.E. Battershill, S.P. Clissold, Octreotide, Drugs, 38 (5) (1989) 658-702.

[16] R. Karongo, J. Horak, M. Lämmerhofer, Comprehensive Online Reversed-Phase × Chiral Two-Dimensional Liquid Chromatography-Mass Spectrometry with Data-Independent Sequential Window Acquisition of All Theoretical Fragment-Ion Spectra-Acquisition for Untargeted Enantioselective Amino Acid Analysis, Anal. Chem., 94 (49) (2022) 17063-17072.

[17] E. Pohl, A. Heine, G.M. Sheldrick, Z. Dauter, K.S. Wilson, J. Kallen, W. Huber, P.J. Pfaffli, Structure of octreotide, a somatostatin analogue, Acta Crystallographica Section D, 51 (1) (1995) 48-59.

[18] R. Cozzi, R. Attanasio, Octreotide for acromegaly, Expert Review of Endocrinology & Metabolism, 2 (2) (2007) 129-145.

[19] W. Bauer, U. Briner, W. Doepfner, R. Haller, R. Huguenin, P. Marbach, T.J. Petcher, J. Pless, SMS 201–995: A very potent and selective octapeptide analogue of somatostatin with prolonged action, Life Sci., 31 (11) (1982) 1133-1140.

[20] K. Shibata, D. Imanishi, K. Abe, M. Suzuki, S. Takahashi, Y. Kera, d-Aspartate N-methyltransferase catalyzes biosynthesis of N-methyl-d-aspartate (NMDA), a well-known selective agonist of the NMDA receptor, in mice, Biochimica et Biophysica Acta (BBA) - Proteins and Proteomics, 1868 (12) (2020) 140527.

[21] G. Genchi, An overview on d-amino acids, Amino Acids, 49 (9) (2017) 1521-1533.

[22] K. Hamase, A. Morikawa, K. Zaitsu, d-Amino acids in mammals and their diagnostic value, J. Chromatogr. B, 781 (1) (2002) 73-91.

[23] P.G. Righetti, T. Caravaggio, Isoelectric points and molecular weights of proteins: A table, J. Chromatogr. A, 127 (1) (1976) 1-28.

[24] A. Freiburg, K. Trombitas, W. Hell, O. Cazorla, F. Fougerousse, T. Centner, B. Kolmerer, C. Witt, J.S. Beckmann, C.C. Gregorio, H. Granzier, S. Labeit, Series of Exon-Skipping Events in the Elastic Spring Region of Titin as the Structural Basis for Myofibrillar Elastic Diversity, Circulation Research, 86 (11) (2000) 1114-1121.

[25] A. Beck, E. Wagner-Rousset, D. Ayoub, A. Van Dorsselaer, S. Sanglier-Cianférani, Characterization of Therapeutic Antibodies and Related Products, Anal. Chem., 85 (2) (2013) 715-736.

[26] E. Buxbaum, Fundamentals of protein structure and function, Springer2007.

[27] S. Fekete, D. Guillarme, P. Sandra, K. Sandra, Chromatographic, Electrophoretic, and Mass Spectrometric Methods for the Analytical Characterization of Protein Biopharmaceuticals, Anal. Chem., 88 (1) (2016) 480-507.

[28] L.A. Khawli, S. Goswami, R. Hutchinson, Z.W. Kwong, J. Yang, X. Wang, Z. Yao, A. Sreedhara, T. Cano, D. Tesar, I. Nijem, D.E. Allison, P.Y. Wong, Y.-H. Kao, C. Quan, A. Joshi, R.J. Harris, P. Motchnik, Charge variants in IgG1: Isolation, characterization, in vitro binding properties and pharmacokinetics in rats, mAbs, 2 (6) (2010) 613-624.

[29] D. Gervais, Protein deamidation in biopharmaceutical manufacture: understanding, control and impact, Journal of Chemical Technology & Biotechnology, 91 (3) (2016) 569-575.

[30] K.E. Butler, J.N. Dodds, T. Flick, I.D.G. Campuzano, E.S. Baker, High-Resolution Demultiplexing (HRdm) Ion Mobility Spectrometry–Mass Spectrometry for Aspartic and Isoaspartic Acid Determination and Screening, Anal. Chem., 94 (16) (2022) 6191-6199.

[31] H. Liu, G. Gaza-Bulseco, D. Faldu, C. Chumsae, J. Sun, Heterogeneity of Monoclonal Antibodies, J. Pharm. Sci., 97 (7) (2008) 2426-2447.

[32] Z. Liu, J. Valente, S. Lin, N. Chennamsetty, D. Qiu, M. Bolgar, Cyclization of N-Terminal Glutamic Acid to pyro-Glutamic Acid Impacts Monoclonal Antibody Charge Heterogeneity Despite Its Appearance as a Neutral Transformation, J. Pharm. Sci., 108 (10) (2019) 3194-3200.

[33] D. Virág, B. Dalmadi-Kiss, K. Vékey, L. Drahos, I. Klebovich, I. Antal, K. Ludányi, Current Trends in the Analysis of Post-translational Modifications, Chromatographia, 83 (1) (2020) 1-10.

[34] L. Liu, Antibody Glycosylation and Its Impact on the Pharmacokinetics and Pharmacodynamics of Monoclonal Antibodies and Fc-Fusion Proteins, J. Pharm. Sci., 104 (6) (2015) 1866-1884.

[35] S. Rosati, E.T.J. van den Bremer, J. Schuurman, P.W.H.I. Parren, J.P. Kamerling, A.J.R. Heck, In-depth qualitative and quantitative analysis of composite glycosylation profiles and other micro-heterogeneity on intact monoclonal antibodies by high-resolution native mass spectrometry using a modified Orbitrap, mAbs, 5 (6) (2013) 917-924.

[36] S. Fukuzaki, H. Urano, K. Nagata, Adsorption of protein onto stainless-steel surfaces, J. Ferment. Bioeng., 80 (1) (1995) 6-11.

[37] S. Fekete, Defining Material Used in Biopharmaceutical Analysis, LCGC Europe, 34 (6) (2021) 245-248.

[38] T. Hanawa, Biocompatibility of titanium from the viewpoint of its surface, Science and Technology of Advanced Materials, 23 (1) (2022) 457-472.

[39] B. Rivera, J.A. Anspach, S. Rao, Bioinert Versus Biocompatible: The Benefits of Different Column Materials in Liquid Chromatography Separations, LCGC Supplements, 36 (6) (2018) 24-29.

[40] C.-K. Kang, Y.-S. Lee, The surface modification of stainless steel and the correlation between the surface properties and protein adsorption, Journal of Materials Science: Materials in Medicine, 18 (7) (2007) 1389-1398.

[41] J.P. Foley, Resolution equations for column chromatography, Analyst, 116 (12) (1991) 1275-1279.

[42] J.J.K. LLoyd R. Snyder, John W. dolan, Introduction to Modern Liquid Chromatography, Third Edition ed., Wiley, Hoboken, New Jersey, 2010.

[43] S. Fekete, H. Ritchie, J. Lawhorn, J.-L. Veuthey, D. Guillarme, Improving selectivity and performing online on-column fractioning in liquid chromatography for the separation of therapeutic biopharmaceutical products, J. Chromatogr. A, (2020) 460901.

[44] U.D. Neue, Peak capacity in unidimensional chromatography, J. Chromatogr. A, 1184 (1) (2008) 107-130.

[45] K. Broeckhoven, D. Cabooter, F. Lynen, P. Sandra, G. Desmet, The kinetic plot method applied to gradient chromatography: Theoretical framework and experimental validation, J. Chromatogr. A, 1217 (17) (2010) 2787-2795.

[46] M. Gilar, U.D. Neue, Peak capacity in gradient reversed-phase liquid chromatography of biopolymers: Theoretical and practical implications for the separation of oligonucleotides, J. Chromatogr. A, 1169 (1) (2007) 139-150.

[47] K. Hormann, T. Müllner, S. Bruns, A. Höltzel, U. Tallarek, Morphology and separation efficiency of a new generation of analytical silica monoliths, J. Chromatogr. A, 1222 (2012) 46-58.

[48] K. Horváth, F. Gritti, J.N. Fairchild, G. Guiochon, On the optimization of the shell thickness of superficially porous particles, J. Chromatogr. A, 1217 (41) (2010) 6373-6381.

[49] H.A. Claessens, M.A. van Straten, Review on the chemical and thermal stability of stationary phases for reversed-phase liquid chromatography, J. Chromatogr. A, 1060 (1) (2004) 23-41.

[50] C. Galea, D. Mangelings, Y. Vander Heyden, Characterization and classification of stationary phases in HPLC and SFC – a review, Anal. Chim. Acta, 886 (2015) 1-15.

[51] B.M. Wagner, S.A. Schuster, B.E. Boyes, T.J. Shields, W.L. Miles, M.J. Haynes, R.E. Moran, J.J. Kirkland, M.R. Schure, Superficially porous particles with 1000Å pores for large biomolecule high performance liquid chromatography and polymer size exclusion chromatography, J. Chromatogr. A, 1489 (2017) 75-85.

[52] J.J. Kirkland, Superficially Porous Silica Microspheres for the Fast High-Performance Liquid Chromatography of Macromolecules, Anal. Chem., 64 (1992) 1239-1245.

[53] K.K. Unger, O. Jilge, J.N. Kinkel, M.T.W. Hearn, Evaluation of advanced silica packings for the separation of biopolymers by high-performance liquid chromatography II. Performance of non-porous monodisperse 1.5-μm Silica beads in the separation of proteins by reversed-phase gradient elution high-performance liquid chromatography, J. Chromatogr. A, 359 (1986) 61-72.

[54] D. Cabooter, K. Broeckhoven, R. Sterken, A. Vanmessen, I. Vandendael, K. Nakanishi, S. Deridder, G. Desmet, Detailed characterization of the kinetic performance of first and second generation silica monolithic columns for reversed-phase chromatography separations, J. Chromatogr. A, 1325 (2014) 72-82.

[55] O. Vyviurska, Y. Lv, B.F. Mann, F. Svec, Comparison of commercial organic polymer-based and silica-based monolithic columns using mixtures of analytes differing in size and chemistry, J. Sep. Sci., 41 (7) (2018) 1558-1566.

[56] C. Luo, J.J. DeStefano, T.J. Langlois, B.E. Boyes, S.A. Schuster, J.M. Godinho, Fundamental to achieving fast separations with high efficiency: A review of chromatography with superficially porous particles, Biomed. Chromatogr., 35 (7) (2021) e5087.

[57] J.J. DeStefano, T.J. Langlois, J.J. Kirkland, Characteristics of Superficially-Porous Silica Particles for Fast HPLC: Some Performance Comparisons with Sub-2-μm Particles, J. Chromatogr. Sci., 46 (3) (2008) 254-260.

[58] S.A. Schuster, B.E. Boyes, B.M. Wagner, J.J. Kirkland, Fast high performance liquid chromatography separations for proteomic applications using Fused-Core® silica particles, J. Chromatogr. A, 1228 (2012) 232-241.

[59] B.M. Wagner, S.A. Schuster, B.E. Boyes, J.J. Kirkland, Superficially porous silica particles with wide pores for biomacromolecular separations, J. Chromatogr. A, 1264 (2012) 22-30.

[60] S.A. Schuster, B.M. Wagner, B.E. Boyes, J.J. Kirkland, Optimized superficially porous particles for protein separations, J. Chromatogr. A, 1315 (2013) 118-126.

[61] S. Fekete, R. Berky, J. Fekete, J.-L. Veuthey, D. Guillarme, Evaluation of a new wide pore core–shell material (Aeris™ WIDEPORE) and comparison with other existing stationary phases for the analysis of intact proteins, J. Chromatogr. A, 1236 (2012) 177-188.

[62] D.K. Wilkins, S.B. Grimshaw, V. Receveur, C.M. Dobson, J.A. Jones, L.J. Smith, Hydrodynamic Radii of Native and Denatured Proteins Measured by Pulse Field Gradient NMR Techniques, Biochemistry, 38 (50) (1999) 16424-16431.

[63] C.T. Mant, N.E. Zhou, R.S. Hodges, Correlation of protein retention times in reversed-phase chromatography with polypeptide chain length and hydrophobicity, J. Chromatogr. A, 476 (1989) 363-375.

[64] J. Kyte, R.F. Doolittle, A simple method for displaying the hydropathic character of a protein, J. Mol. Biol., 157 (1) (1982) 105-132.

[65] S. Fekete, S. Rudaz, J.-L. Veuthey, D. Guillarme, Impact of mobile phase temperature on recovery and stability of monoclonal antibodies using recent reversed-phase stationary phases, J. Sep. Sci., 35 (22) (2012) 3113-3123.

[66] B. Bobály, M. Lauber, A. Beck, D. Guillarme, S. Fekete, Utility of a high coverage phenyl-bonding and wide-pore superficially porous particle for the analysis of monoclonal antibodies and related products, J. Chromatogr. A, 1549 (2018) 63-76.

[67] A.P. Schellinger, D.R. Stoll, P.W. Carr, High speed gradient elution reversed phase liquid chromatography of bases in buffered eluents: Part II. Full equilibrium, J. Chromatogr. A, 1192 (1) (2008) 54-61.

[68] D. Stoll, S. Fekete, D. Guillarme, Tips, Tricks, and Troubleshooting for Separations of Biomolecules, Part I: Contemporary Reversed-Phase Protein Separations, LCGC North America, 36 (7) (2018) 440–446.

[69] S. Fekete, A. Murisier, A. Beck, J. Lawhorn, H. Ritchie, B. Boyes, D. Guillarme, New wide-pore superficially porous stationary phases with low hydrophobicity applied for the analysis of monoclonal antibodies, J. Chromatogr. A, 1642 (2021) 462050.

[70] J.K. Field, M.R. Euerby, P. Petersson, Investigation into reversed phase chromatography peptide separation systems part III: Establishing a column characterisation database, J. Chromatogr. A, 1622 (2020) 461093.

[71] M.C. García, A.C. Hogenboom, H. Zappey, H. Irth, Effect of the mobile phase composition on the separation and detection of intact proteins by reversed-phase liquid chromatography–electrospray mass spectrometry, J. Chromatogr. A, 957 (2) (2002) 187-199.

[72] A. Goyon, L. Dai, T. Chen, B. Wei, F. Yang, N. Andersen, R. Kopf, M. Leiss, M. Mølhøj, D. Guillarme, C. Stella, From proof of concept to the routine use of an automated and robust multi-dimensional liquid chromatography mass spectrometry workflow applied for the charge variant characterization of therapeutic antibodies, J. Chromatogr. A, 1615 (2020) 460740.

[73] D.V. McCalley, D. Guillarme, Evaluation of additives on reversed-phase chromatography of monoclonal antibodies using a 1000 Å stationary phase, J. Chromatogr. A, (2019) 460562.

[74] E. Farsang, D. Guillarme, J.-L. Veuthey, A. Beck, M. Lauber, A. Schmudlach, S. Fekete, Coupling non-denaturing chromatography to mass spectrometry for the characterization of monoclonal antibodies and related products, J. Pharm. Biomed. Anal., 185 (2020) 113207.

[75] F. Füssl, K. Cook, K. Scheffler, A. Farrell, S. Mittermayr, J. Bones, Charge Variant Analysis of Monoclonal Antibodies Using Direct Coupled pH Gradient Cation Exchange Chromatography to High-Resolution Native Mass Spectrometry, Anal. Chem., 90 (7) (2018) 4669-4676.

[76] M. Haberger, M. Leiss, A.-K. Heidenreich, O. Pester, G. Hafenmair, M. Hook, L. Bonnington, H. Wegele, M. Haindl, D. Reusch, P. Bulau, Rapid characterization of biotherapeutic proteins by size-exclusion chromatography coupled to native mass spectrometry, mAbs, 8 (2) (2016) 331-339.

[77] S. Fekete, J.-L. Veuthey, A. Beck, D. Guillarme, Hydrophobic interaction chromatography for the characterization of monoclonal antibodies and related products, J. Pharm. Biomed. Anal., 130 (2016) 3-18.

[78] T.M. Dillon, P.V. Bondarenko, D.S. Rehder, G.D. Pipes, G.R. Kleemann, M.S. Ricci, Optimization of a reversed-phase high-performance liquid chromatography/mass spectrometry method for characterizing recombinant antibody heterogeneity and stability, J. Chromatogr. A, 1120 (1) (2006) 112-120.

[79] Q. Zhao, On the indirect relationship between protein dynamics and enzyme activity, Prog. Biophys. Mol. Biol., 125 (2017) 52-60.

[80] C.E. Eyers, M. Vonderach, S. Ferries, K. Jeacock, P.A. Eyers, Understanding protein–drug interactions using ion mobility–mass spectrometry, Curr. Opin. Chem. Biol., 42 (2018) 167-176.

[81] E. Tyteca, J.-L. Veuthey, G. Desmet, D. Guillarme, S. Fekete, Computer assisted liquid chromatographic method development for the separation of therapeutic proteins, Analyst, 141 (19) (2016) 5488-5501.

[82] S. Fekete, A. Beck, J.-L. Veuthey, D. Guillarme, Proof of Concept To Achieve Infinite Selectivity for the Chromatographic Separation of Therapeutic Proteins, Anal. Chem., 91 (20) (2019) 12954-12961.

[83] S. Fekete, B. Bobály, J.M. Nguyen, A. Beck, J.-L. Veuthey, K. Wyndham, M.A. Lauber, D. Guillarme, Use of Ultrashort Columns for Therapeutic Protein Separations. Part 1: Theoretical Considerations and Proof of Concept, Anal. Chem., 93 (3) (2021) 1277-1284.

[84] S. Terabe, H. Nishi, T. Ando, Separation of cytochromes c by reversed-phase high-performance liquid chromatography, J. Chromatogr. A, 212 (3) (1981) 295-304.

[85] S. Fekete, A. Murisier, J.M. Nguyen, M.J. Bolton, J. Belanger, A. Beck, J.-L. Veuthey, K. Wyndham, M.A. Lauber, D. Guillarme, Use of Ultra-short Columns for Therapeutic Protein Separations, Part 2: Designing the Optimal Column Dimension for Reversed-Phase Liquid Chromatography, Anal. Chem., 93 (3) (2021) 1285-1293.

[86] X. Liu, C. Pohl, New hydrophilic interaction/reversed-phase mixed-mode stationary phase and its application for analysis of nonionic ethoxylated surfactants, J. Chromatogr. A, 1191 (1) (2008) 83-89.

[87] A. Beck, C. Nowak, D. Meshulam, K. Reynolds, D. Chen, D.B. Pacardo, S.B. Nicholls, G.J. Carven, Z. Gu, J. Fang, D. Wang, A. Katiyar, T. Xiang, H. Liu, Risk-Based Control Strategies of Recombinant Monoclonal Antibody Charge Variants, Antibodies, 11 (4) (2022) 73.

[88] A. Goyon, M. Excoffier, M.C. Janin-Bussat, B. Bobaly, S. Fekete, D. Guillarme, A. Beck, Determination of isoelectric points and relative charge variants of 23 therapeutic monoclonal antibodies, J Chromatogr B Analyt Technol Biomed Life Sci, 1065-1066 (2017) 119-128.

[89] D.E. Garfin, Isoelectric focusing, in: M.P. Deutscher (Ed.), Methods Enzymol., Academic Press 1990, pp. 459-477.

[90] E. Gasteiger, C. Hoogland, A. Gattiker, S.e. Duvaud, M.R. Wilkins, R.D. Appel, A. Bairoch, Protein Identification and Analysis Tools on the ExPASy Server, in: J.M. Walker (Ed.), The Proteomics Protocols Handbook, Humana Press, Totowa, NJ, 2005, pp. 571-607.

[91] E. Farsang, A. Murisier, K. Horváth, A. Beck, R. Kormány, D. Guillarme, S. Fekete, Tuning selectivity in cation-exchange chromatography applied for monoclonal antibody separations, part 1: Alternative mobile phases and fine tuning of the separation, J. Pharm. Biomed. Anal., 168 (2019) 138-147.

[92] A. Murisier, M. Lauber, S.J. Shiner, D. Guillarme, S. Fekete, Practical considerations on the particle size and permeability of ion-exchange columns applied to biopharmaceutical separations, J. Chromatogr. A, 1604 (2019) 460487.

[93] E.M. Borges, M.R. Euerby, An appraisal of the chemical and thermal stability of silica based reversed-phase liquid chromatographic stationary phases employed within the pharmaceutical environment, J. Pharm. Biomed. Anal., 77 (2013) 100-115.

[94] G.V. Samsonov, V.A. Pasechnik, Ion Exchange and the Swelling of Ion-exchange Resins, Russian Chemical Reviews, 38 (7) (1969) 547.

[95] U.M. Ingle, A.M. Lali, Significance of porosity and pore accessibility for the selection of ion exchange adsorbents for chromatographic purification of macromolecules, Acta Chromatographica Acta Chromatographica, 29 (1) (2017) 5-24.

[96] M.A. Kappes, Localized corrosion and stress corrosion cracking of stainless steels in halides other than chlorides solutions: a review, Corros. Rev., 38 (1) (2020) 1-24.

[97] H.P. Nguyen, K.A. Schug, The advantages of ESI-MS detection in conjunction with HILIC mode separations: Fundamentals and applications, J. Sep. Sci., 31 (9) (2008) 1465-1480.

[98] M.A. Strege, Hydrophilic Interaction Chromatography−Electrospray Mass Spectrometry Analysis of Polar Compounds for Natural Product Drug Discovery, Anal. Chem., 70 (13) (1998) 2439-2445.

[99] J. Adamíková, M. Antošová, M. Polakovič, Chromatographic purification of recombinant human erythropoietin, Biotechnol. Lett, 41 (4) (2019) 483-493.

[100] L. Piubelli, G. Murtas, V. Rabattoni, L. Pollegioni, The Role of D-Amino Acids in Alzheimer’s Disease, Journal of Alzheimer's Disease, 80 (2021) 475-492.

[101] M.V. Aleksander Swietlow, Brian Gregg, Harold Rode, Ivo Eggen, Anita Szajek, Control Strategies for Synthetic Therapeutic Peptide APIs - Part I: Analytical Consideration, Pharm. Technol., 38 (3) (2014).

[102] M. Morvan, I. Mikšík, Recent Advances in Chiral Analysis of Proteins and Peptides, Separations, 8 (8) (2021) 112.

[103] M. Danielsen, C. Nebel, T.K. Dalsgaard, Simultaneous Determination of L- and D-Amino Acids in Proteins: A Sensitive Method Using Hydrolysis in Deuterated Acid and Liquid Chromatography–Tandem Mass Spectrometry Analysis, Foods, 9 (3) (2020) 309.

[104] S. Bäurer, M. Ferri, A. Carotti, S. Neubauer, R. Sardella, M. Lämmerhofer, Mixed-mode chromatography characteristics of chiralpak ZWIX(+) and ZWIX(−) and elucidation of their chromatographic orthogonality for LC × LC application, Anal. Chim. Acta, 1093 (2020) 168-179.

[105] I. Kawamura, B. Mijiddorj, Y. Kayano, Y. Matsuo, Y. Ozawa, K. Ueda, H. Sato, Separation of D-amino acid-containing peptide phenylseptin using 3,3′-phenyl-1,1′-binaphthyl-18-crown-6-ether columns, Biochimica et Biophysica Acta (BBA) - Proteins and Proteomics, 1868 (8) (2020) 140429.

[106] L. Miller, L. Yue, Chiral separation of underivatized amino acids in supercritical fluid chromatography with chiral crown ether derived column, Chirality, 32 (7) (2020) 981-989.

[107] T. Upmanis, H. Kažoka, P. Arsenyan, A study of tetrapeptide enantiomeric separation on crown ether based chiral stationary phases, J. Chromatogr. A, 1622 (2020) 461152.

[108] Y.K. Ye, B.S. Lord, L. Yin, R.W. Stringham, Enantioseparation of amino acids on a polysaccharide-based chiral stationary phase, J. Chromatogr. A, 945 (1) (2002) 147-159.

[109] C. Geibel, K. Dittrich, U. Woiwode, M. Kohout, T. Zhang, W. Lindner, M. Lämmerhofer, Evaluation of superficially porous particle based zwitterionic chiral ion exchangers against fully porous particle benchmarks for enantioselective ultra-high performance liquid chromatography, J. Chromatogr. A, 1603 (2019) 130-140.

[110] C. Calderón, J. Horak, M. Lämmerhofer, Chiral separation of 2-hydroxyglutaric acid on cinchonan carbamate based weak chiral anion exchangers by high-performance liquid chromatography, J. Chromatogr. A, 1467 (2016) 239-245.

[111] R. Kimura, H. Tsujimura, M. Tsuchiya, S. Soga, N. Ota, A. Tanaka, H. Kim, Development of a cognitive function marker based on D-amino acid proportions using new chiral tandem LC-MS/MS systems, Scientific Reports, 10 (1) (2020) 804.

[112] K.N. Saxena, J.R. Gandhi, Separation and identification of amino acids by two-dimensional paper chromatography, J. Chromatogr. A, 8 (1962) 546-550.

[113] E. Nägele, M. Vollmer, P. Hörth, C. Vad, 2D-LC/MS techniques for the identification of proteins in highly complex mixtures, Expert Review of Proteomics, 1 (1) (2004) 37-46.

[114] M. Iguiniz, S. Heinisch, Two-dimensional liquid chromatography in pharmaceutical analysis. Instrumental aspects, trends and applications, J. Pharm. Biomed. Anal., 145 (2017) 482-503.

[115] B.W.J. Pirok, D.R. Stoll, P.J. Schoenmakers, Recent Developments in Two-Dimensional Liquid Chromatography: Fundamental Improvements for Practical Applications, Anal. Chem., 91 (1) (2019) 240-263.

[116] E.L. Johnson, R. Gloor, R.E. Majors, Coupled column chromatography employing exclusion and a reversed phase: A potential general approach to sequential analysis, J. Chromatogr. A, 149 (1978) 571-585.

[117] K. Zhang, Y. Li, M. Tsang, N.P. Chetwyn, Analysis of pharmaceutical impurities using multi-heartcutting 2D LC coupled with UV-charged aerosol MS detection, J. Sep. Sci., 36 (18) (2013) 2986-92.

[118] F. Erni, R.W. Frei, Two-dimensional column liquid chromatographic technique for resolution of complex mixtures, J. Chromatogr. A, 149 (1978) 561-569.

[119] S.R. Groskreutz, M.M. Swenson, L.B. Secor, D.R. Stoll, Selective comprehensive multi-dimensional separation for resolution enhancement in high performance liquid chromatography. Part I: Principles and instrumentation, J. Chromatogr. A, 1228 (2012) 31-40.

[120] B.W.J. Pirok, A.F.G. Gargano, P.J. Schoenmakers, Optimizing separations in online comprehensive two-dimensional liquid chromatography, J. Sep. Sci., 41 (1) (2018) 68-98.

[121] J.M. Davis, D.R. Stoll, Likelihood of total resolution in liquid chromatography: Evaluation of one-dimensional, comprehensive two-dimensional, and selective comprehensive two-dimensional liquid chromatography, J. Chromatogr. A, 1360 (2014) 128-142.

[122] M. Sarrut, F. Rouvière, S. Heinisch, Theoretical and experimental comparison of one dimensional versus on-line comprehensive two dimensional liquid chromatography for optimized sub-hour separations of complex peptide samples, J. Chromatogr. A, 1498 (2017) 183-195.

[123] M. Gilar, P. Olivova, A.E. Daly, J.C. Gebler, Orthogonality of Separation in Two-Dimensional Liquid Chromatography, Anal. Chem., 77 (19) (2005) 6426-6434.

[124] K.J. Mayfield, R.A. Shalliker, H.J. Catchpoole, A.P. Sweeney, V. Wong, G. Guiochon, Viscous fingering induced flow instability in multidimensional liquid chromatography, J. Chromatogr. A, 1080 (2) (2005) 124-131.

[125] D.R. Stoll, R.W. Sajulga, B.N. Voigt, E.J. Larson, L.N. Jeong, S.C. Rutan, Simulation of elution profiles in liquid chromatography − II: Investigation of injection volume overload under gradient elution conditions applied to second dimension separations in two-dimensional liquid chromatography, J. Chromatogr. A, 1523 (2017) 162-172.

[126] T.R. Covey, A.P. Bruins, J.D. Henion, Comparison of thermospray and ion spray mass spectrometry in an atmospheric pressure ion source, Org. Mass Spectrom., 23 (3) (1988) 178-186.

[127] J. Li, M. Chen, Y. Zhu, Separation and determination of carbohydrates in drinks by ion chromatography with a self-regenerating suppressor and an evaporative light-scattering detector, J. Chromatogr. A, 1155 (1) (2007) 50-56.

[128] J.J. Kirkland, M.A. van Straten, H.A. Claessens, High pH mobile phase effects on silica-based reversed-phase high-performance liquid chromatographic columns, J. Chromatogr. A, 691 (1) (1995) 3-19.

[129] D.R. Stoll, K. Shoykhet, P. Petersson, S. Buckenmaier, Active Solvent Modulation: A Valve-Based Approach To Improve Separation Compatibility in Two-Dimensional Liquid Chromatography, Anal. Chem., 89 (17) (2017) 9260-9267.

[130] X. Jiang, A. van der Horst, P.J. Schoenmakers, Breakthrough of polymers in interactive liquid chromatography, J. Chromatogr. A, 982 (1) (2002) 55-68.

[131] R.J. Vonk, A.F.G. Gargano, E. Davydova, H.L. Dekker, S. Eeltink, L.J. de Koning, P.J. Schoenmakers, Comprehensive Two-Dimensional Liquid Chromatography with Stationary-Phase-Assisted Modulation Coupled to High-Resolution Mass Spectrometry Applied to Proteome Analysis of Saccharomyces cerevisiae, Anal. Chem., 87 (10) (2015) 5387-5394.

[132] B.W.J. Pirok, N. Abdulhussain, T. Aalbers, B. Wouters, R.A.H. Peters, P.J. Schoenmakers, Nanoparticle Analysis by Online Comprehensive Two-Dimensional Liquid Chromatography combining Hydrodynamic Chromatography and Size-Exclusion Chromatography with Intermediate Sample Transformation, Anal. Chem., 89 (17) (2017) 9167-9174.

[133] A.F.G. Gargano, M. Duffin, P. Navarro, P.J. Schoenmakers, Reducing Dilution and Analysis Time in Online Comprehensive Two-Dimensional Liquid Chromatography by Active Modulation, Anal. Chem., 88 (3) (2016) 1785-1793.

[134] D.R. Stoll, E.S. Talus, D.C. Harmes, K. Zhang, Evaluation of detection sensitivity in comprehensive two-dimensional liquid chromatography separations of an active pharmaceutical ingredient and its degradants, Analytical and Bioanalytical Chemistry, 407 (1) (2015) 265-277.

[135] J.N. Dodds, J.C. May, J.A. McLean, Correlating Resolving Power, Resolution, and Collision Cross Section: Unifying Cross-Platform Assessment of Separation Efficiency in Ion Mobility Spectrometry, Anal. Chem., 89 (22) (2017) 12176-12184.

[136] K.R. Jennings, Collision-induced decompositions of aromatic molecular ions, International Journal of Mass Spectrometry and Ion Physics, 1 (3) (1968) 227-235.

[137] D. Douglas, Mechanism of the collision-induced dissociation of polyatomic ions studied by triple quadrupole mass spectrometry, The Journal of Physical Chemistry, 86 (2) (1982) 185-191.

[138] Y. Qi, D.A. Volmer, Electron-based fragmentation methods in mass spectrometry: An overview, Mass Spectrom. Rev., 36 (1) (2017) 4-15.

[139] B. Paizs, S. Suhai, Fragmentation pathways of protonated peptides, Mass Spectrom. Rev., 24 (4) (2005) 508-548.

[140] J.V. Olsen, B. Macek, O. Lange, A. Makarov, S. Horning, M. Mann, Higher-energy C-trap dissociation for peptide modification analysis, Nature Methods, 4 (9) (2007) 709-712.

[141] T.Y. Samgina, E.A. Vorontsov, V.A. Gorshkov, K.A. Artemenko, R.A. Zubarev, A.T. Lebedev, Mass spectrometric de novo sequencing of natural non-tryptic peptides: comparing peculiarities of collision-induced dissociation (CID) and high energy collision dissociation (HCD), Rapid Commun. Mass Spectrom., 28 (23) (2014) 2595-2604.

[142] Z. Guan, N.L. Kelleher, P.B. O'Connor, D.J. Aaserud, D.P. Little, F.W. McLafferty, 193 nm photodissociation of larger multiply-charged biomolecules, Int. J. Mass Spectrom. Ion Processes, 157-158 (1996) 357-364.

[143] E.A. Syrstad, F. Turecček, Toward a general mechanism of electron capture dissociation, J. Am. Soc. Mass. Spectrom., 16 (2) (2005) 208-224.

[144] J.E.P. Syka, J.J. Coon, M.J. Schroeder, J. Shabanowitz, D.F. Hunt, Peptide and protein sequence analysis by electron transfer dissociation mass spectrometry, Proceedings of the National Academy of Sciences, 101 (26) (2004) 9528-9533.

[145] P. Roepstorff, J. Fohlman, Letter to the editors, Biomedical Mass Spectrometry, 11 (11) (1984) 601-601.

[146] K. Biemann, Contributions of mass spectrometry to peptide and protein structure, Biomedical & Environmental Mass Spectrometry, 16 (1-12) (1988) 99-111.

[147] T.B. Coplen, J.K. Böhlke, P.D. Bièvre, T. Ding, N.E. Holden, J.A. Hopple, H.R. Krouse, A. Lamberty, H.S. Peiser, K. Revesz, S.E. Rieder, K.J.R. Rosman, E. Roth, P.D.P. Taylor, R.D. Vocke, Y.K. Xiao, Isotope-abundance variations of selected elements (IUPAC Technical Report), Pure Appl. Chem., 74 (10) (2002) 1987-2017.

[148] Z. Zhang, H. Pan, X. Chen, Mass spectrometry for structural characterization of therapeutic antibodies, Mass Spectrom. Rev., 28 (1) (2009) 147-76.

[149] M.J. MacCoss, IDCalc -- Isotope Distribution Calculator, 2008. https://proteome.gs.washington.edu/software/IDCalc/. (Accessed October 4th, 2023.

[150] H. Kubinyi, Calculation of isotope distributions in mass spectrometry. A trivial solution for a non-trivial problem, Anal. Chim. Acta, 247 (1) (1991) 107-119.

[151] Z. Zhang, H. Pan, X. Chen, Mass spectrometry for structural characterization of therapeutic antibodies, Mass Spectrom. Rev., 28 (1) (2009) 147-176.

[152] J.O. Kafader, R.D. Melani, L.F. Schachner, A.N. Ives, S.M. Patrie, N.L. Kelleher, P.D. Compton, Native vs Denatured: An in Depth Investigation of Charge State and Isotope Distributions, J. Am. Soc. Mass. Spectrom., 31 (3) (2020) 574-581.

[153] D.J. Reid, J.M. Diesing, M.A. Miller, S.M. Perry, J.A. Wales, W.R. Montfort, M.T. Marty, MetaUniDec: High-Throughput Deconvolution of Native Mass Spectra, J. Am. Soc. Mass. Spectrom., 30 (1) (2019) 118-127.

[154] C. Li, S. Chu, S. Tan, X. Yin, Y. Jiang, X. Dai, X. Gong, X. Fang, D. Tian, Towards Higher Sensitivity of Mass Spectrometry: A Perspective From the Mass Analyzers, Frontiers in Chemistry, 9 (2021).

[155] O.T. Schubert, L.C. Gillet, B.C. Collins, P. Navarro, G. Rosenberger, W.E. Wolski, H. Lam, D. Amodei, P. Mallick, B. MacLean, R. Aebersold, Building high-quality assay libraries for targeted analysis of SWATH MS data, Nature Protocols, 10 (3) (2015) 426-441.

[156] I.V. Chernushevich, A.V. Loboda, B.A. Thomson, An introduction to quadrupole–time-of-flight mass spectrometry, J. Mass Spectrom., 36 (8) (2001) 849-865.

[157] Y. Peng, X. Chen, T. Sato, S.A. Rankin, R.F. Tsuji, Y. Ge, Purification and High-Resolution Top-Down Mass Spectrometric Characterization of Human Salivary α-Amylase, Anal. Chem., 84 (7) (2012) 3339-3346.

[158] L. Fornelli, D. Ayoub, K. Aizikov, A. Beck, Y.O. Tsybin, Middle-down analysis of monoclonal antibodies with electron transfer dissociation orbitrap fourier transform mass spectrometry, Anal. Chem., 86 (6) (2014) 3005-12.

[159] I.D.G. Campuzano, C. Netirojjanakul, M. Nshanian, J.L. Lippens, D.P.A. Kilgour, S. Van Orden, J.A. Loo, Native-MS Analysis of Monoclonal Antibody Conjugates by Fourier Transform Ion Cyclotron Resonance Mass Spectrometry, Anal. Chem., 90 (1) (2018) 745-751.

[160] Y. Zhang, B.R. Fonslow, B. Shan, M.-C. Baek, J.R. Yates, III, Protein Analysis by Shotgun/Bottom-up Proteomics, Chem. Rev., 113 (4) (2013) 2343-2394.

[161] A.D. Catherman, O.S. Skinner, N.L. Kelleher, Top Down proteomics: facts and perspectives, Biochem. Biophys. Res. Commun., 445 (4) (2014) 683-93.

[162] P.D. Compton, L. Zamdborg, P.M. Thomas, N.L. Kelleher, On the Scalability and Requirements of Whole Protein Mass Spectrometry, Anal. Chem., 83 (17) (2011) 6868-6874.

[163] R.M. Miller, L.M. Smith, Overview and considerations in bottom-up proteomics, Analyst, 148 (3) (2023) 475-486.

[164] J.N. Dodds, E.S. Baker, Ion Mobility Spectrometry: Fundamental Concepts, Instrumentation, Applications, and the Road Ahead, J. Am. Soc. Mass. Spectrom., 30 (11) (2019) 2185-2195.

[165] A. Chrambach, D. Rodbard, Polyacrylamide Gel Electrophoresis, Science, 172 (3982) (1971) 440-451.

[166] E.A. Mason, H.W. Schamp, Mobility of gaseous lons in weak electric fields, Annals of Physics, 4 (3) (1958) 233-270.

[167] H.E. Revercomb, E.A. Mason, Theory of plasma chromatography/gaseous electrophoresis. Review, Anal. Chem., 47 (7) (1975) 970-983.

[168] J.C. May, C.R. Goodwin, N.M. Lareau, K.L. Leaptrot, C.B. Morris, R.T. Kurulugama, A. Mordehai, C. Klein, W. Barry, E. Darland, G. Overney, K. Imatani, G.C. Stafford, J.C. Fjeldsted, J.A. McLean,

Conformational Ordering of Biomolecules in the Gas Phase: Nitrogen Collision Cross Sections Measured on a Prototype High Resolution Drift Tube Ion Mobility-Mass Spectrometer, Anal. Chem., 86 (4) (2014) 2107-2116.

[169] T. Mairinger, T.J. Causon, S. Hann, The potential of ion mobility–mass spectrometry for non-targeted metabolomics, Curr. Opin. Chem. Biol., 42 (2018) 9-15.

[170] G.A. Eiceman, J.A. Stone, Peer Reviewed: Ion Mobility Spectrometers in National Defense, Anal. Chem., 76 (21) (2004) 390 A-397 A.

[171] M.A. Mäkinen, O.A. Anttalainen, M.E.T. Sillanpää, Ion Mobility Spectrometry and Its Applications in Detection of Chemical Warfare Agents, Anal. Chem., 82 (23) (2010) 9594-9600.

[172] R.T. Kurulugama, E. Darland, F. Kuhlmann, G. Stafford, J. Fjeldsted, Evaluation of drift gas selection in complex sample analyses using a high performance drift tube ion mobility-QTOF mass spectrometer, Analyst, 140 (20) (2015) 6834-6844.

[173] R. Kurulugama, K. Imatani, L. Taylor, The Agilent Ion Mobility Q-TOF Mass Spectrometer System - Technical Overview, Agilent Technolgies, www.agilent.com/chem, 2021.

[174] A. Baglai, A.F.G. Gargano, J. Jordens, Y. Mengerink, M. Honing, S. van der Wal, P.J. Schoenmakers, Comprehensive lipidomic analysis of human plasma using multidimensional liquid- and gas-phase separations: Two-dimensional liquid chromatography–mass spectrometry vs. liquid chromatography–trapped-ion-mobility–mass spectrometry, J. Chromatogr. A, 1530 (2017) 90-103.

[175] M.E. Belov, M.A. Buschbach, D.C. Prior, K. Tang, R.D. Smith, Multiplexed Ion Mobility Spectrometry-Orthogonal Time-of-Flight Mass Spectrometry, Anal. Chem., 79 (6) (2007) 2451-2462.

1.7 List of Figures

1.8 List of Tables

2 Objective of the Thesis

The main goal of the presented work was to develop new methods for the characterisation of proteins, peptides, and amino acids, which is important for applications such as clinical research, development of new biopharmaceuticals as well as their quality control. Protein-based biopharmaceuticals are becoming increasingly important as essential drug products for various therapeutic purposes. On the other hand, these biopharmaceuticals are more challenging to analyse than small molecules due to their high molecular weight and significant structural heterogeneity. Still, their comprehensive characterisation is of utmost importance for drug development and quality control. Hence, the aim of this dissertation was to develop new analytical liquid chromatographic and mass spectrometric methods to address the complexity of this class of pharmaceuticals.

Charge variants of monoclonal antibodies (mAbs) represent an important critical quality attribute (CQA) and must be thoroughly characterized. The gold standard for charge variant analysis is strong-cation exchange chromatography (SCX), but in most cases, SCX uses high amounts of non-volatile salts, which is incompatible with mass spectrometric detection (MS). The goal was to develop an MS-compatible method that can separate as much charge variants as possible (publication I), which was achieved using two-dimensional liquid chromatography (2D-LC) combining SCX in the first dimension and reversed-phase (RP) in the second dimension. The second goal was to optimize the RP separation in terms of the shortest possible analysis time to enable full comprehensive 2D-LC. For that purpose, different RP protein columns were evaluated, and the separation systematically optimized using a design of experiments (DoE) approach.

In a more comprehensive study, the kinetic performance of different RP protein columns was investigated with the goal of better understanding the critical column properties such as pore size, stationary phase chemistry, column morphology and particle size (publication II). Furthermore, one goal was to provide guidance to LC users for the choice of a suitable LC column. A set of 13 different RP columns with three different column morphologies, namely fully porous particle (FPP) columns, superficially porous particle (SPP) columns, and monolithic columns was used for the systematic investigation.

Drug products should be as specific for the potential target such as the anti-tumor protein p53 as possible. Consequently, the goal was to investigate whether different inhibitors bind to the tumour suppressor protein p53, which is a possible target for anti-cancer treatments. If an inhibitor binds, the extend of binding and number of equivalents of inhibitor, which bind to the proteins needs to be investigated as well. This is important in terms of the selectivity of the inhibitor binding to the target protein and can be achieved using LC-MS (publication III).

There is a high demand to increase the sample throughput for analytical methods to obtain faster results and reduce costs. Hence, an ultra-fast liquid chromatographic ion mobility-mass spectrometric method was developed to differentiate and quantify amino acid isomers. The method was successfully applied for the structure elucidation of a natural lipopeptide sample (publication IV and chapter 5.4).

Discrimination between the D- and L-enantiomers, constitutional isomers, and diastereomers of amino acids is an important prerequisite for quality control of food products and pharmaceuticals as well as for the structure elucidation of natural compounds. Therefore, the goal was to develop a new analytical method for the separation of different enantiomers and diastereomers of peptides to gain insight into their biological activity. The absolute configuration of the amino acids of the natural peptide-polyene antimicrobial epifadin was determined using enantioselective LC-MS (publication V, chapter 5.5).

3 Results and Discussion

3.1 Publication I: **Charge variant analysis of protein-based biopharmaceuticals using two-dimensional liquid chromatography hyphenated to mass spectrometry**

3.1.1 Manuscript

Simon Jaag[a], Marina Shirokikh[a], Michael Lämmerhofer[a,*]

[a] Pharmaceutical (Bio-)Analysis, Institute of Pharmaceutical Sciences, University of Tübingen, Auf der Morgenstelle 8, 72076 Tübingen, Germany

*Corresponding author:

E-mail address: michael.laemmerhofer@uni-tuebingen.de (M. Lämmerhofer)

Reprinted with permission from Journal of Chromatography A, 2019, 1636, 461786

DOI: 10.1016/j.chrom.2020.461786

Journal of Chromatography A 000 (2021) 461786

Contents lists available at ScienceDirect

Journal of Chromatography A

journal homepage: www.elsevier.com/locate/chroma

Charge variant analysis of protein-based biopharmaceuticals using two-dimensional liquid chromatography hyphenated to mass spectrometry

Simon Jaag, Marina Shirokikh, Michael Lämmerhofer*

Pharmaceutical (Bio-)Analysis, Institute of Pharmaceutical Sciences, University of Tübingen, Auf der Morgenstelle 8, 72076 Tübingen, Germany

ARTICLE INFO

Article history:
Received 7 September 2020
Revised 16 November 2020
Accepted 6 December 2020
Available online xxx

Keywords:
Strong cation-exchange chromatography
Two-dimensional chromatography
Monoclonal antibodies
Biopharmaceuticals
Charge variant analysis
Mass spectrometry

ABSTRACT

The profile of charge variants represents an important critical quality attribute of protein-based biopharmaceuticals, in particular of monoclonal antibodies, and must therefore becontrolled. In this work, 2D-LC methods for charge variant analysis were developed using a strong cation-exchange chromatography (SCX) as first dimension (^{1}D) separation. Non-porous SCX (3 µm) particle columns and different mobile phases were evaluated using a test mixture of some standard proteins of different size and p*I* (comprising myoglobin, bovine serum albumin, cytochrome c, lysozyme and β-lactoglobulin) and two monoclonal IgG1 antibodies (NIST mAb and Secukinumab). The most promising ^{1}D eluent for SCX was a salt-mediated pH-gradient system using a ternary mobile phase system with 2-(*N*-morpholino)ethanesulfonic acid, 1,3-diamino-2-propanol and sodium chloride. For the second dimension (^{2}D), a desalting reversed-phase liquid chromatography (RP-LC) was chosen to enable the hyphenation of the charge variant separation with mass spectrometric (MS) detection. While for intact mAbs the ^{2}D just served for desalting without additional selectivity, the ^{2}D contributed some orthogonal selectivity for the mAb fragment separation. Various core-shell and monolithic columns were tested and variables such as gradient time and flow rate systematically optimized. Unexpectedly, a C4 400 Å column (3.4 µm diameter with 0.2 µm porous shell) provided higher peak capacities compared to the same 1000 Å column (2.7 µm diameter with 0.5 µm porous shell). A thinner shell appeared to be more advantageous than wider pores under high flow regime. An ultra-fast RP-LC method with a run time of one minute was developed using trifluoroacetic acid which was later replaced by formic acid as additive for better MS compatibility. The successful hyphenation of the two orthogonal separation modes, SCX and RP-LC, could be demonstrated in the multiple heart-cutting and the full comprehensive mode. MS analysis using a high-resolution quadrupole time-of-flight instrument enabled to identify different glycoforms and some major charge variants of the antibody at the intact protein level as well as on the subunit level (Fc/2, Lc, Fd') in a middle-up approach by 2D-LC-ESI-MS analysis.

1. Introduction

Biopharmaceuticals are a fast-growing sector of innovative drugs which are becoming more and more important [1]. From January 2014 to July 2018, 155 biopharmaceuticals have been approved in the US and/or EU, with monoclonal antibodies (mAbs) being the largest group with 68 approvals (44%) [1]. A fundamental difference between monoclonal antibodies and small molecule drugs is the much higher molecular weight and structural complexity of the molecule. Antibodies are characterized by large molecular heterogeneity, resulting from different charge variants, glycoforms and other post-translational modifications, which make their analysis challenging [2,3].

The different charge variants of antibodies have different efficacy and immunogenicity, and must therefore be tightly controlled. Causes for different charge variants include C-terminal lysine clipping, deamidation, glycation, sialic acid bound to N- or O-glycans, adduct formation, succinimide formation or oxidations [4]. For the separation of charge variants, both electrophoresis and ion exchange chromatography (IEX) can be used [5–7]. Cation exchange chromatography (CEX), especially with strong cation exchangers (SCX), is considered the gold standard, since most antibodies have a slightly basic isoelectric point [7–9]. Often non-porous (NP) particles are preferred nowadays, as they do not suffer from intra-particulate mass transfer resistance and therefore

---

* Corresponding author.
E-mail address: michael.laemmerhofer@uni-tuebingen.de (M. Lämmerhofer).

https://doi.org/10.1016/j.chroma.2020.461786

provide better performance [10]. For elution, salt-gradients, pH-gradients or a combination of both can be employed, which is called salt-mediated pH-gradient [11]. IEX is a separation technique in which the proteins retain their native form, in contrast to reversed-phase liquid chromatography (RP-LC), which is denaturing [8]. The frequent use of non-volatile salts and high salt concentrations in IEX makes its coupling with mass spectrometry a challenging task. Direct coupling using volatile salts has already been described in the literature [8,12]. The use of a salt-mediated pH-gradient increases the possibilities in method development and has proven to be advantageous. 2-(*N*-morpholino)ethanesulfonic acid (MES) and 1,3-diamino-2-propanol (DAP) have proven to be suitable buffer salts and the combination with a sodium chloride gradient further reduces the peak width [11]. To enable MS detection, an online de-salting can be performed with two-dimensional chromatography (2D-LC). RP-LC is inherently MS-compatible with the signal being strongly dependent on the composition of the mobile phase, especially additives. Ion pair reagents reduce the peak width in protein separations considerably but suppress the MS signal (ion suppression) [13]. A good MS signal can be obtained with formic acid (FA), but this is at the expense of the peak width and peak shape (tailing) [13,14].

In the case of biopharmaceuticals, special attention must be paid to the design of the stationary phase. The pore size must be large enough to allow unhindered diffusion of the molecules into the pores. Otherwise, large proteins may experience a partial or total pore exclusion effect with insufficient retention and selectivity [15,16]. With increasing pore size, however, the specific surface area decreases and the retentive effect is reduced as well [16–18]. For analytical applications this is less problematic due to steep (i.e. high initial slope of) adsorption isotherms (indicative for high affinity due to multipoint attachment) and application of gradient elution [16]. Typical pore sizes of stationary phases dedicated for protein separations are in the range between 300 and 1000 Å [14,15]. For particle-based columns, the particle design (morphology) is also decisive for the chromatographic performance: Totally porous particles (TPP) are usually inferior to superficially porous particles (SPP) or nonporous particles (NPP) as they may have excessive mass transfer resistance [17]. SPPs have a reduced mass transfer resistance because intraparticulate diffusion only takes place in the porous shell and thus the diffusion distance is significantly shorter. Monolithic silica columns have also been promoted for protein separations. Monolithic (silica) columns, which consist of a continuous polymer bed, have a lower mass transfer resistance and additionally low back pressures but may suffer from bed irregularities [19].

The type of ligand on the stationary phase determines the adsorption of the proteins, thus C4 alkyl ligands are often preferred to C18, especially when hydrophobic proteins are to be analysed. Secondary interactions of free silanol groups can be decreased by end capping. The temperature has a significant influence on the separation as at elevated temperatures the recovery rate is significantly increased and peak width reduced due to accelerated diffusion rates [14,17,20]. For this reason, protein separations are frequently performed at elevated column temperatures.

Hyphenation of IEX to MS was recently reviewed by Farsang et al. discussing both the direct coupling using volatile buffer salts in the mobile phase as well as de-salting through the ^{2}D of a 2D-LC method [8]. Sorensen et al. compared the charge variant profile of three original/biosimilar pairs after IdeS-digestion and TCEP-reduction (middle-up approach) and coupled weak cation exchange chromatography (WCX) to MS via RP in the full comprehensive mode (WCX × RP-MS) in which the entire ^{1}D effluent is transferred to the ^{2}D [21]. A multi-dimensional (4D-LC) approach was established by Goyon et al. using CEX (^{1}D), online reduction (^{2}D), trypsin digestion (^{3}D, bottom-up approach) and RP-LC (^{4}D) [22]. Only selected fractions from the ^{1}D effluent were transferred to the ^{2}D (multiple heart-cutting). A similar 4D-LC setup was presented by Gstöttner et al. with a NaCl salt-gradient and MES buffer system for the ^{1}D WCX separation [23]. The selective comprehensive 2D-LC is an intermediate form between heart-cutting and full comprehensive mode in which only a certain elution range of the ^{1}D is comprehensively transferred to the ^{2}D; it was applied by Stoll et al. for the charge variant analysis of Rituximab (sWCXxRP-MS) with a NaCl salt-gradient in a MES buffer system in the ^{1}D [24]. Similarly, several other publications are also related to the optimization of 2D-LC [25,26] and the analysis of biopharmaceuticals or proteins [27–31].

The goal of the current work is the analysis of charge variants with mass spectrometric detection. To avoid overlap of charge envelopes from distinct charge variants in ESI-MS, their separation prior to MS detection is required. RP has good MS compatibility but lacks selectivity for different charge isoforms. CEX exhibits adequate selectivity but necessitates MS-incompatible conditions. Therefore, an online full comprehensive 2D-LC with RP as ^{2}D is used for de-salting and increasing the peak capacity. A recently published buffer system [11] is utilized for elution on the SCX in the ^{1}D by ternary salt-mediated pH-gradient. Two SCX columns from different manufacturers have been evaluated. Different RP columns were compared and their suitability for ultra-fast separation in ^{2}D is discussed. Finally, the successful hyphenation of the SCX × RP 2D-LC to MS is shown.

2. Experimental

2.1. Materials

Di-sodium hydrogen phosphate anhydrous and thiourea were purchased from Applichem (Darmstadt, Germany). FragIT (immobilized IdeS enzyme) was supplied by Genovis (Luden, Sweden). Acetic acid ($\geq$ 99.8%) and sodium dihydrogen phosphate monohydrate from Merck (Darmstadt, Germany). NIST monoclonal antibody (NISTmAb) reference material (RM) 8671, a humanized IgG1k monoclonal antibody formulated in histidine buffer, was purchased from the National Institute of Standards and Technologies (NIST, Gaithersburg, MD, USA). Cosentyx (Secukinumab) was supplied by Novartis (Nuremberg, Germany). Methanol, ammonium hydroxide 25% solution, tris(2-carboxyethyl)phosphine (TCEP), sodium chloride, potassium chloride, and sodium hydroxide, lysozyme from chicken egg white, cytochrome c from equine heart, β-lactoglobulin B from bovine milk ($\geq$90%) and bovine serum albumin (BSA), 1,3-diamino-2-propanol (DAP) Protein LoBind Tubes 1.5mL from Eppendorf were purchased from Sigma-Aldrich (Merck, Taufkirchen, Germany). Myoglobin from equine heart was from Calbiochem and supplied by Merck. 2-(*N*-morpholino)ethanesulfonic acid monohydrate (MES) was from Fluka and supplied by Merck. Chromolith WP300 RP-4 (4.6 × 50 mm, C4-modified monolithic silica column), BIOshell 400 Å Protein C4 (2.1 × 50 mm, 3.4 µm), BIOshell IgG 1000 Å C4 (2.1 × 20 mm & 2.1 × 50 mm, 2.7 µm) columns were purchased from Merck. Aeris Widepore C4 200 Å (2.1 × 50 mm, 3.6 µm) and ProSwift RP-2H (4.6 × 50 mm, monolithic) column were supplied by Phenomenex (Aschaffenburg, Germany). Bio SCX NP3 column was purchased from Agilent (Waldbronn, Germany) and the Proteomix SCX-NP3 column (2.1 × 100 mm) was purchased from Sepax Technologies (Newark, Delaware, USA). The properties of the columns are summarized in supplementary **Table S 1.** Ultrapure water was obtained from a Purelab Ultra purification system from Elga LabWater (Celle, Germany).

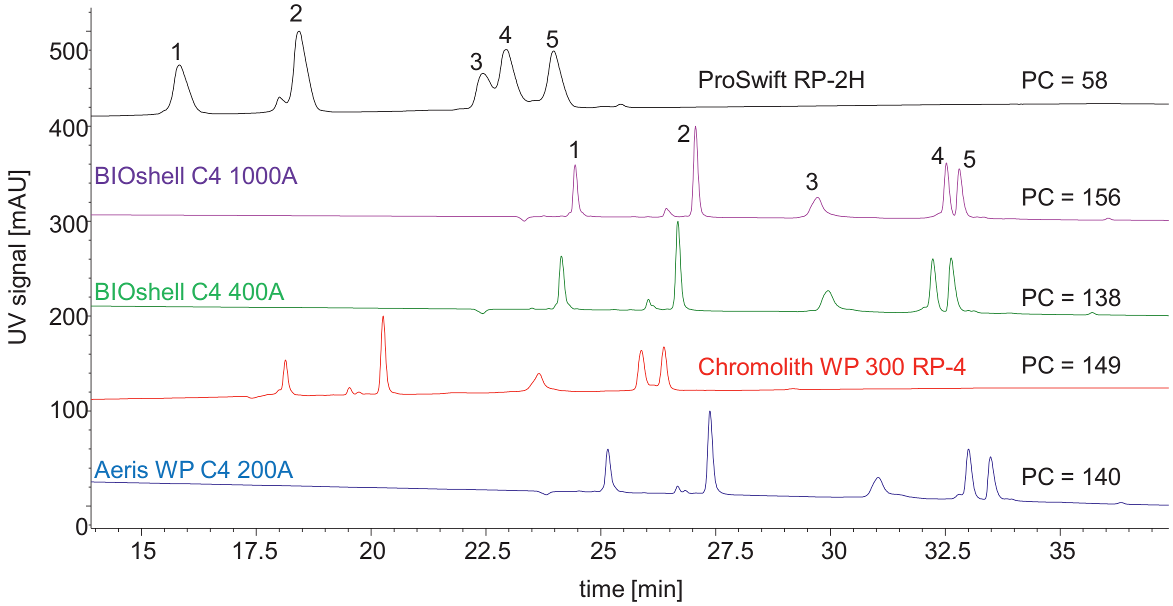

Fig. 1. Chromatograms of the separation of a protein mixture using five different RP-columns. The peak capacity (P_C) calculated for peak 2 is shown in the figure. Gradient: 0-2 min 10% B, 2-32 min 10-50% B, 32-37 min 50% B, 37-47 min 10% B; temperature: 40°C; flow rate: 0.21 mL/min (monoliths: 1 mL/min); solvent A: water: ACN (98:2, v/v) + 0.1% TFA, Solvent B: ACN: water (98:2) + 0.1% TFA. Samples: (1) Cytochrome c (12.4 kDa, p*I* 10.0-10.5), (2) Lysozyme (14.3 kDa, p*I* 11.35), (3): BSA (66.4, p*I* 4.7-4.9), (4): Myoglobin (17.0 kDa, p*I* 7.0), (5): β-Lactoglobulin (18.3 kDa, p*I* 5.13).

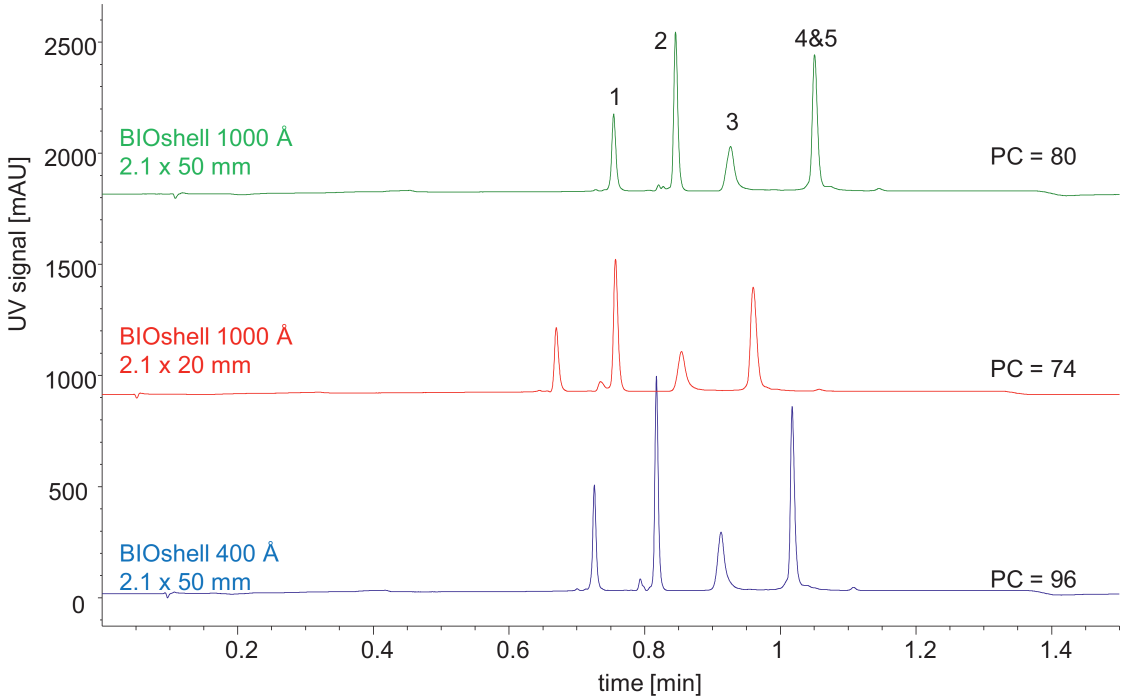

Fig. 2. Fast RP-separation of protein mixture: Gradient: 10-50% B in 1 min; temperature: 50°C; flow rate: 1.2 mL/min; solvent A: water: ACN (98:2, v/v) + 0.1% TFA; solvent B: ACN: water (98:2, v/v) + 0.1% TFA; P_C: peak capacity calculated for peak 2; samples: (1): Cytochrome c, (2): Lysozyme, (3): BSA, (4): Myoglobin, (5): β-Lactoglobulin.

2.2. Instrumentation and software

All LC-instruments were from Agilent Technologies (Waldbronn, Germany). 1D-LC column evaluations were carried out with an Agilent 1100 HPLC system consisting of binary pump (G1312A), autosampler (G1329A), thermostated column compartment (G1316A), variable wavelength detector (G1314A) and degasser (G1322A) as well as with an Agilent 1290 Infinity UHPLC system consisting of binary pump (G4220A), autosampler (G4226A), sample thermostat (G1130B), thermostated column compartment (G1316C) and diode array detector (DAD, G4212A). 2D-LC experiments were performed with an Agilent 1290 Infinity II 2D-LC solution consisting of a quaternary (flexible) pump (G7104A), multisampler (G7167B), multicolumn compartment (G7116B) and variable wavelength UV detector, G7114B, 14 µL flow cell) in the first dimension. A pressure relief kit (G4236-60010) was installed between UV detector and 2D-LC interface. The second dimension consisted of a binary pump (G7120A), multi-column compartment (G7116B), DAD (G7117B with 1 µL flow cell) and valve drives (G1170A). In the full comprehensive mode, a 5pos/10port 2D-LC active solvent modulation (ASM)

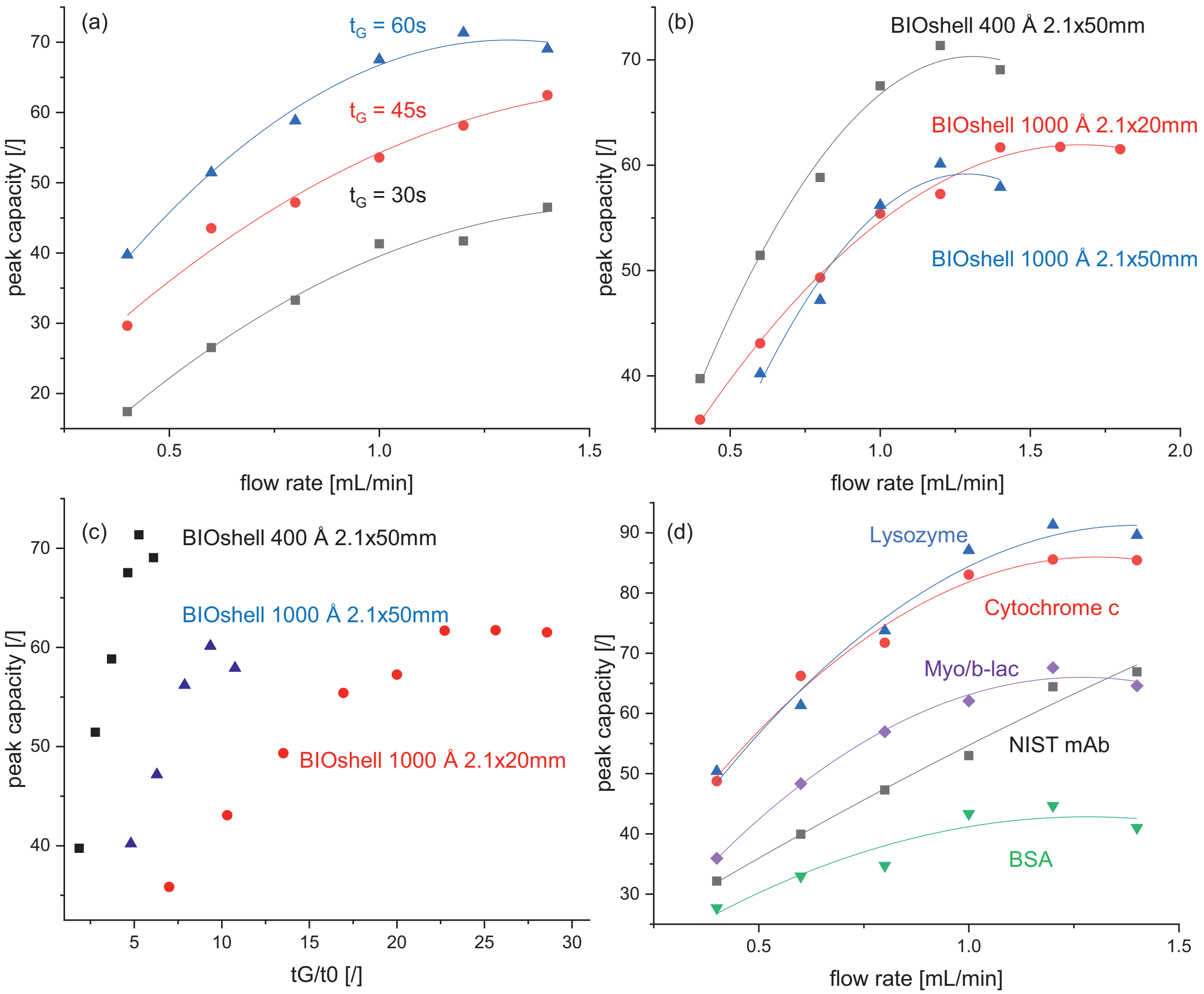

Fig. 3. Evaluation of influence of flow rate on peak capacity. Ultra-fast separations performed using UHPLC with solvent A: water: ACN (98:2, v/v) + 0.1% TFA; solvent B: ACN: water (98:2, v/v) + 0.1% TFA, gradient: 10-50%B, temperature: 50°C, detection: 214nm. (a) the average peak capacity (P_C) of the protein mixture plotted against the flow rate for different gradient times (t_G) for the BIOshell 400Å column. (b) average P_C of protein mixture against flow rate for different BIOshell columns at $t_G = 60$ s. (c) average P_C of protein mixture plotted against t_G/t_0 for different BIOshell columns at $t_G = 60$ s. (d) P_C of the NIST mAb and the protein mixture (average P_C) plotted against the flow rate for the BIOshell 400Å 2.1 × 50mm column $t_G = 60$ s.

valve (#5067-4266) was connected to two sampling loops (#5067-5926) with 40 µL volume. In the multiple heart-cutting mode a 5pos/10port 2D-LC ASM Valve (#5067-4266) was connected to two 6pos/14port valve heads (#5067-4142) (loop deck A and loop deck B) carrying six 40 µL loops each. A 2pos/6port valve (#5067-4282) was used as diverter valve in the 2D-LC-MS setup between the DAD and the QTOF for de-salting in connection with a T-piece (see supplementary **Figure S 1** & **Figure S 2**). Instrument control and data analysis were performed using Open Lab CDS Rev. C.01.07 SR4. GC image LCxLC HRMS V2.7 Edition Software (GC Image, Lincoln, Nebraska, USA) was used to create the contour plots. Chromatographic conditions are specified in the respective figure captions or otherwise in the supplementary material.

Mass spectrometric detection was performed on a Sciex TripleTOF 5600+ instrument (QTOF-MS) (Sciex, Darmstadt, Germany). QTOF-MS measurements were performed using a Duospray ion source (ESI interface) in positive ionization mode. The following MS instrument parameters were used: curtain gas (CUR) 35 psi, ion source gas (nebulizing gas; GS1) 50 psi, heater gas (drying gas; GS2) 40 psi, ion spray voltage floating (ISVF) 5100 V, source temperature (TEM) 550°C, collision energy (CE) 30V and a declustering potential (DP) 230 V. The mass range in the TOF MS was from 500 to 5000 Da with an accumulation time of 500 ms. Data acquisition was performed with Analyst TF 1.7 software (Sciex). Microsoft Excel (Redmond, WA, USA) and Origin (OriginLab, Northapton, MA, USA) were used for data processing. Mass peak assignment was performed using an open source software tool called MoFi [32].

2.3. Sample preparation

A stock solution of the protein samples with a concentration of 5 mg/mL was prepared with water. The stock solutions were diluted 1:5 to get the final concentration of the pure proteins (c = 1 mg/mL). A mixture of the five proteins with a concentration of 1 mg/mL for each protein was prepared by mixing the five stock solutions in equal proportion. NIST mAb was diluted from a concentration of 10 mg/mL to 1 mg/mL with water.

IdeS digestion was performed with FragIT MicroSpin columns following the manufacturer's instructions with a cleavage buffer composed of 10 mM Na_2HPO_4, 140 mM NaCl and 2.7 mM KCl. 20 µL of the antibody solution (c = 10 mg/mL) was diluted with 80 µL cleavage buffer. For digestion this reaction mixture was incubated for 30 min at 37°C and 250 rpm. For further reduction, 20 µL of a 50 mM TCEP solution was added and incubated for 60 min at

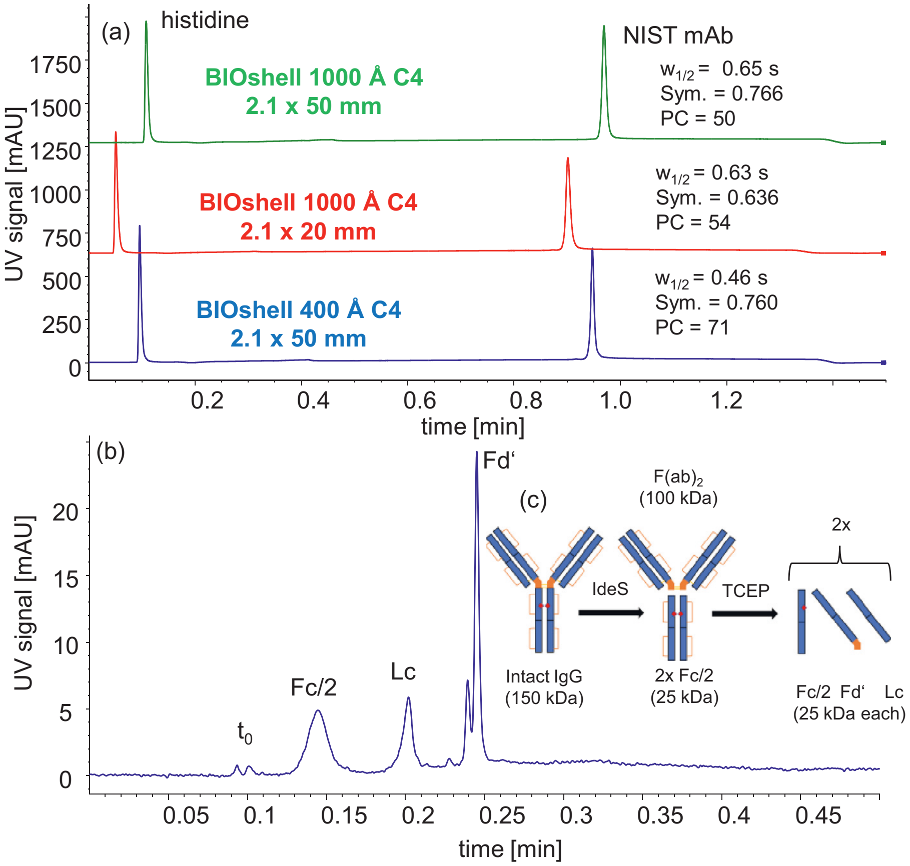

Fig. 4. Ultra-fast separations of intact NIST mAb and subunits. (a) Intact NIST mAb. Gradient: 10-50% B in 1 min; temperature: 50°C; flow rate: 1.2 mL/min; solvent A: water: ACN (98:2, v/v) + 0.1 % TFA; solvent B: ACN: water (98:2, v/v) + 0.1% TFA, detection 214 nm. (b) Fragments obtained after IdeS-digestion and TCEP-reduction. Column: BIOshell Protein C4 400Å, flow rate 1.2 mL/min; mobile phase A: water/ACN 98:2 (v/v) + 0.1% TFA, B: ACN/water 98:2 (v/v) + 0.1% TFA, gradient: 32-85% B in 0.25 min, 85% B 0.25-0.37 min, 32% B 0.38 – 0.5 min; temperature: 50°C; injection volume: 1 µL; detection: 280 nm. (c) Subunit preparation workflow.

60°C and 250 rpm. Subsequently, the buffer was exchanged three times with a Vivaspin 500 spin column (MWCO 10,000) with 10 mM ammonium acetate buffer pH 6.0 at 12 000 g for 5 min.

2.4. Calculations

The comparison of the chromatographic performance of the different columns in gradient separations was performed using the peak capacity (P_C). The peak capacity represents the maximum number of peaks that can be fitted into the chromatographic window between the first and the last eluting peak. Herein, P_Cs were calculated assuming $Rs = 1$ using a simplified equation:

$$P_C = 1 + \frac{t_G - t_0}{W_{4\sigma}} \tag{1}$$

wherein t_{first} was t_0 in this work, with t_0 being the elution time of a non-retained compound (dead time) and t_{last} was t_G, being the gradient (run) time. $w_{4\sigma}$ is the peak width at 4σ.

U.D. Neue described the dependence of P_C on experimental parameters of gradient RPLC for large molecules (like peptides and proteins) by Eq. (1) [33,34]:

$$P_C = 1 + \frac{\sqrt{N}}{4} \cdot \frac{S \cdot \Delta c}{G + 1} \tag{2}$$

wherein N is the column plate number, S is the slope of the plot of ln k vs. organic solvent content (φ), Δc the solvent span between initial and final organic content (φ_{end}-φ_0), and G the gradient steepness factor with

$$G = S \cdot \Delta c \cdot \frac{t_0}{t_G} \tag{3}$$

In a more explicit expression, in which N is substituted by L/H, Eq. (1) can be written as [33]

$$P_C = 1 + \frac{1}{4} \cdot \sqrt{\frac{L}{A \cdot d_p + ((B \cdot t_0)/L) + C \cdot d_p^2 \cdot (L/t_0)}} \cdot \frac{S \cdot \Delta c}{S \cdot \Delta c \cdot \left(\frac{t_0}{t_G}\right) + 1} \tag{4}$$

Wherein A, B, C are the coefficients of the van Deemter equation, d_p is the particle diameter and L the column length.

3. Results and discussion

3.1. Comparison of reversed-phase columns and HPLC conditions

The first step was to develop a suitable RP separation method for the ^{2}D. Therefore, different RP columns (see supplementary **Table S 1**) were evaluated. Except for a poly(styrene-co-divinylbenzene) (PS/DVB) monolith column, all columns contained silica based stationary phases with C4 alkyl ligand based on silica monolith and core-shell particles. The initial separations were performed using a generic linear gradient method using trifluoroacetic acid (TFA) as ion-pairing additive. TFA is known to provide sharper peaks than formic acid as additive and can be used as benchmark for performance evaluations [14]. A standard protein mixture containing five proteins with different size and pI (BSA, cytochrome c, lysozyme, myoglobin and β-lactoglobulin, see Suppl. **Table S 2** for properties) was selected to probe for the chromatographic performance for proteins in the molecular weight range from 12 to 66 kDa. A comparison of the five RP-columns showed similar performance of the Aeris Widepore C4 (200 Å), Chromolith WP300

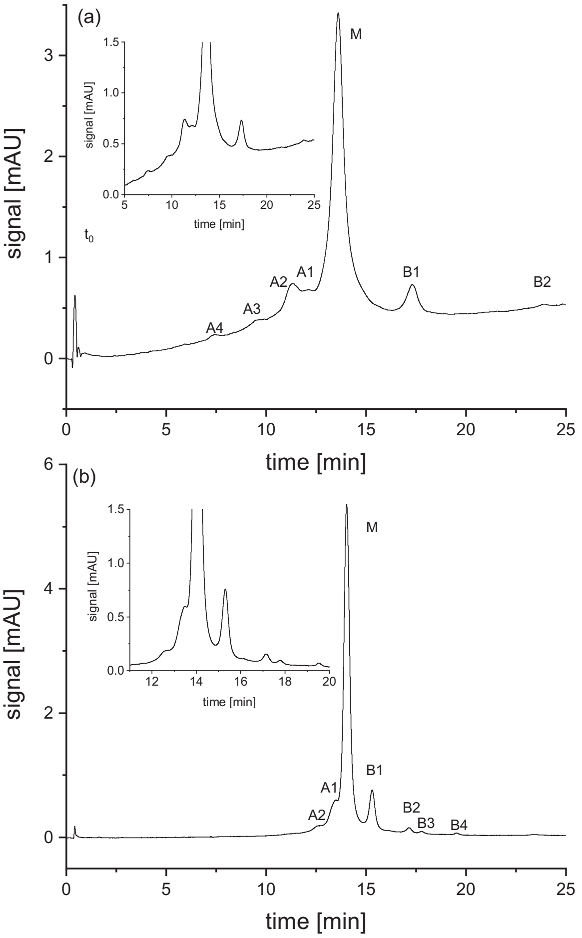

Fig. 5. Charge variant analysis of intact NIST mAb. A1-4: acidic charge variants, B1-4 basic charge variants, M: main charge variant. Column: Agilent Bio SCX, NP3, 3 µm, 2.1 × 100 mm; flow rate: 0.5 mL/min; temperature: 25°C; injection volume: 2 µL; detection: 280 nm. (a) gradient: 80-100% B in 24 min, 100% B from 24-25 min, 80% B from 25-30 min; mobile phase A: 20 mM MES/20 mM DAP (90:10; v/v), B: 20 mM MES/20 mM DAP (30:70 v/v). (b) gradient: 0-24 min: 59.8-42.0% A, 32.2-42.0% B, 8.0-16.0% C; 24-25 min: 42.0% A, 42.0 %B, 16.0% C; 25-30 min: 59.8% A, 32.2% B, 8.0% C; mobile phase A: 20 mM MES/20 mM DAP (90:10; v/v), B: 20 mM MES/20 mM DAP (30:70 v/v), C: 500 mM NaCl in water.

RP-4 (mesopore size of 300 Å, macropore diameter of 2 µm) and both BIOshell C4 columns (400 and 1000 Å) with peak capacities ranging from 138 to 156 (as assessed by peak capacity for peak 2, lysozyme) (see **Fig. 1**). The ProSwift RP-2H column showed also excellent selectivity but its chromatographic efficiency was lower (peak capacity of 58), most probably due to suboptimal pore structure for these analytes. The macropores of ProSwift RP-2H (2.23 µm modal pore diameter) are too large for small sized proteins and the corresponding PS/DVB monolith with smaller 1 µm pore size (RP-1S) was not available for this study. The retention times of the three SPP columns were quite similar with the Aeris WP column (200 Å, 3.6 µm particle diameter with 0.2 µm porous shell) having the highest retention and the BIOshell C4 400 Å column (3.4 µm diameter with 0.2 µm porous shell) with the lowest retention. The lower peak capacity (140) and the higher retention of the Aeris WP column could be the result of the small pore size (200 Å) which can lead to hindered pore diffusion on the one hand leading to broader peaks but an increase in the surface area on the other hand enhancing the retention. The both BIOshell columns, however, showed the opposite trend: The BIOshell C4 1000 Å column (2.7 µm diameter with 0.5 µm porous shell) had a higher retention and a higher peak capacity (156 vs. 138) compared to the BIOshell C4 400 Å column. The particles of both columns not only differ in their pore and particle size (2.7 and 3.4 µm for the 1000 Å and 400 Å column, respectively) but also in their shell thickness (0.5 µm and 0.2 µm). The thicker silica shell of the 1000 Å SPP seems to offer a totally larger interactive surface per column and the wider pores are providing unhindered pore diffusion [18] which is favorable in terms of mass transfer and chromatographic efficiencies, thus explaining the slightly higher peak capacities. The Chromolith WP300 RP-4 showed also exceptional performance (P_C 149) and surprisingly outperformed the SPP columns with similar mesopore size (200 and 400 Å).

3.2. Development of an ultra-fast method for ^{2}D of 2D-LC

The second step of method development was to evaluate the column performance under UHPLC conditions and ultra-fast separations. High flow rates, steep gradients and appropriate pressure resistance of the employed column are important requirements to achieve this goal. The aim was to develop a short method suitable for the ^{2}D in a full comprehensive 2D-LC method. Therefore, assuming ^{1}D peak widths of 1-2 min the overall ^{2}D method cycle time (^{2}D gradient time ^2t_G and ^{2}D re-equilibration time $^2t_{re\text{-}eq}$) should be significantly below one minute to avoid excessive undersampling. As long as the selectivity between the charge isoforms is large enough, a slight undersampling would, however, not compromise the goal of the study. The monolithic columns could not be used because of low pressure resistances (maximal pressure recommended ~ 200 bar; see supplementary **Table S 1**). Consequently, only the SPP containing columns could be tested. Aeris Widepore C4 200 Å was omitted due to its lower P_C in above comparison. The three BIOshell columns were finally selected for this comparison: the 1000 Å column showed the most promising performance in terms of peak capacity and the influence of the pore size (400 vs. 1000 Å) should be evaluated. It was anticipated that slow pore diffusion and high mass transfer resistance, respectively, are the limiting factors for fast protein separations. Wider pores should be beneficial. The 1000 Å column was available in two lengths: the 20 mm column should provide faster separations than the 50 mm column, but is more prone to volume overloading due to large $^2V_{\text{inj}}$ (sampling from ^{1}D). All 3 tested columns had an inner diameter of 2.1 mm in order to minimize the volumetric flow to remain within a range that can be handled by the ESI source. With wider ^{2}D column diameters a flow splitting prior to ESI is recommended.

The resultant chromatograms for the same protein test mixture as above are shown in **Fig. 2**. Somehow counterintuitive and in contrast to above results, the BIOshell 400 Å column had the highest peak (96) capacity of all three columns. The superior performance can be explained by the thinner shell (0.2 µm thickness for the 400 Å column compared to 0.5 µm for the 1000 Å column) which obviously is more beneficial under fast flow regime than wider pores and is in agreement with the literature [35]. The thinner porous shell is advantageous in terms of shorter diffusion paths reducing mass transfer resistance. The small pore size of 400 Å is still large enough to enable unhindered diffusion of the proteins. Pore sizes of 400 Å have been found to be suitable for molecules up to a molecular weight of 500 kDa [17]. While at a low flow rate (0.5 mL/min) and HPLC conditions the BIOshell 1000 Å column performed better than the BIOshell 400 Å column the opposite behaviour was found under UHPLC conditions (fast flow regime in which less time for diffusional mass transfer is available). The difference between the peak capacities of the two 1000 Å columns can be simply explained by the column lengths (50 vs. 20 mm) providing larger plate numbers for the longer column. The larger retention time of the 1000 Å column (50 mm) in comparison to the 400 Å column indicates that more total interactive surface is available in the column with the thicker shell.

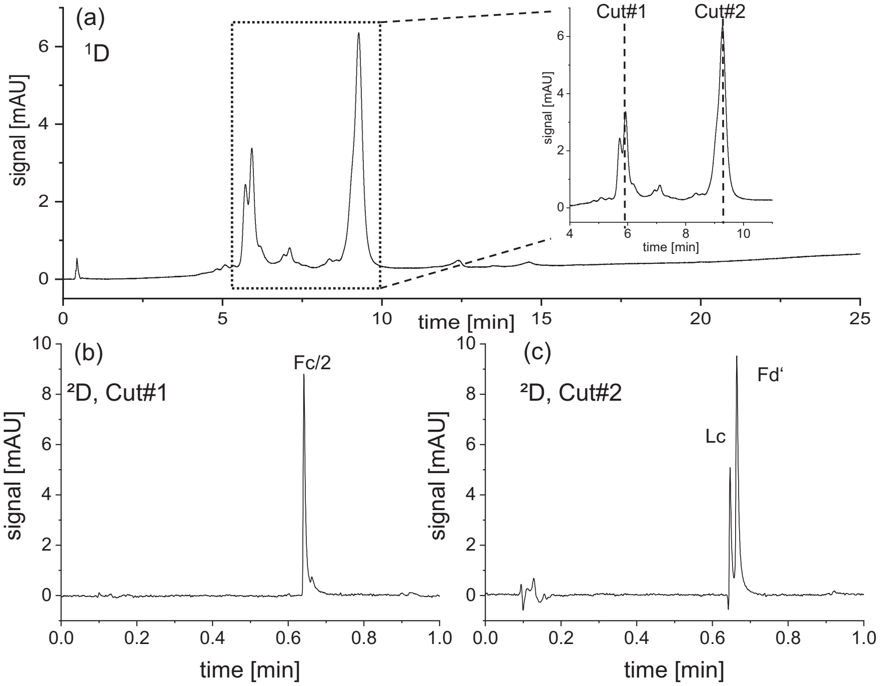

Fig. 6. 2D-LC separation of NIST-IdeS-TCEP sample in multiple heart cutting mode. (a) ^{1}D SCX chromatogram. (b) ^{2}D RP chromatogram of cut #1 containing the Fc/2 fragment and (c) ^{2}D-chromatogram of cut #2 separating the light chain (Lc) and the Fd'-fragment. The same conditions for the ^{1}D separation were used as described in Fig. 5b except of the gradient profile: 0-10 min: 0-30% B and 8% C, 10-24 min 30-70% B and 8-30% C. ^{2}D: 0-0.4 min 5% B; 0.4-0.65 min 5-95% B at 1.2 mL/min; modulation time: 1 min; A: water/ACN 98:2 + 0.1% FA (v/v); B: ACN/water 98:2 +0.1% FA (v/v); temperature: 50°C; injection volume: 4 µL; column: BIOshell Protein C4 400Å 2.1 × 50 mm. For further conditions refer to the supplementary Table S 5.

Once column and mobile phase composition are fixed, solvent span, flow rate and gradient time are available as further variables for optimization of the separation according to Eq. (4). The dependency of the peak capacity on the flow rate and gradient time (t_G 60, 45, and 30 s) is shown in **Fig. 3**. Increasing the gradient time t_G at constant flow rate (constant t_0) provides higher peak capacities as t_0/t_G is decreasing (see Eq. (4) and **Fig. 3a**). Superior peak capacities of the BIOshell 400 Å column could be confirmed over the entire flow rate range (see **Fig. 3b**). The flow rate optimum in terms of the highest peak capacity for the BIOshell 400 Å column and the 50 mm long BIOshell 1000 Å was 1.2 mL/min. Apparently, above this flow rate the lower gradient steepness G (see Eq. (3)) cannot overcompensate the increase in mass transfer resistance any more. The shorter 20 mm BIOshell 1000 Å column has its optimum at higher flow rates (1.4-1.8 mL/min) and provides at these flow rates slightly higher peak capacities than the longer 50 mm column with same pore size. **Fig. 3c** shows the increase of peak capacity with t_G/t_0 for the BIOshell 400 Å and BIOshell 1000 Å (50mm) column. The shorter 20 mm BIOshell 1000 Å column is reaching a plateau at higher t_G/t_0 values. The peak capacity vs. flow rate dependency is plotted in **Fig. 3d** for different protein samples. Similar plots with a maximum peak capacity at 1.2 mL/min were observed for all except the NIST mAb. BSA had the lowest peak capacity even in comparison to the intact NIST mAb what can be explained by its molecular dispersity contributing to peak broadening [36].

The method was subsequently optimized for a monoclonal antibody (namely the NIST mAb) with a higher molecular mass (148.2 kDa, see supplementary **Table S 3**) compared to the standard protein mixture. The BIOshell 400 Å column still showed the highest peak capacity (71) for the NIST mAb (see **Fig. 4a**) while the BIOshell 1000 Å columns had almost the same peak capacities (50 & 54 for the 50 and 20 mm long columns, respectively). Therefore, the BIOshell 400 Å column still outperforms the 1000 Å columns although the sample has a significantly higher molecular mass. This is somehow surprising because the 1000 Å columns are specifically designed to separate monoclonal antibodies [18]. It seems that 400 Å is still large enough to enable unhindered diffusion. Moreover, the shell thickness of the 400 Å column (0.2 µm) is significantly smaller than that of the 1000 Å column (0.5 µm) resulting in a higher effective mass transfer resistance for the thicker shell. The similar peak capacities of the 1000 Å columns with different lengths indicate that even 20 mm short columns are suitable for the separation, most probably due to an efficient refocussing as a consequence of steep adsorption isotherms of large biomolecules. **Fig. 4b** shows the separation of the NIST mAb subunits obtained after IdeS-digestion and subsequent TCEP-reduction (**Fig. 4c**). It was possible to separate all three main fragments (Fc/2-, Fd'-fragment & light chain, all of around 25 kDa) within 30 seconds. The Fd'-fragment provided two peaks which could be due to different intrachain disulphide forms (no, one or two disulphide bonds) [37] or D(P)-clipping resulting in pQ_1-D_{88} and P_{89}-G_{239}-fragments [38]. This ultra-fast RP-separation is suitable for the use in a full comprehensive 2D-LC analysis.

3.3. Charge variant analysis with strong cation exchange chromatography (^{1}D separation)

The goal of the charge variant analysis was to get as many charge variants separated as possible which was deemed to be a prerequisite for their successful characterization and the comprehensive quality control of therapeutic proteins. Non-porous particle-based SCX columns from two different suppliers were evaluated, one from Agilent (Bio SCX NP 3 µm) and the second from Sepax (Proteomix SCX NP 3 µm) both having nearly the same specifications and features. The non-porous particle design provides reduced mass transfer resistance and the particles are grafted with a hydrophilic polymer layer which decreases any secondary interactions of the stationary phase. The use of PS/DVB as support

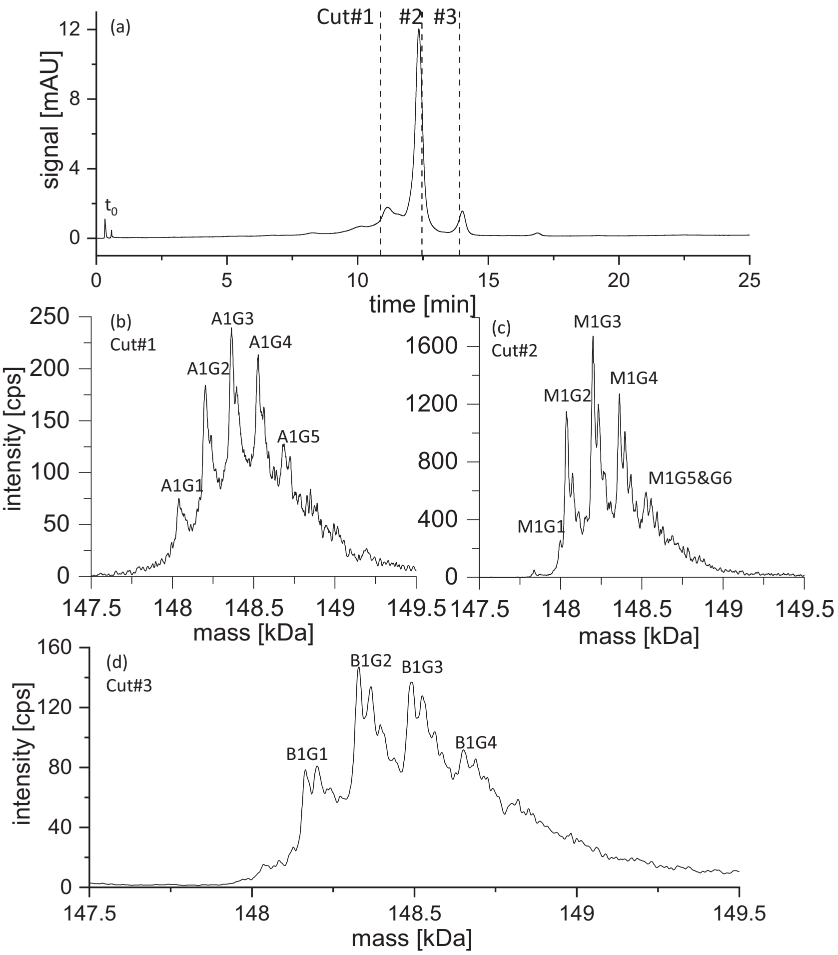

Fig. 7. Multiple heart cutting 2D-LC of NIST mAb. (a) ^{1}D-SCX chromatogram. Cuts indicated with vertical dashed lines. (b-d) Reconstructed mass of cut#1 to #3 revealing the glycoforms of the acidic (A1G1-5), main (M1G1-6) and basic (B1G1-4) charge variants. The same conditions for the ^{1}D separation were used as described in Fig. 5b except of the gradient profile: 0-5 min: 0-84% B 0% C, 5-24 min: 84-98% B 0-2% C; injection volume: 10 µL. For the ^{2}D the same conditions as described in Fig. 6 were used. Further conditions are provided in the supplementary Table S 6 and a peak table in Table S 6.

enables the use of a broad pH range (pH 2 to 12) increasing the design space of pH-gradients. The two columns showed virtually identical separations using a pure pH gradient with almost perfect overlapping of the resolved isoform peaks indicating equivalent performance (see supplementary Figure S 3). The overlay of the chromatograms of the two columns gives a perfect match. As no significant difference between both columns was found, the Bio SCX NP 3 µm column was selected for further experiments.

Several mobile phase systems were evaluated which include three elution modes of IEX: (i) pure salt-gradient, (ii) pure pH-gradient and (iii) salt-mediated pH-gradient representing the combination of the first two modes (see supplementary **Figure S 4** for exemplary chromatograms obtained with distinct buffer systems). A systematic investigation of the factors gradient steepness of the B-solvent (high pH) and the C-solvent (NaCl) as well as the starting concentration of the B-solvent was carried out for intact Secukinumab and is provided in the supplementary (see **Figures S 11-13** and **Table S 11**). After investigating the factors for Secukinumab a method was developed for the NIST mAb as well. The best result (in terms of number of resolved charge isoforms) was obtained using a pure pH-gradient with 20 mM MES/20 mM DAP buffer system at a ratio of MES/DAP 90:10 (v/v; pH = 5.6) as mobile phase A and 30:70 (v/v; pH = 9.9) as mobile phase B running a linear gradient from 80-100% B in 24 min (Fig. 5**a**). At least four acidic variants (A1-4) could be separated as well as two basic variants (B1, B2). However, the peaks were quite broad ($w_{1/2}$ = 0.61 min for the main charge variant, see supplementary **Table S 4**). The addition of sodium chloride provided sharper peaks ($w_{1/2}$ = 0.39 min for the main charge variant), but the resolution of the acidic charge variants deteriorated. On the other hand, some further basic variants could be detected (B3 and B4) (Fig. 5**b**). This charge variants pattern is in good agreement in terms of number of resolved isoforms with a reference electropherogram provided by NIST (see supplementary **Figure S 5**) which shows three acidic variants and two major basic variants. These basic variants result from additional C-terminal lysine residue at one and both heavy chains, respectively [39]. On contrary, the main charge variant (M) has no C-terminal lysine anymore.

3.4. Two-dimensional separations

The next step was to hyphenate the MS-incompatible, charge isoform-selective SCX method with the MS-compatible RP method in an online 2D-LC setup. Two distinct 2D-LC modalities were evaluated: i) Multiple heart cutting and ii) full comprehensive 2D-LC. The used instrumental setup is the same for the two modes except for the interface between ^{1}D and ^{2}D. The quaternary pump in the ^{1}D provided high flexibility for method development as allowed to generate more complex gradients, i.e. mixed pH, buffer, and modifier gradients. UV detectors after ^{1}D column (VWD) and ^{2}D column (DAD) allowed to record chromatograms in each separation dimension. The high speed UHPLC pump with low dwell volume

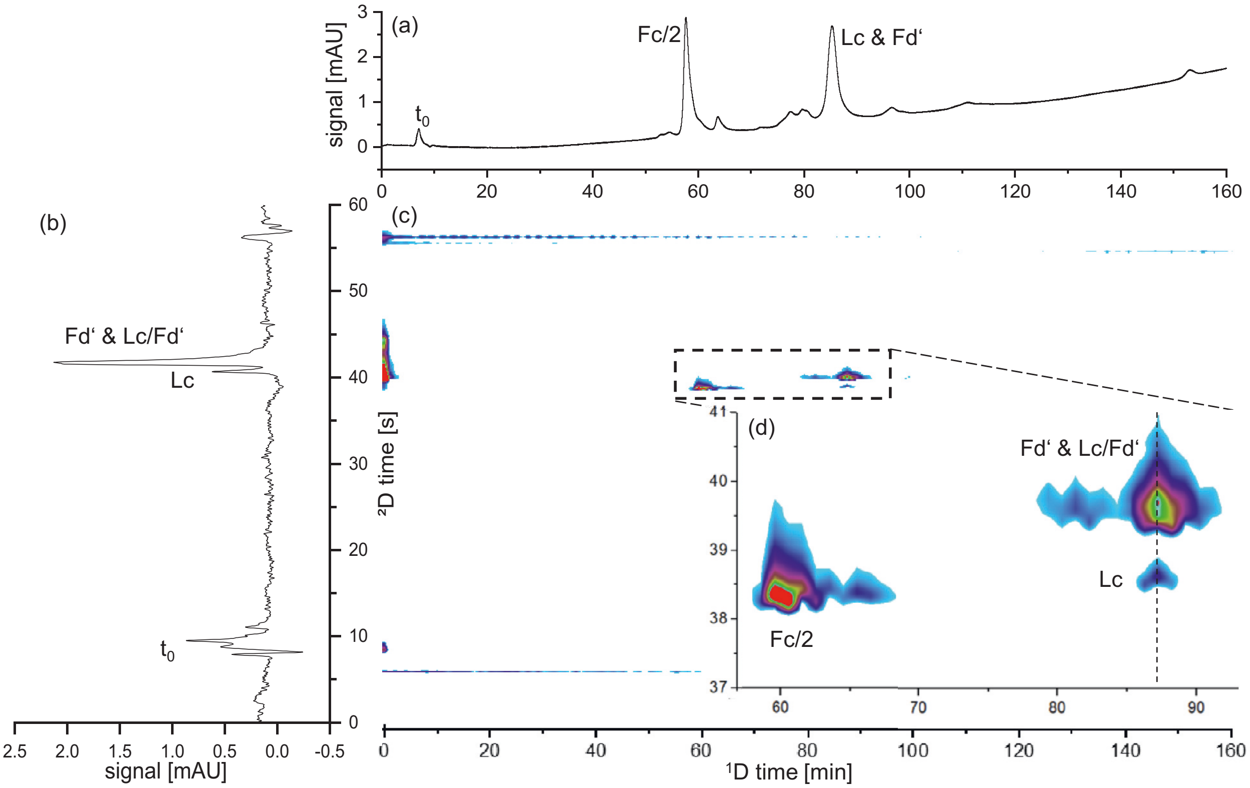

Fig. 8. 2D-LC separation of NIST-IdeS-TCEP sample in full comprehensive mode. (a) Separation of the Fc/2-fragment from light chain (Lc) and Fd'-fragment and several charge variants in the ^{1}D SCX. (b) ²D chromatogram of the cut 87-88 min showing the separation of Lc and Fd'-fragment, (c) contour plot of the SCX × RP separation. (d) zoom-in of the contour plot with a vertical dashed line highlighting the cut shown in panel (b). The same conditions for the ^{1}D separation were used as described in Fig. 5b except of the gradient profile: 0-150 min: 0-80% B and 4-12% C; flow rate: 30 µL/min. For the ²D the same conditions as described in Fig. 6 were used. For further the conditions refer to supplementary Table S 8.

(~120 µL) enabled fast separations in the ^{2}D. The two dimensions were connected by an ASM valve as interface with two 40 µL loops, which are alternatingly employed for sampling and analysis, in the full comprehensive 2D-LC mode and equipped with two loop decks each one having six 40 µL loops for sample storage for the multiple heart cutting mode (as depicted in supplementary **Figure S 1** and **Figure S 2**).

For the reversed-phase method in the ²D method we determined first the minimum de-salting time using a charged aerosol detector (CAD) and varying the time in which the ²D flow is directed to the waste. A minimum de-salting time of 0.4 min was found as suitable. After the re-equilibration time was determined, we just used a linear gradient starting after 0.4 min. A short washing period of 0.1 min at 95 % B should be sufficient to elute strongly retained compounds.

3.4.1. Multiple heart-cutting

First, a multiple heart cutting SCX-RP method was developed. In the ^{1}D, the quaternary pump was utilized to mix a ternary mobile phase system with a pH-gradient from 5.6 to 9.9 in mobile phase A and B, respectively, and sodium chloride in mobile phase C to superimpose a salt-gradient which provided sharper peaks compared to the pure pH-gradient as mentioned above. The NIST mAb fragment mixture (Fc/2, Lc, Fd') was analysed. In the ^{1}D, the Fc/2-fragment could be well separated from the other two fragments, light chain and Fd'-fragment (see **Fig. 6a**). Two fractions were collected in the sampling loops of the interface valve, one from the peak at 5.92 min and the other at 9.32 min (loop filling 100%). The two fractions from the SCX separation were subsequently analysed by RPLC with the BIOshell 400 Å C4 column (50 mm length) using 60 s gradients. Formic acid as mobile phase additive is MS-compatible and, owing to steep gradients (5 to 95% B within 0.25 min, i.e. 15 s), provided sufficiently sharp peaks for the separation of the NIST mAb fragments. The first 24 s (0.4 min) were directed to waste with the diverter valve installed after the ^{2}D DAD detector. The first cut showed only a single peak in the ^{2}D which corresponded to the Fc/2-fragment. In this case, the ²D therefore served just as a de-salting step (**Fig. 6b**). The other two subunits (Lc & Fd') co-eluted in the ^{1}D (cut #2), however, they could be resolved in the ^{2}D (**Fig. 6c**).

The charge variant separation for the intact NIST mAb is shown in **Fig. 7a** (for conditions see supplementary **Table S 6)** with three cuts for an acidic, the main and a basic charge variant (cut#1-3), respectively. The deconvoluted mass spectra are provided in **Fig. 7b-d.** In each spectrum, the main glycoforms of the respective charge variant could be resolved. The main charge variant has no C-terminal lysine at any of the heavy chains while the most abundant basic charge variant has one C-terminal lysine at one of the heavy chains (for details see **Table S 7** and [40]). The most abundant acidic charge variant could be the result of deamidation yielding a mass difference of only one Dalton which is difficult to resolve at the intact protein level. In fact, several deamidated species have been identified in the literature for the intact NIST mAb [40].

3.4.2. Full comprehensive mode

In the full comprehensive 2D-LC mode a slightly different instrumental setup was used in which the interface valve was equipped with two 40 µL loops (see supplementary **Figure S 2**). The ultra-fast method of the ^{2}D had only a run time of 45 s and a cycle time including re-equilibration of 60 s. Consequently, this ²D RP method could be directly used for full comprehensive SCX × RP mode without further modifications. The flow rate of

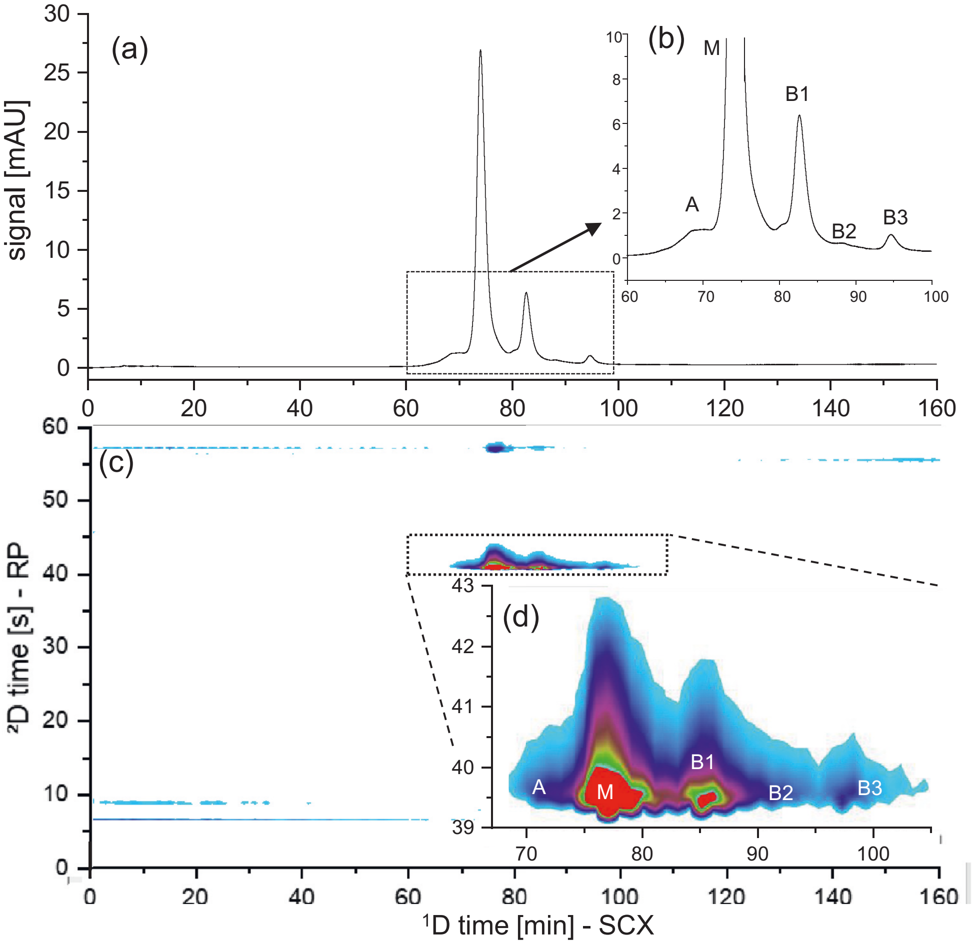

Fig. 9. Full comprehensive 2D-LC separation of the intact Secukinumab. (a) ^{1}D SCX chromatogram with a zoom-in of the elution window (b), the corresponding contour plot (c) and zoom-in (d). An acidic charge variant (A), the main charge variant (M) and three basic charge variants (B1-3) could be separated. The same conditions for the ^{1}D separation were used as described in Fig. 5b except of the gradient profile: 0-150min: 23-40% B and 4-12% C; flow rate: 30 µL/min. For the ^{2}D the same conditions as described in Fig. 6 were used. For further conditions refer to supplementary Table S 10.

the ^{1}D was reduced from 0.5 mL/min to 30 µL/min enabling the transfer of the entire effluent from the ^{1}D to the ^{2}D. A fraction of 30 µL ^{1}D effluent was taken every minute (75% loop filling) and injected into the ^{2}D. Active solvent modulation was not required, however, the effluent of the first part of the ^{2}D chromatogram (0 to 0.4 min) was again directed to waste with the diverter valve. Using the optimized conditions for both the SCX separation and the RP separation it was possible to establish a full comprehensive SCX × RP-separation of the IdeS-digested and TCEP-reduced NIST mAb (**Fig. 8**). The 2D-contour plot shows that, unlike in the one-dimensional separations, all three main fragments (Fc/2, Fd' and light chain) could be separated as well as some charge variants. The separation obtained in the 2D-LC-UV method between the light chain and the Fd'-subunit was partly lost in the ESI-MS coupling due to additional extra-column volume from transfer capillary and ESI-sprayer (see supplementary **Figure S 6a & b**). The still existing separation, however, can be visualized using extracted ion chromatograms (XICs) which demonstrate some selectivity between the light chain and Fd'-subunit that elutes a few seconds later (see supplementary **Figure S 6c & d**). Hyphenation of this SCX-UV × RP-DAD 2D-LC separation with ESI-QTOF-MS enabled the identification of the fragment peaks (see supplementary **Figure S 7** and **Figure S 8**). Due to additional dilution effects of the ^{2}D, the sensitivity was not enough to identify the low abundant charge variants with current low protein quantities injected (corresponding to 1 µg). If minor charge isoforms should be identified, higher sample loads are recommended. The Fc/2- and the F(ab)$_2$-subunits of the NIST mAb after IdeS-digestion could be also well separated and some charge variants were observed (see supplementary **Figure S 9**). The separation of the intact NIST mAb by full comprehensive SCX-UV × RP-DAD shows satisfying separation of the basic charge variants (see supplementary **Figure S 10a & b**). However, the superimposed sodium chloride gradient led to worse separation of the acidic charge variants compared to the pure pH-gradient (**Fig. 5**). The contour plot shows besides the main charge isoform weak spots for the three basic isoforms and a shoulder for the acidic isoforms in front of the main peak (see supplementary **Figure S 10c & d**). The ^{2}D serves here only as de-salting step for MS-compatibility as no selectivity for isoforms was provided.

Finally, the SCX × RP 2D-LC method was adapted for the analysis of Secukinumab as a second biopharmaceutical. Conditions were optimized by a design of experiment approach (see Suppl.). Therefore, the SCX method was slightly changed (see supplementary **Table S 10**). The starting ratio of the B solvent (high pH) was lower (23%) compared to the NIST mAb (48%). The ^{1}D chromatogram shows the separation of several charge variants, especially the basic ones are well separated (see **Fig. 9**). The charge isoform separation is visible in the contour plot which again shows that the selectivity is entirely related to the SCX separation. As for the NIST mAb, no further separation took place in the ^{2}D which, however, was necessary for desalting to enable subsequent MS-detection.

4. Conclusions

Charge variant analysis is a critical quality attribute for protein-based biopharmaceuticals such as monoclonal antibodies. The gold standard for the charge variant analysis is ion-exchange chromatography which usually employs non-volatile salts which make it incompatible for direct coupling to electrospray ionization-mass spectrometry. The current work showed the successful hyphenation of mass spectrometry and two-dimensional chromatography. It enabled the identification of some major charge variants. From the evaluated mobile phases for SCX the MES/DAP buffer system combined with a sodium chloride gradient showed the best results for charge variant separation in combination with a non-porous sulfonated cation-exchanger. Several mAb charge variants could be resolved chromatographically at the intact protein level as well as on the subunit level. A couple of RP columns were tested for the suitability as ^{2}D column and an ultra-fast method was developed for desalting in the ^{2}D prior to ESI-MS. Subunits of the monoclonal antibodies were successfully separated und the main glycoforms could be identified using MS in both the full comprehensive and the multiple heart-cutting mode.

Declaration of Competing Interest

The authors declare that they have no known competing financial interests or personal relationships that could have appeared to influence the work reported in this paper.

CRediT authorship contribution statement

Simon Jaag: Investigation, Methodology, Formal analysis, Data curation, Visualization, Writing - original draft, Writing - review & editing. **Marina Shirokikh:** Investigation. **Michael Lämmerhofer:** Conceptualization, Methodology, Supervision, Writing - review & editing, Resources, Funding acquisition.

Acknowledgements

We are grateful to Agilent Technologies for support of this research by an Agilent Research Award (#4068). The authors thank Dr. Stephan Buckenmaier (Agilent Technologies, Waldbronn, Germany) and Prof. Dr. Dwight R. Stoll (Department of Chemistry, Gustavus Adolphus College, Saint Peter, Minnesota, USA) for technical advice and valuable discussions. We thank Dr. Benjamin Peters from Merck KGaA, Darmstadt, Germany for generous gift of research samples of Chromolith columns.

Supplementary materials

Supplementary material associated with this article can be found, in the online version, at doi:10.1016/j.chroma.2020.461786.

References

[1] G. Walsh, Biopharmaceutical benchmarks 2018, Nat. Biotechnol. 36 (12) (2018) 1136–1145, doi:10.1038/nbt.4305.

[2] A. Beck, E. Wagner-Rousset, D. Ayoub, A. Van Dorsselaer, S. Sanglier-Cianférani, Characterization of therapeutic antibodies and related products, Anal. Chem. 85 (2) (2013) 715–736, doi:10.1021/ac3032355.

[3] K. Sandra, M. Steenbeke, I. Vandenheede, G. Vanhoenacker, P. Sandra, The versatility of heart-cutting and comprehensive two-dimensional liquid chromatography in monoclonal antibody clone selection, J. Chromatogr. A 1523 (2017) 283–292, doi:10.1016/j.chroma.2017.06.052.

[4] Y. Du, A. Walsh, R. Ehrick, W. Xu, K. May, H. Liu, Chromatographic analysis of the acidic and basic species of recombinant monoclonal antibodies, mAbs 4 (5) (2012) 578–585, doi:10.4161/mabs.21328.

[5] G. Ponniah, C. Nowak, A. Neill, H. Liu, Characterization of charge variants of a monoclonal antibody using weak anion exchange chromatography at subunit levels, Anal. Biochem. 520 (2017) 49–57, doi:10.1016/j.ab.2016.12.017.

[6] X. Zhang, L. Chemmalil, J. Ding, N. Mussa, Z. Li, Imaged capillary isoelectric focusing in native condition: a novel and successful example, Anal. Biochem. 537 (2017) 13–19, doi:10.1016/j.ab.2017.08.014.

[7] A. Goyon, M. Excoffier, M.C. Janin-Bussat, B. Bobaly, S. Fekete, D. Guillarme, A. Beck, Determination of isoelectric points and relative charge variants of 23 therapeutic monoclonal antibodies, J. Chromatogr. B Analyt. Technol. Biomed. Life Sci. 1065-1066 (2017) 119–128, doi:10.1016/j.jchromb.2017.09.033.

[8] E. Farsang, D. Guillarme, J.-L. Veuthey, A. Beck, M. Lauber, A. Schmudlach, S. Fekete, Coupling non-denaturing chromatography to mass spectrometry for the characterization of monoclonal antibodies and related products, J. Pharm. Biomed. Anal. 185 (2020) 113207, doi:10.1016/j.jpba.2020.113207.

[9] A. Murisier, M. Lauber, S.J. Shiner, D. Guillarme, S. Fekete, Practical considerations on the particle size and permeability of ion-exchange columns applied to biopharmaceutical separations, J. Chromatogr. A 1604 (2019) 460487, doi:10.1016/j.chroma.2019.460487.

[10] S. Fekete, A. Beck, J.-L. Veuthey, D. Guillarme, Ion-exchange chromatography for the characterization of biopharmaceuticals, J. Pharm. Biomed. Anal. 113 (2015) 43–55, doi:10.1016/j.jpba.2015.02.037.

[11] E. Farsang, A. Murisier, K. Horváth, A. Beck, R. Kormány, D. Guillarme, S. Fekete, Tuning selectivity in cation-exchange chromatography applied for monoclonal antibody separations, part 1: Alternative mobile phases and fine tuning of the separation, J. Pharm. Biomed. Anal. 168 (2019) 138–147, doi:10.1016/j.jpba.2019.02.024.

[12] Y. Leblanc, V. Faid, M.A. Lauber, Q. Wang, N. Bihoreau, G. Chevreux, A generic method for intact and subunit level characterization of mAb charge variants by native mass spectrometry, J. Chromatogr. B 1133 (2019) 121814, doi:10.1016/j.jchromb.2019.121814.

[13] M.C. Garcıá, A.C. Hogenboom, H. Zappey, H. Irth, Effect of the mobile phase composition on the separation and detection of intact proteins by reversed-phase liquid chromatography–electrospray mass spectrometry, J. Chromatogr. A 957 (2) (2002) 187–199, doi:10.1016/S0021-9673(02)00345-X.

[14] D.V. McCalley, D. Guillarme, Evaluation of additives on reversed-phase chromatography of monoclonal antibodies using a 1000 Å stationary phase, J. Chromatogr. A (2019) 460562, doi:10.1016/j.chroma.2019.460562.

[15] W. Chen, K. Jiang, A. Mack, B. Sachok, X. Zhu, W.E. Barber, X. Wang, Synthesis and optimization of wide pore superficially porous particles by a one-step coating process for separation of proteins and monoclonal antibodies, J. Chromatogr. A 1414 (2015) 147–157, doi:10.1016/j.chroma.2015.08.043.

[16] R. Hahn, Methods for characterization of biochromatography media, J. Sep. Sci. 35 (22) (2012) 3001–3032, doi:10.1002/jssc.201200770.

[17] S.A. Schuster, B.M. Wagner, B.E. Boyes, J.J. Kirkland, Optimized superficially porous particles for protein separations, J. Chromatogr. A 1315 (2013) 118–126, doi:10.1016/j.chroma.2013.09.054.

[18] B.M. Wagner, S.A. Schuster, B.E. Boyes, T.J. Shields, W.L. Miles, M.J. Haynes, R.E. Moran, J.J. Kirkland, M.R. Schure, Superficially porous particles with 1000Å pores for large biomolecule high performance liquid chromatography and polymer size exclusion chromatography, J. Chromatogr. A 1489 (2017) 75–85, doi:10.1016/j.chroma.2017.01.082.

[19] A.M. Siouffi, About the C term in the van Deemter's equation of plate height in monoliths, J. Chromatogr. A 1126 (1) (2006) 86–94, doi:10.1016/j.chroma.2006.05.036.

[20] B. Bobály, M. Lauber, A. Beck, D. Guillarme, S. Fekete, Utility of a high coverage phenyl-bonding and wide-pore superficially porous particle for the analysis of monoclonal antibodies and related products, J. Chromatogr. A 1549 (2018) 63–76, doi:10.1016/j.chroma.2018.03.043.

[21] M. Sorensen, D.C. Harmes, D.R. Stoll, G.O. Staples, S. Fekete, D. Guillarme, A. Beck, Comparison of originator and biosimilar therapeutic monoclonal antibodies using comprehensive two-dimensional liquid chromatography coupled with time-of-flight mass spectrometry, MAbs 8 (7) (2016) 1224–1234, doi:10.1080/19420862.2016.1203497.

[22] A. Goyon, L. Dai, T. Chen, B. Wei, F. Yang, N. Andersen, R. Kopf, M. Leiss, M. Mølhøj, D. Guillarme, C. Stella, From proof of concept to the routine use of an automated and robust multi-dimensional liquid chromatography mass spectrometry workflow applied for the charge variant characterization of therapeutic antibodies, J. Chromatogr. A 1615 (2020) 460740, doi:10.1016/j.chroma.2019.460740.

[23] C. Gstöttner, D. Klemm, M. Haberger, A. Bathke, H. Wegele, C. Bell, R. Kopf, Fast and automated characterization of antibody variants with 4D HPLC/MS, Anal. Chem. 90 (3) (2018) 2119–2125, doi:10.1021/acs.analchem.7b04372.

[24] D.R. Stoll, D.C. Harmes, J. Danforth, E. Wagner, D. Guillarme, S. Fekete, A. Beck, Direct identification of rituximab main isoforms and subunit analysis by online selective comprehensive two-dimensional liquid chromatography–mass spectrometry, Anal. Chem. 87 (16) (2015) 8307–8315, doi:10.1021/acs.analchem.5b01578.

[25] B.W.J. Pirok, A.F.G. Gargano, P.J. Schoenmakers, Optimizing separations in online comprehensive two-dimensional liquid chromatography, J. Sep. Sci. 41 (1) (2018) 68–98, doi:10.1002/jssc.201700863.

[26] B.W.J. Pirok, D.R. Stoll, P.J. Schoenmakers, Recent developments in two-dimensional liquid chromatography: fundamental improvements for practical applications, Anal. Chem. 91 (1) (2019) 240–263, doi:10.1021/acs.analchem.8b04841.

[27] L. Wang, H.K. Trang, J. Desai, Z.D. Dunn, D.D. Richardson, R.K. Marcus, Fiber-based HIC capture loop for coupling of protein A and size exclusion chromatography in a two-dimensional separation of monoclonal antibodies, Anal. Chim. Acta 1098 (2020) 190–200, doi:10.1016/j.aca.2019.11.023.

[28] A.F.G. Gargano, J.B. Shaw, M. Zhou, C.S. Wilkins, T.L. Fillmore, R.J. Moore, G.W. Somsen, L. Paša-Tolić, Increasing the separation capacity of intact histone proteoforms chromatography coupling online weak cation exchange-HILIC to reversed phase LC UVPD-HRMS, J. Proteome Res. 17 (11) (2018) 3791–3800, doi:10.1021/acs.jproteome.8b00458.

[29] A. Ehkirch, A. Goyon, O. Hernandez-Alba, F. Rouviere, V. D'Atri, C. Dreyfus, J.-F. Haeuw, H. Diemer, A. Beck, S. Heinisch, D. Guillarme, S. Cianferani, A novel online four-dimensional SEC×SEC-IM×MS methodology for characterization of monoclonal antibody size variants, Anal. Chem. 90 (23) (2018) 13929–13937, doi:10.1021/acs.analchem.8b03333.

[30] D.R. Stoll, D.C. Harmes, G.O. Staples, O.G. Potter, C.T. Dammann, D. Guillarme, A. Beck, Development of comprehensive online two-dimensional liquid chromatography/mass spectrometry using hydrophilic interaction and reversed-phase separations for rapid and deep profiling of therapeutic antibodies, Anal. Chem. 90 (9) (2018) 5923–5929, doi:10.1021/acs.analchem.8b00776.

[31] K. Sandra, G. Vanhoenacker, I. Vandenheede, M. Steenbeke, M. Joseph, P. Sandra, Multiple heart-cutting and comprehensive two-dimensional liquid chromatography hyphenated to mass spectrometry for the characterization of the antibody-drug conjugate ado-trastuzumab emtansine, J. Chromatogr. B 1032 (2016) 119–130, doi:10.1016/j.jchromb.2016.04.040.

[32] W. Skala, T. Wohlschlager, S. Senn, G.E. Huber, C.G. Huber, MoFi: a software tool for annotating glycoprotein mass spectra by integrating hybrid data from the intact protein and glycopeptide level, Anal. Chem. 90 (9) (2018) 5728–5736, doi:10.1021/acs.analchem.8b00019.

[33] U.D. Neue, Peak capacity in unidimensional chromatography, J. Chromatogr. A 1184 (1) (2008) 107–130, doi:10.1016/j.chroma.2007.11.113.

[34] A. Fernández-Pumarega, J.L. Dores-Sousa, S. Eeltink, A comprehensive investigation of the peak capacity for the reversed-phase gradient liquid-chromatographic analysis of intact proteins using a polymer-monolithic capillary column, J. Chromatogr. A 1609 (2020) 460462, doi:10.1016/j.chroma.2019.460462.

[35] K. Horváth, F. Gritti, J.N. Fairchild, G. Guiochon, On the optimization of the shell thickness of superficially porous particles, J. Chromatogr. A 1217 (41) (2010) 6373–6381, doi:10.1016/j.chroma.2010.08.013.

[36] M. de Frutos, A. Cifuentes, J.C. Díez-Masa, E. Camafeita, E. Méndez, Multiple peaks in HPLC of proteins: Bovine serum albumin eluted in a reversed-phase system, J. High Resolut. Chromatogr. 21 (1) (1998) 18–24, doi:10.1002/(sici)1521-4168(19980101)21:1⟨18::Aid-jhrc18⟩3.0.Co;2-5.

[37] S. Wu, M. Shen, An Integrated workflow for intact and subunits of monoclonal antibody accurate mass measurements, Agilent Technol., www.agilent.com/chem, 2018.

[38] T. Formolo, M. Ly, M. Levy, L. Kilpatrick, S. Lute, K. Phinney, L. Marzilli, K. Brorson, M. Boyne, D. Davis, J. Schiel, Determination of the NISTmAb primary structure, state-of-the-art and emerging technologies for therapeutic monoclonal antibody characterization volume 2. biopharmaceutical characterization: the NISTmAb case study, american chemical society 2015, pp. 1-62. 10.1021/bk-2015-1201.ch001

[39] A. Turner, J.E. Schiel, Qualification of NISTmAb charge heterogeneity control assays, Anal. Bioanal. Chem. 410 (8) (2018) 2079–2093, doi:10.1007/s00216-017-0816-6.

[40] Y. Yan, A.P. Liu, S. Wang, T.J. Daly, N. Li, Ultrasensitive characterization of charge heterogeneity of therapeutic monoclonal antibodies using strong cation exchange chromatography coupled to native mass spectrometry, Anal. Chem. 90 (21) (2018) 13013–13020, doi:10.1021/acs.analchem.8b03773.

3.1.2 Supporting Information

Charge variant analysis of protein-based biopharmaceuticals using two-dimensional liquid chromatography hyphenated to mass spectrometry

Simon Jaag[a], Marina Shirokikh[a], Michael Lämmerhofer [a,*]

[a] Pharmaceutical (Bio-)Analysis, Institute of Pharmaceutical Sciences, University of Tübingen, Auf der Morgenstelle 8, 72076 Tübingen, Germany

*Author for correspondence:

Prof. Dr. Michael Lämmerhofer
Pharmaceutical (Bio-)Analysis
Institute of Pharmaceutical Sciences
University of Tübingen
Auf der Morgenstelle 8
72076 Tübingen, Germany
T +49 7071 29 78793, F +49 7071 29 4565
E-mail: michael.laemmerhofer@uni-tuebingen.de

Table S 1: **Column overview:** I.D. x L column dimensions (diameter x length), *d_P:* Particle diameter, Chem.: Surface chemistry, Press.: maximum allowed backpressure, PS/DVB: polystyrene/divinylbenzene.

Trade name	I.D. x L [mm]	d_P [µm]	Pore size [Å]	Chem.	Press. [bar]	support
ProSwift RP-2H	4.6x50	n/a	No mesopores (2.2 µm macropores)	Phenyl	193	Monolithic (PS/DVB)
Chromolith WP300 RP-4	4.6x50	n/a	300 (2 µm macropores)	C4	200	Monolithic (silica)
Aeris Widepore C4 200 Å	2.1x50	3.6	200	C4	600	Core shell (0.2µm shell, silica)
BIOshell IgG 1000 Å C4	2.1x50	2.7	1000	C4	1000	Core shell (0.5µm shell, silica)
BIOhell IgG 1000 Å C4	2.1x20	2.7	1000	C4	1000	Core shell (0.5µm shell, silica)
BIOshell Å 400 Protein C4	2.1x50	3.4	400	C4	600	Core shell (0.2µm shell, silica)
Bio SCX NP3	2.1x100	3	Non-porous	$-SO_3H$	551	PS/DVB (coated with hydrophilic layer)
Proteomix SCX	2.1x100	3	Non-porous	$-SO_3H$	551	PS/DVB (coated with hydrophilic layer)

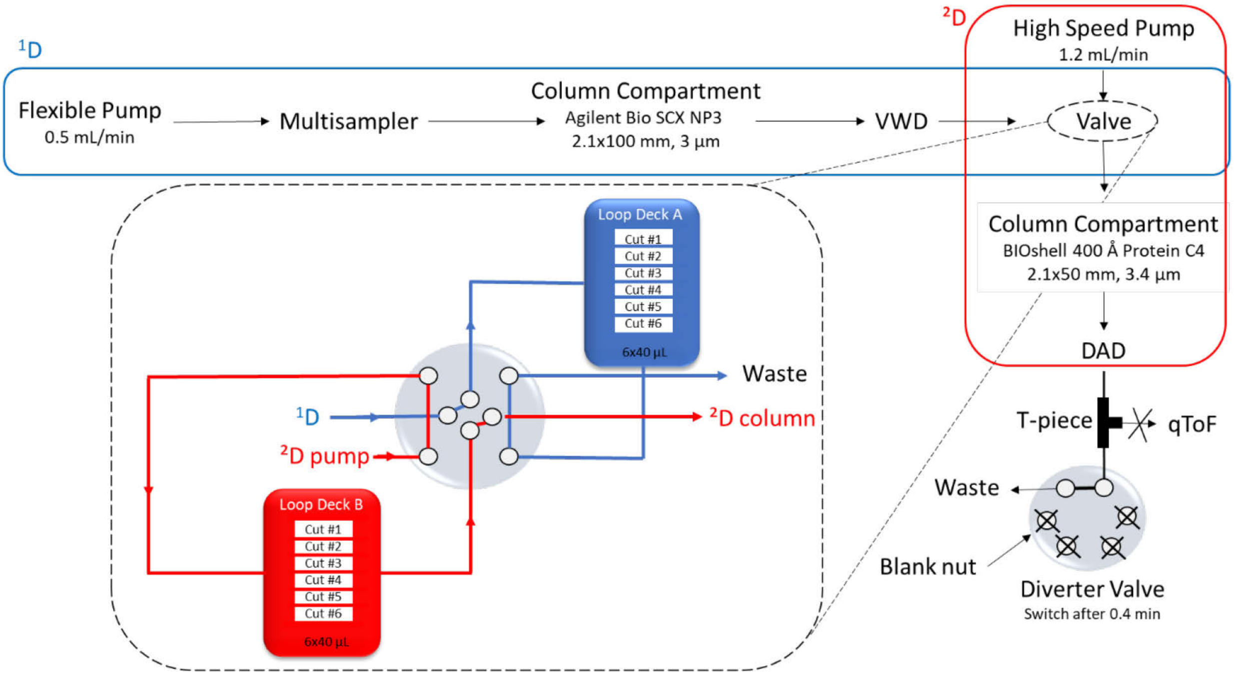

Figure S 1: 2D-LC-MS configuration for the multiple heart cutting mode. If the diverter valve is switched to the waste (as shown), there is no flow to the qToF MS because of the increased resistance in the flow path to the MS.

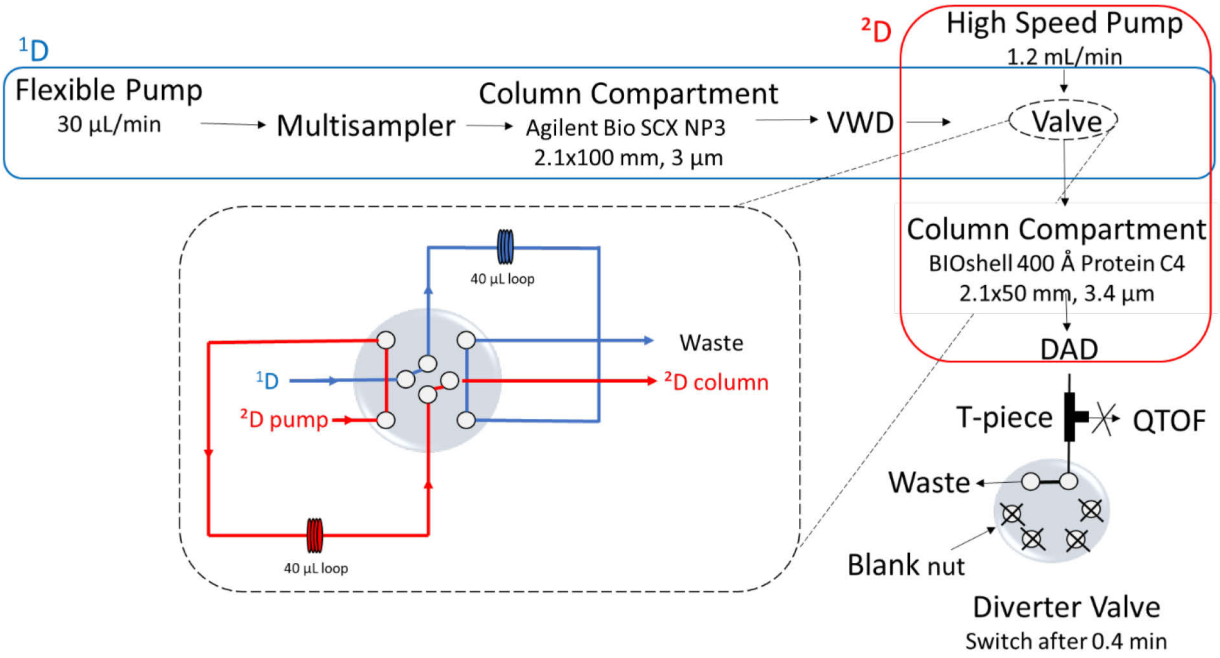

Figure S 2: 2D-LC-MS configuration for the full comprehensive mode. If the diverter valve is switched to the waste (as shown), there is no flow to the qToF MS because of the increased resistance in the flow path to the MS.

Table S 2: Molecular weights (MW), isoelectric points (p*I*) and grand average of hydropathy (GRAVY) of the standard proteins.

Protein	MW [Da]	p*I*	GRAVY
Bovine serum albumin (BSA)	66,430.3	4.7- 4.9	-0.475
Cytochrome c, equine heart	12,384	10.0-10.5	-0.902
Lysozyme, chicken white egg	14,307	11.35	-0.472
Myoglobin, equine	16,951.49	7.0	-0.396
β-Lactoglobulin B, bovine	18,277	5.13	-0.162

Table S 3: International nonproprietary name (INN), brand name (BN), molecular weight (MW), isoelectric point (p*I*) and structure of the biopharmaceutical samples.

INN	BN	MW [Da]	p*I*	structure
NIST mAb	n/a	148,199.3[1]	9.18	humanized IgG1κ
Secukinumab	Cosentyx	147,940[2]	n/a	human IgG1κ

---

[1] G0F/G1F glycoform

[2] Aglycosylated form

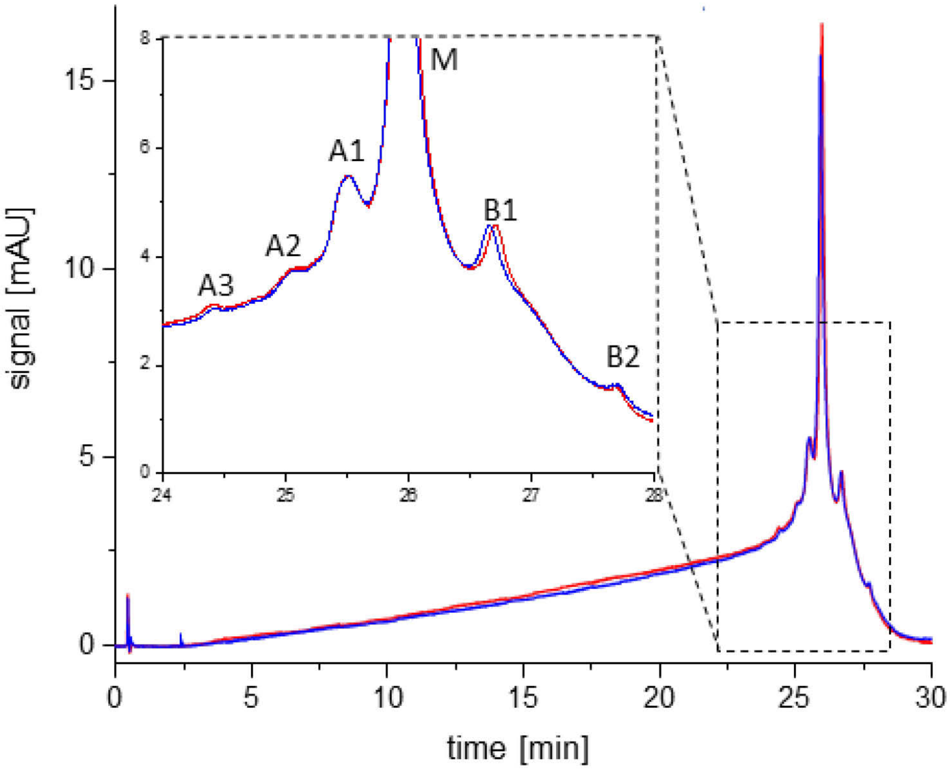

Figure S 3: Charge variant analysis of intact NIST mAb. Columns: Agilent Bio SCX NP 3 µm (red) and Sepax Proteomix SCX NP 3 µm (blue) (both 2.1x100 mm). M: main charge variant, A1-3: acidic variants, B1-2: basic variants. Mobile phase A: 20 mM MES/ 20 mM DAP (90:10; v/v) pH = 5.6; B: 20 mM MES/ 20 mM DAP (30:70 v/v) pH = 9.9. Flow rate: 0.5 mL/min. Gradient 0-100 % B in 24 min, 24-25 min 100 % B, 25-30 min 0 % B, Temp: 25 °C; Injection volume: 2 µL, detection 280 nm.

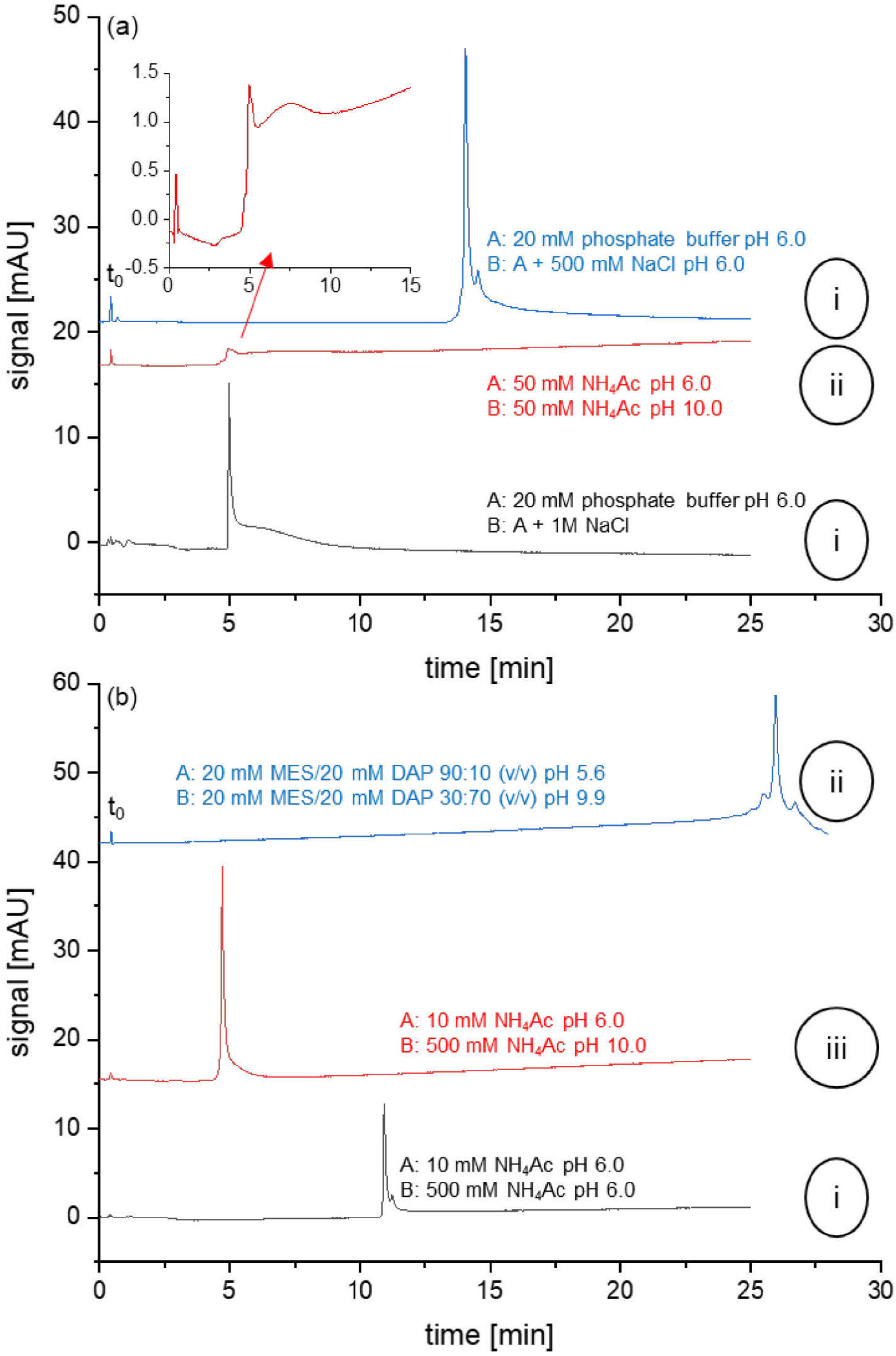

Figure S 4: Comparison of different mobile phases for the separation of the intact NIST mAb using either pure salt-gradient (i), pure pH-gradient (ii) or a salt-mediated-pH-gradient (iii). The dead time (t_0) and the mobile phase A & B composition are indicated in the figure. Column: Agilent SCX NP3 2.1x100 mm. Flow rate: 0.5 mL/min, gradient: 0-100 % B in 24 min, 24-25 min 100 % B, 25-30 min 0 % B, temperature: 25 °C, injection volume: 2 µL, detection 280 nm.

Table S 4: Peak table for the SCX chromatograms of the NIST mAb provided in Figure 5 of the main manuscript.

panel	variant	t_R [min]	$w_{1/2}$ [min]	h [mAU]	Symmetrie
(a)	M	13.596	0.6087	2.80	0.832
(b)	M	14.023	0.3872	5.30	0.848
(a)	B1	17.302	0.4754	0.29	0.845
(b)	B1	15.3	0.4095	0.67	1.177

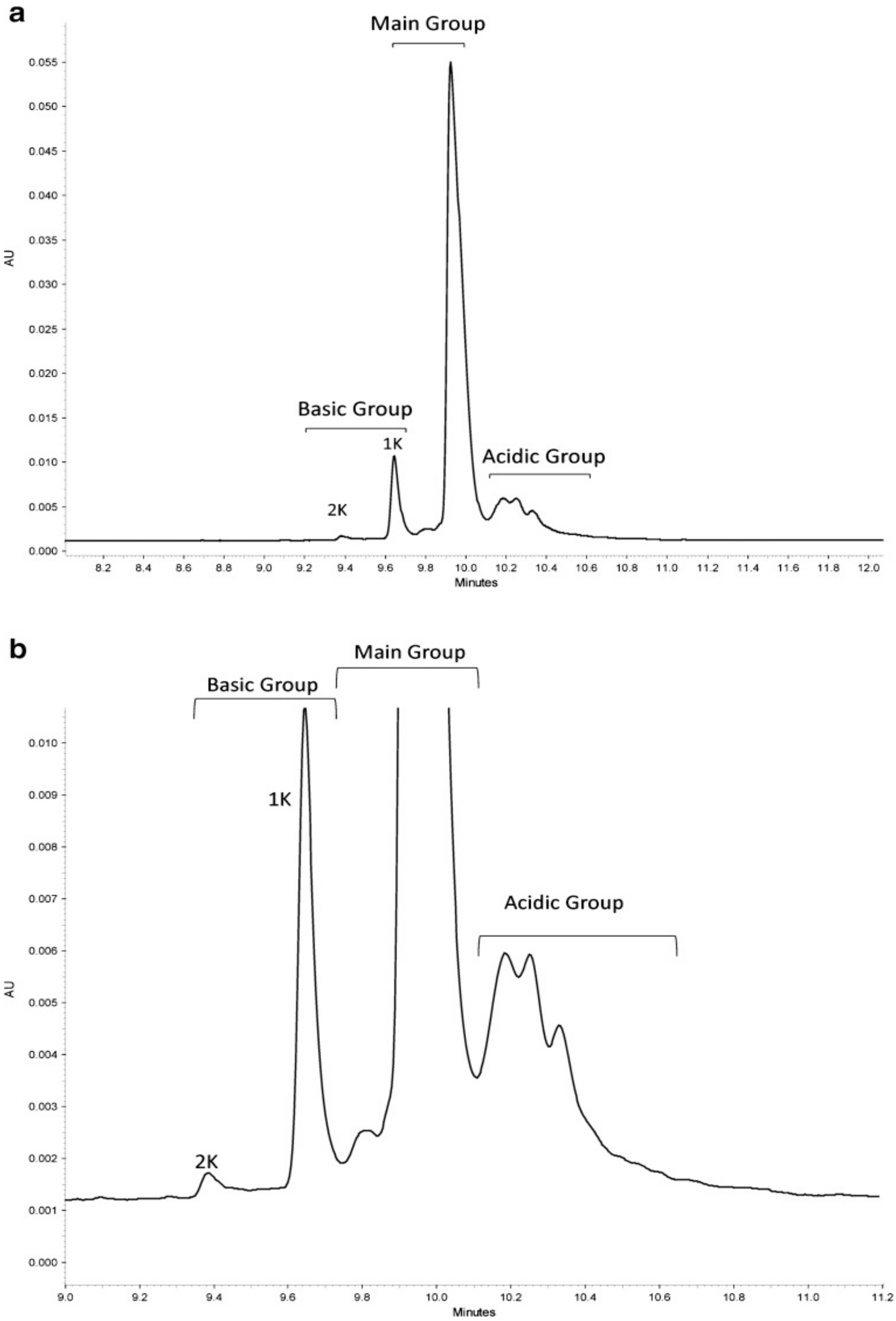

Figure S 5: Capillary zone electropherogram of the NIST mAb. The main charge variant as well as the basic and acidic variants are indicated. The basic variants are due to additional lysine residues (K). Printed with permission from [1].

Table S 5: 2D-LC conditions for the multiple heart-cutting method of the NIST-IdeS-TCEP sample shown in Figure 6 in the main document.

^{1}D

Column: Agilent Bio SCX 2.1x100 mm, NP3
A: 20 mM MES/20 mM DAP 90:10 (v/v) pH 5.6
B: 20 mM MES/20 mM DAP 30:70 (v/v) pH 9.9
C: 500 mM NaCl
Flow: 0.5 mL/min; V(inj): 4 µL
Temp.: 25 °C; dection: 280 nm

time [min]	A [%]	B [%]	C [%]	F [mL/min]
0	92	0	8	0.5
10	62	30	8	0.5
24	0	70	30	0.5
25	0	70	30	0.5
25.01	92	0	8	0.5
30	92	0	8	0.5

^{2}D

Column: Bioshell A400 Protein C4 2.1x50mm, 3.4 µm
A: water/ACN 98:2 + 0.1% FA
B: ACN/water 98:2 + 0.1% FA
Flow (F): 1.2 mL/min
Temp: 50°C
Detection: 280 nm

time [min]	A [%]	B [%]	F [mL/min]	comment
0	95	5	1.2	De-salting →waste
0.4	95	5	1.2	
0.65	5	95	1.2	gradient
0.75	5	95	1.2	washing
0.76	95	5	1.2	Re-equilibration
1	95	5	1.2	

Table S 6: Conditions of the 2D-LC separation for the multiple heart cutting analysis of the intact NIST mAb shown in Figure 7 in the main document.

^{1}D

Column: Agilent Bio SCX 2.1x100 mm, NP3
A: 20 mM MES/20 mM DAP 90:10 (v/v) pH 5.6
B: 20 mM MES/20 mM DAP 30:70 (v/v) pH 9.9
C: 500 mM NaCl
Flow: 0.5 mL/min; V(inj): 10 µL
Temp.: 25 °C; dection: 280 nm

time [min]	A [%]	B [%]	C [%]	F [mL/min]
0	20	00	0	0.5
5	15.8	84.2	0	0.5
24	0	98	2	0.5
25	0	98	2	0.5
25.01	20	80	0	0.5
30	20	80	0	0.5

^{2}D

Column: Bioshell A400 Protein C4 2.1x50mm, 3.4 µm
A: water/ACN 98:2 + 0.1% FA
B: ACN/water 98:2 + 0.1% FA
Flow (F): 1.2 mL/min
Temp: 50°C
Detection: 280 nm

time [min]	A [%]	B [%]	F [mL/min]	comment
0	95	5	1.2	De-salting →waste
0.4	95	5	1.2	
0.65	5	95	1.2	gradient
0.75	5	95	1.2	washing
0.76	95	5	1.2	Re-equilibration
1	95	5	1.2	

Table S 7: Peak table for the chromatograms from Figure 7[3].

Peak	^{1}D cut [min]	Species	Glycoform	Theo. masses [Da]	Exp. masses [Da]	Delta [Da]	Errors [ppm]
A1G1	10.87-10.95	deamidated?	G0F/G0F	148038.1	148036.9	-1.2	-8.4
A1G2			G0F/G1F	148200.3	148205.2	4.9	33.2
A1G3			G1F/G1F	148362.4	148364.2	1.8	12.0
A1G4			G1F/G2F	148524.6	148524	-0.6	-3.8
A1G5			G2F/G2F	148686.7	148688.2	1.5	10.1
M1G1	12.46-12.54	main	G0F/G1F – GlcNAc	147996.1	147997.3	1.2	8.1
M1G2			G0F/G0F	148037.2	148038.3	1.1	7.4
M1G3			G0F/G1F	148199.3	148201	1.7	11.5
M1G4			G1F	148361.4	148363.5	2.1	14.2
M1G5			G1F/G2F	148523.6	148521.6	-2	-13.5
M1G6			G2F/G2F	148685.7	148687.3	1.6	10.8
B1G1	13.90-13.98	main + K	G0F/G0F	148165.3	148168.4	3.1	20.9
B1G2			G0F/G1F	148327.5	148329.6	2.1	14.2
B1G3			G1F/G1F	148489.5	148488.8	-0.7	-4.7
B1G4			G1F/G2F	148651.8	148651.4	-0.4	-2.7

---

[3] External mass calibration was performed at the beginning of the 2D-LC analysis; mass accuracy also compromised by low concentrations

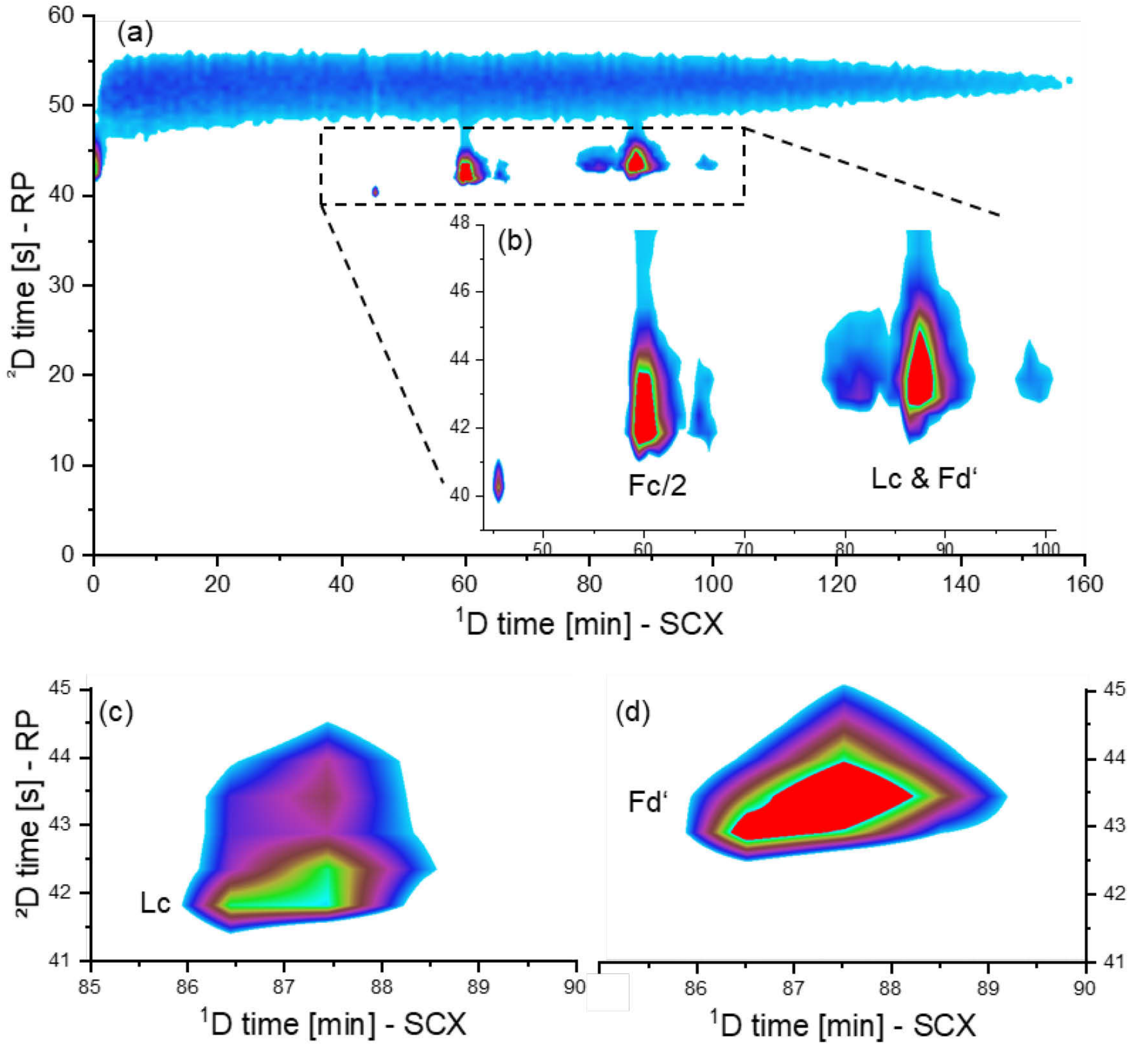

Figure S 6: 2D-LC-MS contour plot of the NIST-IdeS-TCEP sample in full comprehensive mode. Same 2D-LC run as in Figure 7. **(a)** Total ion chromatogram (TIC), **(b)** zoom-in of elution window, **(c)** extracted ion chromatogram (XIC) of the light chain (Lc) and **(d)** XIC of the Fd’-subunit.

Table S 8: Conditions of the full comprehensive 2D-LC separation of the NIST mAb fragments shown in Figure 8 and Figure S 9.

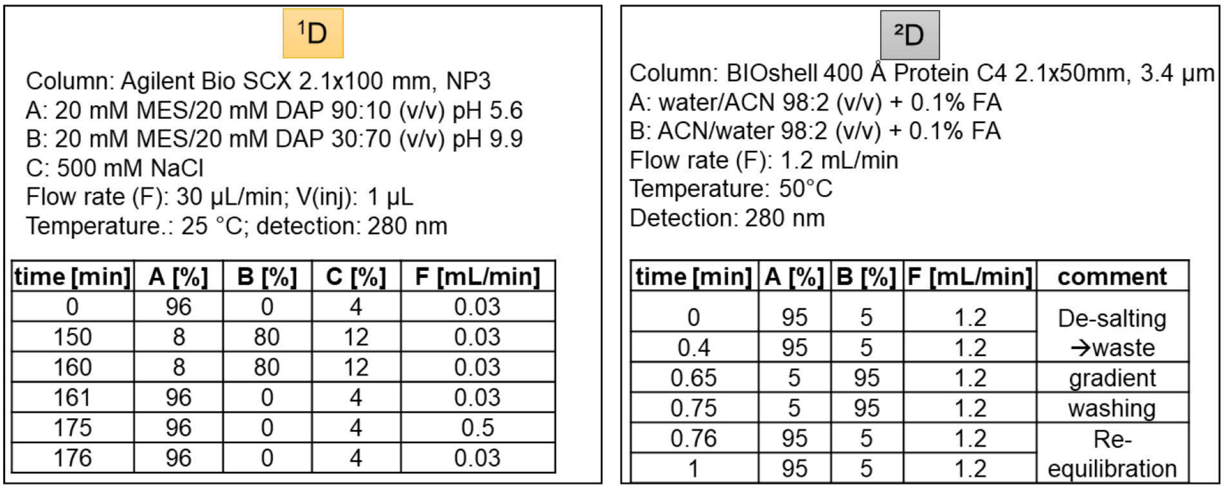

^{1}D

Column: Agilent Bio SCX 2.1x100 mm, NP3
A: 20 mM MES/20 mM DAP 90:10 (v/v) pH 5.6
B: 20 mM MES/20 mM DAP 30:70 (v/v) pH 9.9
C: 500 mM NaCl
Flow rate (F): 30 µL/min; V(inj): 1 µL
Temperature.: 25 °C; detection: 280 nm

time [min]	A [%]	B [%]	C [%]	F [mL/min]
0	96	0	4	0.03
150	8	80	12	0.03
160	8	80	12	0.03
161	96	0	4	0.03
175	96	0	4	0.5
176	96	0	4	0.03

^{2}D

Column: BIOshell 400 Å Protein C4 2.1x50mm, 3.4 µm
A: water/ACN 98:2 (v/v) + 0.1% FA
B: ACN/water 98:2 (v/v) + 0.1% FA
Flow rate (F): 1.2 mL/min
Temperature: 50°C
Detection: 280 nm

time [min]	A [%]	B [%]	F [mL/min]	comment
0	95	5	1.2	De-salting →waste
0.4	95	5	1.2	
0.65	5	95	1.2	gradient
0.75	5	95	1.2	washing
0.76	95	5	1.2	Re-equilibration
1	95	5	1.2	

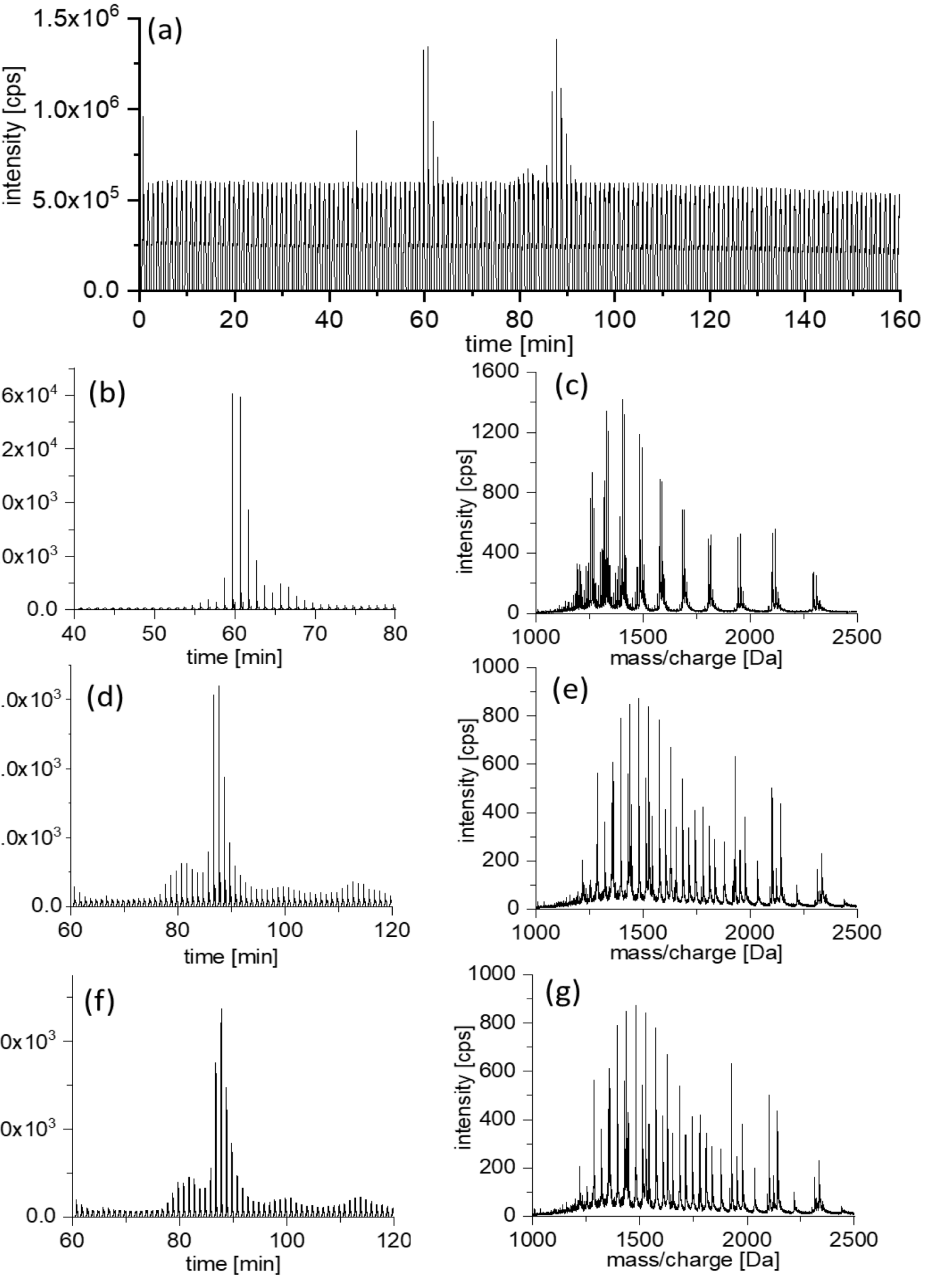

Figure S 7: MS data of the NIST-IdeS-TCEP sample after SCX×RP 2D-LC. **(a)** Total ion current over the entire 2D-LC analysis time. Extracted ion chromatograms of the **(b)** Fc/2-subunit, **(d)** light chain, **(f)** Fd'-subunit and spectrum of **(c)** Fc/2-subunit, **(e)** light chain and **(g)** Fd'-subunit.

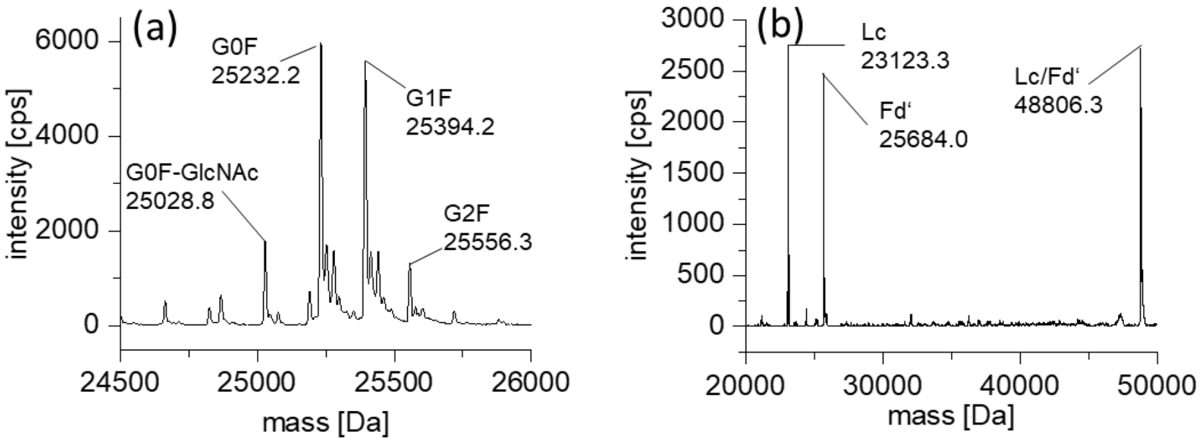

Figure S 8: Reconstructed masses of the NIST-IdeS-TCEP sample. **(a)** the different glycoforms of the Fc/2. **(b)** the light chain (Lc) and Fd’-fragments and an adduct of both fragments (Lc/Fd’) could be identified which was the consequence of disulphide bond reformation after extended storage time.

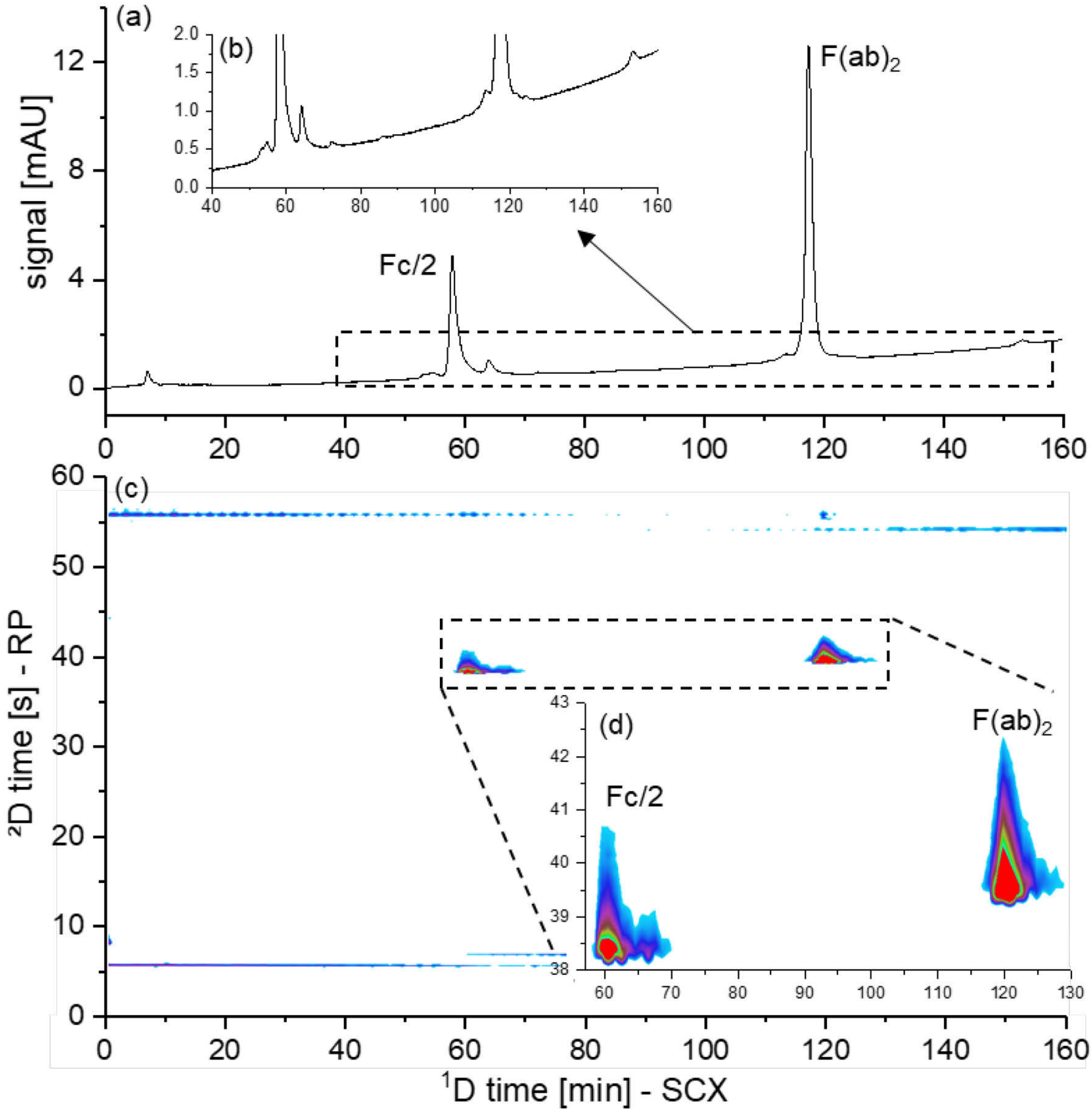

Figure S 9: Full comprehensive 2D-LC separation of the IdeS-digested NIST mAb. The ^{1}D SCX chromatogram is shown in **(a)** with a zoom-in of the elution window **(b)**, the corresponding contour plot **(c)** and the zom-in **(d)**. For conditions refer to supplementary Table S 8.

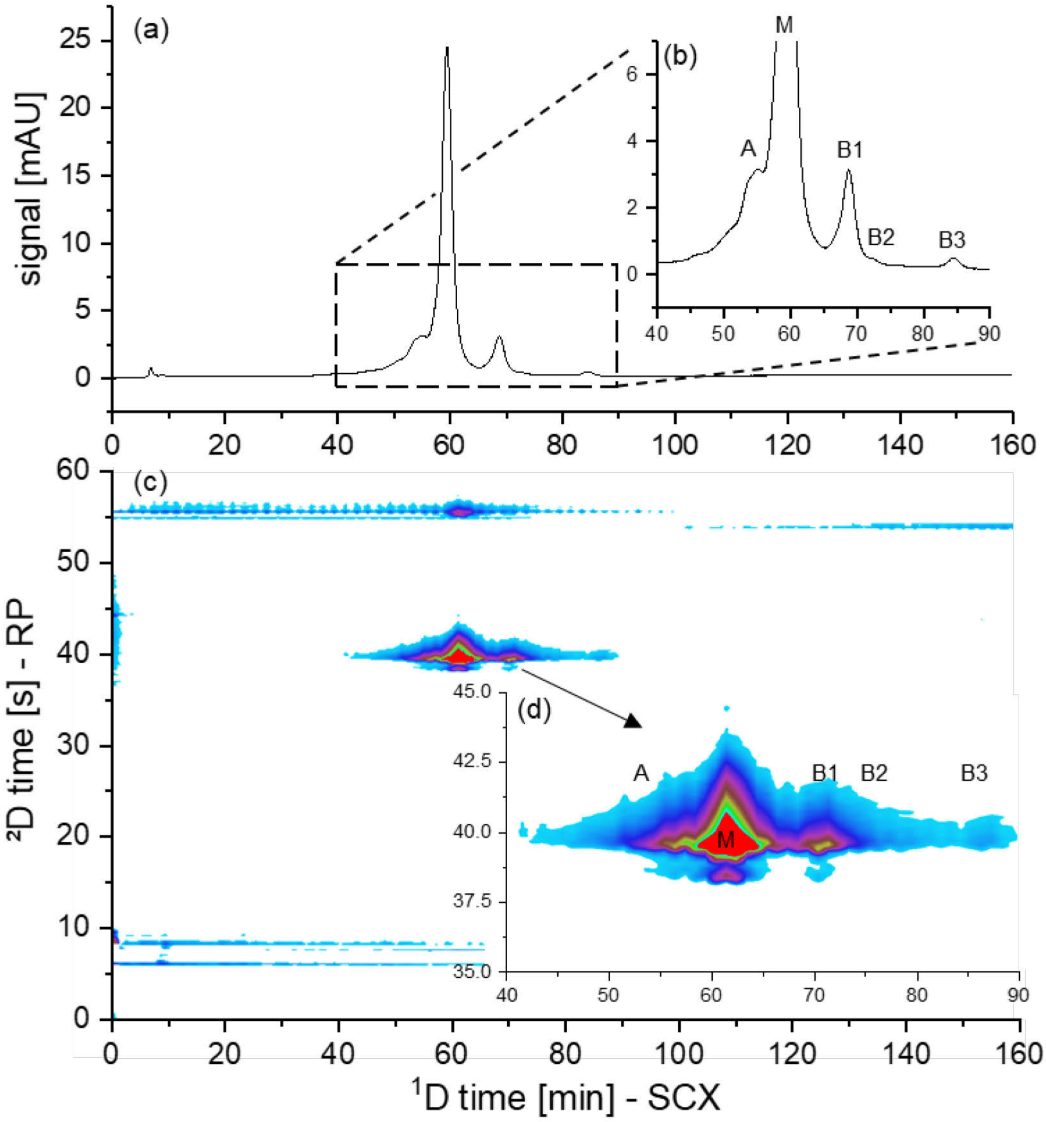

Figure S 10: Full comprehensive 2D-LC separation of the intact NIST mAb. The ^{1}D SCX chromatogram is shown in **(a)** with a zoom-in of the elution window **(b)**, the corresponding contour plot **(c)** and the zoom-in **(d)**. An acidic charge variant (A), the main charge variant (M) and three basic charge variants (B1-3) could be separated. For conditions refer to supplementary Table S 9.

Table S 9: Conditions of the full comprehensive 2D-LC separation of the intact NIST mAb shown in Figure S 10.

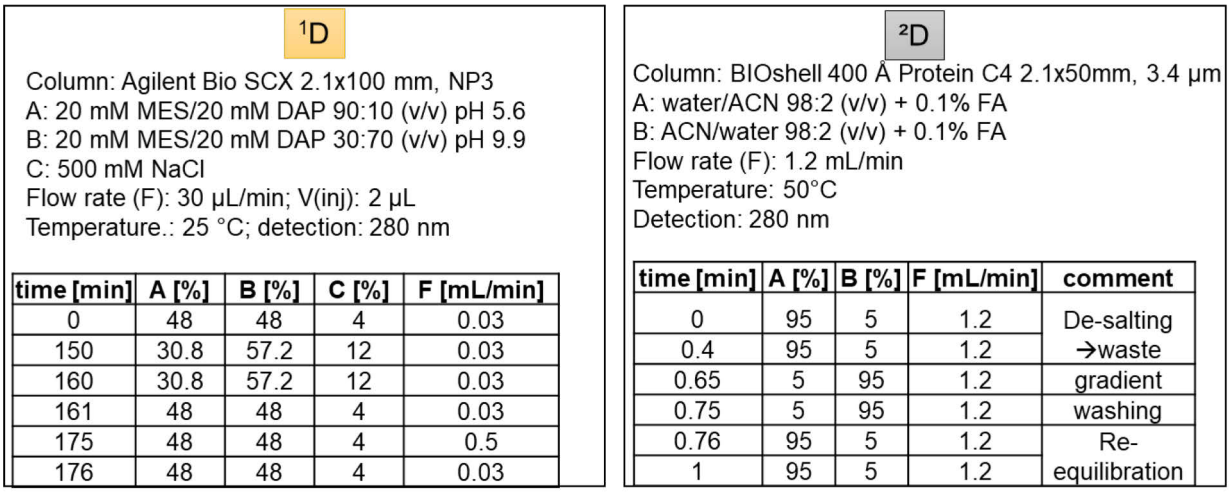

^{1}D

Column: Agilent Bio SCX 2.1x100 mm, NP3
A: 20 mM MES/20 mM DAP 90:10 (v/v) pH 5.6
B: 20 mM MES/20 mM DAP 30:70 (v/v) pH 9.9
C: 500 mM NaCl
Flow rate (F): 30 µL/min; V(inj): 2 µL
Temperature.: 25 °C; detection: 280 nm

time [min]	A [%]	B [%]	C [%]	F [mL/min]
0	48	48	4	0.03
150	30.8	57.2	12	0.03
160	30.8	57.2	12	0.03
161	48	48	4	0.03
175	48	48	4	0.5
176	48	48	4	0.03

^{2}D

Column: BIOshell 400 Å Protein C4 2.1x50mm, 3.4 µm
A: water/ACN 98:2 (v/v) + 0.1% FA
B: ACN/water 98:2 (v/v) + 0.1% FA
Flow rate (F): 1.2 mL/min
Temperature: 50°C
Detection: 280 nm

time [min]	A [%]	B [%]	F [mL/min]	comment
0	95	5	1.2	De-salting →waste
0.4	95	5	1.2	
0.65	5	95	1.2	gradient
0.75	5	95	1.2	washing
0.76	95	5	1.2	Re-equilibration
1	95	5	1.2	

Table S 10: Conditions of the full comprehensive 2D-LC separation of the intact Secukinumab shown in Figure 9 in the main document.

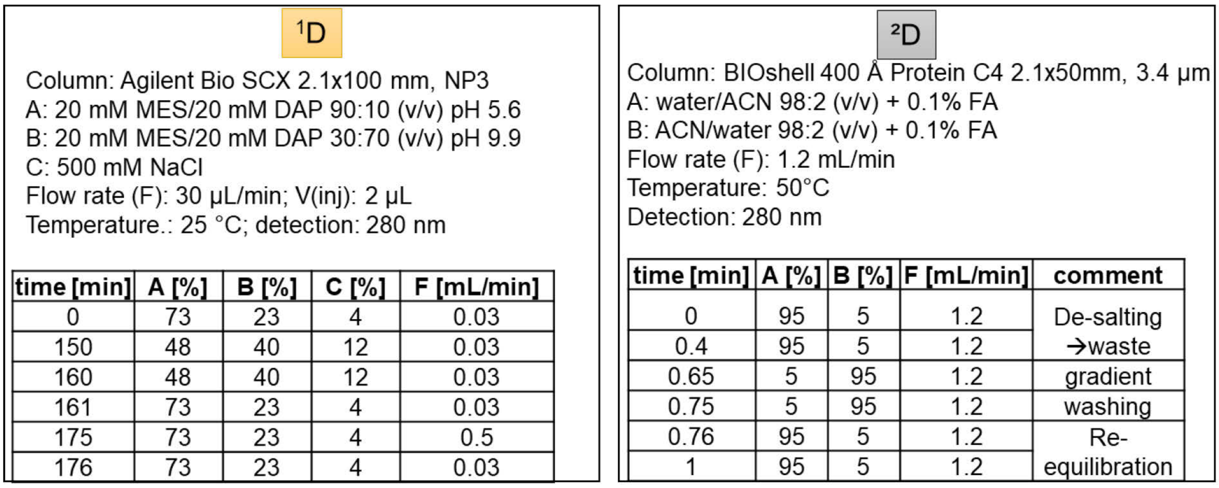

^{1}D

Column: Agilent Bio SCX 2.1x100 mm, NP3
A: 20 mM MES/20 mM DAP 90:10 (v/v) pH 5.6
B: 20 mM MES/20 mM DAP 30:70 (v/v) pH 9.9
C: 500 mM NaCl
Flow rate (F): 30 µL/min; V(inj): 2 µL
Temperature.: 25 °C; detection: 280 nm

time [min]	A [%]	B [%]	C [%]	F [mL/min]
0	73	23	4	0.03
150	48	40	12	0.03
160	48	40	12	0.03
161	73	23	4	0.03
175	73	23	4	0.5
176	73	23	4	0.03

^{2}D

Column: BIOshell 400 Å Protein C4 2.1x50mm, 3.4 µm
A: water/ACN 98:2 (v/v) + 0.1% FA
B: ACN/water 98:2 (v/v) + 0.1% FA
Flow rate (F): 1.2 mL/min
Temperature: 50°C
Detection: 280 nm

time [min]	A [%]	B [%]	F [mL/min]	comment
0	95	5	1.2	De-salting →waste
0.4	95	5	1.2	
0.65	5	95	1.2	gradient
0.75	5	95	1.2	washing
0.76	95	5	1.2	Re-equilibration
1	95	5	1.2	

Design-of-experiment (DoE) approach for the optimization of the ^{1}D separation conditions for the charge variant separation of Secukinumab

Three experimental variables were considered as factors in the design matrix, starting concentration of B, gradient steepness of B and C (composition of A, B and C see caption of Fig. S11). As criteria to assess the quality of the separation we selected three parameters as response factors, viz. the critical resolution ($R_{s,crit}$). MODDE 12.1 (from Umetrics Software, distributed by Sartorius) was employed for the modelling of the responses and statistics.

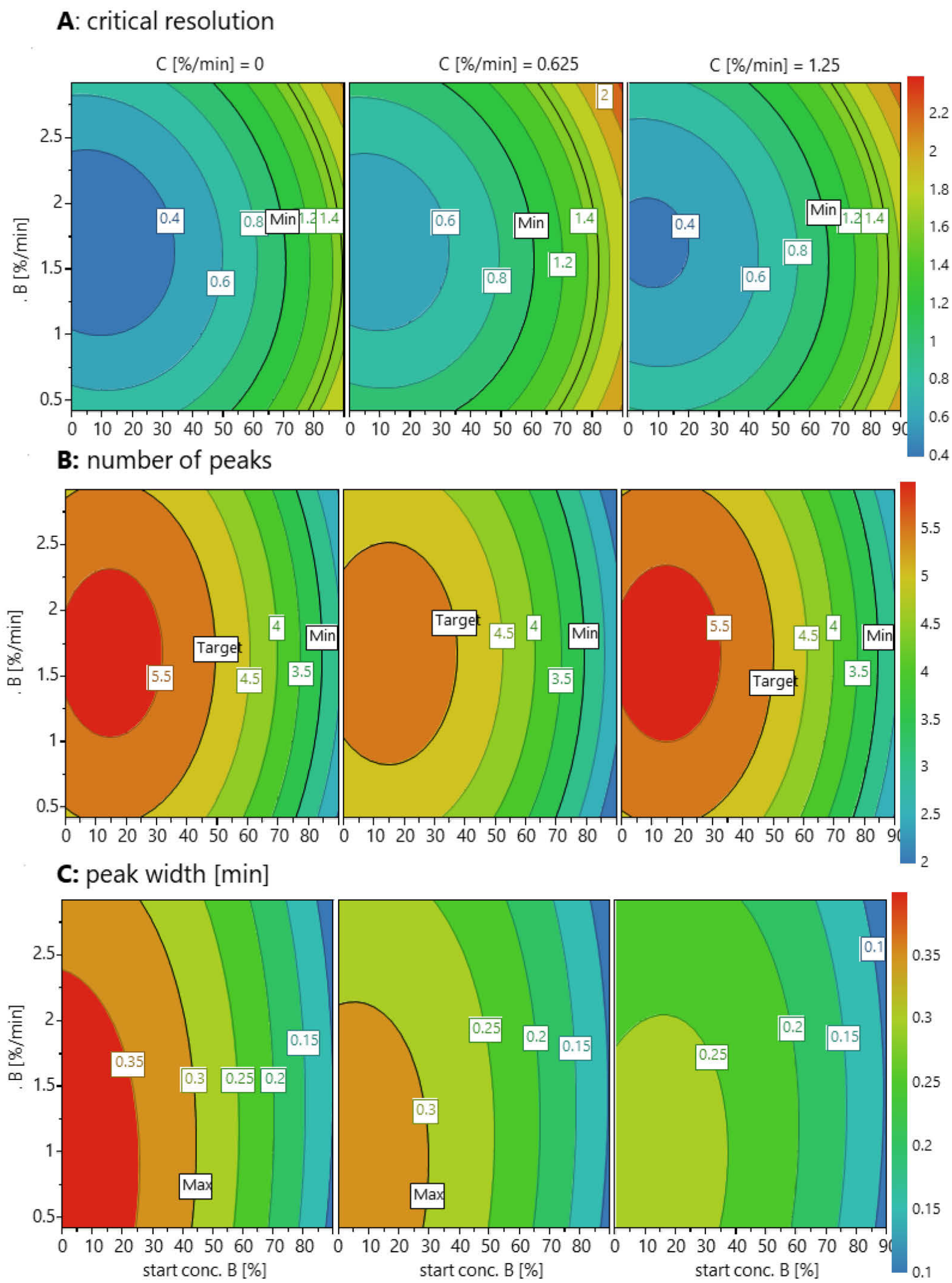

Figure S 11: Design of experiment optimization of the ternary strong cation-exchange gradient profile for intact Secukinumab. The starting concentration of the B-solvent and its gradient steepness has been optimized (x-, and y- axis, respectively) as well as the gradient steepness of the C-solvent (shown in three different columns). The gradient was optimized for three different responses: critical resolution being the resolution of the least separated peak pair (**A**), number of observed peaks (**B**) and the peak width of the broadest peak (**C**). Column: Agilent Bio SCX 2.1x100 mm, NP3, mobile phase A: 20 mM MES/20 mM DAP 90:10 (v/v) pH 5.6, mobile phase B: 20 mM MES/20 mM DAP 30:70 (v/v) pH 9.9, mobile phase C: 500 mM NaCl, flow rate: 0.5 mL/min, temperature: 25 °C.

The critical resolution (refer **Figure S 11** panel **A**), defined as the resolution of the least separated peak pair, has its maximum at high starting concentration of the B-solvent (high pH) which was the variable with the strongest influence. One important observation was that the critical resolution increased if the number of peaks decreased, therefore, this response factor has some bias. The opposite trend for the optimum of the resolution could be found for the optimum of the number of peaks (panel **B**). A starting concentration of the B-solvent of about 20 % and a medium gradient steepness of the B-solvent resulted in the maximum number of peaks while at the same conditions the critical resolution had its minimum (refer also **Figure S 13**). An increase in the gradient steepness of the C-solvent (NaCl) provides sharper peaks but can also decrease the number of peaks or the critical resolution. A compromise must be found between the number of peaks, critical resolution and peak width. Thus, we decided to use a ranking for each response and deemed the number of peaks as the most important response. The maximum number of peaks observed in the input experiments was five which was then the minimum we wanted. The next response factor in the ranking was the critical resolution (minimum value = 0.7) and as the last response factor the peak width was selected (maximum value = 0.3 min). Using these limits, a sweet spot plot was created using the Modde software (refer **Figure S 12**) where the sweet spot area (red) represents conditions where all three criteria were met. As the sweet spot area is quite small these conditions are not very robust. Still the data provide useful information about the trends and helps developing the method. In addition to the three mentioned response factors also considerations about the peak shape and the kind of charge variants observed (acidic or basic) were considered. For example, only the experiments N2 and N4 showed an acidic charge variant in the chromatogram.

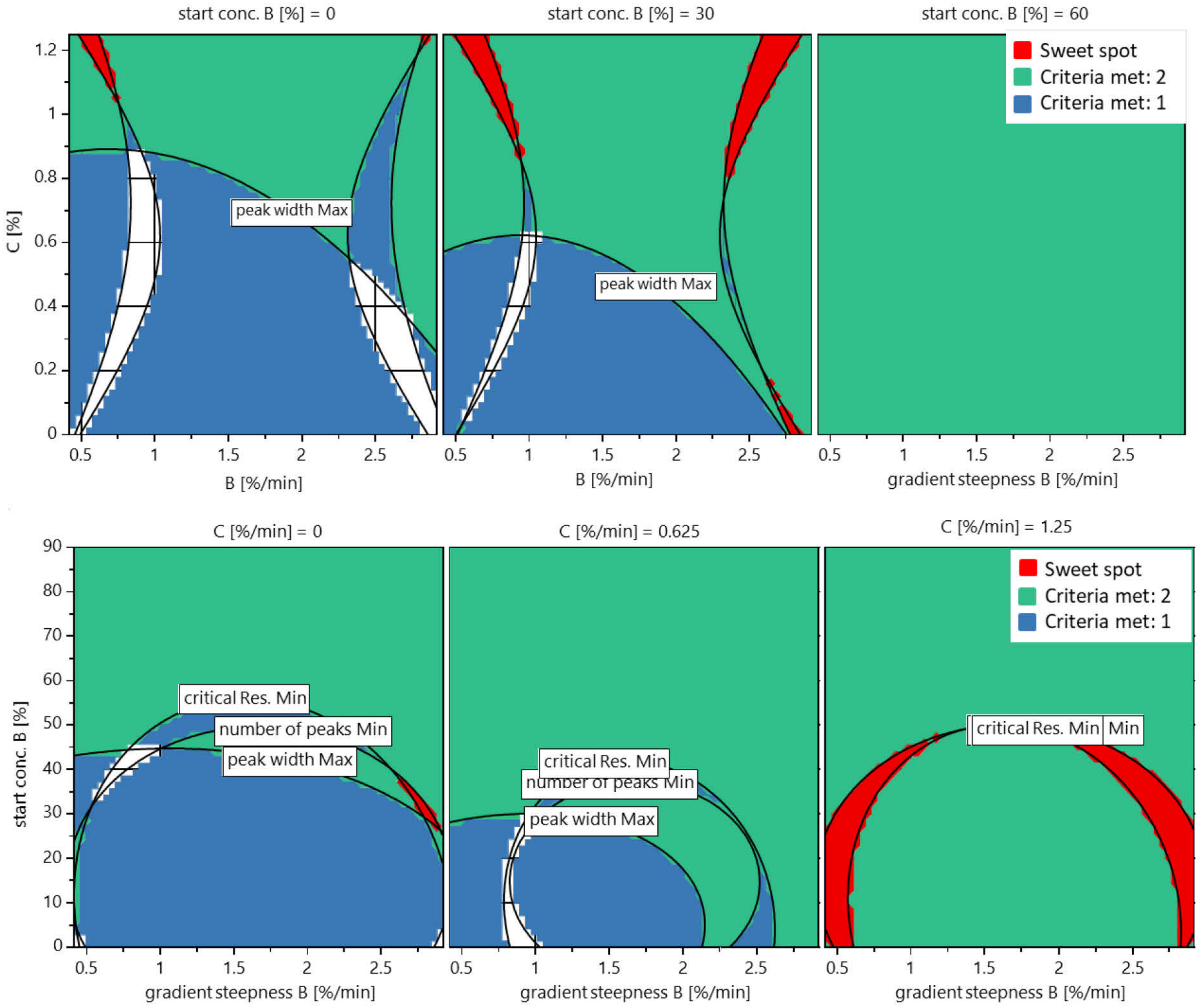

Figure S 12: Sweet spot plot of the separation of intact Secukinumab. The same variables as in Figure S 11 have been used. The response limits were minimum number of peaks = 5, maximum peak width = 0.3 min and minimum critical resolution = 0.7. The sweet spot where all criteria are met is indicated in red while green and blue regions indicate that only two or one criteria were met, respectively.

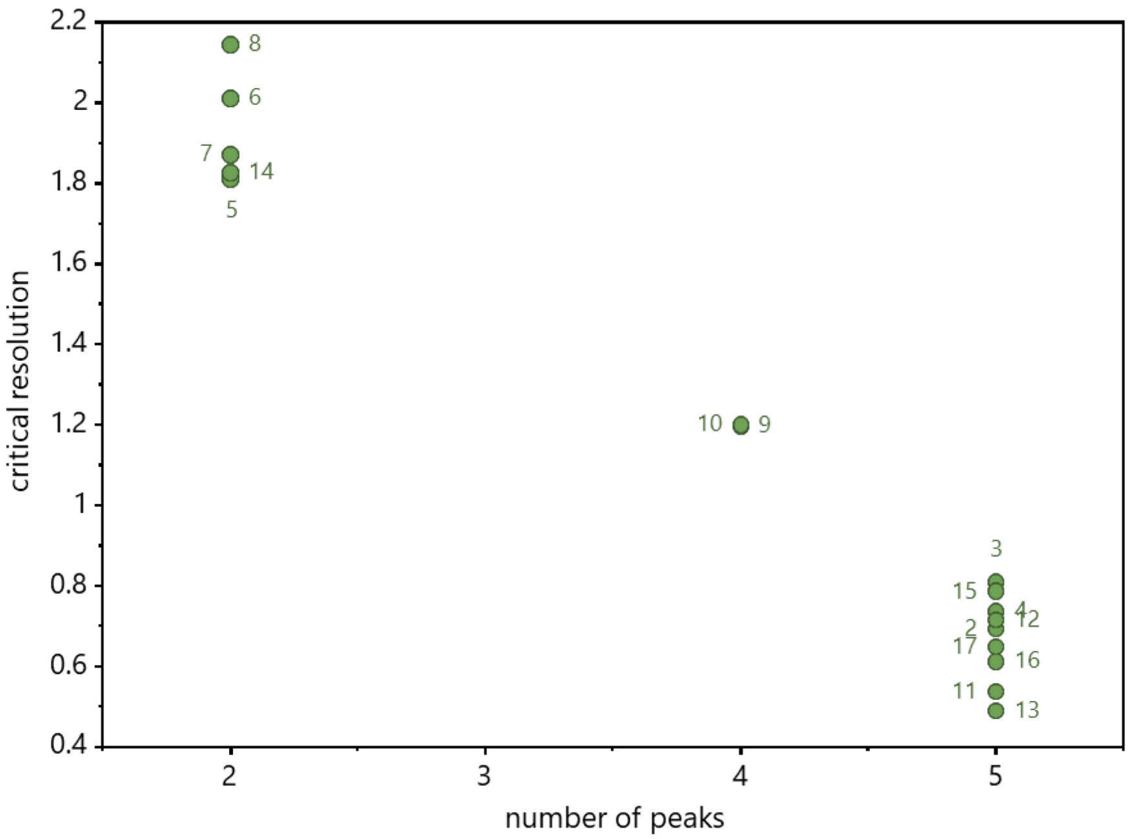

Figure S 13: Pareto-plot of the input experiments of the design of experiment optimization. Each point indicates one experiment (n = 17). The number of peaks observed versus the resolution of the least separated peak pair (critical resolution) is plotted.

Table S 11: Experimental data obtained for the input experiments of the design of experiment optimization of the ternary strong cation-exchange gradient profile. The red rectangle indicates the design space where five peaks could be observed. Exp. No is the number of experiment, Exp. Name the experiment name, Incl/Excl if the experiment was used for the modelling, Δ B is the gradient steepness of the B-solvent, Δ c is the gradient steepness of the C-solvent and c_0 (B) is the starting concentration of the B-solvent. Experiment N1 was excluded because the peaks eluted after the linear gradient.

Exp. No	Exp. Name	Run Order	Incl/Excl	Δ B [%/min]	Δ c [%/min]	c_0 (B) [%]	no. of peaks	$R_{critical}$	$w_{1/2}$ [min]
3	N3	13	Incl	0.42	1.25	0	5	0.81	0.265
15	N15	11	Incl	1.67	0.63	45	5	0.79	0.278
4	N4	10	Incl	2.92	1.25	0	5	0.73	0.200
12	N12	9	Incl	1.67	1.25	45	5	0.71	0.230
2	N2	8	Incl	2.92	0.00	0	5	0.69	0.327
17	N17	15	Incl	1.67	0.63	45	5	0.65	0.266
16	N16	4	Incl	1.67	0.63	45	5	0.61	0.274
11	N11	7	Incl	1.67	0.00	45	5	0.54	0.278
13	N13	2	Incl	1.67	0.63	0	5	0.49	0.316
10	N10	3	Incl	2.92	0.63	45	4	1.20	0.225
9	N9	6	Incl	0.42	0.63	45	4	1.19	0.257
1	N1	12	Excl	0.42	0.00	0	4	0.79	0.251
8	N8	17	Incl	2.92	1.25	90	2	2.14	0.069
6	N6	16	Incl	2.92	0.00	90	2	2.01	0.076
7	N7	1	Incl	0.42	1.25	90	2	1.87	0.084
14	N14	5	Incl	1.67	0.63	90	2	1.82	0.087
5	N5	14	Incl	0.42	0.00	90	2	1.81	0.089

References

[1] A. Turner, J.E. Schiel, Qualification of NISTmAb charge heterogeneity control assays, Analytical and bioanalytical chemistry 410(8) (2018) 2079-2093. https://doi.org/10.1007/s00216-017-0816-6.

3.2 Publication II: **Kinetic performance comparison of superficially porous, fully porous and monolithic reversed-phase columns by gradient kinetic plots for the separation of protein biopharmaceuticals**

3.2.1 Manuscript

Simon Jaag[a], Chunmei Wen[a], Benjamin Peters[b], Michael Lämmerhofer[a,*]

[a] Pharmaceutical (Bio-)Analysis, Institute of Pharmaceutical Sciences, University of Tübingen, Auf der Morgenstelle 8, 72076 Tübingen, Germany

[b] Instrumental Analytics R&D, Merck KGaA, Frankfurter Str. 250, 64293 Darmstadt, Germany

*Corresponding author:

E-mail address: michael.laemmerhofer@uni-tuebingen.de (M. Lämmerhofer)

Reprinted with permission from Journal of Chromatography A, 2022, 1676, 463251

DOI: 10.1016/j.chroma.2022.463251

Journal of Chromatography A 1676 (2022) 463251

Contents lists available at ScienceDirect

Journal of Chromatography A

journal homepage: www.elsevier.com/locate/chroma

Kinetic performance comparison of superficially porous, fully porous and monolithic reversed-phase columns by gradient kinetic plots for the separation of protein biopharmaceuticals

Simon Jaag[a], Chunmei Wen[a], Benjamin Peters[b], Michael Lämmerhofer[a,*]

[a] Pharmaceutical (Bio-)Analysis, Institute of Pharmaceutical Sciences, University of Tübingen, Auf der Morgenstelle 8, 72076 Tübingen, Germany
[b] Instrumental Analytics R&D, Merck KGaA, Frankfurter Str. 250, 64293 Darmstadt, Germany

ARTICLE INFO

Article history:
Received 8 March 2022
Revised 31 May 2022
Accepted 13 June 2022
Available online 14 June 2022

Keywords:
Gradient kinetic plots
Monolithic columns
Core shell particle
Fully porous particle
UHPLC

ABSTRACT

To find the best performing column for the analysis of protein-based biopharmaceuticals is a significant challenge as meanwhile numerous modern columns with distinct stationary phase morphologies are available for reversed-phase liquid chromatography. Especially when besides morphology also several other column factors are different, it is hard to decide about the best performing column *a priori*. To cope with this problem, in the present work 13 different reversed-phase columns dedicated for protein separations were systematically tested by the gradient kinetic plot method. A comprehensive comparison of columns with different morphologies (monolithic, fully porous and superficially porous particle columns), particle sizes and pore diameters as well as column length was performed. Specific consideration was also given to various monolithic columns which recently shifted a bit out of the prime focus in the scientific literature. The test proteins ranged from small proteins starting from 12 kDa, to medium sized proteins (antibody subunits obtained after IdeS-digestion and disulphide reduction) and an intact antibody. The small proteins cytochrome c, lysozyme and β-lactoglobulin could be analysed with similar performance by the best columns of all three column morphologies while for the antibody fragments specific fully porous and superficially porous particle columns were superior. A 450 Å 3,5 µm superficially porous particle column showed the best performance for the intact antibody while a 1.7 µm fully porous particle column with 300 Å showed equivalent performance to the best superficially porous column with thin shell and 400 Å pore size for proteins between 12 and 25 kDa. While the majority of the columns had C4 bonding chemistry, the silica monolith with C18 bonding and 300 Å mesopore size approximated the best performing particle columns and outperformed a C4 300 Å wide-pore monolith. The current work can support the preferred choice for the most suitable reversed-phase column for protein separations.

1. Introduction

Biopharmaceuticals are playing an increasingly important role in the pharmaceutical market. In the period from January 2015 to July 2018 there were 53 new drug approvals by the US FDA, 20 were from biological origin which makes around 38% [1]. Thereby, monoclonal antibodies (mAbs) account for 53% of all biopharmaceuticals [2]. Monoclonal antibodies are more challenging to analyse due to their higher molecular mass and molecular heterogeneity consisting of glycoforms, high and low molecular weight variants and post-translational modifications including charge variants [3]. Reversed-phase liquid chromatography (RP-LC) is one of the most important techniques for the analytical characterization of intact proteins and separates variants based on their hydrophobicity. RP-LC is inherently compatible with mass spectrometric (MS) detection which makes RP-LC-MS a powerful analytical platform. Unfortunately, RP-LC is a denaturing technique thus the proteins lose their native structure, yet this may be associated with improved chromatographic efficiencies. Depending on the kind of organic modifier, different selectivity can be obtained [4]. The recovery of the proteins can be increased strongly by using elevated temperature because this reduces the secondary interactions with the stationary phase [5,6]. Mobile phase additives affect the peak shape (tailing), peak width but also the ion suppression of MS

Abbreviations: UHPLC, Ultra-high performance liquid chromatography; SPP, Superficially porous particle; FPP, Fully porous particle; KPL, kinetic performance limit.

[*] Corresponding author at: Pharmaceutical (Bio-)Analysis, Institute of Pharmaceutical Sciences, University of Tübingen, Auf der Morgenstelle 8, 72076 Tübingen, Germany.
E-mail address: michael.laemmerhofer@uni-tuebingen.de (M. Lämmerhofer).

https://doi.org/10.1016/j.chroma.2022.463251

detection [5,7]. While trifluoroacetic acid is a strong ion-pairing agent and provides sharp peaks, formic acid is better suitable for MS detection due to its lower ion-suppression effects. RP-LC for proteins has an on-off like retention behaviour (due to steep adsorption isotherms) as at low elution strength the protein is completely retained while above a certain percentage of organic modifier the protein is not retained any more at all [8,9]. This is the reason why RP-LC for proteins is only done in gradient elution mode. However, this makes the comparison of different columns more challenging.

Special attention should be paid to the selection of a suitable pore size which is large enough to enable unhindered diffusion and avoid partial or total pore exclusion [10]. On the other hand, as the pore size increases, the specific surface area decreases, resulting in a decrease in retention and sample capacity. Pore sizes from 300 to 1000 Å are typically recommended for protein separations [11,12]. C4 alkyl and phenyl phases are usually used as stationary phases, since C18 phases were thought to bear the risk of irreversible binding of proteins to the column surface due to their strong hydrophobicity. Newer publications state that the recovery is mostly affected by ligand density, surface coverage, flexibility of the ligand, carbon load, relative hydrophobicity and the degree of exposure of the surface silanols [13]. Secondary interactions with the stationary phase can have a strong, negative effect on the separation and should be minimized with end-capping of free silanol groups (silica-based columns) and the use of higher temperatures or adding ancillary solvents like 1-butanol [5,6].

The column technology plays a key role for protein separations especially considering the mass transfer kinetics [14]. Non-porous particles are the most favourable in terms of the intra-particle mass transfer resistance but have the lowest surface area and are usually not used for RP-LC but for ion-exchange chromatography. Fully porous particles (FPPs) show the highest intra particle mass transfer resistance as the entire particle is accessible for diffusion. Superficially porous particles (SPPs) consist of a solid core covered by a porous shell. Therefore, the diffusion paths are significantly reduced and so is the mass transfer resistance [12]. Monolithic columns do not consist of individual particles but of a continuous chromatographic bed. They have large macropores which enable a low back pressure even at high flow rates and they have smaller mesopores for the actual solute interaction [15,16]. The support type of protein columns can be either silica-based or based on organic polymers. One advantage of the organic polymer-based supports is the better stability at higher pH-values and high temperatures.

A convenient method to evaluate the performance of columns with different lengths, diameters, and stationary phase morphologies are kinetic plots [17–19]. They are well known for isocratic LC, but rarely employed for gradient elution which is the common situation in protein separations, as mentioned above. The evaluation of the column performance in gradient RP using the gradient kinetic plots was introduced by Broeckhoven et al. [20] and the concept was already applied to RP-LC of proteins by Fekete et al. [21]. The performance of some SPP and FPP columns for proteins has been compared by Wagner et al. and Bobály et al. [10,22]. Fekete et al. recently published on the usage of ultra-short columns for protein separations and investigated new stationary phases for widepore columns [4,8].

The current work extends on these prior reports and is devised as a comprehensive, systematic column comparison study applying the gradient kinetic plot concept for many popular protein RP columns for the first time. Different column technologies differing in the stationary phase morphology were evaluated for a total of 13 columns, including three monolithic, six SPP and four FPP columns. Three different sample mixtures were used for the evaluation consisting of (i) a protein mixture with small proteins (cytochrome c, β-lactoglobulin and lysozyme), (ii) antibody fragments obtained after IdeS-digestion and disulphide reduction and (iii) an intact antibody to cover a wide range of molecular mass. After some initial screening runs, conditions for an appropriate comparison based on the gradient kinetic plot were evaluated and later used for the column comparison. To the best of our knowledge, there was no such comprehensive study on the performance of protein columns from different column technologies and suppliers reported until now, and in particular specific focus is paid to monolithic columns for which the recent literature is relatively lean. The groups of Teutenberg and Eeltink also applied gradient kinetic plots and compared packed bed and monolithic columns in capillary or microbore column format [23–25]. The influence of the column technology, particle size and pore size is thoroughly discussed.

2. Experimental

2.1. Materials

Chromolith WP300 RP-4 (4.6 × 50 mm, C4-modified monolithic silica column), Chromolith WP300 RP-18 (2.0 × 100 mm), Chromolith HR RP-18e (2.0 × 100 mm, high resolution research sample, C18-modified), BIOshell 400 Å Protein C4 (2.1 × 50 mm, 3.4 µm), BIOshell IgG 1000 Å C4 (2.1 × 20 mm & 2.1 × 50 mm, 2.7 µm) columns were generously provided by Merck (Darmstadt, Germany). Aeris Widepore C4 200 Å (2.1 × 50 mm, 3.6 µm) was supplied by Phenomenex (Aschaffenburg, Germany). The AdvanceBio RP-mAb C4 (2.1 × 50 mm, 3.5 µm) column was purchased from Agilent (Waldbronn, Germany). The BioResolve RP mAb (2.1 × 50 mm, 2.7 µm) and the Acquity UPLC protein BEH C4 (2.1 × 50 mm, 1.7 µm) columns were purchased from Waters (Eschborn, Germany) and the MAbPac RP column (4.0 × 50 mm, 4 µm) from Thermo Scientific (Waltham, Ma, USA). The Solas C4 400 Å and 1000 Å (both 2.1 × 50 mm, 1.7 µm) were obtained from Glantreo (Cork, Ireland). The properties of the columns are summarized in Tables 1–3. NIST monoclonal antibody (NISTmAb) reference material (RM) 8671, a humanized IgG1κ monoclonal antibody formulated in histidine buffer, was purchased from the National Institute of Standards and Technologies (NIST, Gaithersburg, MD, USA). Acetic acid ($\geq$ 99.8%) and sodium dihydrogen phosphate monohydrate were from Merck. Tris(2-carboxyethyl)phosphine (TCEP), sodium chloride, potassium chloride, and sodium hydroxide, lysozyme from chicken egg white, cytochrome c from equine heart, β-lactoglobulin B from bovine milk ($\geq$90%) and bovine serum albumin (BSA), Protein LoBind Tubes 1.5 mL from Eppendorf were purchased from Sigma-Aldrich (Merck, Taufkirchen, Germany). Di-sodium hydrogen phosphate anhydrous and thiourea were purchased from Applichem (Darmstadt, Germany). FragIT (immobilized IdeS enzyme) was supplied by Genovis (Luden, Sweden). Ultrapure water was obtained from a Purelab Ultra purification system from Elga LabWater (Celle, Germany).

2.2. Instrumentation and software

The LC-instrument was from Agilent Technologies (Waldbronn, Germany). Agilent 1290 Infinity UHPLC system consisting of binary pump (G4220A), autosampler (G4226A), sample thermostat (G1130B), thermostated column compartment (G1316C) and diode array detector (DAD, G4212A). The instrument was equipped with an ultra-low dispersion kit and the extra-column volume and dwell volume was determined as 11.7 µL and 175 µL, respectively. Instrument control and data analysis were performed using OpenLab CDS 2.5.0.

Microsoft Excel 2019 (Redmond, WA, USA) and OriginPro 2021b (OriginLab, Northapton, MA, USA) were used for data processing.

Table 1
Properties of superficially porous particle (SPP) columns. d_p: particle diameter, L × I.D.: column length and internal diameter, *d*(core): diameter of the SPP, shell: shell thickness of the SPP, ΔP_{max}: maximum pressure limit of the column, T_{max}: maximum column temperature, C [%]: carbon load, K_v: column permeability, Φ: flow resistance.

Column	d_p [µm]	L × I.D. [mm]	pore size [Å]	d (core) [µm]	shell [µm]	ΔP_{max} [bar]	support	stationary phase	pH range	$T_{max.}$ [°C]	C [%]	K_v [m²]	Φ[/]
AdvanceBio RP-mAb C4	3.5	50 × 2.1	450	3	0.25	600	silica	C4	1 to 8	90	n/a	$1.12*10^{-14}$	$1.10*10^{3}$
Aeris Widepore C4	3.6	50 × 2.1	200	3.2	0.2	600	silica	C4	1.5 to 9	90	n/a	$9.14*10^{-15}$	$1.42*10^{3}$
BioResolve RP mAb	2.7	50 × 2.1	450	1.9	0.4	689	silica	Phenyl	2 to 7.5	90	5.48	$8.08*10^{-15}$	$9.03*10^{2}$
BIOshell A400 Protein C4	3.4	50 × 2.1	400	3	0.2	600	silica	C4	2 to 9	60	0.4	$7.82*10^{-15}$	$1.48*10^{3}$
BIOshell IgG 1000A C4	2.7	50 × 2.1	1000	1.7	0.5	1000	silica	C4	2 to 9	60	0.6	$7.25*10^{-15}$	$1.01*10^{3}$
BIOshell IgG 1000A C4	2.7	20 × 2.1	1000	1.7	0.5	1000	silica	C4	2 to 9	60	0.6	$5.85*10^{-15}$	$1.25*10^{3}$

Table 2
Properties of fully porous particle columns. d_p: particle diameter, L × I.D.: column length and internal diameter, ΔP_{max}: maximum pressure limit of the column, T_{max}: maximum column temperature, C [%]: carbon load, K_v: column permeability, Φ: flow resistance.

Column	d_p [µm]	L × I.D. [mm]	pore size [Å]	ΔP_{max} [bar]	stationary phase	support	pH range	$T_{max.}$ [°C]	C [%]	K_v [m²]	Φ[/]
Acquity UPLC Protein BEH C4	1.7	50 × 2.1	300	1000	C4	ethylene silica hybrid	1 to 12	90	7.95	$3.31*10^{-15}$	$8.74*10^{2}$
MAbPac RP	4	50 × 2.1	1500	275	Phenyl	DVB	0 to 14	110	n/a	$5.81*10^{-15}$	$2.75*10^{3}$
Solas C4 1000A	1.7	50 × 2.1	1000	700	C4	silica	2 to 9	90	0.33	$2.48*10^{-15}$	$1.16*10^{3}$
Solas, C4 400A	1.7	50 × 2.1	400	700	C4	silica	2 to 9	90	0.69	$2.29*10^{-15}$	$1.26*10^{3}$

Table 3
Properties of monolithic columns. L × I.D.: column length and internal diameter, ΔP_{max}: maximum pressure limit of the column, T_{max}: maximum column temperature, C [%]: carbon load.

Column	L × I.D. [mm]	Macropore size [µm] [a]	Meso-pore size [Å]	porosity	ΔP_{max} [bar]	pH range	T_{max}[°C]	Support	Stationary phase	C [%]
Chromolith WP300 RP-4	50 × 4.6	2	300	>80%	200	1.5 to 7.5	60	silica	C4	3.5
Chromolith WP300 RP-18	100 × 2	2.0	300	>80%	200	1.5 to 7.5	60	silica	C18	9
Chromolith HR RP-18e	100 × 2	1.15	150	>80%	200	2.0 to 7.5	50	silica	C18	15

[a] Values taken from Chromolith column brochure at https://www.sigmaaldrich.com/

DryLab 4.3.5 (Molnár-Institute, Berlin, Germany) as design of experiment software.

2.3. Sample preparation

A stock solution of the protein samples cytochrome c, β-lactoglobulin, lysozyme and BSA with a concentration of 5 mg/mL has been prepared with water. The stock solutions were diluted 1:5 with 10 mM ammonium acetate (pH 6) to get the final concentration of the pure proteins (c = 1 mg/mL). A mixture of the four proteins with a concentration of 1 mg/mL for each protein was prepared by mixing the four stock solutions and dilution by 10 mM ammonium acetate. NIST mAb was diluted from a concentration of 10 mg/mL to 1 mg/mL with 10 mM ammonium acetate.

IdeS digestion was performed with FragIT MicroSpin columns following the manufacturer's instructions with a cleavage buffer composed of 10 mM Na_2HPO_4, 140 mM NaCl and 2.7 mM KCl. 20 µL of the antibody solution (c = 10 mg/mL) was diluted with 80 µL cleavage buffer. For digestion this reaction mixture was incubated for 30 min at 37 °C and 250 rpm. For further reduction, 20 µL of a 50 mM TCEP solution was added and incubated for 60 min at 60 °C and 250 rpm. Subsequently, the buffer was exchanged three times with a Vivaspin 500 spin column (MWCO 10,000) with 10 mM ammonium acetate buffer pH 6.0 at 12 000 g for 5 min.

2.4. Gradient kinetic plot method

The gradient kinetic plots concept has been described by Broeckhoven et al. [20] and the same methodology was used herein with some minor adjustments. In pre-experiments the column dead times and the system back pressure were measured isocratically by injection of thiourea as dead time marker with the mobile phase composition with the highest viscosity during the gradient which is for an acetonitrile/water mixture at 25% for the gradient ranges from 25–50% ACN [26]. The back pressure was measured with the column installed (ΔP_{total}) and with a zero-dead volume union installed instead of the column (ΔP_{ec}). Thus, the corrected column back pressure (ΔP_{column}) could be calculated by $\Delta P_{column} = \Delta P_{total} - \Delta P_{ec}$. The maximum flow rate was determined according to the maximum allowed column pressure given by the manufacturer. Eight data points representing eight different flow rates were considered as sufficient for creation of the gradient kinetic plots. The highest flow rate was dictated by the maximum allowed column pressure $\Delta P_{column,\ max}$ thus the remaining seven flow rates were selected considering the lowest flow rate with sufficient flow accuracy specified by the instrument manufacturer (0.1 mL/min) and the remaining six flow rates were in equal intervals in between. DryLab screening runs were performed for each column to check for appropriate conditions considering the column temperature and the gradient design (start and end condition of acetonitrile and gradient time). Three different gradient times (10, 20 and 30 min) were used at two different temperatures (30 and 60 °C) at a flow rate of 0.5 mL/min for the screening and determination of log k_w and *S*-values, thus in total six gradient runs were performed. For the DryLab model only the 10 and 30 min runs were used as input and the 20 min gradient time was used to determine the method and sample dependent *S*-value according to a method described by Zhang et al. [27] with some adjustments explained in the supplementary chapter 1. Based on the linear solvent strength theory the log k_w and *S*-values can be calculated as intercept and slope, respectively, of *log k* vs. φ plots (φ: modifier content).

For each column the lowest possible gradient time was used to get still a separation of all peaks with a minimal resolution of 1.5. As the intact NISTmAb samples has only one peak the lowest possible gradient time was used and the retention time of the NISTmAb peak was set to 2/3 of the gradient time.

One important prerequisite for the gradient kinetic plots is that for each flow rate the sample experienced the same mobile phase history [20]. Therefore, $\beta \cdot t_0$ must be constant, where β is the gradient steepness and t_0 is the column dead time.

The gradient steepness β can be expressed as [20] (Eq. (1))

$$\beta = \frac{\varphi_{end} - \varphi_0}{t_{end} - t_{start}} = \frac{\Delta\varphi}{t_G} \tag{1}$$

Where t_{end} and t_{start} are the gradient end and start time and φ_{end} and φ_0 are the final and initial organic modifier percentage, respectively.

In the current study, columns with different stationary phases were used why it might not be enough to keep $\beta \cdot t_0$ constant. Zhang et al. suggested to consider the S-value and keep $S \cdot \beta \cdot t_0$ constant.

The comparison of the chromatographic performance of the different columns in gradient separations was performed using the peak capacity (n_p). The peak capacity represents the maximum number of peaks that can be fitted into the chromatographic window between the first and the last eluting peak. Herein, n_p was calculated assuming $Rs = 1$ using a simplified equation [28]:

$$n_p = 1 + \frac{t_G - t_0}{W_{4\sigma}} = 1 + \frac{t_G - t_0}{1.7 \cdot W_{50\%}} \tag{2}$$

with t_0 being the elution time of a non-retained compound (dead time) and t_G being the gradient (run) time. $w_{4\sigma}$ is the peak width at 4σ and $w_{50\%}$ is the peak width at half height. $w_{50\%}$ was used because it can be determined more accurately by the software and is less prone to errors.

The maximum column performance limit is reached at its kinetic performance limit (KPL) which is at the maximum pressure limit (ΔP_{max}) either of the column or the system, whichever is the lower. Therefore, the column length rescaling factor λ was used to calculate the peak capacity at the KPL [20].

$$\lambda = \frac{\Delta P_{max}}{\Delta P_{exp}} \tag{3}$$

Where ΔP_{exp} is the experimental pressure drop caused by the column.

The peak capacity at the KPL can be calculated as follows based on the experimentally obtained peak capacity $n_{p,exp}$:

$$n_{p,KPL} = 1 + \sqrt{\lambda} \cdot (n_{p,exp} - 1) \tag{4}$$

The retention time at the KPL limit can be calculated as follows:

$$t_{R,KPL} = \lambda \cdot t_{R,exp} = t_{0,\,KPL}(1 + k) \tag{5}$$

In the final KPL methods the gradient range was from 25 – 55% ACN and a column temperature of 60 °C was used for all columns.

3. Results and discussion

3.1. Validation of the gradient kinetic plot concept for proteins

First, the validity of the gradient kinetic plot model for proteins as solutes was investigated using two columns which only differed in their column length viz. BIOshell 1000 Å 50 mm and 20 mm length. For this reason, the KPL curves of the two columns should overlap proving the validity of the model [20]. The sample set consisted of proteins covering a molecular weight range from 12.4 to 148.2 kDa, isoelectric points (pI) ranging from 4.7 to 11.35 and different hydrophobicities (Table S 1). Three sample mixtures were used: A standard protein mixture consisting of cytochrome c, lysozyme and β-lactoglobulin covers the molecular weight range from 12.4 to 18.3 kDa representing small proteins (note, BSA was also present and hence appears in the chromatograms; however, due to molecular dispersity and uncommonly broad peaks it was omitted from the study of KPL curves). Antibody fragments obtained after IdeS-digestion and disulphide reduction resulting in light chain (LC), Fc/2- and Fd-fragments are frequently analysed in middle-up approaches and represent intermediate-sized proteins with a molecular weight of approximately 25 kDa. The intact NISTmAb sample was the protein with the highest molecular weight in the study sample set.

Based on the DryLab screening runs similar conditions for the gradient range and the start and end percentage of acetonitrile (25 – 55%) as well as a temperature of 60 °C were found to be appropriate for all columns. The use of higher temperatures than 60 °C for columns with a higher maximum temperature limit will certainly have an influence on the column performance as it is affecting the selectivity, S-value of the solutes, on-column protein stability, the mobile phase viscosity and consequently the back pressure and therefore the maximum possible flow rate. Due to the multiple parallel effects of the temperature on the separation, it would be difficult to deconvolute the stationary phase effects responsible for the differences in column performance. Therefore, a fixed temperature of 60 °C was used for all columns as a compromise. Two different conditions have been tested for an overlap. First $\beta \cdot t_0$ was kept constant and a value of 0.02 was selected based on the screening runs. This approach is the original method from Broeckhoven et al. testing columns with the same stationary phase. Second $S \cdot \beta \cdot t_0$ was set constant as suggested by Zhang et al. [27] which takes the different retention behaviour of varying stationary phases for the same analyte into account. $S \cdot \beta \cdot t_0 = 2$ was found to be considerable based on the DryLab screening runs. For the first case with $\beta \cdot t_0 = 0.02$, a very good overlap could be observed for lysozyme (Fig. 1a), the antibody fragments (Fig. 1c) and the intact NISTmAb (Fig. 1e). Minor deviations were found for cytochrome c and β-lactogobulin (Fig. 1a). The overlap for the second condition $S \cdot \beta \cdot t_0 = 2$ was perfect for all sample proteins (Fig. 1b, d) with exception for the intact NISTmAb (Fig. 1f) which showed a minor deviation. Both tested conditions showed acceptable results but in total the condition $S \cdot \beta \cdot t_0 = 2$ seemed to be superior because only the NISTmAb showed a minor deviation and this might result from inaccurate determination of the S-value of the antibody.

3.2. Evaluation of superficially porous particle columns

The current study included six superficially porous particle (SPP) columns which differed mainly in shell thickness and pore size, while they had nearly the same particle diameter (2.7—3.5 µm) (Table 1). Example chromatograms for SPP columns (AdvanceBio RP mAb C4 and BIOshell 400 Å, respectively) are given in Fig. 2a-c and Fig. S 1 in the supplementary material for the intact NISTmAb, the NIST-IdeS-TCEP sample and the protein mixture. All main peaks of the NISTmAb fragments (Fig. 2b) as well as the protein mix samples (Fig. 2c) were baseline separated from each other.

The interpretation of the KPL curves is straightforward. From a practical viewpoint KPL plots of distinct columns can be conveniently used to select the system which can provide a certain efficiency (i.e. peak capacity n_p) in the shortest possible time t_R when they are operated at their pressure maximum ΔP_{max} (see Table 1). Vice versa, it allows to select the system that gives the highest peak capacity with a certain pre-selected speed t_R. For example, when looking at the KPL curves of different SPP columns for cytochrome c (Fig. 3a), $n_p = 100$ can be achieved in the shortest possible time with the BIOshell 400 Å column ($t_R = 55.9$ s, other columns: BIOshell 1000 Å 20 mm: 67.8 s; BioResolve RP mAb: 78.5 s; BIOshell 1000 Å 50 mm: 84.7 s; Advance Bio 89.6 s; Aeris Widepore C4: 94.3 s). The shortest analysis time for $n_p = 250$,

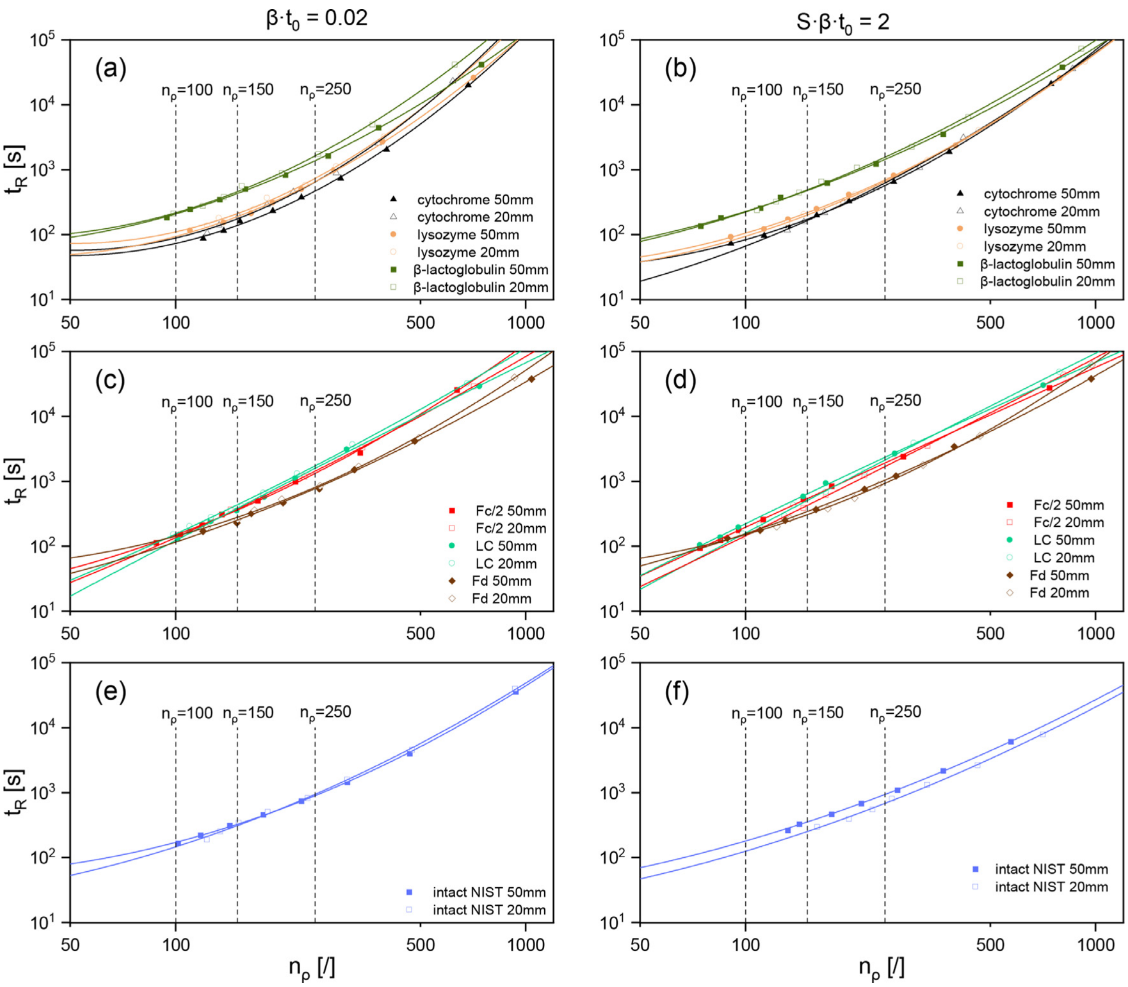

Fig. 1. Gradient kinetic plot method validation for protein samples using columns of different lengths. Protein mix sample (a-b) contained cytochrome c, lysozyme and β-lactoglobulin, (c-d) NISTmAb subunits comprised of Fc/2-, Fd-fragments and light chain (LC), and (e-f) intact NISTmAb. Columns: BIOshell 1000 Å 2.1 mm I.D., 50 and 20 mm length, respectively; column temperature = 60 °C; 8 flow rates from 0.1 to 1.5 in 0.2 mL/min steps; mobile phase A: 0.1% (v/v) TFA in water, B: 0.1% (v/v) TFA in ACN, gradient: 25–55% B; gradient time set to keep $\beta \cdot t_0 = 0.02$ (a, c, e) or $S \cdot \beta \cdot t_0 = 2$ (b, d, f) constant.

however, was observed for the BIOshell 1000 Å 50 mm column ($t_R = 565.2$ s). In general, the BIOshell 400 Å column showed superior performance especially for the fast method regime (low retention times; slant horizontal asymptote; C-term region) compared to the other SPP columns for the small proteins cytochrome c, lysozyme and β-lactoglobulin (Fig. 3a-c). At low flow rates and slow method regime (i.e. under conditions corresponding to the vertical asymptote; B-term region) the highest peak capacities were reached with the BIOshell 1000 Å columns. A similar trend was found for the lysozyme and β-lactoglobulin samples (Fig. 3b-c). These data suggest that the benefit of enhanced pore diffusion with 1000 Å material cannot be realized under conditions of high flow rates (fast separation regime; C-term region) due to the longer diffusion paths (0.5 µm shell thickness) of the BIOshell 1000 Å compared to BIOshell 400 Å (0.2 µm). Even for small proteins shorter diffusion paths (thin shell) bring more benefits at high flow rates than wider pores, the advantage in terms of unhindered pore diffusion can only be exploited at low flow rates if the diffusion paths are relatively long like for thick-shell SPP columns (such as BIOshell 1000 Å).

For intermediate-sized proteins, such as NISTmAb fragments, the BIOshell 400 Å column had the best performance amongst the tested SPP columns over the entire flow rate/column length range (Fig. 3d-f). Again, the outstanding performance of the BIOshell 400 Å column was most likely mainly due to the thinner porous shell (0.2 µm) with its shorter diffusion paths and enhanced mass transfer also for intermediate-size proteins. The larger the protein, the smaller is the diffusion coefficient and the higher is the mass transfer contribution to the band broadening. Thus, a better performance of the BIOshell 1000 Å was expected but was not realized, probably due to a more favourable striking effect from shorter diffusion paths of the BIOshell 400 Å material (Fig. 3d-f). The Aeris Widepore C4 column has the same shell thickness, but a much smaller pore size of 200 Å which seems to be too narrow and can lead to hindered pore diffusion. Therefore, it is not a surprise that it showed the worst performance of all SPP columns tested.

While the BIOshell 400 Å column was the best choice for proteins with a molecular weight from 12.4 to about 25 kDa, the AdvanceBio RP mAb C4 was superior to the other SPP columns for the intact NIST mAb (Fig. 3g). Without more in-depth characterizations and investigations of individual peak dispersion contributions it is hard to explain why it was superior to the BIOshell 400 Å column as they largely resemble each other in shell thickness (0.25 vs. 0.2 µm), particle size (3.5 vs. 3.4 µm) and pore size (450 vs. 400 Å). The permeability of the BIOshell 400 Å is 30 % lower while the flow resistance is 35 % higher compared to the AdvanceBio column which may indicate some significant differences in the morphology (see supplementary chapter 2.3 and Fig. S 2–3). Possible explanations for the shifted KPL curve of AdvanceBio RP mAb C4 in relation to the BIOshell 400 Å are differences in surface chem-

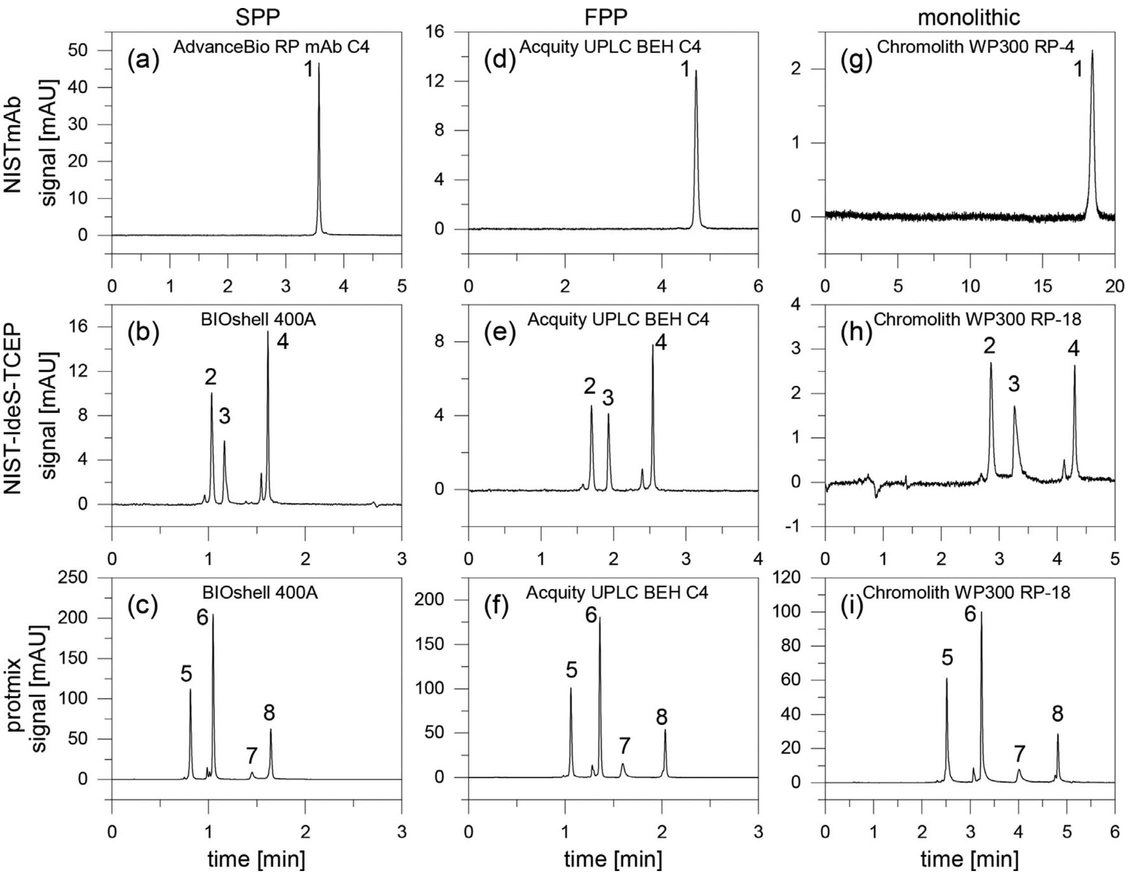

Fig. 2. Chromatograms of the best performing columns for each column technology. Superficially porous particle (SPP) columns (a, d, g); fully porous particle (FPP) columns (b, e, h); monolithic columns (c, f, i) Samples: intact NISTmAb (a-c), NISTmAb fragments (NIST-IdeS-TCEP: d-f) and protein mixture (g-i). Column temperature = 60 °C, flow rate = 0.5 mL/min, mobile phase A: 0.1% (v/v) TFA in water, B: 0.1% (v/v) TFA in ACN, gradient 25–55% B. Gradient time was set for each column and sample mixture to keep $S{\cdot}\beta{\cdot}t0 = 2$.

istry including bonding density, endcapping and secondary interactions of the stationary phase, pore structure, pore and particle diameter distributions, and so forth. The suitability of the BIOshell columns for ultra-fast protein separations (<1.5 min) has been recently demonstrated by their application for full comprehensive 2D-LC analysis [29].

For comparison of the KPL curves of different proteins on the same SPP column, the interested reader is referred to the supplementary material (Fig. S 4). To conclude, the relative order of kinetic performance of the tested SPP columns is mainly driven by the shell thickness, unless the pore diameter is too small like for the 200 Å material. A significant gain in the kinetic performance with 1000 Å pore size can only be materialized in the slow method regime (due to thicker shell). To investigate the influence of the pressure limit on the performance comparison, a KPL plot with a constant maximum pressure (600 bar) limit was created (see supplementary Fig. S 5) but still the same trends were observed without any significant changes. The current work confirms that the 400 Å materials with thin 0.2 µm shell are a good compromise regarding kinetic performance.

3.3. Evaluation of fully porous particle columns

Four different fully porous particle (FPP) columns have been investigated in the current study differing in particle size (1.7 and 4 µm), pore size (300 to 1500 Å) and backbone chemistry (silica, ethylene bridged silica hybrid, polystyrene materials) (Table 2). In the direct column-to-column comparison the Acquity UHPLC BEH C4 (1.7 µm, 300 Å) column outperformed clearly all other FPP columns among all the examined proteins and the entire tested flow rate range (Fig. 4). The difference in performance between the Acquity and the Solas columns could be partially explained by the lower maximum pressure limit of the Solas columns (700 bar vs. 1000 bar). As a consequence, the Solas columns allowed the use of lower maximum flow rates up to 0.8 mL/min only, while the Acquity column could be run at up to 1.5 mL/min. Therefore, faster protein analysis can be realized with the Acquity column. The Solas columns possess also a low carbon content (Table 2). One could further speculate that due to low ligand coverage residual silanols are accessible to protein interactions at the surface leading to reduced efficiencies. On the other hand, the wide-pore (1500 Å) 4 µm MAbPac RP column was performing worst for the small proteins in terms of speed-efficiency compromise and kinetic performance limits, respectively, under the selected conditions (60 °C) most likely owing to its larger particle size that is associated with larger Eddy diffusion terms and increased mass transfer resistance (Fig. 4). Here it should be mentioned that MAbPac RP is usually used at higher temperatures at which it shows significantly better performance. As the size of the proteins increased, the MAbPac RP column gained in KPL performance and indeed its best KPL-curves amongst the tested proteins were obtained for the intact NISTmAb and its fragments (Fig. S 6a). This observation can be explained by the large pore size of 1500 Å which is specifically appropriate for very large proteins. For the Acquity UPLC BEH C4 column the KPL curves show less variance between the distinct proteins but again the NISTmAb sample and the Fd-fragment exhibited the best KPL-curves (Fig. S 6b). One further advantage of the Acquity column may be the broader pH range from pH 1 to 12 due to the bridged

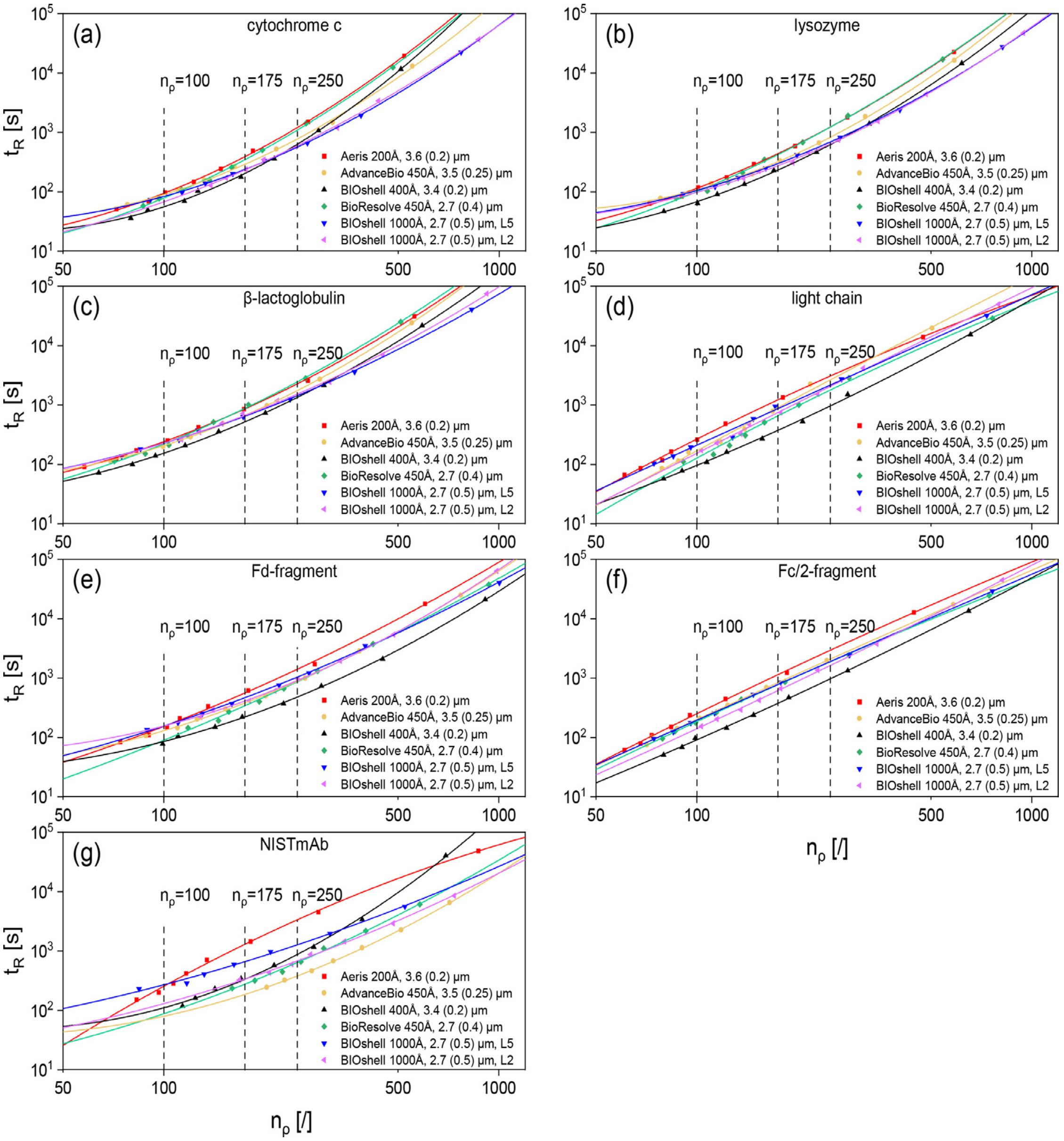

Fig. 3. Gradient kinetic plots for the same protein and different superficially porous particle columns. (a) Cytochrome c, (b) lysozyme, (c) β-lactoglobulin, (d) light chain, (e) Fd-fragment, (f) Fc/2-fragment, (g) NIST mAb. Column temperature = 60 °C, mobile phase A: 0.1% (v/v) TFA in water, B: 0.1% (v/v) TFA in ACN; gradient: 25–55% B; 8 flow rates were used according to the columns maximum pressure limit and the gradient time adjusted to keep $S{\cdot}\beta{\cdot}t_0 = 2$ constant. The figure legend provides the column brand name, pore size, total particle diameter, in brackets the shell thickness and the label L2 and L5 represent the column length of 20 and 50 mm, respectively.

ethylene hybrid (BEH) technology. Usually proteins are analysed at low pH-values but there might be some special applications where a high pH-value could provide some orthogonal selectivity or might be more beneficial for proteins with low isoelectric point. For the latter higher pH-value could enable the use of negative ionisation mode in ESI-MS-analysis [30,31]. Further, to column stability is expected to be better and it offers the possibility to use high pH for column regeneration. All tested FPP columns can be used at elevated temperatures up to 90 °C while the MAbPac column tolerates even 110 °C. This is beneficial in terms of better recovery, lower back pressure due to reduced mobile phase viscosity shifting the KPL curves to increased efficiencies and higher peak capacities, respectively. One particular disadvantage of the MAbPac column is its limited maximal pressure (275 bar) that is a result of the wide pores with limited pressure stability. It could therefore only be used at lower maximum flow rates (0.5 vs. 1.5 mL/min for most of the other tested columns) and had consequently higher retention times. Moreover, the rescaling factor λ at lower flow rates was smaller than for columns with higher pressure limits. On the other hand, the MAbPac column offers the broadest pH range (from 1 to 14) of all columns because of its polymeric support. Consequently, it can provide different selectivities because the stationary phase is based on pendant phenyl groups (divinylbenzene copolymer). The two Solas columns, however, showed their best performance for cytochrome c and lysozyme amongst the different proteins (Fig. S 6c-d). Compared to the other FPP columns, they exhibited reasonable kinetic performance for these small proteins. For the larger proteins (NISTmAb and fragments) the 400 Å Solas column is not competitive in terms of kinetic performance with the Acquity UPLC BEH C4 column, for the NISTmAb the same is seen for the 1000 Å Solas column unexpectedly. At this point it should be mentioned that both Solas columns are specified with a column maximal pressure of 700 bar, but especially the column with the 1000 Å wide pores may have limited column longevity

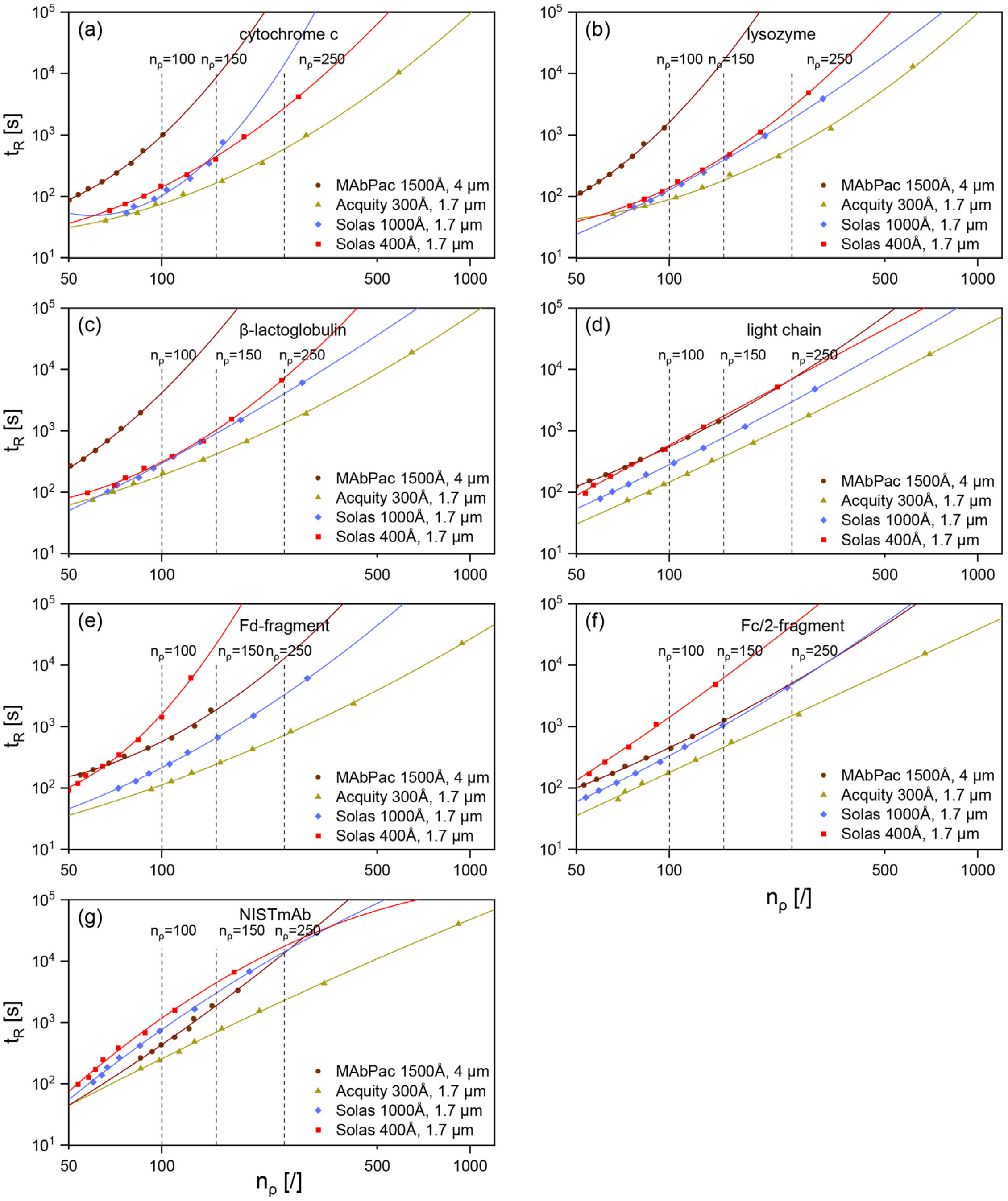

Fig. 4. Gradient kinetic plots for the same protein and different fully porous particle columns. (a) Cytochrome c, (b) lysozyme, (c) β-lactoglobulin, (d) light chain, (e) Fd-fragment, (f) Fc/2-fragment, (g) NIST mAb. Other conditions are the same as in Fig. 3. The figure legend provides the column brand name, pore size and total particle diameter.

if it is operated for prolonged period at this maximal pressure. The same trends are observed when a constant pressure limit of 700 bar is used instead of the individual column pressure limits (see supplementary Fig. S 7). Overall, the Acquity UPLC BEH C4 column showed the best kinetic performance within this class of columns regardless of protein size.

3.4. Evaluation of monolithic columns

Three monolithic columns, which differed in macropore size (and hence in domain size as well i.e. the combined length scale of mean macropore and silica skeleton diameters), mesopore size of the silica skeleton (300 and 150 Å), column dimension (4.6 and 2 mm I.D.) and alkyl-bonding (C18 vs C4), were investigated in the current study (Table 3). Of those monoliths, only the Chromolith WP300 RP-4 is dedicated for protein separations, while the Chromolith WP300 RP-18 has its application scope for larger peptides. The Chromolith HR RP-18e has its primary scope of application for small molecules and small peptides. In spite of that all three Chromoliths were investigated here for protein separations due to lack of alternatives of its kind and to illustrate performance differences that are associated with their altered morphologies, i.e. pore size, macropore and skeleton diameter that are correlated (narrower macropores are associated with thinner skeletons and smaller domain size). Hormann et al. determined macropore diameters of 1.98 ± 0.76 vs 1.33 ± 0.48 µm, skeleton diameters of 1.17 ± 0.32 vs

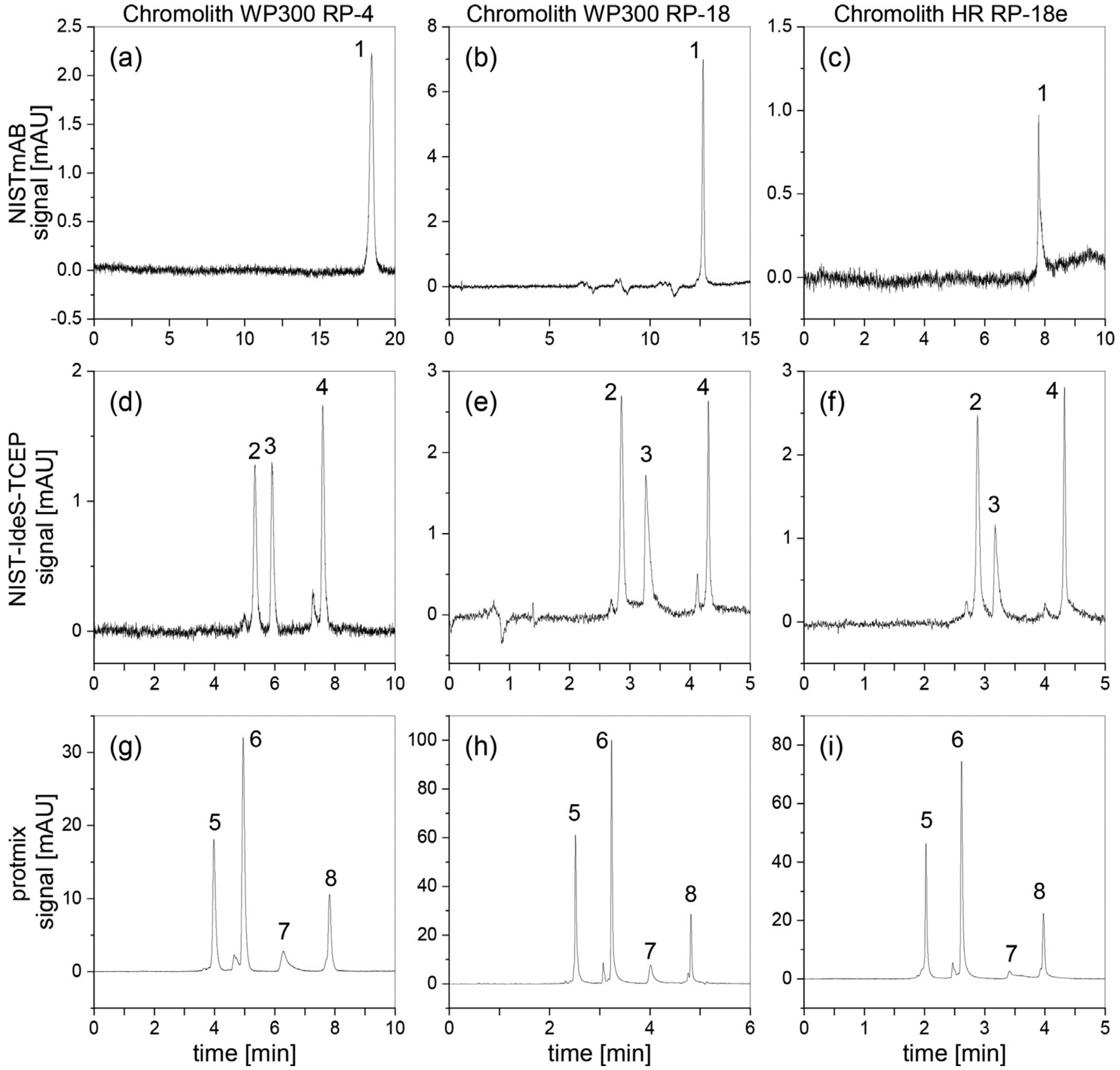

Fig. 5. Chromatogram comparison of the monolithic columns. (a-c) NISTmAb (1), (d-f) NIST-IdeS-TCEP with (2) Fc/2-, (3) light chain- and (4) Fd-fragment and protmix (g-i) containing (5) cytochrome c, (6) lysozyme, (7) BSA and (8) β-lactoglobulin. (a, d, g) Chromolith WP300 RP-4, (b, e, h) Chromolith WP 300 RP-18 and (c, f, i) Chromolith HR RP-18e columns. Column temperature = 60 °C, flow rate = 0.5 mL/min, mobile phase A: 0.1% (v/v) TFA in water, B: 0.1% (v/v) TFA in ACN, gradient 25–55% B. Gradient time was set for each column and sample mixture to keep $S{\cdot}\beta{\cdot}t_0 = 2$.

0.90 ± 0.29 µm and domain size of 3.15 vs 2.23 µm for 1st and 2nd (HR) generation of 4.6 mm I.D. Chromolith columns [32]. These dimensions are slightly downscaled for the 2 mm I.D. Chromolith columns (Table 3).

All three columns showed a good performance and could separate the two test mixtures with three sample constituents with the same elution order and similar selectivities (Fig. 5). The Chromolith WP300 RP-18 had the best performing KPL-curves for the small standard proteins cytochrome c, lysozyme and β-lactoglobulin (Fig. 6a-c). For the separation of the NISTmAb light chain and the Fd-fragment, the best kinetic performance at high flow rates (i.e. at the fast separation regime with low t_R) exhibited the Chromolith WP300 RP-18, while the Chromolith HR RP-18e performed better at lower flow rates (high peak capacity regime corresponding to the slow separation speeds see Fig. 6d-e). The Chromolith HR RP-18e is not tailored for large size proteins, but small molecule separations. Its better kinetic performance in the slow separation regime may originate from a thinner skeleton size and smaller domain size, respectively, compared to the two wide-pore monoliths, which results in lower mass transfer resistance. In the fast separation regime this advantage gets lost and the wide pore monoliths behave better and are certainly advantageous. The two C18 monoliths had a very similar performance for the Fc/2-fragment as solute (Fig. 6f).

The findings from the KPL curves for the intact NISTmAb sample were unexpected, challenging to interpret and might be easily misleading. The KPL curves shown in Fig. 6g pretend the best kinetic performance for the Chromolith HR RP-18e, especially in the slow separation speed regime. However, a low recovery was observed for this monolith which is not surprising and might be related to the hydrophobic C18 alkyl chemistry and problems in diffusional mass transfer in the narrow mesopores or even pore exclusion and blockage accompanied by analyte loss. With a hydrodynamic diameter of about 9 nm for the NISTmAb and 15 nm pore diameter, yielding a ratio $\lambda_m \sim 0.6$, effective diffusion is estimated to be significantly less than 10 % of unhindered diffusion in free solution which may partly explain the recovery loss [10]. A similar problem, however, was also found for the Chromolith WP300 RP-18 which may indicate that also the C18 surface chemistry and possibly residual silanols contribute to this poor recovery as well. The recovery was becoming worse with an increase in flow rate especially for the intact NISTmAb and the two C18 monoliths while

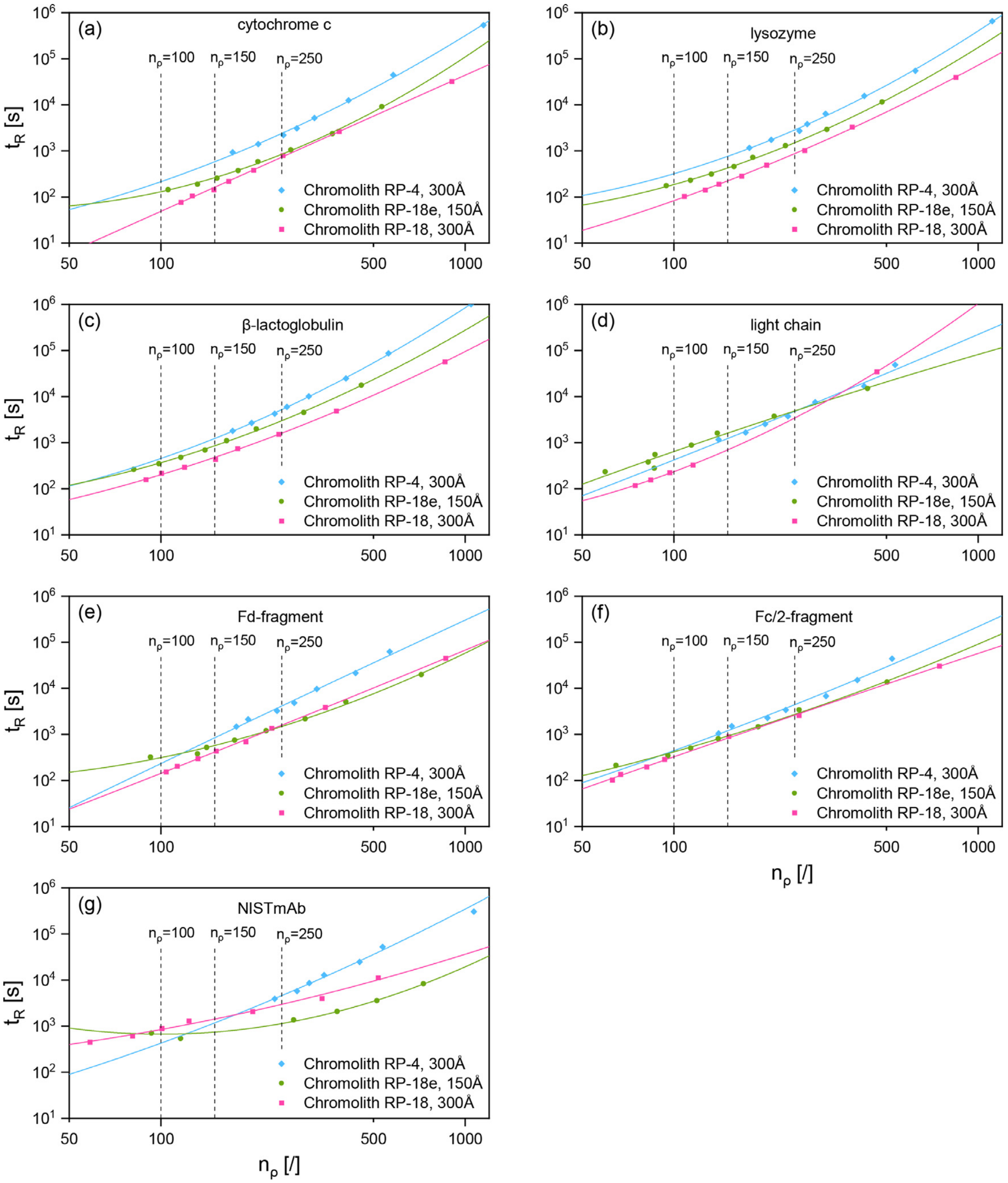

Fig. 6. Gradient kinetic plots for the same protein and different monolithic columns. (a) Cytochrome c, (b) lysozyme, (c) β-lactoglobulin, (d) light chain, (e) Fd-fragment, (f) Fc/2-fragment, (g) NIST mAb. Other conditions are the same as in Fig. 3. The figure legend provides the column brand name, stationary phase chemistry and pore size.

the C4 monolith was less affected (Fig. S 8). The recovery issue was much less problematic for the antibody fragments and the small standard proteins (Fig. S 9–10). Hence, the 300 Å wide-pore, C4 monolith column is the preferred choice, in particular for larger proteins. All protein samples had a similar KPL-curve for the Chromolith WP300 RP-4 column (Fig S 11).

3.5. Comparison of column technologies

KPL curves have the advantage that they enable a reasonable direct comparison of columns with different dimensions and stationary phase morphologies. Hence, such kinetic plots are a good approach to figure out which column provides the best performance across distinct morphologies for a given application. For this purpose, a comparison of the columns from all designs was finally carried out. The chromatograms of the best performing column from each column technology at the same flow rate are depicted in Fig. 2. The KPL-curves from the best and least performing column of each column technology are shown in (Fig. 7a-g). A detailed discussion focused on the pore size influence of a representative pair of columns from each column morphology is furthermore provided in the supplementary information (chapter 2.7 and Fig. S 12).

The best columns for SPP, FPP and monolith technology were the BIOshell 400 Å, Acquity UHPLC protein BEH C4 and Chromolith WP300 RP-18 columns, respectively. Across all protein sizes, except for NISTmAb the BIOshell 400 Å column showed the best kinetic performance. It was outperformed, though, by the Acquity UHPLC protein BEH C4 and Chromolith WP300 RP-18 columns in

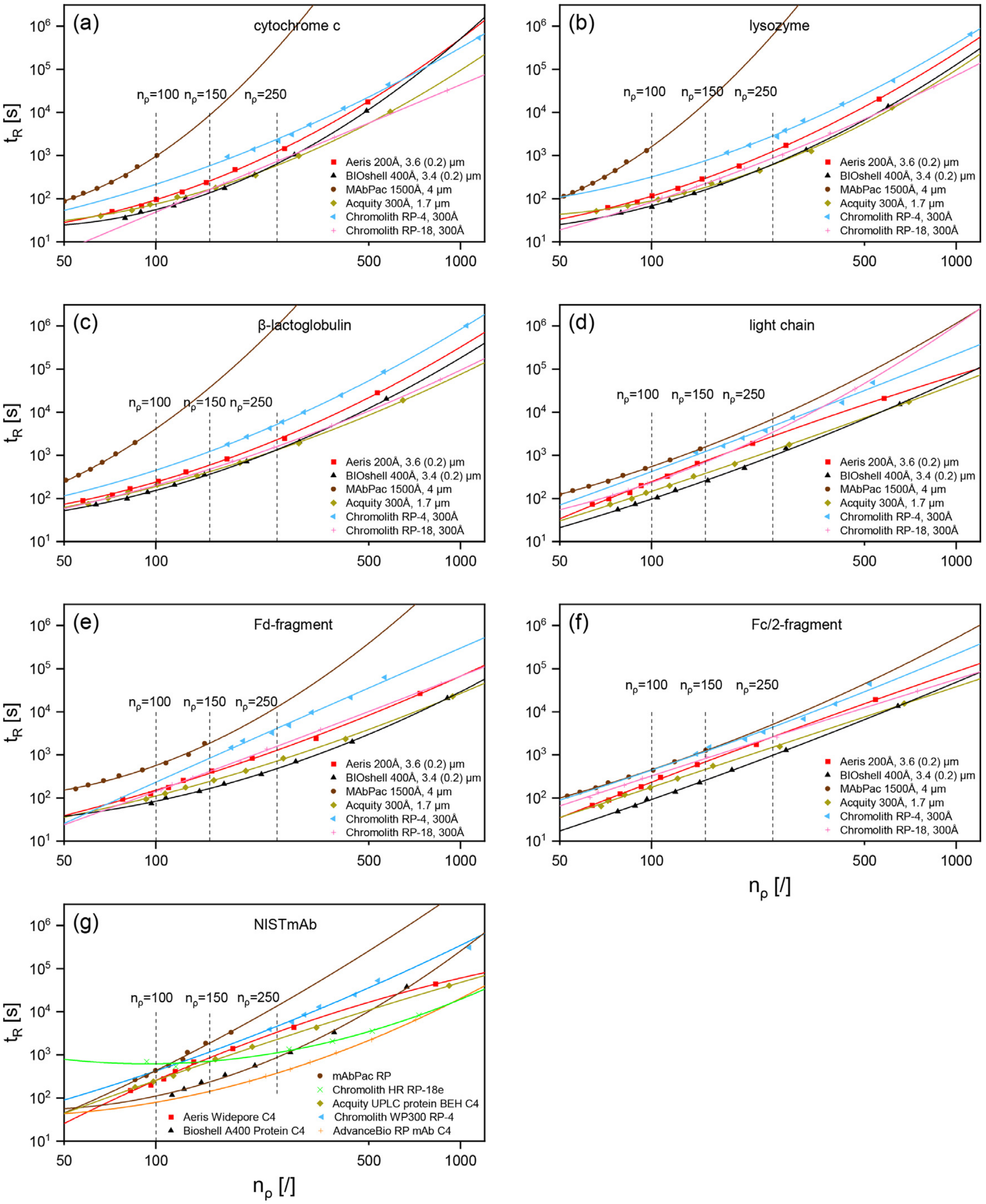

Fig. 7. Gradient kinetic plot comparison of best and worst column for each column technology and a certain protein. Other conditions are the same as in Fig. 3. The figure legend provides the column brand name, pore size, total particle diameter, in brackets the shell thickness and the label L2 and L5 represent the column length of 20 and 50 mm, respectively.

the low speed region for the small proteins. The Acquity UHPLC protein BEH C4 column showed comparable performance for the small proteins but fell short, compared to BIOshell 400 Å, for the larger protein sizes. Even the SPP with the lowest performance, the Aeris Widepore C4 column, showed only a little worse performance and was still a good candidate for the separation of small proteins. The MAbPac RP column was clearly less favourable in terms of kinetic performance, yet since the 1500 Å pores are fully accessible even for larger proteins it may offer favourable interactive surface and selectivity depending on the protein mixture. The KPL-curves for the intact NISTmAb were considerably different compared to all smaller protein samples (Fig. 7g). The SPP AdvanceBIO RP mAb C4 had clearly the best performance, followed by the BIOshell 400 Å. The KPL-curve of the Aeris Widepore C4 (200 Å) largely matched the one of FPP Acquity UHPLC BEH protein C4 (300 Å). The shorter diffusion paths of the former might compensate for the favourable wider pores of the latter. As expected, the pore size of the Chromolith HR RP-18e is too small for protein separations resulting in recovery problems (vide supra). On the other hand, the Chromolith WP300 RP-18 was quite competitive to the best performing columns Acquity UHPLC BEH C4 (FPP) and BIOshell 400 Å (SPP) for the small proteins. For large proteins like mAbs the Chromolith WP300 RP-4 is the preferred choice and its KPL approximate the SPP (Aeris Widepore C4) and FPP columns (Acquity UHPLC BEH protein C4) with similar pore size. Major limitations of the monoliths were their low maximum pressure drop (originating mostly due to the fragile PEEK cladding) and the large total porosity. The maximum pressure limit for the Chromolith columns was at only 200 bar which was the lowest for all the 13 columns and effected the KPL curves through the rescaling factor λ. In spite of the low pressure limit, it was still possible to use a high flow rate of 1.5 mL/min due to the low column back pressure. Overall the SPP columns (BIOshell 400 Å and AdvanceBIO RP mAb C4) showed the best performance and the FPP Acquity UHPLC BEH C4 also an excellent performance for the small proteins and antibody fragments.

4. Conclusions

Gradient kinetic plots are a powerful tool for the evaluation of the column performance and can be conveniently applied even when they have distinct stationary phase morphologies. The current work provides an extended performance evaluation of new and relatively established modern columns for the separation of proteins. For that purpose, a set of proteins was used to cover a molecular weight range from 12.4 to 148 kDa and consisted of standard proteins (cytochrome c, lysozyme and β-lactoglobulin), an intact monoclonal antibody (NISTmAb) and its fragments after IdeS-digestion and disulphide reduction. Superficially porous particle (SPP) columns, in particular with thin shell, showed overall the best performance among all the tested columns due to their outstanding mass transfer kinetics in combination with the possibility to be used at ultra-high pressure. This enables their usage for ultra-fast separations what is a continuous demand from the (pharmaceutical) industry and important for full comprehensive two-dimensional liquid chromatography. In the fast separation regime, a thinner porous shell was outperforming wider pore size. A sub-2 µm fully porous particle (FPP) column and monolithic columns could compete with the superficially porous columns for small sized proteins but were clearly outperformed by the SPP column with thin shell for the analysis of the antibody and its fragments. Mass transfer resistance has the biggest contribution to band broadening especially at high flow rates, therefore, the diffusion path lengths must be reduced by using thin porous shell for SPP columns and reducing the particle size for FPPs. The pore size has a critical influence on the mass transfer kinetics and a value of around 400 Å seems to be optimal for a broad range of protein sizes but larger pore can be more beneficial if the diffusion path is longer. Monolithic columns benefit from a low column back pressure but due to their lower pressure stability they can be damaged more easily by ultra-high pressure systems. However, the selection of columns for protein separations should not solely be based on the kinetic performance but should also consider factors like protein recovery (adsorption), selectivity, silanol activity and temperature stability to mention a few. Overall, the current study may guide column selection for specific protein sizes.

Declaration of Competing Interest

The authors declared no conflicts of interest.

CRediT authorship contribution statement

Simon Jaag: Investigation, Methodology, Formal analysis, Visualization, Writing – original draft. **Chunmei Wen:** Investigation, Formal analysis, Visualization, Methodology, Writing – review & editing. **Benjamin Peters:** Methodology, Data curation, Writing – review & editing. **Michael Lämmerhofer:** Conceptualization, Methodology, Supervision, Writing – review & editing, Resources.

Acknowledgements

We thank Benjamin Peters from Merck KGaA, Darmstadt, Germany for generous gift of research samples of Chromolith columns.

Supplementary materials

Supplementary material associated with this article can be found, in the online version, at doi:10.1016/j.chroma.2022.463251.

References

[1] C. Morrison, Fresh from the biotech pipeline—2019, Nat. Biotechnol. 38 (2) (2020) 126–131, doi:10.1038/s41587-019-0405-7.

[2] G. Walsh, Biopharmaceutical benchmarks 2018, Nat. Biotechnol. 36 (12) (2018) 1136–1145, doi:10.1038/nbt.4305.

[3] A. Beck, E. Wagner-Rousset, D. Ayoub, A. Van Dorsselaer, S. Sanglier-Cianférani, Characterization of therapeutic antibodies and related products, Anal. Chem. 85 (2) (2013) 715–736, doi:10.1021/ac3032355.

[4] S. Fekete, A. Murisier, A. Beck, J. Lawhorn, H. Ritchie, B. Boyes, D. Guillarme, New wide-pore superficially porous stationary phases with low hydrophobicity applied for the analysis of monoclonal antibodies, J. Chromatogr. A 1642 (2021) 462050, doi:10.1016/j.chroma.2021.462050.

[5] D.V. McCalley, D. Guillarme, Evaluation of additives on reversed-phase chromatography of monoclonal antibodies using a 1000 Å stationary phase, J. Chromatogr. A (2019) 460562, doi:10.1016/j.chroma.2019.460562.

[6] S. Fekete, S. Rudaz, J.-L. Veuthey, D. Guillarme, Impact of mobile phase temperature on recovery and stability of monoclonal antibodies using recent reversed-phase stationary phases, J. Sep. Sci. 35 (22) (2012) 3113–3123, doi:10.1002/jssc.201200297.

[7] M.C. Garcıá, A.C. Hogenboom, H. Zappey, H. Irth, Effect of the mobile phase composition on the separation and detection of intact proteins by reversed-phase liquid chromatography–electrospray mass spectrometry, J. Chromatogr. A 957 (2) (2002) 187–199 https://doi.org/10.1016/S0021-9673(02)00345-X.

[8] S. Fekete, B. Bobály, J.M. Nguyen, A. Beck, J.-L. Veuthey, K. Wyndham, M.A. Lauber, D. Guillarme, Use of ultrashort columns for therapeutic protein separations. Part 1: theoretical considerations and proof of concept, Anal. Chem. 93 (3) (2021) 1277–1284, doi:10.1021/acs.analchem.0c04082.

[9] L.R. Snyder, M.A. Stadalius, M.A. Quarry, Gradient elution in reversed-phase HPLC-separation of macromolecules, Anal. Chem. 55 (14) (1983) 1412A–1430A, doi:10.1021/ac00264a001.

[10] B.M. Wagner, S.A. Schuster, B.E. Boyes, T.J. Shields, W.L. Miles, M.J. Haynes, R.E. Moran, J.J. Kirkland, M.R. Schure, Superficially porous particles with 1000 Å pores for large biomolecule high performance liquid chromatography and polymer size exclusion chromatography, J. Chromatogr. A 1489 (2017) 75–85, doi:10.1016/j.chroma.2017.01.082.

[11] W. Chen, K. Jiang, A. Mack, B. Sachok, X. Zhu, W.E. Barber, X. Wang, Synthesis and optimization of wide pore superficially porous particles by a one-step coating process for separation of proteins and monoclonal antibodies, J. Chromatogr. A 1414 (2015) 147–157, doi:10.1016/j.chroma.2015.08.043.

[12] S.A. Schuster, B.M. Wagner, B.E. Boyes, J.J. Kirkland, Optimized superficially porous particles for protein separations, J. Chromatogr. A 1315 (2013) 118–126, doi:10.1016/j.chroma.2013.09.054.

[13] D. Stoll, S. Fekete, D. Guillarme, Tips, tricks, and troubleshooting for separations of biomolecules, part i: contemporary reversed-phase protein separations, LCGC North Am. 36 (7) (2018) 440–446.

[14] K. Horváth, F. Gritti, J.N. Fairchild, G. Guiochon, On the optimization of the shell thickness of superficially porous particles, J. Chromatogr. A 1217 (41) (2010) 6373–6381, doi:10.1016/j.chroma.2010.08.013.

[15] J.L. Dores-Sousa, A. Fernández-Pumarega, J. De Vos, M. Lämmerhofer, G. Desmet, S. Eeltink, Guidelines for tuning the macropore structure of monolithic columns for high-performance liquid chromatography, J. Sep. Sci. 42 (2) (2019) 522–533, doi:10.1002/jssc.201801092.

[16] D. Cabooter, K. Broeckhoven, R. Sterken, A. Vanmessen, I. Vandendael, K. Nakanishi, S. Deridder, G. Desmet, Detailed characterization of the kinetic performance of first and second generation silica monolithic columns for reversed-phase chromatography separations, J. Chromatogr. A 1325 (2014) 72–82, doi:10.1016/j.chroma.2013.11.047.

[17] J.L. Dores-Sousa, J. De Vos, S. Eeltink, Resolving power in liquid chromatography: a trade-off between efficiency and analysis time, J. Sep. Sci. 42 (1) (2019) 38–50, doi:10.1002/jssc.201800891.

[18] T.J. Causon, K. Broeckhoven, E.F. Hilder, R.A. Shellie, G. Desmet, S. Eeltink, Kinetic performance optimisation for liquid chromatography: Principles and practice, J. Sep. Sci. 34 (8) (2011) 877–887, doi:10.1002/jssc.201000904.

[19] G. Desmet, D. Cabooter, K. Broeckhoven, Graphical data representation methods to assess the quality of LC columns, Anal. Chem. 87 (17) (2015) 8593–8602, doi:10.1021/ac504473p.

[20] K. Broeckhoven, D. Cabooter, F. Lynen, P. Sandra, G. Desmet, The kinetic plot method applied to gradient chromatography: theoretical framework and experimental validation, J. Chromatogr. A 1217 (17) (2010) 2787–2795, doi:10.1016/j.chroma.2010.02.023.

[21] S. Fekete, R. Berky, J. Fekete, J.-L. Veuthey, D. Guillarme, Evaluation of a new wide pore core–shell material (Aeris^{TM} WIDEPORE) and comparison with other existing stationary phases for the analysis of intact proteins, J. Chromatogr. A 1236 (2012) 177–188, doi:10.1016/j.chroma.2012.03.018.

[22] B. Bobály, M. Lauber, A. Beck, D. Guillarme, S. Fekete, Utility of a high coverage phenyl-bonding and wide-pore superficially porous particle for the analysis of monoclonal antibodies and related products, J. Chromatogr. A 1549 (2018) 63–76, doi:10.1016/j.chroma.2018.03.043.

[23] L. Nováková, A. Vaast, C. Stassen, K. Broeckhoven, M. De Pra, R. Swart, G. Desmet, S. Eeltink, High-resolution peptide separations using nano-LC at ultra-high pressure, J. Sep. Sci. 36 (7) (2013) 1192–1199, doi:10.1002/jssc.201201087.

[24] A. Vaast, K. Broeckhoven, S. Dolman, G. Desmet, S. Eeltink, Comparison of the gradient kinetic performance of silica monolithic capillary columns with columns packed with 3 μm porous and 2.7 μm fused-core silica particles, J. Chromatogr. A 1228 (2012) 270–275, doi:10.1016/j.chroma.2011.07.089.

[25] T. Hetzel, C. Blaesing, M. Jaeger, T. Teutenberg, T.C. Schmidt, Characterization of peak capacity of microbore liquid chromatography columns using gradient kinetic plots, J. Chromatogr. A 1485 (2017) 62–69, doi:10.1016/j.chroma.2017.01.018.

[26] J.W. Thompson, T.J. Kaiser, J.W. Jorgenson, Viscosity measurements of methanol–water and acetonitrile–water mixtures at pressures up to 3500 bar using a novel capillary time-of-flight viscometer, J. Chromatogr. A 1134 (1) (2006) 201–209, doi:10.1016/j.chroma.2006.09.006.

[27] Y. Zhang, X. Wang, P. Mukherjee, P. Petersson, Critical comparison of performances of superficially porous particles and sub-2 μm particles under optimized ultra-high pressure conditions, J. Chromatogr. A 1216 (21) (2009) 4597–4605, doi:10.1016/j.chroma.2009.03.071.

[28] M. Gilar, U.D. Neue, Peak capacity in gradient reversed-phase liquid chromatography of biopolymers: theoretical and practical implications for the separation of oligonucleotides, J. Chromatogr. A 1169 (1) (2007) 139–150, doi:10.1016/j.chroma.2007.09.005.

[29] S. Jaag, M. Shirokikh, M. Lämmerhofer, Charge variant analysis of protein-based biopharmaceuticals using two-dimensional liquid chromatography hyphenated to mass spectrometry, J. Chromatogr. A 1636 (2021) 461786, doi:10.1016/j.chrom.2020.461786.

[30] L. Konermann, D.J. Douglas, Unfolding of proteins monitored by electrospray ionization mass spectrometry: a comparison of positive and negative ion modes, J. Am. Soc. Mass. Spectrom. 9 (12) (1998) 1248–1254 https://doi.org/10.1016/S1044-0305(98)00103-2.

[31] I. Liko, J.T.S. Hopper, T.M. Allison, J.L.P. Benesch, C.V. Robinson, Negative ions enhance survival of membrane protein complexes, J. Am. Soc. Mass. Spectrom. 27 (6) (2016) 1099–1104, doi:10.1007/s13361-016-1381-5.

[32] K. Hormann, T. Müllner, S. Bruns, A. Höltzel, U. Tallarek, Morphology and separation efficiency of a new generation of analytical silica monoliths, J. Chromatogr. A 1222 (2012) 46–58, doi:10.1016/j.chroma.2011.12.008.

3.2.2 Supporting Information

Kinetic performance comparison of superficially porous, fully porous and monolithic reversed-phase columns by gradient kinetic plots for the separation of protein biopharmaceuticals

Simon Jaag[a], Chunmei Wen[a], Benjamin Peters[b], Michael Lämmerhofer[a],*

[a] Pharmaceutical (Bio-)Analysis, Institute of Pharmaceutical Sciences, University of Tübingen, Auf der Morgenstelle 8, 72076 Tübingen, Germany

[b] Instrumental Analytics R&D, Merck KGaA, Frankfurter Str. 250, 64293 Darmstadt, Germany

*Author for correspondence:

Prof. Dr. Michael Lämmerhofer
Pharmaceutical (Bio-)Analysis
Institute of Pharmaceutical Sciences
University of Tübingen
Auf der Morgenstelle 8
72076 Tübingen, Germany
T +49 7071 29 78793, F +49 7071 29 4565
E-mail: michael.laemmerhofer@uni-tuebingen.de

1. Determination of the S-values

The S-values of the protein samples for each column were calculated based on the DryLab screening runs at 60°C and 3 different gradient times (10, 20 and 30 min). The actual, experimental retention times of the proteins were transferred to an Excel file. Three gradient time-based steepness values ($\beta = t_{G1}/t_{G2}$) were obtained (20/30: 1.5; 10/20 = 2; 10/30 = 3). Retention time t_R can be predicted using the S- and log k_0-values based on equation S1 [1, 2]:

$$t_R = \frac{t_0}{b} * \log\left(2.3 * b * k_0 * \left(1 - \left(\frac{t_D}{t_0 * k_0}\right)\right) + 1\right) + \mathrm{t_0} + \mathrm{t_D} \qquad \text{(S 1)}$$

With t_0 as the column dead time, b as the gradient steepness (eq. S2), k_0 as the retention factor at the beginning of the gradient, t_D is the dwell time.

$$b = \frac{t_0 \Delta\varphi S}{t_G} \qquad \text{(S 2)}$$

With $\Delta\varphi$ as the difference of the modifier content.

$$S = \frac{b \cdot t_G}{t_0 \Delta\varphi} \qquad \text{(S 3)}$$

With t_G as the gradient time.

$$\log k_0 = \left[\frac{b(t_{R1} - t_0 - t_D)}{t_0}\right] - \log(2.3b) \qquad \text{(S 4)}$$

$$\log k_w = \log k_0 + S\varphi_0 \qquad \text{(S 5)}$$

The retention time can be predicted using equation S1 and different values of S- and k_0 can be evaluated using the Solver-Add in in Excel to find proper values with the smallest difference between the predicted and the experimental retention times.

2. Results and discussion

2.1 Protein sample properties

Table S 12: Molecular weights (MW), isoelectric points (p*I*) and grand average of hydropathy (GRAVY) of the standard proteins.

Protein	MW [Da]	p*I*	GRAVY[4]
Cytochrome c, equine heart	12,384	10.0-10.5	-0.902
Lysozyme, chicken white egg	14,307	11.35	-0.472
β-Lactoglobulin B, bovine	18,277	5.13	-0.162
Light chain	23,123.49	7.76[4]	-0.403
Fc/2-fragment	25,231.95[5]	7.16[4]	-0.601
Fd-fragment	25,684.85[6]	8.64[4]	-0.191
Bovine serum albumin (BSA)	66,430.3	4.7- 4.9	-0.475
Intact NISTmAb	148,199.3[7]	9.18	n/a

---

[4] Calculated by protparam from Expasy. Does not consider glycoforms

[5] G0F glycoform

[6] pyro-glutamate form

[7] G0F/Galp1F glycoform

2.2 Example chromatograms BIOshell column

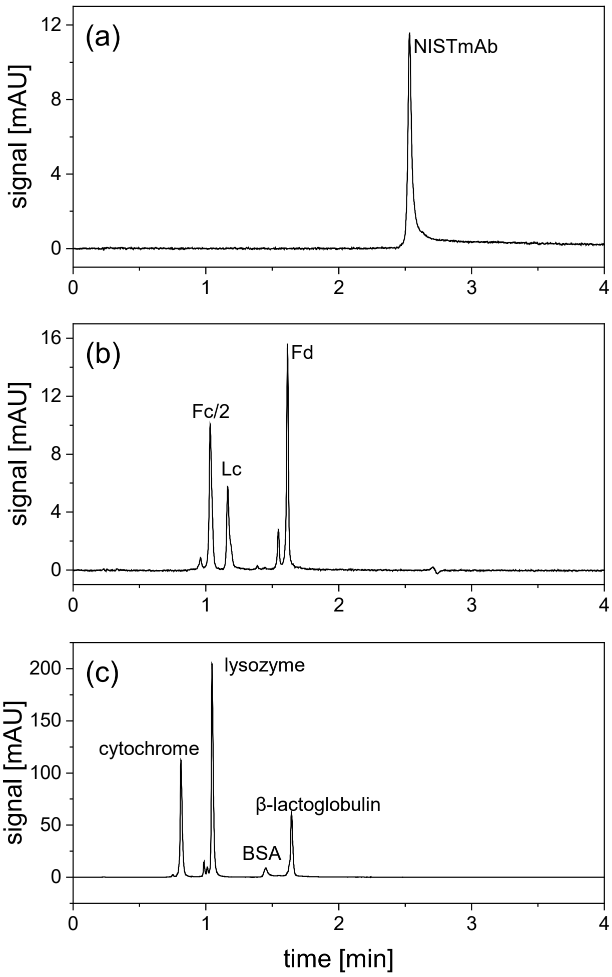

Fig. S 1: Example chromatograms of BIOshell 400Å column. (a) NISTmAb (peak capacity at kinetic performance limit: np = 277); (b) NIST-IdeS-TCEP (np: Fc/2 = 184, LC = 202, Fd = 288) and (c) protein mixture samples (np: cytochrome c = 211, lysozyme = 225, BSA = 109, β-lactoglobulin = 198). Column temperature = 60°C; flow rate = 0.5 mL/min; mobile phase A: 0.1% TFA in water, B: 0.1% TFA in ACN; gradient: 25-55% B; gradient time set to keep $S \cdot \beta \cdot t0 = 2$ constant: (a) 5.03 min (b) 2.77 min and (c) 2.35 min.

2.3 Column permeability and flow resistance

The flow resistance Φ and the column permeability K_v was determined for the superficially and fully porous particle columns at several different flow rates and a mobile phase composition of 20 % ACN at 50°C. The column permeability was calculated based on the superficial velocity u_s using Darcy's law and the column pressure ΔP_{column} drop after subtracting the system back pressure.

$$K_v = \frac{u_S \cdot \eta \cdot L}{\Delta P_{column}} \tag{S-6}$$

Where η is the mobile phase viscosity (in this case 0.60 cP for 20 % ACN at 50°C) and L the column length.

Based on the particle diameter d_p and K_v the flow resistance is given by:

$$\phi = \frac{d_p^2}{K_v} \tag{S-7}$$

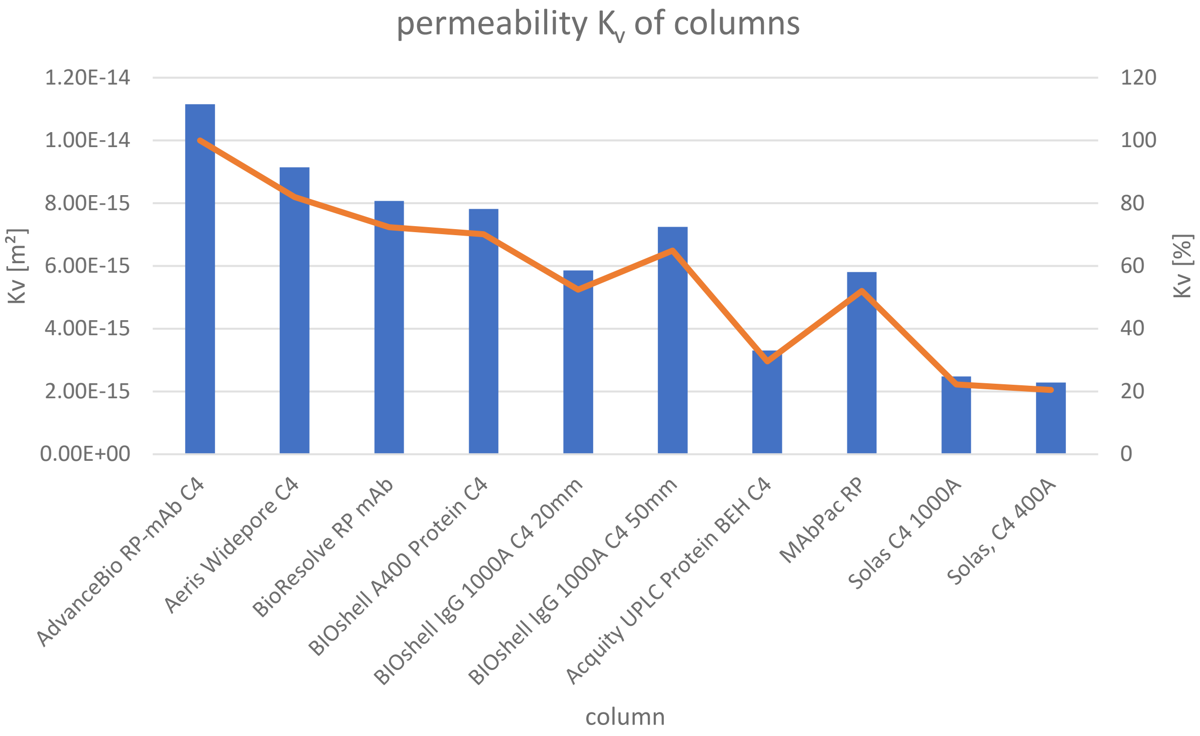

Fig. S 2: Column permeability comparison of the superficially and fully porous particle columns. The blue bars represent the absolute permeability while the orange line (right hand y-axis) shows the normalized permeability with 100 % for the highest permeability value.

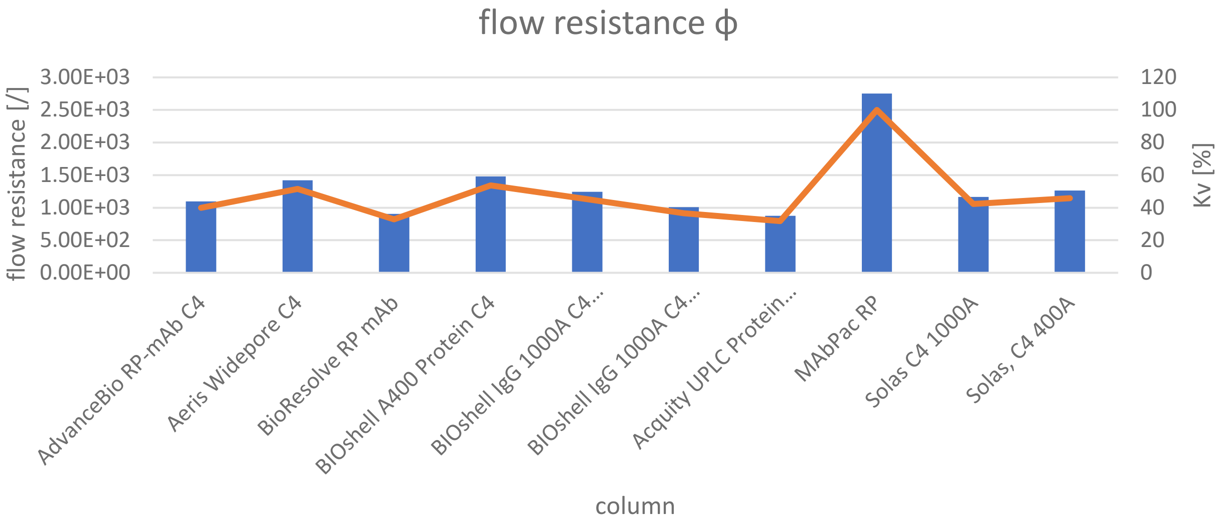

Fig. S 3: Column flow resistance comparison of the superficially and fully porous particle columns. The blue bars represent the absolute flow resistance while the orange line (right hand y-axis) shows the normalized flow resistance with 100 % for the highest permeability value.

2.4 Evaluation of superficially porous particle columns

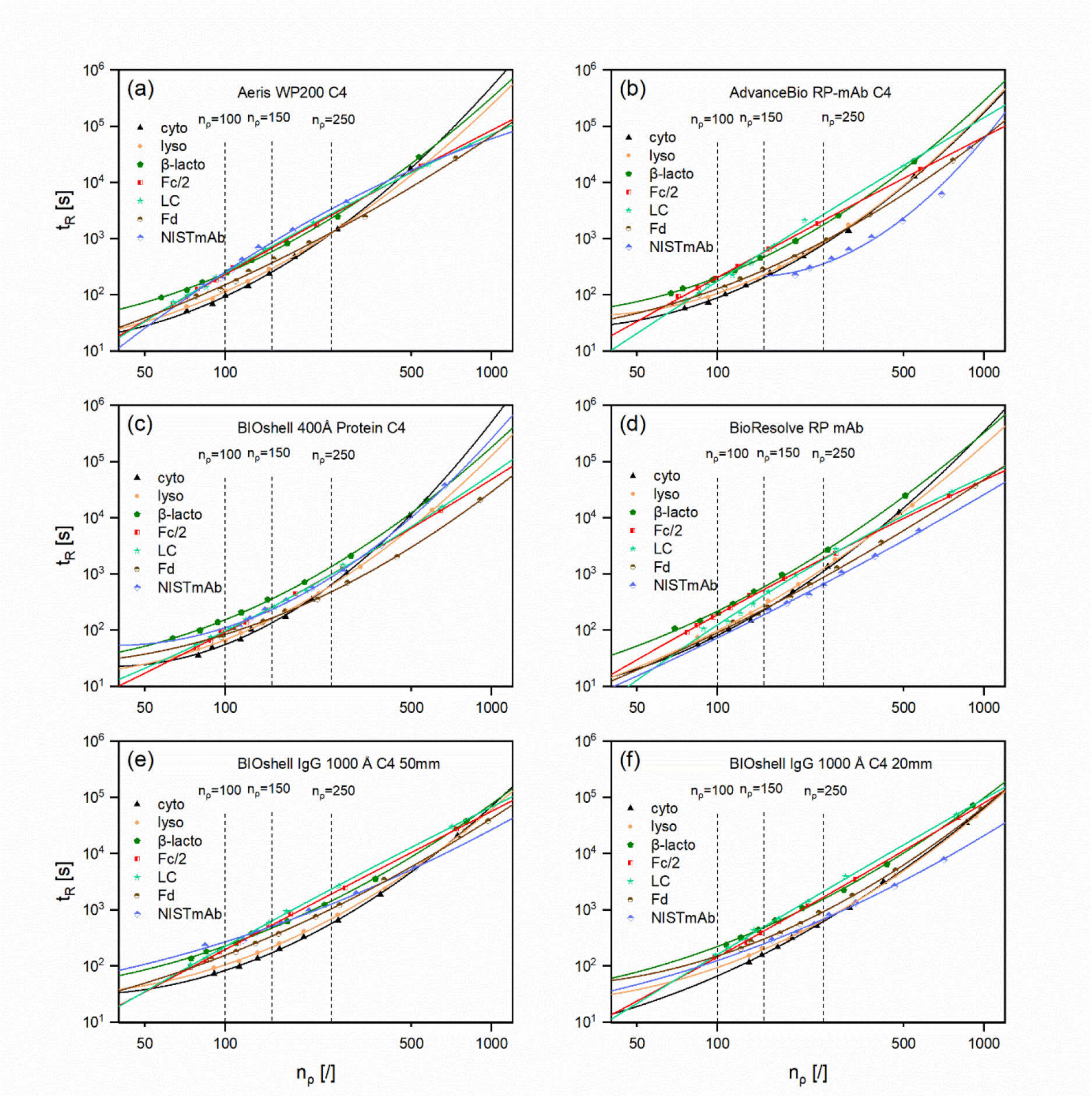

Fig. S 4: Gradient kinetic plots for the same superficially porous particle column and different proteins. Columns: (a) Aeris WP200 C4, (b) AdvanceBio RP-mAb C4, (c) BIOshell A400 Protein C4, (d) BioResolve RP mAb, (e) BIOshell IgG 1000A C4 50mm, (f) BIOshell IgG 1000A C4 20mm. Column temperature = 60°C, mobile phase A: 0.1% (v/v) TFA in water, B: 0.1% (v/v) TFA in ACN; gradient: 25-55% B; 8 flow rates were used according to the columns maximum pressure limit and the gradient time adjusted to keep $S{\cdot}\beta{\cdot}t_0$ = 2 constant.

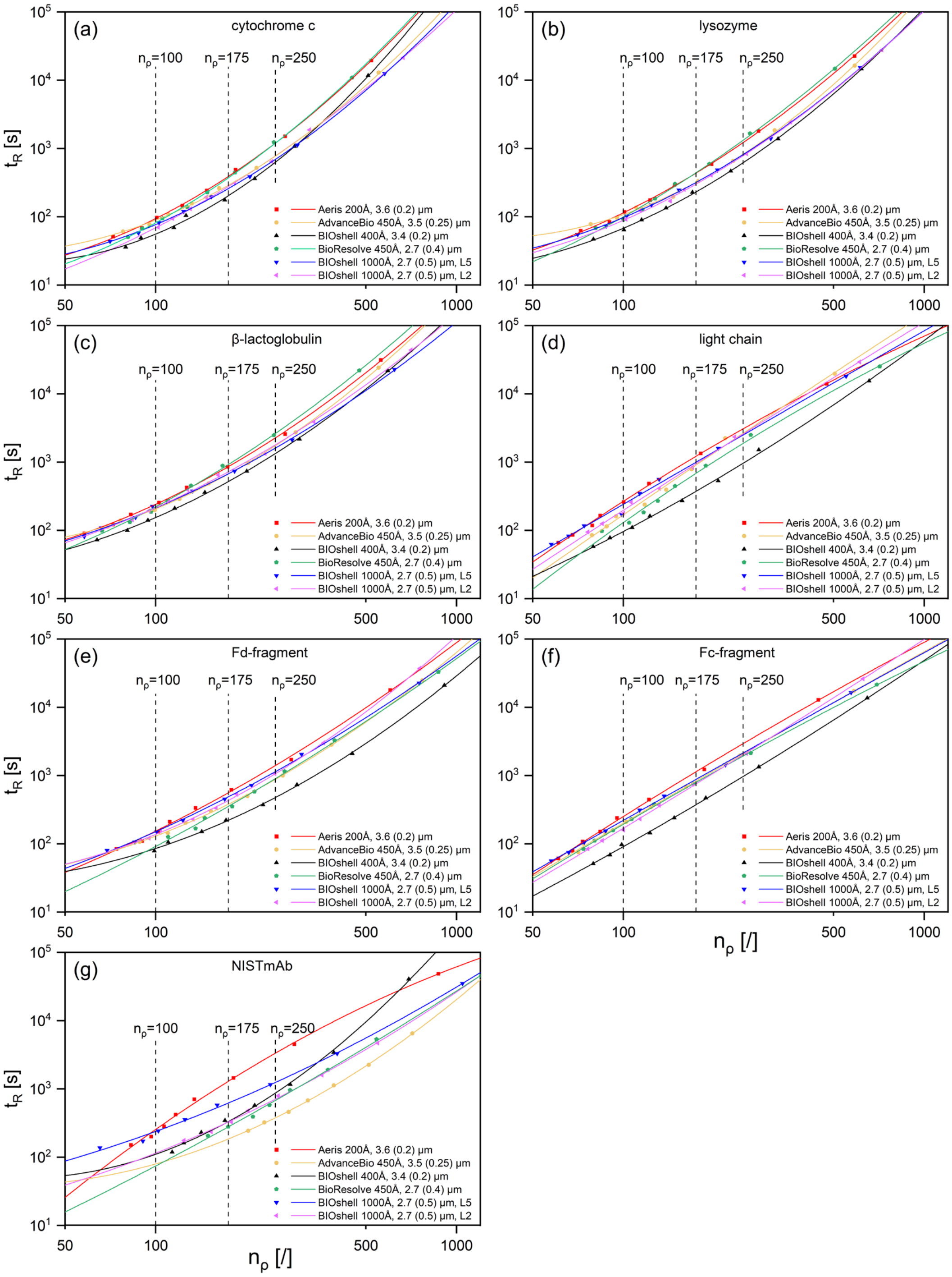

Fig. S 5: Gradient kinetic plots for the same protein and different superficially porous particle columns at same maximum pressure limit (600 bar). (a) Cytochrome c, (b) lysozyme, (c) β-lactoglobulin, (d) light chain, (e) Fd-fragment, (f) Fc/2-fragment, (g) NIST mAb. Column temperature = 60°C, mobile phase A: 0.1% (v/v) TFA in water, B: 0.1% (v/v) TFA in ACN; gradient: 25-55% B; 8 flow rates were used according to the columns maximum pressure limit and the gradient time adjusted to keep S·β·t0 = 2 constant. The figure legend provides the column brand name, pore size, total particle diameter, in brackets the shell thickness and the label L2 and L5 represent the column length of 20 and 50 mm, respectively.

2.5 Evaluation of fully porous particle columns

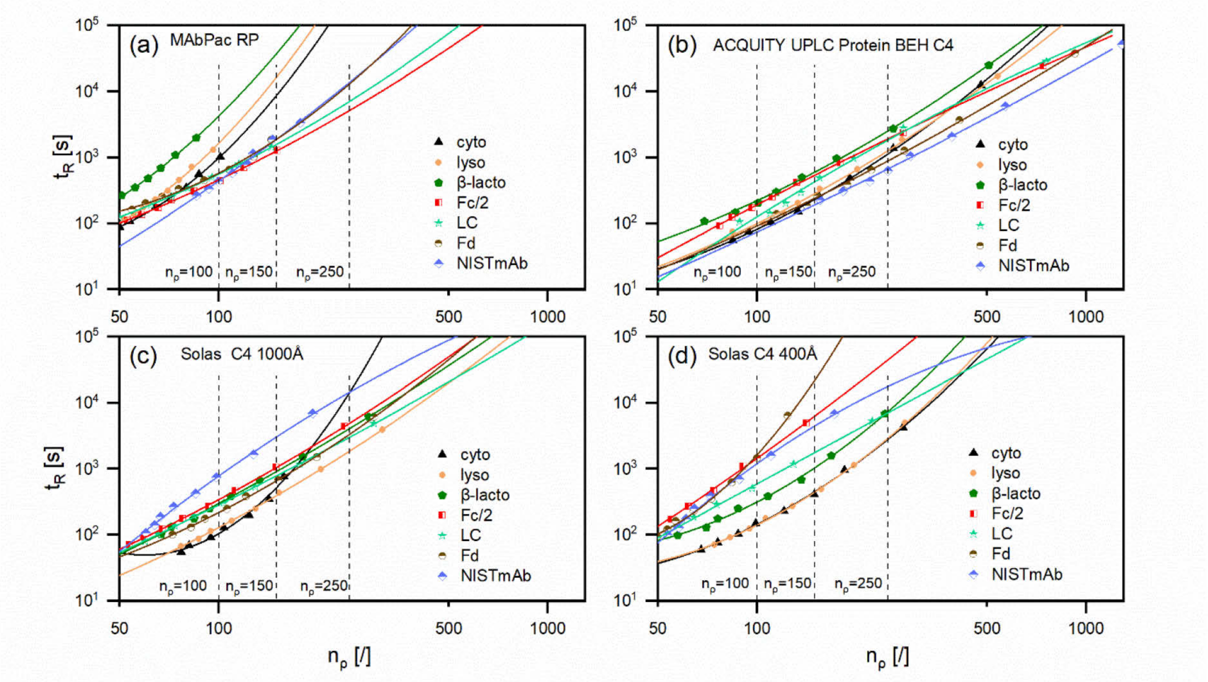

Fig. S 6: Gradient kinetic plots for the same fully porous particle column and different proteins. Columns: (a) MAbPac RP, (b) ACQUITY UPLC Protein BEH C4, (c) Solas C4 1000Å, (d) Solas C4 400Å. Column temperature = 60°C, mobile phase A: 0.1% (v/v) TFA in water, B: 0.1% (v/v) TFA in ACN; gradient: 25-55% B; 8 flow rates were used according to the columns maximum pressure limit and the gradient time adjusted to keep $S \cdot \beta \cdot t_0 = 2$ constant.

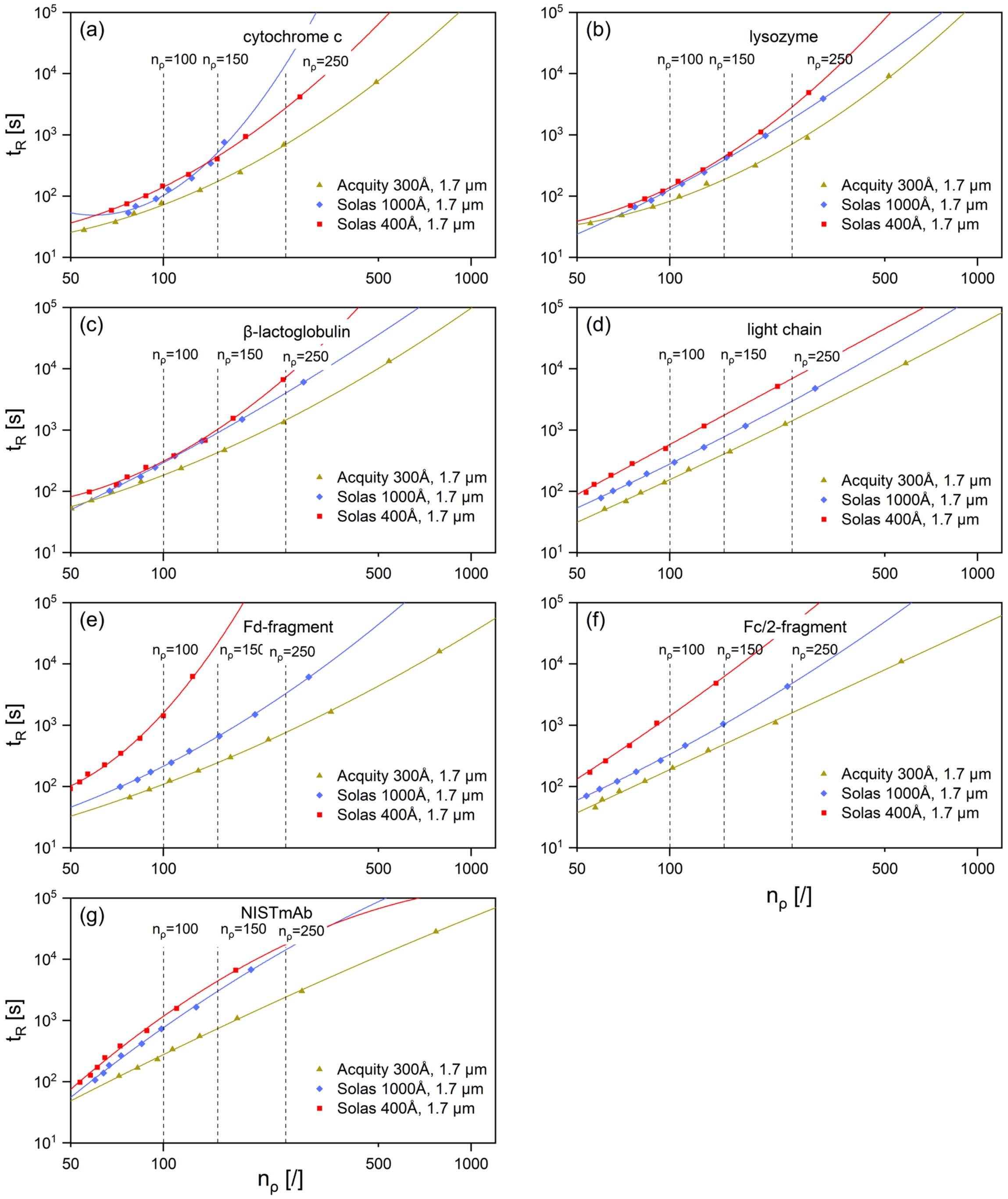

Fig. S 7: Gradient kinetic plots for the same protein and different fully porous particle columns at the same pressure limit (700 bar). (a) Cytochrome c, (b) lysozyme, (c) β-lactoglobulin, (d) light chain, (e) Fd-fragment, (f) Fc/2-fragment, (g) NIST mAb. Other conditions are the same as in Fig. 3. The figure legend provides the column brand name, pore size and total particle diameter.

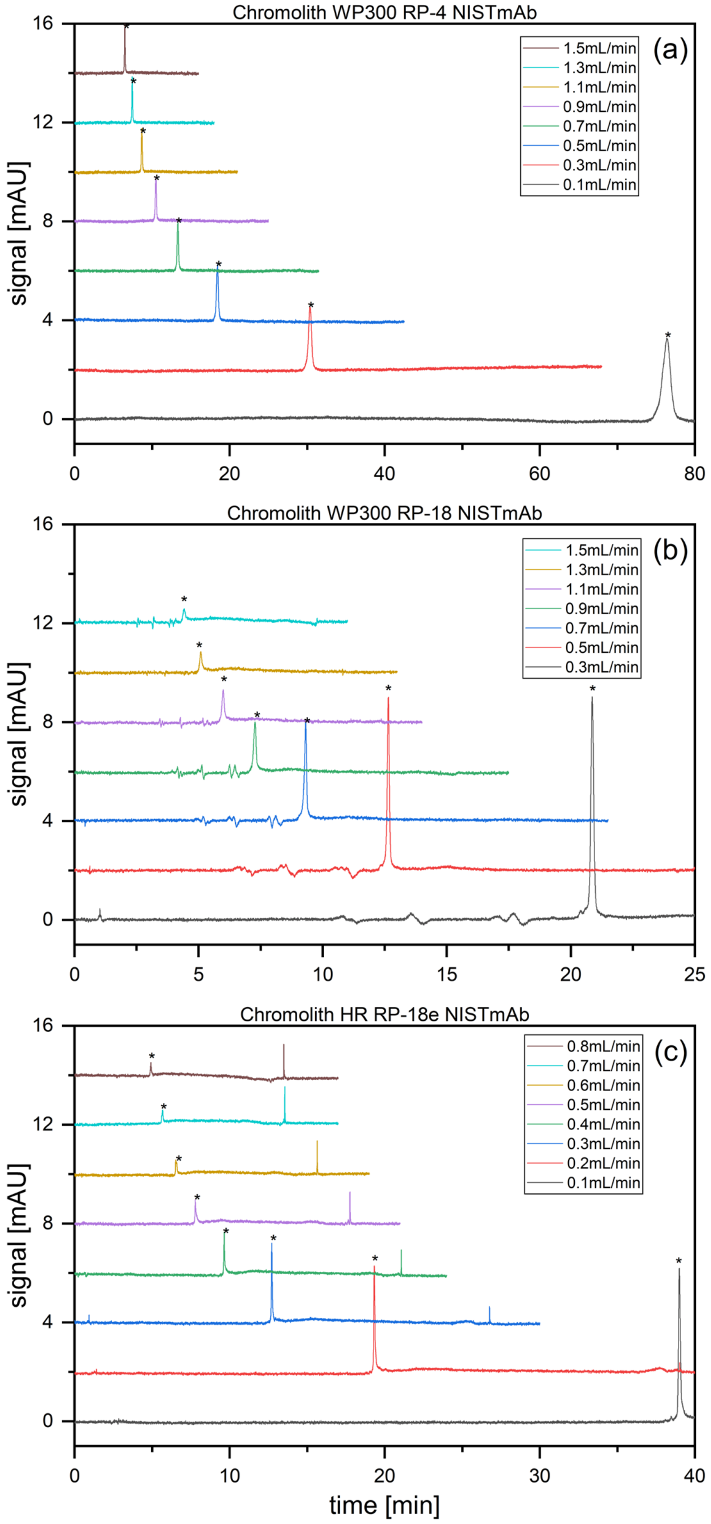

Fig. S 8: Chromatograms of the monolithic columns for the NISTmAb sample at different flow rates. (a) Chromolith WP300 RP-4, (b) Chromolith WP300 RP-18, (c) Chromolith HR RP-18e. Column temperature = 60°C, mobile phase A: 0.1% (v/v) TFA in water, B: 0.1% (v/v) TFA in ACN; gradient: 25-55% B; UV at 280 nm; 8 flow rates were used according to the columns maximum pressure limit and the gradient time adjusted to keep $S \cdot \beta \cdot t_0 = 2$ constant.

2.6 Evaluation of monolithic columns

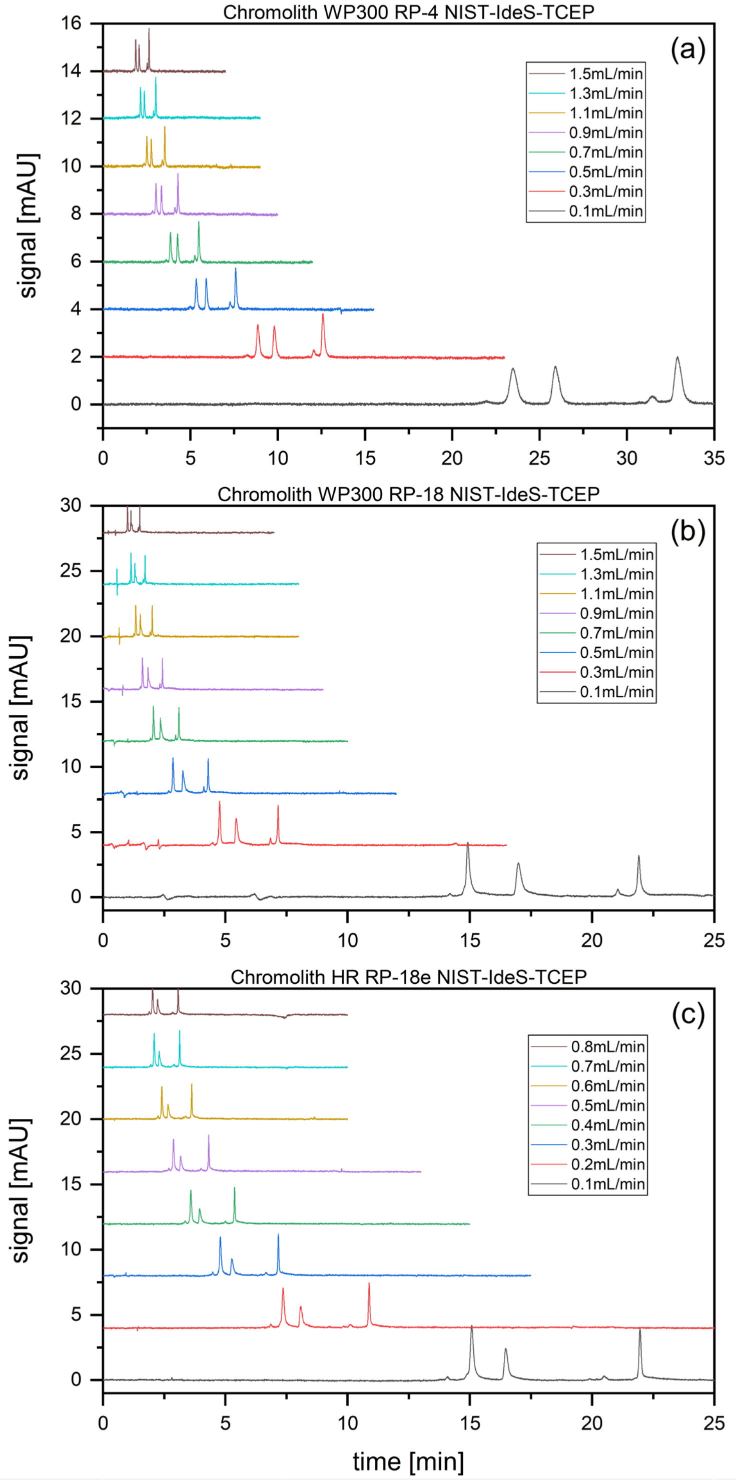

Fig. S 9: Chromatograms of the monolithic columns for the NIST-IdeS-TCEP sample at different flow rates. (a) Chromolith WP300 RP-4, (b) Chromolith WP300 RP-18, (c) Chromolith HR RP-18e. Column temperature = 60°C, mobile phase A: 0.1% (v/v) TFA in water, B: 0.1% (v/v) TFA in ACN; gradient: 25-55% B; UV at 280 nm; 8 flow rates were used according to the columns maximum pressure limit and the gradient time adjusted to keep $S \cdot \beta \cdot t_0$ = 2 constant.

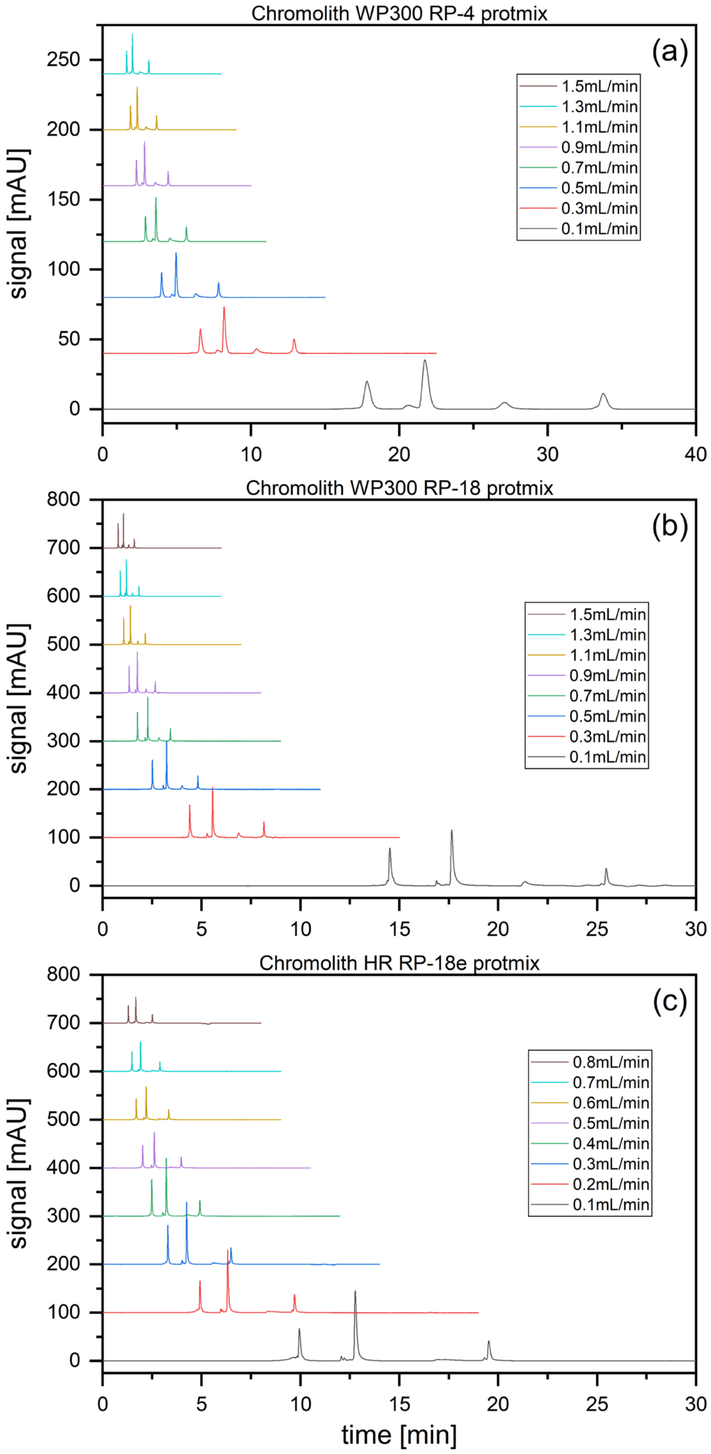

Fig. S 10: Chromatograms of the monolithic columns for the protmix sample at different flow rates. (a) Chromolith WP300 RP-4, (b) Chromolith WP300 RP-18, (c) Chromolith HR RP-18e. Column temperature = 60°C, mobile phase A: 0.1% (v/v) TFA in water, B: 0.1% (v/v) TFA in ACN; gradient: 25-55% B; UV at 280 nm; 8 flow rates were used according to the columns maximum pressure limit and the gradient time adjusted to keep $S \cdot \beta \cdot t_0 = 2$ constant.

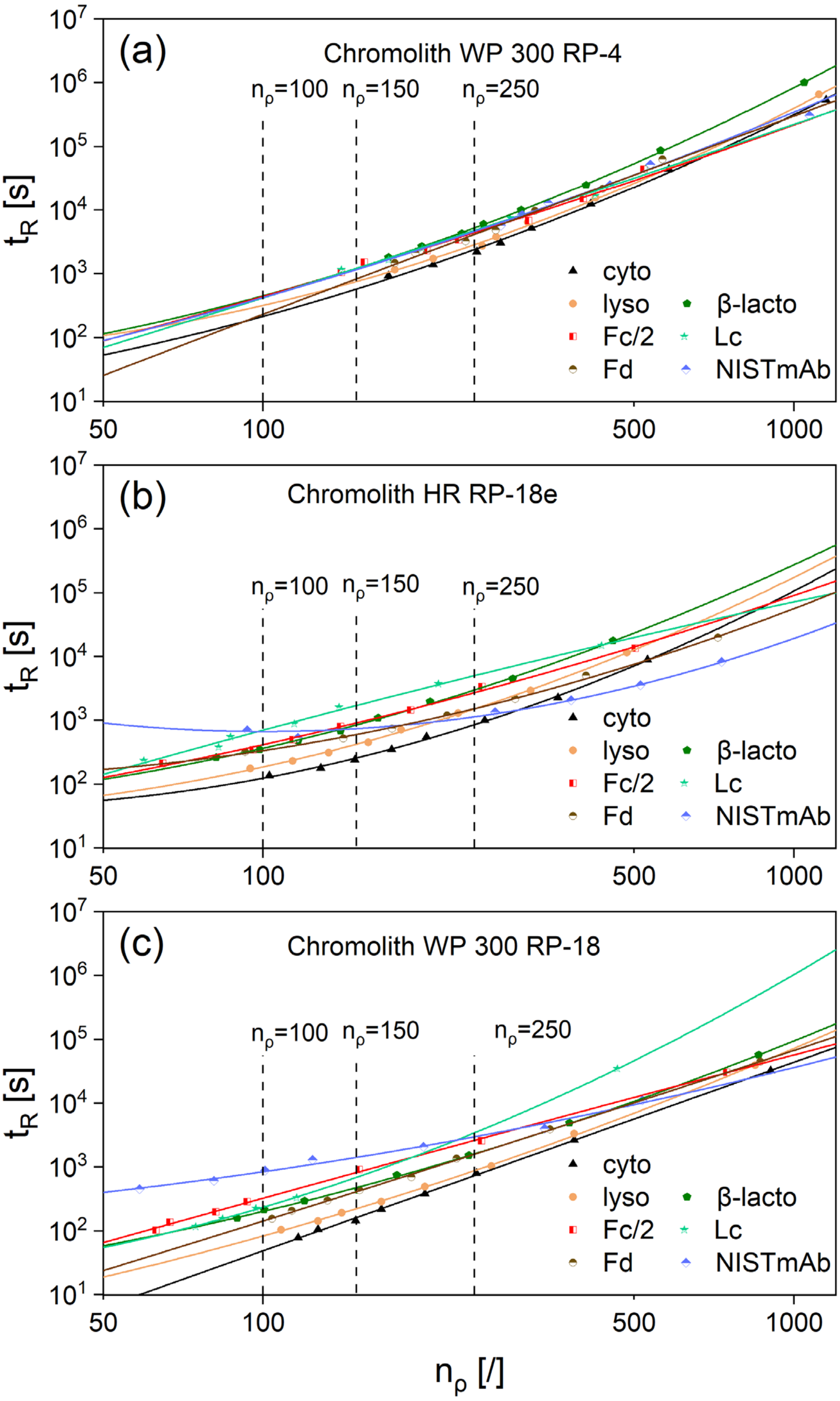

Fig. S 11: Gradient kinetic plots for the same monolithic column and different proteins. Columns: (a) Chromolith WP 300 RP-4, (b) Chromolith HR RP-18e, (c) Chromolith WP 300 RP-18. Column temperature = 60°C; mobile phase A: 0.1% (v/v) TFA in water, B: 0.1% (v/v) TFA in ACN; gradient: 25-55% B; 8 flow rates were used according to the columns maximum pressure limit and the gradient time adjusted to keep $S \cdot \beta \cdot t_0$ = 2 constant.

2.7 The columns pore size influence

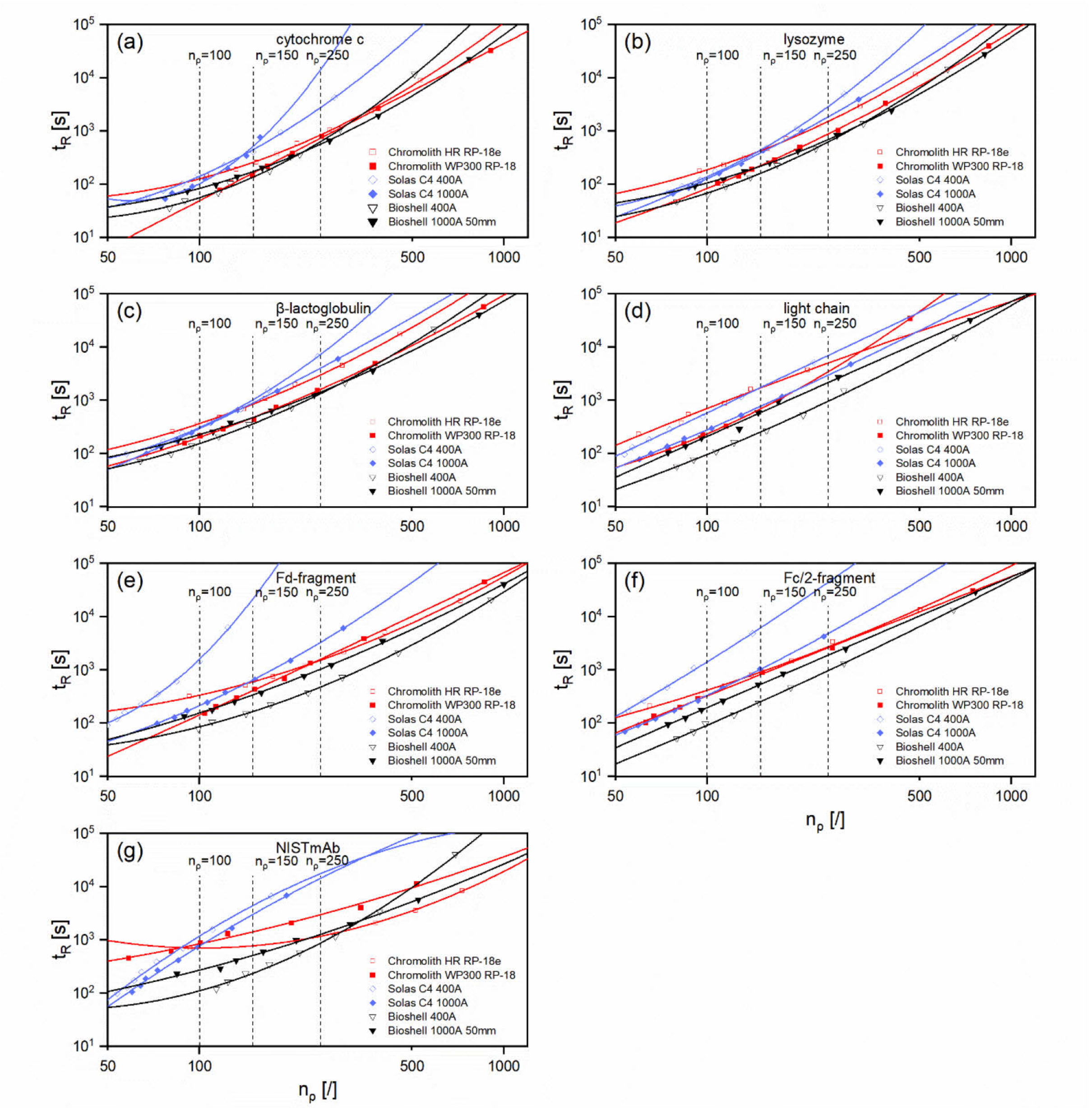

Fig. S 12: Gradient kinetic plots for pore size comparison of the same stationary phase columns. (a) Cytochrome c, (b) lysozyme, (c) β-lactoglobulin, (d) light chain, (e) Fd-fragment, (f) Fc/2-fragment, (g) NIST mAb. Column temperature = 60°C, mobile phase A: 0.1% (v/v) TFA in water, B: 0.1% (v/v) TFA in ACN; gradient: 25-55% B; 8 flow rates were used according to the columns maximum pressure limit and the gradient time adjusted to keep $S \cdot \beta \cdot t_0 = 2$ constant.

The pore size is a key parameter for protein separations and will be discussed in this chapter in a more detailed way by direct comparisons of columns which mainly vary in their pore size. Three column pairs were selected for each column technology and the KPL-curves were plotted (**Fig. S 12**).The BIOshell 400 Å column was superior to the BIOshell 1000 Å column especially at high flow rates (low retention times) for the standard protein samples (**Fig. S 12a-c**) while at lower flow rates (high t_R) a higher peak capacity can be achieved with the 1000 Å column. With the NISTmAb fragments as sample, the 400 Å SPP column outperformed the 1000 Å one over the entire tested flow rate range (**Fig. S 12d-f**). The outstanding performance of the BIOshell 400 Å can be explained by the lower mass transfer contribution which is a consequence of the low shell thickness (0.2 µm). The pore size of 400 Å seems to be sufficient even for the 148 kDa large NISTmAb what is in agreement with the literature that described this pore size as suitable for proteins with a molecular weight up to 500 kDa [3, 4]. At lower flow rates the BIOshell 1000 Å (0.5 µm shell thickness) could achieve higher peak capacities for some proteins (**Fig. S 12a-c, g**) probably because the longer diffusion distances were not limiting the performance anymore because there was enough time for diffusional mass transfer. The two Solas columns showed the opposite pore size effect. The Solas 1000 Å column was superior over the entire tested flow rate range for all proteins except cytochrome c, where only at higher flow rates the 1000 Å column was better. This trend can again be explained by mass transfer resistance but as the Solas columns are fully porous, the diffusion path length was the same as the particle size which was for both columns 1.7 µm. Here the bigger pore size of 1000 Å could be beneficial because the pore diffusion should be less hindered for larger pores. The two monolithic columns Chromolith WP300 RP-18 and the research sample Chromolith HR RP-18e differed mainly in their pore size structure and domain size (**Table 3**). The widepore (WP300) column had a mesopore size of 300 Å while the high-resolution research sample HR RP-18e had only a mesopore size of 150 Å. Furthermore, their macropore size as well as domain size differed, which were both lower for the Chromolith HR. The widepore Chromolith column showed a better performance for the small proteins (**Fig. S 12a-c**) and the Fc/2-fragment (**Fig. S 12f**) over the entire tested flow rate range. The main reason for the lower performance of the high-resolution column was the low mesopore size which will lead to hindered diffusion into the pores. Although the Chromolith HR RP-18e column pretends a better performance for the

NISTmAb sample, this performance is not real as the pores are most likely not penetrated and the recovery is extremely low, emphasizing once more that the mesopore size of 150 Å is too small for protein separations as expected.

3. References

[1] X. Wang, D.R. Stoll, A.P. Schellinger, P.W. Carr, Peak Capacity Optimization of Peptide Separations in Reversed-Phase Gradient Elution Chromatography: Fixed Column Format, Anal. Chem. 78(10) (2006) 3406-3416. https://doi.org/10.1021/ac0600149.

[2] J.J.K. LLoyd R. Snyder, John W. dolan, INTRODUCTION TO MODERN LIQUID CHROMATOGRAPHY, Third Edition ed., Wiley, Hoboken, New Jersey, 2010.

[3] W. Chen, K. Jiang, A. Mack, B. Sachok, X. Zhu, W.E. Barber, X. Wang, Synthesis and optimization of wide pore superficially porous particles by a one-step coating process for separation of proteins and monoclonal antibodies, J. Chromatogr. A 1414 (2015) 147-157. https://doi.org/https://doi.org/10.1016/j.chroma.2015.08.043.

[4] S.A. Schuster, B.M. Wagner, B.E. Boyes, J.J. Kirkland, Optimized superficially porous particles for protein separations, J. Chromatogr. A 1315 (2013) 118-126. https://doi.org/https://doi.org/10.1016/j.chroma.2013.09.054.

3.3 Publication III: **Revisiting a challenging p53 binding site: a diversity-optimized HEFLib reveals diverse binding modes in T-p53C-Y220C**

Jason Stahlecker[a], Theresa Klett[a], Martin Schwer[a], Simon Jaag[b],

Marcel Dammann[a], Larissa N. Ernst[a], Michael B. Braun[c],

Markus O. Zimmermann[a], Markus Kramer[d], Michael Lämmerhofer[b], Thilo Stehle[c],

Murray Coles[e] and Frank M. Boeckler*[af]

[a] Lab for Molecular Design & Pharm. Biophysics, Institute of Pharmaceutical Sciences, Department of Pharmacy and Biochemistry, Eberhard Karls Universität Tübingen, Auf der Morgenstelle 8, 72076 Tübingen, Germany.
E-mail: frank.boeckler@uni-tuebingen.de
[b] Institute of Pharmaceutical Sciences, Pharmaceutical (Bio-)Analysis, University of Tübingen, Auf der Morgenstelle 8, 72076, Tübingen, Germany
[c] Interfaculty Institute of Biochemistry, Eberhard Karls Universität Tübingen, Auf der Morgenstelle 34, 72076 Tübingen, Germany
[d] Institute of Organic Chemistry, Eberhard Karls Universität Tübingen, Auf der Morgenstelle 18, 72076 Tübingen, Germany
[e] Department of Protein Evolution, Max Planck Institute for Biology Tübingen, Max-Planck-Ring 5, 72076 Tübingen, Germany
[f] Interfaculty Institute for Biomedical Informatics (IBMI), Eberhard Karls Universität Tübingen, Sand 14, 72076 Tübingen, Germany

*Author for correspondence:

E-Mail address: frank.boeckler@uni-tuebingen.de (F. Boeckler)

Reprinted with permission from RSC Medicinal Chemistry, 2022, 13 (12), 1575

DOI: 10.1039/d2md00246a

RSC
Medicinal Chemistry

RESEARCH ARTICLE

View Article Online
View Journal

Cite this: DOI: 10.1039/d2md00246a

Revisiting a challenging p53 binding site: a diversity-optimized HEFLib reveals diverse binding modes in T-p53C-Y220C

Jason Stahlecker, [a] Theresa Klett, [a] Martin Schwer,[a] Simon Jaag,[b] Marcel Dammann,[a] Larissa N. Ernst,[a] Michael B. Braun, [c] Markus O. Zimmermann,[a] Markus Kramer,[d] Michael Lämmerhofer,[b] Thilo Stehle,[c] Murray Coles [e] and Frank M. Boeckler *[af]

Received 24th July 2022,
Accepted 5th September 2022

DOI: 10.1039/d2md00246a

rsc.li/medchem

The cellular tumor antigen p53 is a key component in cell cycle control. The mutation Y220C heavily destabilizes the protein thermally but yields a druggable crevice. We have screened the diversity-optimized halogen-enriched fragment library against T-p53C-Y220C with STD-NMR and DSF to identify hits, which we validated by $^{1}H,^{15}N$-HSQC NMR. We could identify four hits binding in the Y220C cleft, one hit binding covalently and four hits binding to an uncharacterized binding site. Compound 1151 could be crystallized showing a flip of C220 and thus opening subsite 3. Additionally, 4482 was identified to alkylate cysteines. Data shows that the diversity-optimized HEFLib leads to multiple diverse hits. The identified scaffolds can be used to further optimize interactions with T-p53C-Y220C and increase thermal stability.

1 Introduction

The cellular tumor antigen p53 plays a crucial role in cell cycle regulation.[1] Upregulation can lead to *e.g.* cell cycle arrest and apoptosis.[2,3] p53 acts as a tumor suppressor and is most frequently inactivated in cancer either through direct mutation of p53 or through perturbation of its associated pathways. As a consequence, reactivation of p53 function in tumors is perceived as a prime target for therapeutic intervention.[4–8]

The low thermal stability makes handling and thus research of p53 and/or the DNA binding domain (p53C, residues 94–312) challenging. A quadruple mutant (M133L/V203A/N239Y/N268D) was designed, increasing thermal stability by about 5.6 °C.[9] This thermally stabilized mutant, commonly called "T-p53", has become a standard for biophysical experiments.

The mutation Y220C, located in the core domain, is one of the well-known hotspots.[10] The substitution of tyrosine to cysteine thermally destabilizes the core domain by about 8 °C.[11] However, this mutation yields a small, hydrophobic cleft. Early work in targeting this Y220C cavity has yielded a carbazole derivate, PK083 that stabilizes T-p53C-Y220C by

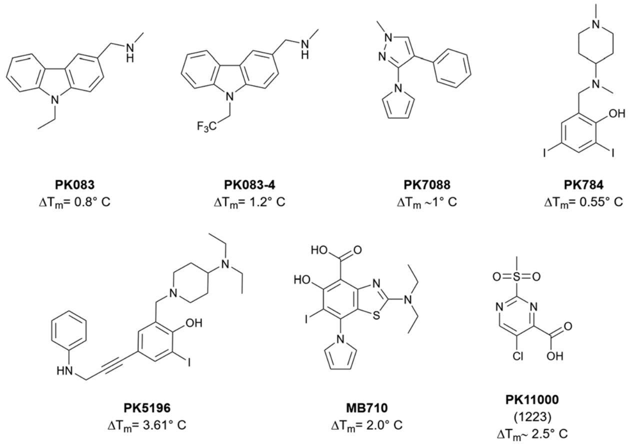

Fig. 1 An exemplary selection of published T-p53C-Y220C binders.[12–17] Compounds PK083 and PK784 occupy the central cavity and subsite 1, while PK5196, PK7088 and MB710 additionally bind subsite 2. The pyrrole group of PK784 and MB710 also enables them to engage to the deep subsite 3. PK11000 showed covalent addition to multiple cysteines.

---

[a] *Lab for Molecular Design & Pharm. Biophysics, Institute of Pharmaceutical Sciences, Department of Pharmacy and Biochemistry, Eberhard Karls Universität Tübingen, Auf der Morgenstelle 8, 72076 Tübingen, Germany. E-mail: frank.boeckler@uni-tuebingen.de*

[b] *Institute of Pharmaceutical Sciences, Pharmaceutical (Bio-)Analysis, University of Tübingen, Auf der Morgenstelle 8, 72076, Tübingen, Germany*

[c] *Interfaculty Institute of Biochemistry, Eberhard Karls Universität Tübingen, Auf der Morgenstelle 34, 72076 Tübingen, Germany*

[d] *Institute of Organic Chemistry, Eberhard Karls Universität Tübingen, Auf der Morgenstelle 18, 72076 Tübingen, Germany*

[e] *Department of Protein Evolution, Max Planck Institute for Biology Tübingen, Max-Planck-Ring 5, 72076 Tübingen, Germany*

[f] *Interfaculty Institute for Biomedical Informatics (IBMI), Eberhard Karls Universität Tübingen, Sand 14, 72076 Tübingen, Germany*

0.8 °C (125 μM cmpd. conc.).[12] Trifluorination at the *N*-ethyl anchor of PK083 improved the stabilization to 1.2 °C (125 μM cmpd. conc.) by benefiting from multipolar interactions and fluorine–sulfur contacts.[13] This compound and other selected are depicted in Fig. 1.

Quantum chemical analysis of the cavity showed that Leu145 can be addressed by halobenzene moieties, which initially led to the design of a halogen-enriched fragment library.[14] The 2,4-diiodophenol derivative PK784 was identified and crystallized, showing that a halogen bond with Leu145 as postulated is formed. Also, the compound increases the melting temperature by 0.55 °C (250 μM cmpd. conc.). Optimization of this scaffold led to PK5196, stabilizing T-p53C-Y220C by 3.61 °C (250 μM cmpd. conc.) using an acetylene linker to extend into subsite 2, illustrated in Fig. 2.[14]

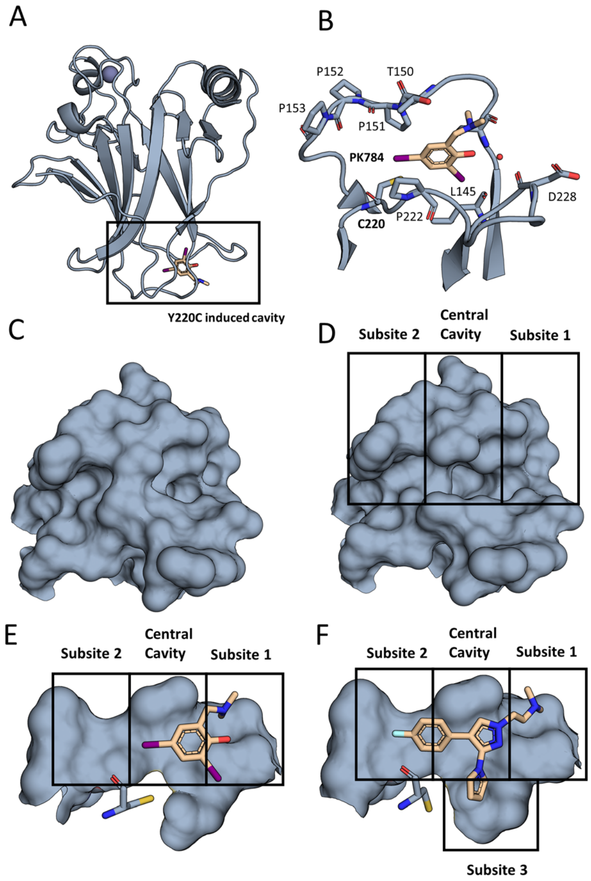

Fig. 2 The Y220C mutation leads to a druggable cleft. (A) Overall view of T-p53C-Y220C bound to PK784 (4AGL[14]). The location of the mutation is highlighted, leading to a druggable cleft. (B) PK784 engages in a halogen bond with L145. The other iodine points towards subsite 2 and can be used as vector for ligand growing. (C) Surface representation of Y220 and surrounding amino acids in T-p53C (1UOL[18]). (D) The mutation opens the central cavity, connecting subsite 1 and subsite 2 (4AGL[14]). (E) The lower part of the cleft is not targeted as C220 points towards the compound. (F) Upon binding of an electron rich group, *e.g.* pyrrole in PK7242, the cysteine is displaced enlarging subsite 3 and enabling targeting (3ZME[15]).

Later efforts identified PK7088 from a fragment library as a Y220C cleft binder, bearing a different scaffold. Interestingly, the pyrrole sidechain of this compound points into a deep internal cavity (subsite 3, Fig. 2) formed by a flip of C220, leading to a stabilization of 1 °C (350 μM cmpd. conc.).[15]

Based on this discovery, the aminobenzothiazole derivative MB710 was synthesized, linking the diiodophenol scaffold to the pyrrolo sidechain. This structure yields a thermal stabilization by 2 °C (250 μM cmpd. conc.).[16]

These promising results were the basis for the design of a diversity-optimized halogen-enriched fragment library (HEFLib).[19] In this generalized HEFLibs approach, aiming for a collection of chemical probes for investigating halogen bonding by fragment-based drug discovery,[20] library design and selection principles became independent from the initial target-focused approach.[14] From kinase drug discovery, we learned that molecular design of halogen bonds at an advanced state of the lead optimization process can be quite challenging and does not necessarily reach its full potential to improve ligand affinities.[21] Thus, we concluded that focusing on the earliest stages of the drug discovery process by generalizing our HEFLib's strategy can also provide the chance to establish unconventional binding modes based on specific halogen bonding motifs and allows to harness the chemotypes of such hits as novel lead structures with great impact on patentability.[19,20] As the design was led by diversity and limited by availability, only 14 of the 191 compounds contain an iodine. This also means that compounds with strongly tuning groups were not specifically selected. The compounds based on PK784 on the other hand contain an iodine and a positive charge, leading to strong tuning effects.[22]

In principle, there is a multitude of suitable electron-rich interaction partners for accepting a halogen bond in a typical binding site:[23] the backbone carbonyl,[24,25] the peptide bond,[26] the sulfur of methionine[27] or cysteine, the nitrogen of histidine,[28] the oxygen of the hydroxyl group of serine, threonine or tyrosine, the carboxamides of asparagine and glutamine, as well as the carboxylates of aspartate and glutamate,[29] and the π-systems of phenylalanine, tyrosine, tryptophan, or histidine.

Based on this abundance of interaction partners and the different construction of the generalized HEFLib, we deemed it an interesting experiment to revisit the challenging binding site of T-p53C-Y220C with such an unbiased library. It is noteworthy that this diversity-optimized HEFLib has been thoroughly tested and characterized, resulting in many different hits on various targets.[30–32]

Another approach for stabilization was identified by covalent modification of cysteines other than C220.[17] A 2-sulfonylpyrimidine was identified that covalently modifies C182 and C277, increasing the T_m up to about 2.5 °C without losing affinity towards DNA. This effect is independent of the Y220C mutation, which makes it a great candidate for a general T-p53C stabilization approach.

As the thermal destabilization of the Y220C mutation is of greatest concern, we performed differential scanning fluorimetry (DSF) as one of our primary screening techniques. Additionally, we used saturation transfer difference (STD) NMR for hit identification. Comparing target binding to its functional results by these two techniques can yield valuable insights for the drug discovery process. All hits found by these independent techniques were validated by ^{1}H,^{15}N-HSQC. Thus, binding modes independent of the Y220C induced cleft were detectable during primary screening as well and were classified through the validation process.

2 Results and discussion

In total, 14 hits were identified by the primary screens, of which ten were confirmed by ^{1}H,^{15}N-HSQC. A compound was considered as a hit if either the STD signal was sufficiently larger than the local background noise or if the ΔT_m was greater than 0.5 °C,[33] measured by DSF. Because it was shown that fragments can also stabilize T-p53C-Y220C through alkylation of surface-exposed cysteines rather than binding in the Y220C cleft,[17] we performed GSH reactivity measurements with each ^{1}H,^{15}N-HSQC hit as a surrogate assay for covalent binding. These measurements were also used for general stability assessment, as it is possible that strongly tuned halogenated fragments can be degraded *via* a $\mathrm{S_NAr}$-type reaction.[30] All hits identified in this study are summarized in Table 1. For clarity and simplicity the HEFLib IDs were reduced to their last four digits.

The DSF results of the triplicate measurement of the STD and DSF hits during the screen are shown in Fig. 3. The compounds that were considered hits are all significant ($p <$ 0.05) compared to the reference.

Table 1 All hits identified in this study are listed. A compound was considered as a hit if either the STD signal was present or the ΔT_m was larger than 0.5 °C. The ^{1}H,^{15}N-HSQC indicates if significant peak shifts were observed. The GSH column indicates the measured stability with GSH. Because compound 1151 does not contain a C–H bond, no STD spectrum can be recorded. Only ^{1}H,^{15}N-HSQC hits were measured for GSH stability. For the STD experiments a protein to ligand ratio of 20 μM : 1 mM (1 : 50), for DSF 6 μM : 1 mM (1 : 125) and HSQC 65 μM : 2 mM (1 : 30) was used

Compound	ΔT_m [°C]	STD	HSQC	$t_{1/2}$ GSH [h]
0116	−0.05	Yes	Yes	>100
0403	0.05	Yes	No	—
0404	−0.10	Yes	Yes	>100
0459	−0.05	Yes	Yes	>100
0522	0.30	Yes	No	—
0660	0.10	Yes	No	—
1151	0.80	NA	Yes	>100
1218	−0.20	Yes	Yes	>100
1223	2.0–2.55	Yes	Yes	0.81
1243	−0.25	Yes	Yes	>100
1246	0.15	Yes	No	—
4482	0.5–1.75	No	Yes	2.8
7394	−0.15	Yes	Yes	61
7405	0.20	Yes	Yes	>100

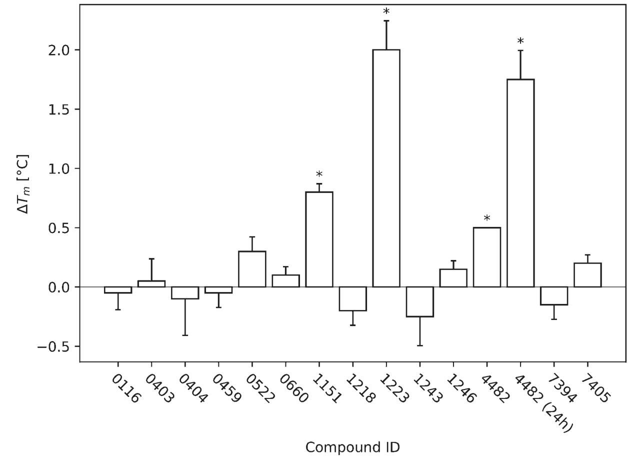

Fig. 3 The DSF screening results of all identified initial hits are displayed. The T-p53C-Y220C concentration was 8 μM and the ligand concentration 1 mM (ratio 1 : 125). The DSF runs were started after 30 min of incubation. All temperature changes that were significant ($p <$ 0.05) compared to the reference (T-p53C-Y220C without ligand) of the respective run are marked with an asterisk. During the run of 4482, all three measurements showed exactly the same difference to the reference and therefore no error bar is displayed. Additionally, for 4482 another run with 24 h incubation is displayed, showing time dependent increase in stabilization.

Based on the ^{1}H,^{15}N-HSQC data, hits could be categorized into three groups. By comparing the peak shifts with the ^{1}H,^{15}N-HSQC spectra of crystallographically confirmed Y220C cleft binders,[12,14] one group was identified as the Y220C cleft binding group. Another group was confirmed to bind covalently to T-p53C-Y220C. The third set contained significant peak shifts but does not suggest Y220C cleft binding. The chemical structure and corresponding group are depicted in Fig. 4.

2.1 Targeting the Y220C cleft

Four compounds (0459, 1151, 7394 and 7405) showed at least one peak shift, common to published cleft binders. However, none of the ^{1}H,^{15}N-HSQC hits yielded fittable ITC spectra (data not shown), they contain partially new scaffolds. The compound 7405 contains a *meta*-di-halogen moiety vicinal to an H-bond donor (amine). This compound has similarity to the first structure with confirmed halogen bonding to T-p53C-Y220C (PK784, Fig. 1 and 2). This scaffold can give rise to new synthetic routes and modifications.

Of the proposed cleft-binding compounds, only compound 1151 stabilized the protein by more than 0.5 °C. The ^{1}H,^{15}N-HSQC spectrum (Fig. 5A) shows multiple peak shifts indicating cleft binding. The DSF curves with addition of 1151 (ratio 1 : 125), shown in Fig. 5B, are shifted by 0.8 °C.

Compounds 0459 and 1151 both contain a pyrazole scaffold with a halogen in position 4. A structure was solved of T-p53C-Y220C bound to 1151 (PDB: 8A92). Data collection and refinement statistics are displayed in Table 2. The structure, especially in chain A, indicates multiple binding

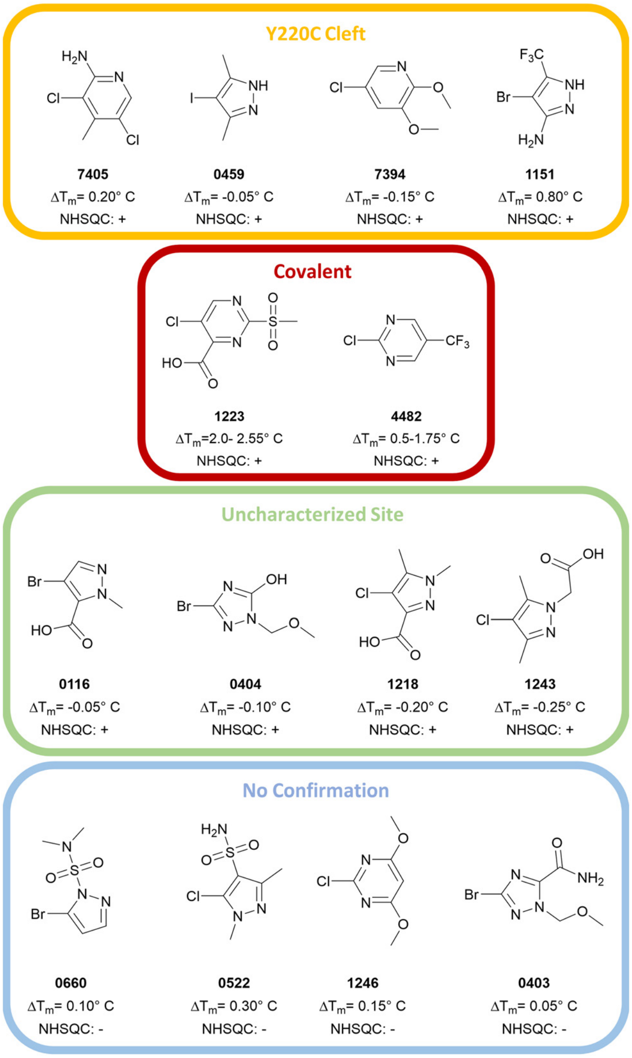

Fig. 4 Overview of the hits from the primary screens. Hits confirmed by ^{1}H,^{15}N-HSQC were categorized as either Y220C cleft binders (0459, 1151, 7394, 7405), covalent binders (1223/PK11000, 4482) or binders to an uncharacterized site (0116, 0404, 1218, 1243). The compounds 0660, 0522, 1246 and 0403 could not be confirmed by ^{1}H,^{15}N-HSQC.

poses, which could be identified by the anomalous signal of the bromine (Fig. 6). For chain B the occupancy was low and only one pose was built. The poses show that the CF_3 group points towards the cleft and the bromine pointing towards L145 or the subsite 2. The electron-rich CF_3 group displaces C220, opening subsite 3. This binding pose is similar to the ones containing a pyrrole ring, *e.g.* MB710 (Fig. 1 and 2). Even though the compound has a low K_D value (>1 mM, based on non-fittable ITC data) it stabilizes T-p53C-Y220C by about 0.8 °C. It is likely that the binding is driven by hydrophobic interactions of the CF_3 group to the cleft. No electron density could be observed for the amine.

In one pose the bromine points towards the backbone oxygen of L145 with a distance of 3.0 Å and an angle of 153.4°. Based on this pose we calculated the adduct-formation energy of the compound and *N*-methylacetamide

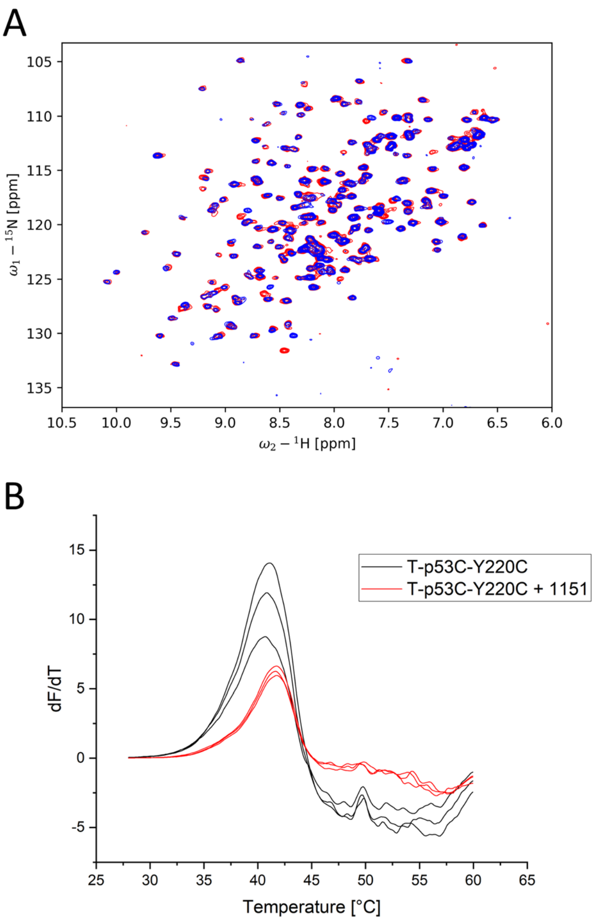

Fig. 5 (A) ^{1}H,^{15}N-HSQC of T-p53C-Y220C with 1151 at 2 mM (blue) and without addition of a ligand (red). Multiple peak shifts can be observed, all of which indicate Y220C cleft binding. (B) First derivative of the melting curves of T-p53C-Y220C and T-p53C-Y220C with 1151 of the initial screen (30 min incubation).

as a backbone model. In order to estimate the effect of the CF_3-group we calculated the $V_{\max}$ at an isodensity level of 0.02 au and the adduct-formation energy (ΔE) of 1151 and closely related scaffolds at the MP2/TZVPP level of theory. The results are displayed in Fig. 7. In addition, this bromine accepts an orthogonal hydrogen bond from the backbone nitrogen of T230.

The CF_3 group is the main contributor for the tuning of the system, increasing the $V_{\max}$ from 0.1597 au to 0.1737 au, comparable with iodobenzene (0.182 au).[34] As the amine only has a small effect on tuning, the vector could be used for fragment growing. Another approach could be converting the amine to a tertiary amine, adding a positive charge and once more strongly tune the system.[22]

2.2 Covalent modification

Because the 2-sulfonylpyrimidine PK11000 (Fig. 1) was added to the HEFLib with the ID 1223, a positive control for covalent modification was present. The glutathione assays confirmed that each fragment measured was stable with a

Table 2 Data collection and refinement statistics of the dataset of T-p53C-Y220C soaked with compound 1151 (PDB: 8A92). Values in parentheses indicate the respective value of the highest resolution bin

	Compound 1151 (PDB: 8A92)
Wavelength [Å]	0.92
Space group	$P2_12_12_1$
Cell dimensions	
a, b, c [Å]	65.1, 74.1, 105.2
α, β, γ [°]	90, 90, 90
Resolution range [Å]	50–1.37 (1.45–1.37)
Redundancy	13.2 (13.3)
Completeness [%]	100 (100)
Mean $I/\sigma(I)$	14.4 (1.0)
R-meas [%]	11.7 (256.8)
CC1/2 [%]	99.9 (49.7)
Wilson B [Å^2]	22.8
Resolution included [Å]	43.68–1.37
$R_{\text{work}}/R_{\text{free}}$ [%]	15.32/18.32
Bond RMSD [Å]	0.008
Angle RMSD [°]	0.99
Ramachandran [%] (favored/allowed/outliers)	98.98/1.02/0
Rotamer outliers [%]	1.43
All-atom Clashscore	1.44
Average B factor [Å^2]	
Overall	22.34
Protein	20.03
Ligand	41.4
Water	35.58

half-life greater than 20 h, with the exception of 4482 and the positive control as aforementioned. A half-life of 2.8 h was observed for compound 4482, which indicated a covalent reaction with the protein. The ^{1}H,^{15}N-HSQC, as displayed in Fig. 8, shows large peak shifts, similar to PK11000, also suggesting covalent modification. We were able to confirm covalent binding by mass spectrometry. The deconvoluted ESI-MS spectrum (Fig. 8, panel C) indicates that after 4 h of incubation with a molar protein-to-compound ratio of 1:125 up to three molecules of 4482 were bound to T-p53C-Y220C. Among them, the species with two attached molecules showed highest intensity. Unmodified protein was not detectable. In contrast, the MS spectrum of the triple mutant C124/182/277S, shows only the species with one bound fragment. Unmodified protein could be identified. This indicates that covalent binding of 4482 to the now absent cysteines occurs. Using DSF measurements, a time-dependent stabilization could be identified (Fig. 8). The ΔT_m of T-p53C-Y220C increased from 0.9 °C after 4 h incubation up to 1.75 °C after a 24 h incubation period.

In comparison, PK11000 resulted in a larger stabilization of T-p53C-Y220C up to a maximum ΔT_m of about 2.5 °C. In contrast to 4482, a maximum number of two modified cysteines was evident in the ESI-MS spectra of PK11000. This highlights the selectivity of PK11000 for specific p53 cysteines.[17]

Interestingly, Bauer *et al.*[17] could not detect any stabilization by the compound 2-chloro-5-(fluoromethyl)-pyrimidine. We measured significant stabilization with 4482, the trifluoro analog of the compound. This emphasizes the need of the CF_3 moiety as a strong electron-withdrawing group (EWG) for covalent binding. In general, compound 4482 contains a similar scaffold to the known covalent modifier PK11000. Both are pyrimidines with leaving groups in position 2 and additional EWGs to enhance S_NAr reactivity. These structural similarities should explain their comparable behavior towards T-p53C and T-p53C-Y220C. Moreover, it demonstrates the potential of their common scaffold as a covalent, Y220C-cleft independent, rescue for the oncogenic p53-Y220C mutant.

2.3 Identification of an uncharacterized site

Compounds 0116, 0404, 1218, 1243 and did not show typical peak shifts of previously described peaks. Examples of these peak shifts are displayed in Fig. 9. As there is no structural confirmation of another binding site, it is difficult to interpret the reason for the peak shift. The lack

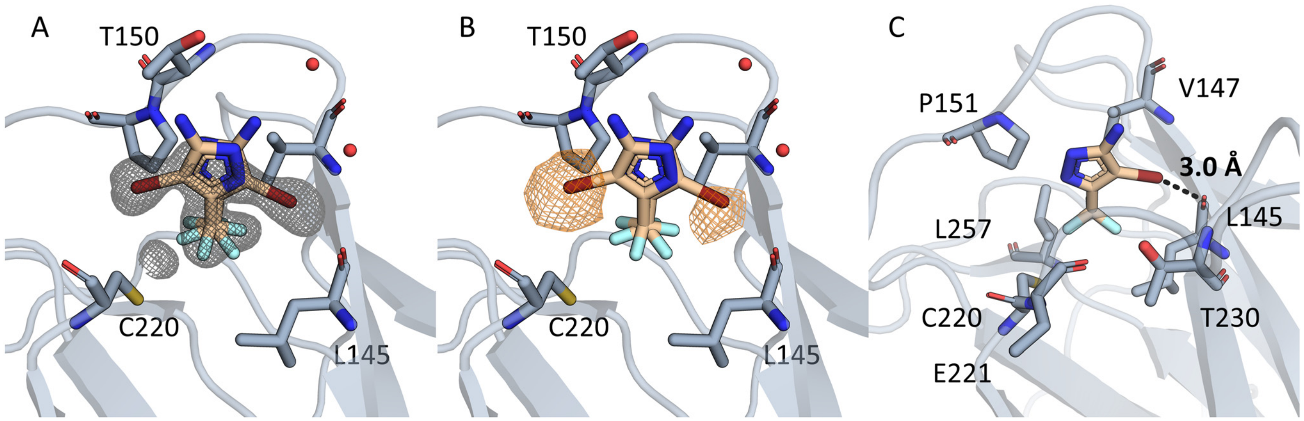

Fig. 6 (A) Electron density is displayed in grey around the compound 1151 as an unbiased omit map contoured at 3σ. In chain A two binding poses can be seen. In both poses the CF_3 group points towards C220 and engages in hydrophobic contacts. (B) The unbiased anomalous difference map is contoured at 4.5σ in orange. The signal shows that the bromine is located in two positions, but not towards C220. (C) The halogen engages in a halogen bond, with a distance of 3.0 Å and an angle of 153.4°. Residues in 4.5Å around the CF_3 group are displayed.

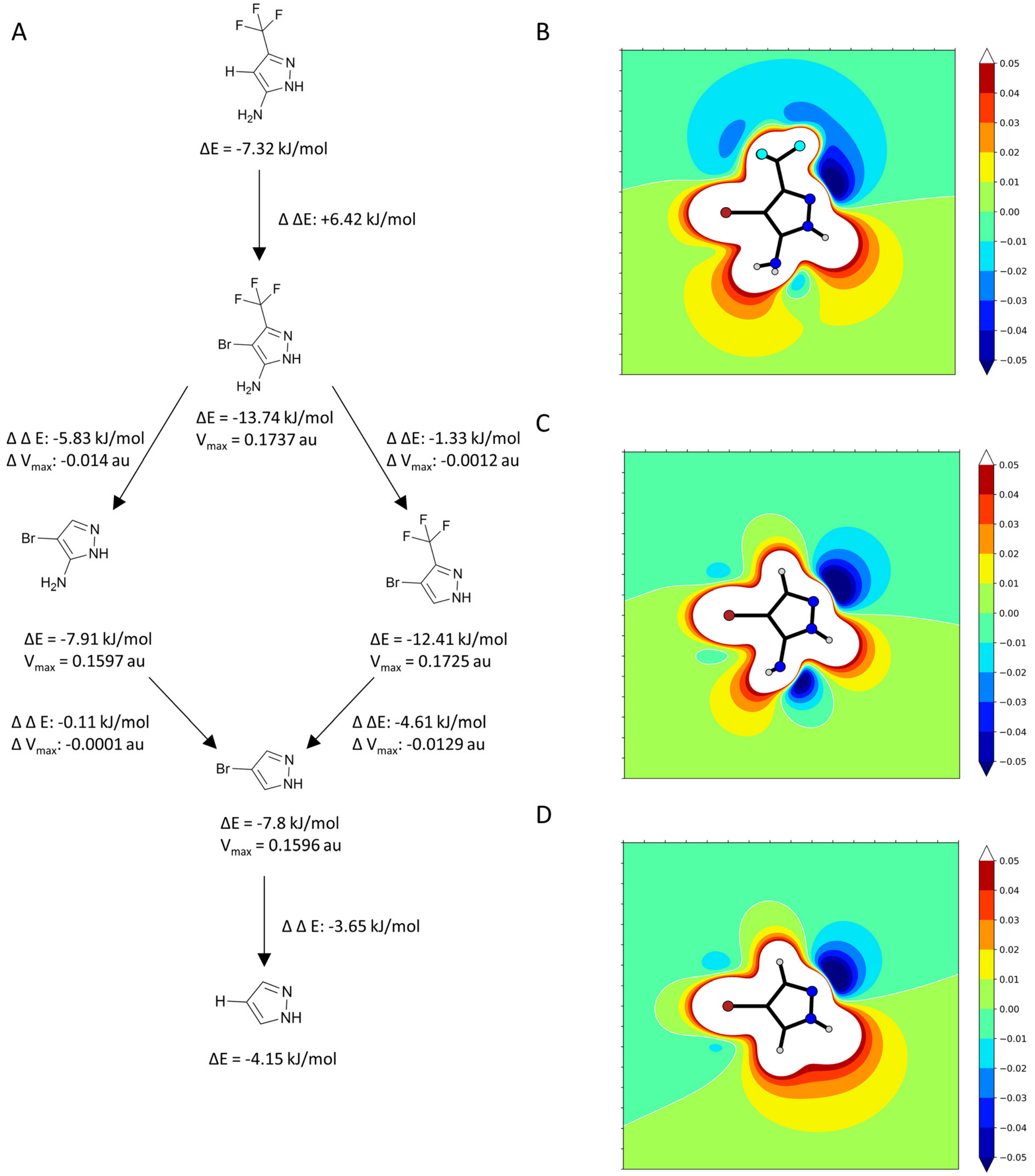

Fig. 7 (A) Flowchart of the effects on adduct-formation energy (ΔE) and V_{max} by systematically adding or removing substituents based on 1151. The CF_3 group has the largest effect on ΔE and V_{max}. (B) ESP plot of 1151. (C) ESP plot of 1151 after removing the CF_3 group. (D) ESP plot of 1151 after removing the CF_3 and NH_2 group.

of a deep cavity or cleft makes targeting of p53C very difficult. All compounds with the exception of 0404 contain a carboxyl group, which could engage in loose binding to the positively charged DNA binding interface of p53C and lead to the aforementioned peak shifts. Comparing the two prominent shifts (ω_1 = 130.29 ppm, ω_2 = 8.8 ppm; ω_1 = 110.9 ppm, ω_2 = 8.73 ppm) to the spectra of PK11000 or 4482, similar shifts can be observed. This could indicate, that the mostly uncharacterized binding site is near any of the alkylated cysteines.

3 Conclusion

The lack of specific cancer treatment for p53-Y220C and high amount of annual cases of an estimated 130 000 underlines the importance of continuous drug discovery for this

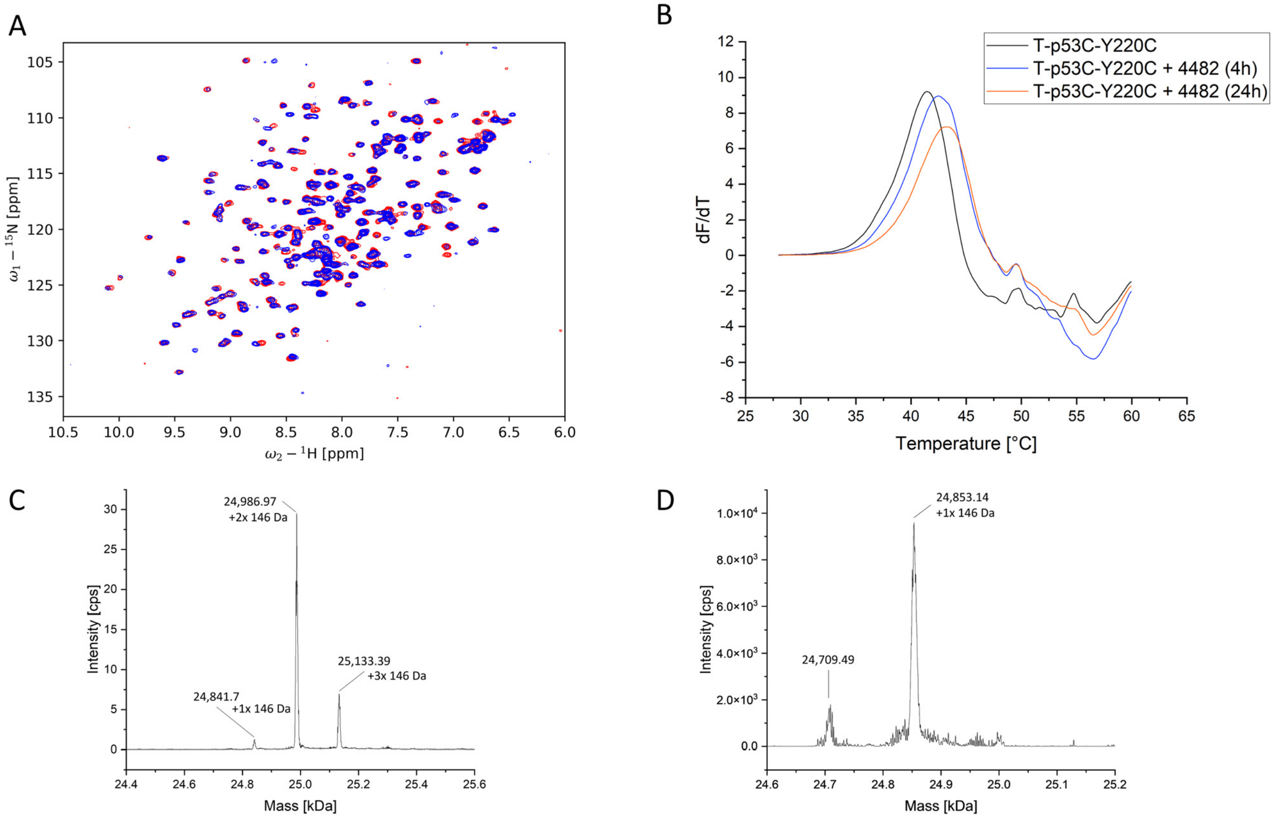

Fig. 8 (A) ^{1}H,^{15}N-HSQC of T-p53C-Y220C without compound (red) and 2 mM 4482 (blue). Multiple prominent peak shifts can be observed. (B) First derivative of the melting curve of T-p53C-Y220C and T-p53C-Y220C with 4482 after 4 h and 24 h incubation. (C) Deconvoluted ESI-MS spectrum of T-p53C-Y220C (50 μM) with 6.25 mM 4882 after 4 h incubation at 20 °C. The shift of the peaks is about 146 Da, which corresponds to the size of the attached 4482. (D) Deconvoluted ESI-MS spectrum of T-p53C-C124/182/277S (50 μM) with 6.25 mM 4482 after 4 h incubation at 20 °C. The major peak corresponds to the single alkylated protein.

target.[35–38] The first confirmation of halogen bonding in T-p53C-Y220C led to the development of the diversity-optimized HEFLib. A total of ten hits from this diversity-optimized library could be confirmed by ^{1}H,^{15}N-HSQC. The development of a $V_{\max}$-optimized HEFLib could lead to an improvement of the hit rate.[30] The diversity-optimized HEFLib did not yield another low Millimolar binding compound, but identified a multitude of diverse scaffolds binding to the protein. These scaffolds can now be further exploited by optimizing target binding and more importantly stabilization.

The HEFLib additionally produced more unconventional binding modes, by containing a covalent binder. This modification is independent of the Y220C mutation and could potentially lead to general purpose stabilizers with much broader applicability in the rescue of destabilized p53 cancer mutants. Another aim could be modifying these scaffolds to reestablish or modulate DNA binding in hot-spot mutations which loose their function based on altered DNA contacts.

Many of the identified and confirmed hits did not interact in the Y220C mutation-induced cavity as we had anticipated. For these hits further studies are needed to reveal their binding site and its possible implication for altering or rescuing p53 function. It should be noted that besides loss-of-function mutations, there are also oncogenic gain-of-function mutations known for p53.[39–41] Thus, new binding modes could provide avenues for therapeutic intervention for both aspects of altered p53 function. Of course, tractability and druggability need to be shown for such a new binding site.[42]

The compound 1151 could be further characterized and used as a spy molecule for FAXS NMR.[43,44] This could further facilitate screening experiments for the identification of novel fragments binding to the Y220C-induced cleft.

4 Materials and methods

4.1 Molecular biology

In general, expression and purification was performed as previously described.[16] The plasmid was cloned into BL21pLysS cells and the protein was expressed over night at 24 °C. The lysed sample in lysis buffer (KP_i 50 mM, NaCl 300 mM, imidazole 10 mM, TCEP 2 mM, pH = 8) was loaded onto a NiNTA column (Cytiva) and eluted using a gradient from 0–100% elution buffer (KP_i 50 mM, NaCl 300 mM, imidazole 250 mM, TCEP 2 mM, pH = 8). Then, the tag was cleaved over night using the tobacco etch virus protease. The sample was diluted 8-fold with heparin buffer A (KP_i 25 mM, NaCl 0 mM, DTT 5 mM, pH = 7.5) before it was loaded onto a HiTrap

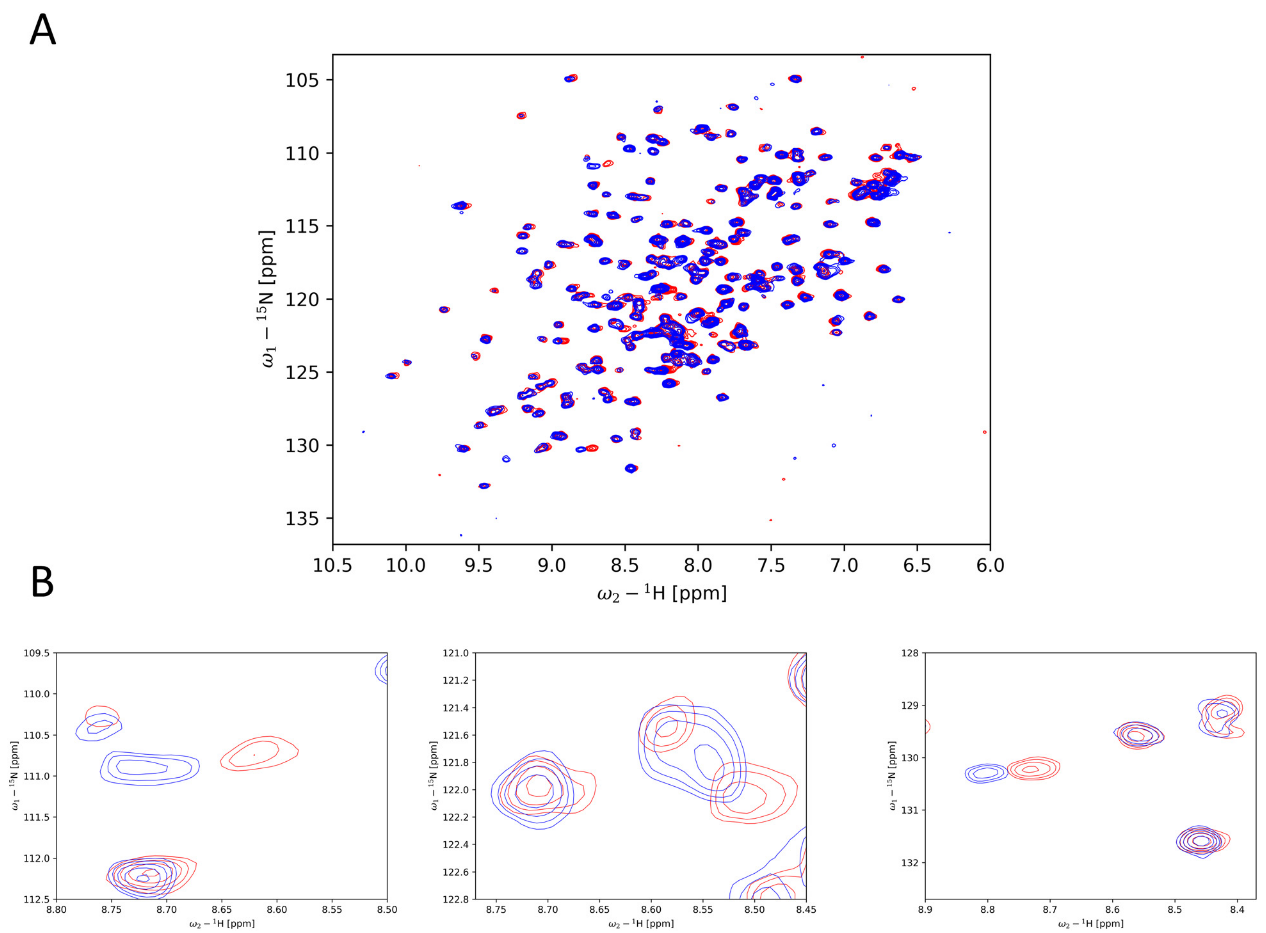

Fig. 9 Example of peak shifts of an uncharacterized binding site. (A) Overlay of peak shifts shown by compound 0116 at 2 mM (blue) in comparison to reference (no ligand) (red). (B) Typical peak shifts observed in the subgroup of the binders to an uncharacterized binding site.

Heparin HP (GE Healthcare) column. The sample was eluted with 40% heparin buffer B (KP_i 25 mM, NaCl 2 M, DTT 5 mM, pH = 7.5). A final size exclusion chromatography step using a HiLoad 26/60 Superdex 75 pg (GE Healthcare) was performed (KP_i 25 mM, NaCl 150 mM, DTT 5 mM, pH = 7.2). Fractions containing protein were finally pooled and flash frozen in liquid nitrogen.

For labelled expression, M9 minimal medium[45] was used supplemented with 1 g L^{-1} of $^{15}NH_4Cl$ prior to inoculation.

For mutagenesis, a pET24a-HLT vector with the thermostable p53 core domain (94–312) served as template. The Q5 site-directed mutagenesis kit (New England BioLabs) was used to produce the triple cysteine mutant C124/182/277S.

All constructs used, are displayed in Table 3.

4.2 Differential scanning fluorimetry (DSF)

The melting temperature of T-p53C-Y220C in the presence or absence of fragments was determined by differential scanning fluorimetry (DSF). DSF measurements were performed on a Qiagen Rotor-Q Model-5-Plex HRM real-time PCR instrument using SYPRO Orange as fluorescent dye (final concentration 5×). 8 μM protein in phosphate buffer (25 mM KPi, 150 mM NaCl, 1 mM TCEP, pH 7.2, 5% DMSO [v/v]), and a final compound concentration of 1 mM were used.[17] The temperature was ramped from 28 °C to 60 °C with a heating rate of 270 °C h^{-1}.[14] Excitation and emission filters were set to 490 and 580 nm. For time-dependent DSF measurements, the samples were incubated at 20 °C on a rotating shaker. The melting temperature of T-p53C-Y220C with or without compounds was determined from the maximum of the first derivative of the melting curve using OriginPro2020. All measurements were performed in triplicates. ΔT_m was calculated by subtracting the resulting T_m of T-p53C-Y220C from the T_m of the compound samples. A temperature increase of at least 0.5 °C was defined as a parameter for a fragment hit.[33]

4.3 Saturation transfer difference (STD) NMR

The STD experiments were performed as previously described, using the same mixtures.[30] The spectra were recorded on a Bruker Avance III HDX 700 with a 5 mm Prodigy TCI cryo probehead. Compounds were considered as a hit, if the signal was sufficiently larger than the local background noise.

Table 3 All sequences used are displayed. The biophysical screens are DSF, STD, ESI-MS and ^{1}H,^{15}N-HSQC. For crystallization a construct lacking the linker GGS was used

Construct	Sequence (N′–C′)
T-p53C-Y220C (biophysical screens)	GGSSS SVPSQ KTYQG SYGFR LGFLH SGTAK SVTCT YSPAL NKLFC QLAKT CPVQL WVDST PPPGT RVRAM AIYKQ SQHMT EVVRR CPHHE RCSDS DGLAP PQHLI RVEGN LRAEY LDDRN TFRHS VVVPC EPPEV GSDCT TIHYN YMCYS SCMGG MNRRP ILTII TLEDS SGNLL GRDSF EVRVC ACPGR DRRTE EENLR KKGEP HHELP PGSTK RALPN NT
T-p53C-Y220C (crystallization)	SSSVP SQKTY QGSYG FRLGF LHSGT AKSVT CTYSP ALNKL FCQLA KTCPV QLWVD STPPP GTRVR AMAIY KQSQH MTEVV RRCPH HERCS DSDGL APPQH LIRVE GNLRA EYLDD RNTFR HSVVV PCEPP EVGSD CTTIH YNYMC YSSCM GGMNR RPILT IITLE DSSGN LLGRD SFEVR VCACP GRDRR TEEEN LRKKG EPHHE LPPGS TKRAL PNNT
T-p53C-Y220C (C124/182/277S)	GGSSS SVPSQ KTYQG SYGFR LGFLH SGTAK SVTST YSPAL NKLFC QLAKT CPVQL WVDST PPPGT RVRAM AIYKQ SQHMT EVVRR CPHHE RSSDS DGLAP PQHLI RVEGN LRAEY LDDRN TFRHS VVVPC EPPEV GSDCT TIHYN YMCYS SCMGG MNRRP ILTII TLEDS SGNLL GRDSF EVRVC ASPGR DRRTE EENLR KKGEP HHELP PGSTK RALPN NT

4.4 ^{1}H,^{15}N-Heteronuclear single quantum coherence NMR

Spectra were recorded on an 800 MHz Bruker Avance-III at 293 K using a final protein concentration of 65 μM (5% DMSO-d6 [v/v]) and a final ligand concentration of 2 mM.

In total, 1024 data points were collected in the direct dimension (^{1}H) and 128 in the indirect dimension (^{15}N). Data processing was performed using Bruker Topspin 4.1 and analysis using NMRFAM-SPARKY 3.19.[46] Peak shifts were considered significant, if

$$\Delta\delta\left({}^{1}\mathrm{H}/{}^{15}\mathrm{N}\right) = \sqrt{\left(\Delta\delta\left({}^{1}\mathrm{H}\right)\right)^{2} + \left(\frac{\Delta\delta\left({}^{15}\mathrm{N}\right)}{5}\right)^{2}} \tag{1}$$

was larger than 0.04 ppm.[14,47] All NMR figures were prepared using the nmrglue Python package.[48]

4.5 Glutathione assay

GSH stability studies were performed according to a protocol established for heterocyclic electrophilic fragments by Keeley *et al.*[49]

Reaction conditions were PBS buffer pH 7.4, 10% acetonitrile, 100 μM ketoprofen as an internal standard, 250 μM fragment, and 5 mM GSH excess at 37 °C. Measurement times were after 0, 1, 2, 4, 8, 12, and 24 h. For very reactive fragments ($t_{1/2} < 5$ h) analysis was performed every 20 min. The mixture was analyzed by HPLC with UV-detection. The reaction of the compounds was detected by measuring the decreasing area under the curve (AUC) of the fragment relative to the internal standard. The declining AUC was fitted to pseudo-first order kinetics and $t_{1/2}$ was calculated using the following equation:

$$t_{1/2} = \ln\left(\frac{2}{k}\right) \tag{2}$$

Measurements were performed as duplicates with GSH. In addition, single measurements without GSH in PBS buffer were carried out for each fragment to check for hydrolytic degradation.

4.6 Mass spectrometry

T-p53C-Y220C or T-p53C-C124/182/277S (50 μM) in phosphate buffer (25 mM KP$_i$, 150 mM NaCl, 1 mM DTT, pH 7.2) were incubated with 125 mM compound dissolved in DMSO, yielding a final concentration of 5% [v/v] DMSO and 6.25 mM protein with a protein to compound ratio of 1:125. The mixture was incubated for 4 h at 20 °C while shaking.[17]

The UHPLC-system consisted of an Agilent (Waldbronn, Germany) 1290 Infinity binary pump (G4220A) and a thermostated column compartment (G1316C). Between the column and the ion source a Valco EHMA diverter valve (2-pos/6-port) from VICI (Schenkon, Switzerland) was installed for online de-salting of the samples. Mobile phase A was water + 0.1% (v/v) formic acid and mobile phase B was ACN + 0.1% (v/v) formic acid. The flow rate was set to 0.5 mL min^{-1} with the following gradient: 0–2 min: 5% B (de-salting of sample, flow to waste), 2–10 min: 5–80% B, 10–12 min: 80% B, 12–17 min: 5% B. The column temperature was set to 50 °C. A TripleTOF 5600+ mass spectrometer from Sciex (Darmstadt, Germany) was used with a Duospray ion source (ESI interface) in positive ionization mode. The following MS instrument parameters were used: curtain gas (CUR): 35 psi, nebulizing gas (GS1): 50 psi, heater gas (GS2): 40 psi, ion spray voltage floating: 5100 V, source temperature: 550 °C, collision energy (CE): 30 V, declustering potential (DP): 220 V. The mass range in TOF MS mode was set from 500 to 5000 *m*/*z* with an accumulation time of 500 ms. The IntactProteinMode script from Sciex was used to optimize advanced MS settings for protein analysis. Data acquisition was performed with Analyst TF 1.8.1 software (Sciex). Data analysis was performed using PeakView software 2.2.0 (Sciex) using the BioToolKit (2.2.0.) for deconvolution of the mass spectra.

4.7 Crystallization and data collection

The protein was concentrated to 5 mg mL^{-1} and mixed 1:1 with reservoir solution (100 mM HEPES (pH = 7.15), 19% PEG4000 and 10 mM DTT) using the sitting drop vapor diffusion technique and by performing streak seeding. Crystals grew within a few days. For soaking, crystals were transferred in a 50 mM or saturated compound solution in a cryo-protectant buffer (reservoir solution and an additional 20% glycerol) over night.

Data sets were obtained at the Swiss Light Source (SLS) (Villigen, Switzerland) at the X06DA (PXIII) beamline, using a Pilatus-2 M-F detector.

Data processing and reduction was performed using XDS.[50] To obtain initial phases by molecular replacement, 4AGL was used as a search model for PHASER included in the CCP4 suite.[14,51,52] Structure and phase improvement was performed using multiple cycles of manual model building in Coot and structure refinement using PHENIX.[53,54] The anomalous difference map was generated using CAD and fft, both from the CCP4 suite.[55–57] Ligand restraints were generated using AceDRG.[58,59]

4.8 V_{max} and adduct formation energy calculations

4.8.1 MP2 structure optimizations and single point calculations. Geometry optimizations and single point calculations were carried out using TURBOMOLE 7.4.1.[60] A triple-ζ basis set (def2-TZVPP) was used throughout the study.[61] MP2 calculations were done in combination with the resolution of identity (RI) technique and the frozen core approximation.[61–64] The frozen core orbitals were attributed by the default setting in TURBOMOLE by which all orbitals possessing energies below 3.0 au are considered as core orbitals. The SCF convergence criterion was increased to 10^{-8} Hartree for all calculations. Heavy atoms of the model systems were kept frozen during optimization.

4.8.2 Adduct formation calculations. The ligand and the halogen bond accepting moiety (represented as *N*-methylacetamide) were optimized using MP2/TZVPP. Heavy atoms were kept frozen during optimization. For the calculations of the putative adduct formations, the modified ligands were freely optimized using MP2/TZVPP-level of theory. The ligands were subsequently matched onto the geometry of the crystal structure using three atoms of the ligand. The complex formation energies were calculated through single points as the difference between the complex and the sum of the two separate molecules.

4.8.3 2D electrostatic potential (ESP) plots and V_{max} calculations. All ligands were oriented after their geometry optimization employing an in-house script by placing the halogen atom into the negative *X*-axis and the respective ring system into the *XZ*-plane. Electrostatic potentials were calculated using TURBOMOLE 7.4.1 on a regular 2D grid. Visualization was done using a custom Python script. The V_{max} values were extracted at 0.02 au electron isodensity.

Author contributions

Conceptualization was performed by FMB. JS and MC carried out and analyzed $^1H,^{15}N$-HSQC experiments. MD and MK performed the STD experiments, JS and MD analyzed them. TK performed and analyzed the DSF studies. MS performed the GSH assays. SJ and ML performed and analyzed the ESI-MS experiments. Mutagenesis was done by LE. Crystallographic data reduction and refinement was performed by JS, MB and TS. FMB, JS, TK and MS wrote the final manuscript.

Conflicts of interest

There are no conflicts to declare.

Acknowledgements

We thank Georg Zocher for his help and advice in crystallography. We also thank Andreas Joerger for his expertise in crystallizing T-p53C-Y220C. We gratefully acknowledge the Swiss Light Source (SLS, Switzerland) for beam time.

Notes and references

1 D. P. Lane, *Nature*, 1992, **358**, 15–16.

2 B. Vogelstein, D. Lane and A. J. Levine, *Nature*, 2000, **408**, 307–310.

3 A. C. Joerger and A. R. Fersht, *Annu. Rev. Biochem.*, 2008, **77**, 557–582.

4 A. C. Joerger and A. R. Fersht, *Cold Spring Harbor Perspect. Biol.*, 2010, **2**, a000919.

5 C. J. Brown, S. Lain, C. S. Verma, A. R. Fersht and D. P. Lane, *Nat. Rev. Cancer*, 2009, **9**, 862–873.

6 K. G. Wiman, *Oncogene*, 2010, **29**, 4245–4252.

7 G. M. Popowicz, A. Dömling and T. A. Holak, *Angew. Chem., Int. Ed.*, 2011, **50**, 2680–2688.

8 A. Petitjean, E. Mathe, S. Kato, C. Ishioka, S. V. Tavtigian, P. Hainaut and M. Olivier, *Hum. Mutat.*, 2007, **28**, 622–629.

9 P. V. Nikolova, J. Henckel, D. P. Lane and A. R. Fersht, *Proc. Natl. Acad. Sci. U. S. A.*, 1998, **95**, 14675–14680.

10 L. Bouaoun, D. Sonkin, M. Ardin, M. Hollstein, G. Byrnes, J. Zavadil and M. Olivier, *Hum. Mutat.*, 2016, **37**, 865–876.

11 M. R. Bauer, A. Krämer, G. Settanni, R. N. Jones, X. Ni, R. Khan Tareque, A. R. Fersht, J. Spencer and A. C. Joerger, *ACS Chem. Biol.*, 2020, **15**, 657–668.

12 F. M. Boeckler, A. C. Joerger, G. Jaggi, T. J. Rutherford, D. B. Veprintsev and A. R. Fersht, *Proc. Natl. Acad. Sci. U. S. A.*, 2008, **105**, 10360–10365.

13 M. R. Bauer, R. N. Jones, M. G. J. Baud, R. Wilcken, F. M. Boeckler, A. R. Fersht, A. C. Joerger and J. Spencer, *ACS Chem. Biol.*, 2016, **11**, 2265–2274.

14 R. Wilcken, X. Liu, M. O. Zimmermann, T. J. Rutherford, A. R. Fersht, A. C. Joerger and F. M. Boeckler, *J. Am. Chem. Soc.*, 2012, **134**, 6810–6818.

15 X. Liu, R. Wilcken, A. C. Joerger, I. S. Chuckowree, J. Amin, J. Spencer and A. R. Fersht, *Nucleic Acids Res.*, 2013, **41**, 6034–6044.

16 M. G. Baud, M. R. Bauer, L. Verduci, F. A. Dingler, K. J. Patel, D. Horil Roy, A. C. Joerger and A. R. Fersht, *Eur. J. Med. Chem.*, 2018, **152**, 101–114.

17 M. R. Bauer, A. C. Joerger and A. R. Fersht, *Proc. Natl. Acad. Sci. U. S. A.*, 2016, **113**, E5271–E5280.

18 A. C. Joerger, M. D. Allen and A. R. Fersht, *J. Biol. Chem.*, 2004, **279**, 1291–1296.

19 J. Heidrich, L. E. Sperl and F. M. Boeckler, *Front. Chem.*, 2019, **7**, 9.

20 M. O. Zimmermann, A. Lange, R. Wilcken, M. B. Cieslik, T. E. Exner, A. C. Joerger, P. Koch and F. M. Boeckler, *Future Med. Chem.*, 2014, **6**, 617–639.

21 A. Lange, M. Günther, F. M. Büttner, M. O. Zimmermann, J. Heidrich, S. Hennig, S. Zahn, C. Schall, A. Sievers-Engler, F. Ansideri, P. Koch, M. Laemmerhofer, T. Stehle, S. A. Laufer and F. M. Boeckler, *J. Am. Chem. Soc.*, 2015, **137**, 14640–14652.

22 R. Wilcken, M. O. Zimmermann, M. R. Bauer, T. J. Rutherford, A. R. Fersht, A. C. Joerger and F. M. Boeckler, *ACS Chem. Biol.*, 2015, **10**, 2725–2732.

23 R. Wilcken, M. O. Zimmermann, A. Lange, A. C. Joerger and F. M. Boeckler, *J. Med. Chem.*, 2013, **56**, 1363–1388.

24 R. Wilcken, M. O. Zimmermann, A. Lange, S. Zahn and F. M. Boeckler, *J. Comput.-Aided Mol. Des.*, 2012, **26**, 935–945.

25 M. O. Zimmermann, A. Lange and F. M. Boeckler, *J. Chem. Inf. Model.*, 2015, **55**, 687–699.

26 M. O. Zimmermann and F. M. Boeckler, *Med. Chem. Commun.*, 2016, **7**, 500–505.

27 R. Wilcken, M. O. Zimmermann, A. Lange, S. Zahn, B. Kirchner and F. M. Boeckler, *J. Chem. Theory Comput.*, 2011, **7**, 2307–2315.

28 A. Lange, M. O. Zimmermann, R. Wilcken, S. Zahn and F. M. Boeckler, *J. Chem. Inf. Model.*, 2013, **53**, 3178–3189.

29 M. O. Zimmermann, A. Lange, S. Zahn, T. E. Exner and F. M. Boeckler, *J. Chem. Inf. Model.*, 2016, **56**, 1373–1383.

30 M. Dammann, M. Kramer, M. O. Zimmermann and F. M. Boeckler, *Front. Chem.*, 2022, **9**, 815567.

31 S. Della Volpe, P. Linciano, R. Listro, E. Tumminelli, M. Amadio, I. Bonomo, W. Elgaher, S. Adam, A. Hirsch, F. Boeckler, F. Vasile, D. Rossi and S. Collina, *Bioorg. Chem.*, 2021, **116**, 105305.

32 M. Dammann, J. Stahlecker, M. O. Zimmermann, T. Klett, K. Rotzinger, M. Kramer, M. Coles, T. Stehle and F. M. Boeckler, *J. Med. Chem.*, in press.

33 J. L. Kaar, N. Basse, A. C. Joerger, E. Stephens, T. J. Rutherford and A. R. Fersht, *Protein Sci.*, 2010, **19**, 2267–2278.

34 A. Lange, J. Heidrich, M. O. Zimmermann, T. E. Exner and F. M. Boeckler, *J. Chem. Inf. Model.*, 2019, **59**, 885–894.

35 K. C. de Andrade, E. E. Lee, E. M. Tookmanian, C. A. Kesserwan, J. J. Manfredi, J. N. Hatton, J. K. Loukissas, J. Zavadil, L. Zhou, M. Olivier, M. N. Frone, O. Shahzada, W. J. R. Longabaugh, C. P. Kratz, D. Malkin, P. Hainaut and S. A. Savage, *Cell Death Differ.*, 2022, **29**, 1071–1073.

36 H. Sung, J. Ferlay, R. L. Siegel, M. Laversanne, I. Soerjomataram, A. Jemal and F. Bray, *Ca-Cancer J. Clin.*, 2021, **71**, 209–249.

37 J. Ferlay, M. Colombet, I. Soerjomataram, D. M. Parkin, M. Piñeros, A. Znaor and F. Bray, *Int. J. Cancer*, 2021, **149**, 778–789.

38 C. Kandoth, M. D. McLellan, F. Vandin, K. Ye, B. Niu, C. Lu, M. Xie, Q. Zhang, J. F. McMichael, M. A. Wyczalkowski, M. D. M. Leiserson, C. A. Miller, J. S. Welch, M. J. Walter, M. C. Wendl, T. J. Ley, R. K. Wilson, B. J. Raphael and L. Ding, *Nature*, 2013, **502**, 333–339.

39 G. Blandino, A. J. Levine and M. Oren, *Oncogene*, 1999, **18**, 477–485.

40 M. Oren and V. Rotter, *Cold Spring Harbor Perspect. Biol.*, 2010, **2**, a001107.

41 E. Alvarado-Ortiz, K. G. de la Cruz-López, J. Becerril-Rico, M. A. Sarabia-Sánchez, E. Ortiz-Sánchez and A. García-Carrancá, *Front. Cell Dev. Biol.*, 2021, **8**, 607670.

42 K. K. Brown, M. M. Hann, A. S. Lakdawala, R. Santos, P. J. Thomas and K. Todd, *Med. Chem. Commun.*, 2018, **9**, 606–613.

43 C. Dalvit, P. E. Fagerness, D. T. A. Hadden, R. W. Sarver and B. J. Stockman, *J. Am. Chem. Soc.*, 2003, **125**, 7696–7703.

44 C. Dalvit and A. Vulpetti, *J. Med. Chem.*, 2019, **62**, 2218–2244.

45 A. Geerlof, *M9 mineral medium*, **https://www.helmholtz-muenchen.de/fileadmin/PEPF/Protocols/M9-medium_150510.pdf**.

46 W. Lee, M. Tonelli and J. L. Markley, *Bioinformatics*, 2015, **31**, 1325–1327.

47 M. P. Williamson, *Prog. Nucl. Magn. Reson. Spectrosc.*, 2013, **73**, 1–16.

48 J. J. Helmus and C. P. Jaroniec, *J. Biomol. NMR*, 2013, **55**, 355–367.

49 A. Keeley, P. Ábrányi Balogh and G. M. Keserű, *Med. Chem. Commun.*, 2019, **10**, 263–267.

50 W. Kabsch, *Acta Crystallogr., Sect. D: Biol. Crystallogr.*, 2010, **66**, 125–132.

51 A. J. McCoy, R. W. Grosse-Kunstleve, P. D. Adams, M. D. Winn, L. C. Storoni and R. J. Read, *J. Appl. Crystallogr.*, 2007, **40**, 658–674.

52 M. D. Winn, C. C. Ballard, K. D. Cowtan, E. J. Dodson, P. Emsley, P. R. Evans, R. M. Keegan, E. B. Krissinel, A. G. W. Leslie, A. McCoy, S. J. McNicholas, G. N. Murshudov, N. S. Pannu, E. A. Potterton, H. R. Powell, R. J. Read, A. Vagin and K. S. Wilson, *Acta Crystallogr., Sect. D: Biol. Crystallogr.*, 2011, **67**, 235–242.

53 P. Emsley, B. Lohkamp, W. G. Scott and K. Cowtan, *Acta Crystallogr., Sect. D: Biol. Crystallogr.*, 2010, **66**, 486–501.

54 D. Liebschner, P. V. Afonine, M. L. Baker, G. Bunkóczi, V. B. Chen, T. I. Croll, B. Hintze, L.-W. Hung, S. Jain, A. J. McCoy, N. W. Moriarty, R. D. Oeffner, B. K. Poon, M. G. Prisant, R. J. Read, J. S. Richardson, D. C. Richardson, M. D. Sammito, O. V. Sobolev, D. H. Stockwell, T. C. Terwilliger, A. G. Urzhumtsev, L. L. Videau, C. J. Williams and P. D. Adams, *Acta Crystallogr., Sect. D: Biol. Crystallogr.*, 2019, **75**, 861–877.

55 A. Immirzi, *Crystallographic Computing Techniques*, ed. F. R. Ahmed, Munksgaard, 1966, p. 399.

56 L. F. Ten Eyck, *Acta Crystallogr., Sect. A: Cryst. Phys., Diffr., Theor. Gen. Crystallogr.*, 1973, **29**, 183–191.

57 R. J. Read and A. J. Schierbeek, *J. Appl. Crystallogr.*, 1988, **21**, 490–495.

58 F. Long, R. A. Nicholls, P. Emsley, S. Gražulis, A. Merkys, A. Vaitkus and G. N. Murshudov, *Acta Crystallogr., Sect. D: Biol. Crystallogr.*, 2017, **73**, 112–122.

59 F. Long, R. A. Nicholls, P. Emsley, S. Gražulis, A. Merkys, A. Vaitkus and G. N. Murshudov, *Acta Crystallogr., Sect. D: Biol. Crystallogr.*, 2017, **73**, 103–111.

60 *TURBOMOLE V7.2 2017*, a development of University of Karlsruhe and Forschungszentrum Karlsruhe GmbH, 1989–2007, TURBOMOLE GmbH, since 2007, available from **https://www.turbomole.com**.

61 F. Weigend and R. Ahlrichs, *Phys. Chem. Chem. Phys.*, 2005, **7**, 3297.

62 C. Hättig, *Phys. Chem. Chem. Phys.*, 2005, **7**, 59–66.

63 M. Feyereisen, G. Fitzgerald and A. Komornicki, *Chem. Phys. Lett.*, 1993, **208**, 359–363.

64 F. Weigend, M. Häser, H. Patzelt and R. Ahlrichs, *Chem. Phys. Lett.*, 1998, **294**, 143–152.

3.4 Publication IV: **Three-Minute Enantioselective Amino Acid Analysis by Ultra-High Performance Liquid Chromatography Drift Tube Ion Mobility-Mass Spectrometry Using a Chiral Core-Shell Tandem Column Approach**

Simon Jaag[a], Younes Valadbeigi[b], Tim Causon[c,*], Harald Gross[d], Michael Lämmerhofer[a,*]

[a] Pharmaceutical (Bio-)Analysis, Institute of Pharmaceutical Sciences, University of Tuebingen, Auf der Morgenstelle 8, 72076 Tuebingen, Germany

[b] Department of Chemistry, Faculty of Science, Imam Khomeini International University, 3414896818 Qazvin, Iran

[c] University of Natural Resources and Life Sciences, Vienna Department of Chemistry, Institute of Analytical Chemistry, Muthgasse 18, 1190 Vienna, Austria

[d] Pharmaceutical Biology, Institute of Pharmaceutical Sciences, University of Tuebingen, 72076 Tuebingen, Germany

*Corresponding authors:

E-Mail address: michael.laemmerhofer@uni-tuebingen.de (M. Lämmerhofer)

E-Mail address: tim.causon@boku.ac.at (T. Causon)

Analytical Chemistry 2024

DOI: 10.1021/acs.analchem.3c05426

3.4.1 Abstract

Enantioselective amino acid analysis is of great importance in (bio)pharmaceutical, biomedical, and food science and high throughput is often mandatory. Fast LC enantiomer separation was achieved after precolumn derivatization with 6-aminoquinolyl-*N*-hydroxysuccinimidyl carbamate (AQC) using a chiral core-shell particle tandem column based on weak anion-exchange and zwitterionic type quinine carbamate selectors with less than 3 min run times. All L and D-enantiomers of the proteinogenic amino acids and some isomeric ones (24 in total plus achiral glycine) were baseline separated (R_s > 1.5 except for glutamic acid with R_s = 1.3) while peaks of distinct amino acids and structural isomers (constitutional isomers and diastereomers of leucine and threonine) of the same configuration overlapped to various degrees. For this reason, drift tube ion mobility-mass spectrometry was coupled to this enantioselective LC (LC-IM-MS) as additional selectivity filter without extending run times. The orthogonal IM separation dimension in combination with high resolution demultiplexing (HRdm) enabled the separation of threonine isomers (threonine, *allo*-threonine, homoserine) due to conformational stabilization by hydrogen bond formation between hydroxyl side chain and urea group which resulted in larger differences of the drift-tube collisional cross-section ($^{DT}CCS_{N2}$) values for nitrogen as drift gas. In contrast, the key isomer sets, leucine, isoleucine and *allo*-isoleucine, have almost identical $^{DT}CCS_{N2}$ values so that IM did not provide further selectivity to support the partial LC separation (isoleucine and leucine almost baseline separated, but *allo*-isoleucine co-elutes with isoleucine). Density functional theory calculations of the CCS values supported these findings, which can be rationalized by the almost uniform impact of the AQC label on the size of the ions as well as the free rotation of alkyl chains leading to an averaged $^{DT}CCS_{N2}$. A preliminary validation of the enantioselective LC-IM-MS method for quantitative analysis showed compliance of accuracy and precision with common limits in bioanalytical methods. Application for the absolute configuration elucidation of a natural lipopeptide and therapeutic synthetic peptide after their hydrolysis indicated the applicability of this method.

Keywords

Chiral, amino acid analysis, ion mobility-mass spectrometry, enantioselective metabolomics, therapeutic peptides

3.4.2 Introduction

Enantioselective amino acid analysis has an increasing importance in pharmaceutical sciences, biomedical research, food science and other fields. While the L-configuration dominates in biological samples, there are several examples of natural products in which D-amino acids are part of a ribosomal or non-ribosomal (lipo)peptide [1-3], while also some synthetic therapeutic peptides have D-amino acids incorporated to increase proteolytic stability [4]. Enantioselective analysis of these products is crucial as racemization during the synthesis of peptides may lead to diastereomeric impurities with D-amino acids as aberrant moiety in such products [5]. Furthermore, D-amino acids have also gained interest in biomedicine as biomarkers of diseases like atherosclerosis, cancer and Alzheimer's disease [6, 7]. For this reason, a growing number of studies are reported on enantioselective metabolomics in which enantioselective amino acid analysis can be considered the most important subdiscipline [8]. To determine the enantiomeric amino acid composition of proteins or peptides, hydrolysis using deuterated chloric acid (DCl) and deuterium oxide (D_2O) to account for hydrolysis-induced racemisation are employed [9]. Consequently, there is a significant interest to develop fast analytical methods for a comprehensive assessment of the amino acid composition to distinguish amino acid enantiomers, diastereomers (e.g. L-Ile/L-*a*Ile) and constitutional isomers (e.g. L-Leu and L-Ile) for quality control purposes.

To this end, LC is the method of choice for enantioselective LC analysis of amino acids as it can be performed either i) directly without prior derivatization or after achiral derivatisation on a chiral stationary phase (CSP); or ii) indirectly after derivatization with a chiral derivatizing agent (CDA) and use of an achiral stationary phase (usually reversed-phase) [8]. For direct LC enantiomer separation of free amino acids, Crownpak CR-I [10], Chiralpak ZWIX(+) [11], and Chirobiotic T [12] and TAG [13, 14] (with teicoplanin as well as teicoplanin aglycone selector) have shown broad enantioselectivity. For example, all free proteinogenic amino acids, except for Pro, can be directly resolved by HPLC-ESI-MS/MS in 5 min using Crownpak CR-I(+) column [10]. Millet et al. showed separation of the 18 primary amino acid enantiomer pairs, but not the secondary amino acid Pro, using a Crownpak CR-I(+) column within three minutes using supercritical fluid chromatography (SFC) [15]. Derivatization can be used to improve the enantioselectivity for CSPs, introduce a strong fluorophore or chromophore for spectroscopic detection, or a moiety with improved ionization efficiency for mass spectrometric (MS) detection and (ideally) characteristic fragment ions for tandem MS (MS/MS) experiments. Examples of this approach with CSPs and achiral derivatisation are the use of 9-fluorenylmethyl-chloroformate (Fmoc-Cl) [16], dansyl chloride (Dns-Cl) [17], 1-fluoro-2,4-dinitrobenzene (DNB-F), 4-fluoro-7-nitrobenzofurazan (NBD-F) [18-20] and 6-aminoquinolyl-*N*-hydroxysuccinimidyl carbamate (AQC) [21, 22]. These LC separations of complex amino acid mixtures are typically performed in the 5-30 min time scale. To overcome limited chemoselectivity for separation of the challenging suite of Leu isomers, Karongo et al. used two-dimensional liquid chromatography (2D-LC) with achiral reversed-phase liquid chromatography (RP-LC) in the first dimension and a chiral tandem QN-AX / ZWIX(+) column in the second dimension providing separation of 24 amino acid enantiomer pairs as well as the achiral Gly in a total analysis time of 60 min [22]. With similar goals in mind, Oyaide et al. used an offline 2D-LC method to analyse Ser, Thr and *allo*-Thr (*a*Thr) after NBD-F derivatization using RP as first and chiral Pirkle-type CSP as second dimension [20]. Multiple heart cutting and full comprehensive 2D-LC have been implemented, to resolve them by achiral RP-LC in the first dimension followed by a fast chiral separation in the second dimension, but these methods are technically complex and total run times are long (> 30 min) [19, 22, 23]. Very recently, Hamase and coworkers suggested a 3D-LC approach for enantioselective analysis of aliphatic amino acids in urine with RP in the first, a mixed-mode column having remarkable selectivity for the structural isomers of Leu (Leu/Ile/*a*Ile) in the second dimension, and an enantioselective column in the third dimension [24]. On the other hand, numerous indirect LC enantiomer separation methods have been reported in the literature (for a recent overview see e.g. ref. [8]). They also experienced a renaissance recently in enantioselective metabolomics. However, all indirect methods must be employed with care, especially when relative quantification is applied deriving enantiomer ratios directly from peak areas of the corresponding enantiomers [8]. Kinetic resolution due to incomplete derivatization, racemization, distinct detector response of the detected diastereomers (e.g. distinct ESI ionization efficiency, different fragmentation rates in tandem MS) and enantiomeric impurities in the CDA may easily introduce bias and need proper consideration by calibration and in the course of validation [8]. Like in LC, these problems may also exist in IM-MS and can be alleviated by direct enantiomer separation methods.

Due to the low-throughput nature of LC enantiomer separation methods, the potential of adding ion mobility (IM) separation for addressing different types of isomers in ms time scale has been explored in recent years [25]. IM can separate isomeric ions in the gas phase based on their mobility differences observed under influence of an electric field applied across a drift cell filled with inert buffer gas such as nitrogen or helium. Importantly, IM separation provides some orthogonality to mass spectrometry that separates ions according to the mass-to-charge ratio (*m/z*), which is realized using hybrid IM-MS instrumentation. However, under typical IM-MS conditions, enantiomers exhibit identical mobilities and IM-derived collision cross-sections (*CCS*) [18] meaning that chiral auxiliaries are required to permit their separation. Indeed, several studies have shown proof-of-principle enantioselective amino acid analysis using IM-MS with additional chiral chelating agents (forming ternary metal complexes) [26], cyclodextrins [27] or linear oligosaccharides [28] as chiral sectors. Distinction of enantiomers in such cases is enabled via formation of diastereomeric complexes or supramolecular assemblies with D- and L-amino acid enantiomers, which exhibit distinct mobilities and can therefore be separated via IM. On the other hand, a number of indirect approaches employing CDAs to form diastereomers prior to analysis by IM-MS have also been published and several have achieved enantiomer separations for a larger set of amino acids. For example, trapped ion mobility-MS (TIM-MS) in combination with CDAs such as (+)-1-(9-fluorenyl)ethyl chloroformate (FLEC) [29] was used to separate proteinogenic amino acids according to their distinct mobilities of the resultant diastereomers. Will et al. used (*S*)-naproxen chloride as CDA in a fully automated TIM-MS method with a short SCX-based ion-exclusion sample pre-separation and a total analysis time of three minutes [30]. While the simultaneous enantioselective analysis of all proteinogenic amino acids within a single method remains challenging for IM-MS, progress has been made in recent studies making use of estradiol-3-benzoate-17β-chloroformate derivatization and analysis with a U-shaped IM-QqQ-MS [31] and use of *N*-(2,4-dinitro-5-fluorophenyl)-L-alaninamide (FDAA, Marfey's reagent) with TIM-MS [32] as CDAs separating 23 and 19 amino acid enantiomer pairs, respectively. Yet, resolution for several diastereomeric pairs was limited and IMS resolution at half height for most Leu isomers could not be achieved [33]. For this reason, the goal was to develop a rapid, enantioselective amino acid analysis method with a 1-5 min analysis time scale. Fast LC enantiomer separations in a one-minute time scale have been accomplished on chiral superficially porous particle (SPP) columns recently for individual enantiomer pairs of various analytes including amino acid (derivatives) [34-38]. However, in such rapid LC enantiomer separations of a complex mixture of amino acids, many peak overlaps of distinct amino acids are observed due to limited chemoselectivity and insufficient peak capacity of CSPs. Mass spectrometric detection can provide selectivity to distinguish between the majority of the overlapped peaks except for some isobaric and isomeric amino acids (structural isomers of Thr and Leu). On contrary, it has been demonstrated that IM can resolve constitutional isomers and diastereomers in the ms time scale [33]. Hence, the current work focuses on the combination of fast enantioselective LC with SPP columns with IM-MS for selective analysis amino acid enantiomers including their structural isomers (i.e. enantiomers, constitutional isomers and diastereomers). Ion suppression effects resulting from the LC co-elutions due to co-ionizations in the ESI-source should be compensated for by D- and L-uniformly-$^{13}C^{15}N$-labelled amino acid internal standards. It is the first time that direct LC enantiomer separation is coupled to IM-MS yielding comprehensive enantioselective amino acid analysis in the 1-5 min time scale. In contrast to reported indirect IM-MS enantiomer separations, the presented new method does not suffer from problems like kinetic resolution, bias from enantiomeric impurities in CDA, and complications that arise from detection of diastereomers (such as different detector responses and fragmentation rates in tandem MS), relevant especially when relative quantification is employed for determination of enantiomer ratios. Its potential for enantioselective amino acid profiling is evaluated by application to a non-ribosomal lipopeptide and a synthetic therapeutic peptide and the quantitative performance was elucidated as well.

3.4.3 Experimental

3.4.3.1 Materials

Octreotide peptide sample was obtained from Avachem Scientific (San Antonio, TX, USA) and BOC Sciences (Shirley, NY, USA), respectively. 6-Aminoquinolyl-*N*-hydroxysuccinimidyl carbamate (AQC) was purchased from BLDpharm (Kaiserslautern, Germany). D- and L-amino acids (see Supporting Information Table S1) were from Sigma Aldrich (Schnelldorf, Germany). A uniformly L-$^{13}C^{15}N$ (U-$^{13}C^{15}N$)-labelled cell free amino acid mixture as internal standard (IS, for composition see Supporting Information Table S2) was purchased from Cambridge Isotope Laboratories (Andover, MA, USA). Acetonitrile (ACN), formic acid (FA) and methanol (MeOH) were from Carl Roth (Karlsruhe, Germany) or Sigma Aldrich (Vienna, Austria).

Prototype core-shell ZWIX(+) and QN-AX columns (both 3.0x50mm, 2.7 µm, 160 Å) were from former studies (Schmitt et al.[37]; Geibel et al.[38]). Ammonium formate (NH_4FA), boric acid, deuterium chloride (DCl), deuterium oxide (D_2O), dithiothreitol (DTT), hydrochloric acid (HCl), iodoacetamide (IAA) and sodium hydroxide (NaOH) were purchased from Sigma Aldrich. Ultra-pure water was provided from a Water Purelab Analytics Purification system from Elga (Celle, Germany) or a Milli-Q IQ 7000 purification system equipped with an LC-Pak polisher cartridge (Merck Chemicals and Life Science GmbH, Vienna).

3.4.3.2 Instrumentation and Software

Evaluation of the single column and tandem column performances was done on an Agilent 1290 Infinity II LC-Instrument (Agilent Technologies, Waldbronn, Germany) with a binary pump (G4220A), thermostated column compartment (G1316A), hyphenated to an HTS PAL Autosampler (CTC Analytics, Zwingen, Switzerland) and an API 4000 triple quadrupole mass spectrometer (Sciex, Darmstadt, Germany) controlled by the Analyst 1.7 software (Sciex).

An Agilent 1290 Infinity II UHPLC system was used for the chromatographic separation with a tandem column consisting of first a QN-AX and second of a ZWIX(+) core shell column. The injection volume was 2 µL and the column temperature 50°C. Drift tube ion mobility-mass spectrometry (DTIM-MS) measurements was made using an Agilent 6560 IM-QTOFMS equipped with a Dual AJS ESI Ion Source (Agilent Technologies) using the same chromatographic conditions and controlled using MassHunter Acquisition software. The following source conditions were used: drying gas flow 8 L/min at 275°C, sheath gas flow 12 L/min at 350°C, nebulizer gas pressure of 30 psi, capillary voltage of 3500 V, and nozzle voltage of 500 V. Reference masses (purine and HP-921) were constantly infused into the second nebulizer to ensure accurate mass determination. Using the 4-bit multiplexed operation mode, a trap filling time of 1250 µs, trap release time of 150 µs, and a maximum drift (arrival) time of 50 ms, a total of 5 IM transients were summed into each data frame. The TOFMS was operated in the 1700 Extended Dynamic Range mode (2 GHz) and was tuned and calibrated using the vendor-recommended ESI-L tune mix (G1969-85000, and 0.1 mmol/L HP-0321 from Agilent Biopolymer Reference Kit, Agilent Technologies). Additional external calibration for ${}^{DT}CCS_{N2}$ determination followed previously elaborated protocols using the same tune mix ions as calibrants [39].

3.4.3.3 Data Analysis

LC-DTIM-TOFMS data were pre-processed using a combination of vendor and open-source tools. All datafiles were demultiplexed using the PNNL Pre-processor (2021.04.21) and mass re-calibrated using the IM-MS Reprocessor (Agilent Technologies). ${}^{DT}CCS_{N2}$ determination was performed using the IM-MS Browser 10.0 (Agilent Technologies) to determine and subsequently apply the linear regression coefficients to calibrate all datafiles [39]. Additional high-resolution demultiplexing (HRdm) [40] of selected examples was also performed (see Supporting Information chapter 1.2 for all pre-processing settings for standard and high-resolution demultiplexing workflows).

Skyline 22.2 was used for targeted data evaluation and extraction of EICs including IM-filtered examples. Origin Pro 2022 was used to generate graphs and Microsoft Excel 2019 for calculations.

3.4.3.4 Sample Preparation

Peptide hydrolysis

1 mg of lipopeptide sample was dissolved in 6 M DCl in D_2O and sealed in a 1.5 mL glass hydrolysis vial under nitrogen protection. Full hydrolysis was carried out at 110°C for 16 h. The sample was evaporated to dryness and re-dissolved in 1 mL 0.4 M sodium borate buffer pH 8.8, vortexed and centrifuged at 16,000 g for 60 s.

Stock solutions

Amino acid stock solutions were prepared at a concentration of 62.5 mM in 0.1 M HCl except for tyrosine which was dissolved in 0.5 M HCl. The following mixtures of amino acids were prepared by mixing the amino acid stock solutions and dilution with 0.1 M HCl where required: Single amino acid reference standards for both D- and L-enantiomers separately at 2.5 mM. A Mix of 25 proteinogenic amino acids (see Table S1) with c = 2.5 mM for the D- and L-enantiomers, respectively. A mix of D-Leu:L-Leu:D-Ile:L-Ile and D-Thr:L-Thr:D-*a*Thr:L-*a*Thr with 1:2:3:4 mM, respectively.

AQC-derivatization

For S-alkylation, 50 µL of sample were mixed with 250 µL of 0.4 M sodium borate buffer pH 8.8 and 25 µL of 10 mM DTT. After each mixing step the sample was vortexed 60 s and centrifuged at 3,000g for 60 s prior incubation. Reduction of disulfides by DTT was allowed to proceed for 10 min at 55°C. Subsequently, samples were alkylated by addition of 50 µL of 10 mM IAA and incubated for 10 min at 55°C. Unreacted IAA was quenched by addition of 25 µL DTT and incubation for 10 min at 55°C. 200 µL of this solution was transferred to a new vial and diluted with 50 µL 0.4 M sodium borate buffer. 55.5 µL of this solution was mixed with 394.5 µL of 0.4 M sodium borate buffer and 50 µL of 4 mg/mL AQC solution (in ACN) and incubated for 10 min at 55°C.

Preparation of U-$^{13}C^{15}N$-labelled IS and spiking

A U-$^{13}C^{15}N$-amino acid mix consisting of the 20 proteinogenic L-amino acids (c = 5 mg/mL in 0.1 M HCl) was alkylated and AQC-derivatized in the same way as described above and then racemised by incubation at 95°C for 6 h. 450 µL of sample and 50 µL of internal standard were mixed together.

For long-term storage and transportation, the samples were aliquoted to 100 µL, lyophilised at 0.050 mbar overnight using a FreeZone Benchtop Freeze Dryer 4.5 L, -105°C from Labconco (Kansas City, MO, USA). Prior to usage, the samples were reconstituted with 100 µL H_2O/MeOH 1:1 (v/v), vortexed 60 s, centrifuged at 3,000 g for 60 s and finally transferred to an HPLC vial with micro insert.

A second sample set with a calibrant series was prepared using a pipetting robot and further details can be found in the Supporting Information chapter 1.3 (Table S3 and Figures S1-4).

3.4.3.5 Calculation of chromatographic parameters

The net retention time t'_R was calculated by $t'_R = t_R - t_0$ with t_R as the analytes' retention time and t_0 as the void-time. The gradient retention factor k^* was calculated as follows:

$$k^* = \frac{t'_{R_2}}{t'_{R_1}}$$

(eq. 1)

With t'_{R2} and t'_{R1} as the net retention times of the second and first eluting peaks, respectively.

The selectivity α was calculated by:

$$\alpha = \frac{k_2^*}{k_1^*}$$

(eq. 2)

The resolution R_s was calculated by:

$$R_s = 1.18 \cdot \frac{t_{R_2} - t_{R_1}}{w_{1/2_1} + w_{1/2_2}}$$

(eq. 3)

wherein $w_{1/2}$ is the peak width at half height for the respective peaks.

3.4.3.6 Computational methods

Structures of all conformers of protonated AQC-derivatized amino acids were fully optimized by density functional theory (DFT) with ωB97xD functional. The basis set 6–311++G(d,p) including both diffuse and polarization functions was used for the calculations. Frequency calculations were performed at the same level of theory at 298.15 K to find optimized structures for local minima. Charge distribution was calculated using the Merz-Kollman (MK) method. Gaussian 16 software was used for the DFT calculations [41]. The Gaussian output files containing geometrical parameters of the optimized structures and MK charges were used to build input files for CCS_{N2} calculations. CCS_{N2} calculations were performed using MOBCAL-MPI software using the trajectory method (TM) at 298 K [42].

3.4.4 Results and discussion

3.4.4.1 Separation of enantiomers by single and tandem columns

LC conditions were optimized with the goal of achieving both a short (< 5 min) analysis time and simultaneously separating all proteinogenic amino acids in one run. To this end, two different chiral columns and their combination in a tandem arrangement [23, 43] were evaluated. The resolution results (Table 1) show that baseline separation ($R_s \geq 1.5$) for 23 of 24 amino acid enantiomer pairs can be achieved using the single QN-AX column with only Arg ($R_s = 0.98$, Figure S5a) and Asp ($R_s = 0.79$, Figure S5b) not fully separated. The basic Arg exhibits weak retention on the QN-AX column, which can be explained by repulsive effects between the positively charged Arg and the positively charged quinuclidine moiety of the stationary phase. Conversely, the basic amino acids His ($R_s = 3.25$) and Lys ($R_s = 4.13$) can be resolved well by the QN-AX column, which can be rationalized by the lower basicity of His ($pKa = 6.04$) compared to Arg ($pKa = 12.10$) and bis-derivatization of Lys, which leads to a neutral side chain without repulsive electrostatic effects. The low resolution of Asp enantiomers on the QN-AX column is mainly a result of the dominating ionic interactions of α– and side chain carboxylate groups with the anion-exchange site of the stationary phase, which occur mostly non-stereoselectively i.e. are largely of equal strength for both enantiomers leading to low enantioselectivity. Stereoselective interactions of other functional groups like the urea of AQC-Asp and carbamate group of the chiral selector seem to be of limited relative strength and influence.

Table 1. Resolution of enantiomer pairs using the single QN-AX, ZWIX(+) or the combined tandem columns. Mobile phase A: 10 mM NH_4FA and 10 mM FA in ACN/MeOH/H_2O (49:49:2; v/v/v), mobile phase B: 50 mM NH_4FA and 50 mM FA in ACN/MeOH/H_2O (49:49:2; v/v/v); flow rate: 1.25 mL/min, gradient: 0-0.4 min 0 %B, 0.4-1.0 min 0-100 %B, 1.0-3.0 min 100 %B, 3.0-3.2 min 100-0 %B, 3.2-4.0 min 0 %B, column temperature: 50°C.

AA-AQC	QN-AX	ZWIX(+)	tandem
*a*Ile	3.30	0.00	4.27
Ala	1.97	0.44	2.75
Arg	0.98	6.49	7.67
Asn	7.08	3.86	7.08
Asp	0.79	2.36	2.11
*a*Thr	4.06	2.79	3.70
Cys-IAA	3.93	2.88	4.60
Gln	2.60	1.84	2.83
Glu	1.92	1.31	1.27
His	3.25	4.17	5.72
Hse	3.30	2.36	2.83
Ile	3.30	0.00	4.08
Leu	2.56	0.00	2.29
Lys-bis-AQC	4.13	1.93	3.78
Met	3.67	0.98	3.98
*n*Leu	3.41	0.00	4.06
Phe	5.02	1.57	3.78
Pro	1.70	0.00	1.89
Ser	4.33	4.60	5.78
Thr	5.19	2.79	3.75
*t*Leu	4.87	0.00	4.03
Trp	4.72	8.58	9.87
Tyr	4.98	2.70	5.38
Val	6.74	1.18	5.77

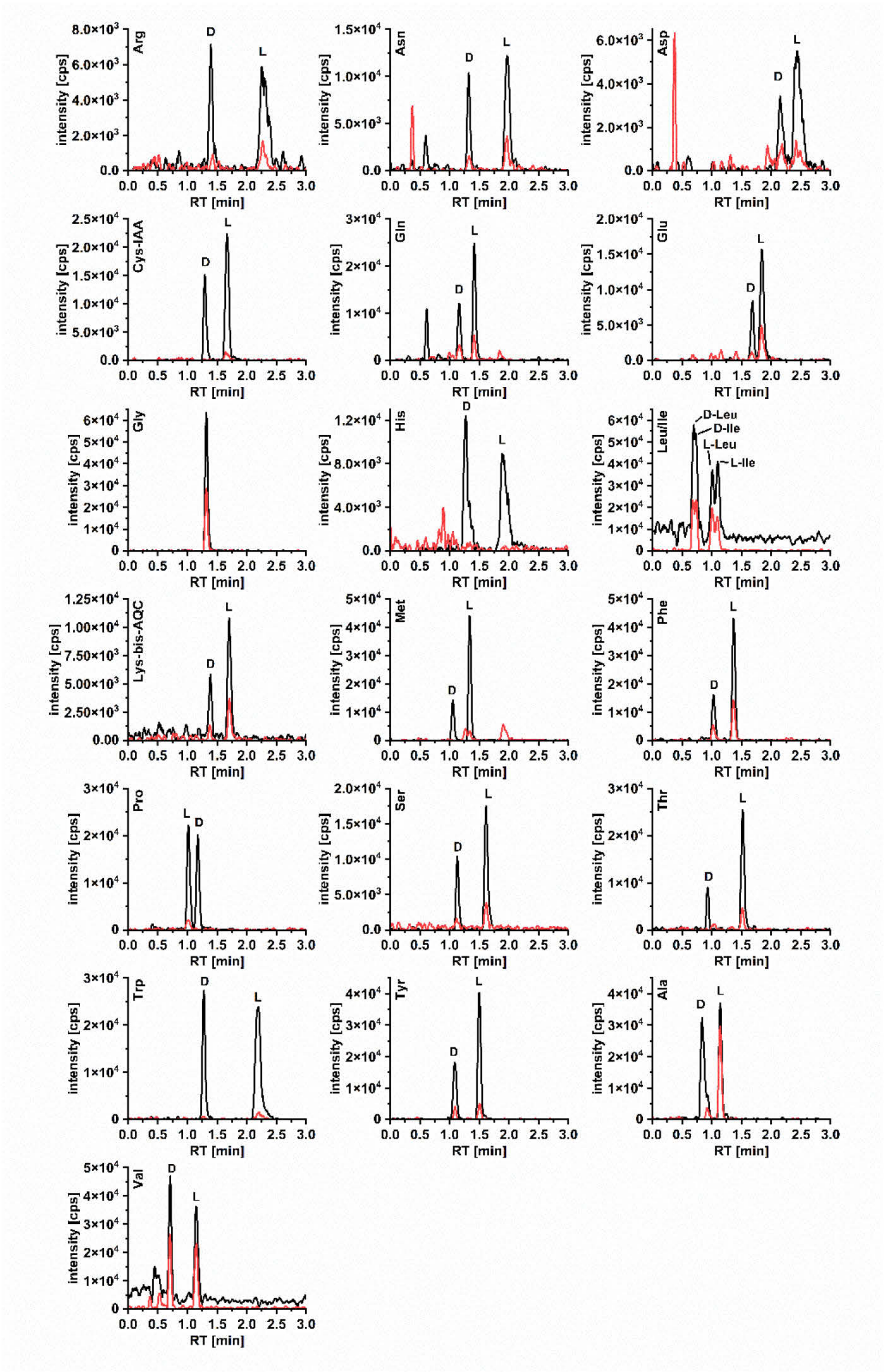

Figure 1. Extracted ion chromatograms (EIC) (intensity vs. LC retention times) of the 20 proteinogenic amino acids (black trace) and their respective U-13C-15N standards. Tandem column: QN-AX + ZWIX(+) prototype core shell columns (3.0x50 mm, 2.7µm, respectively). Mobile phase A: 10 mM NH4FA and 10 mM FA in ACN/MeOH/H2O (49:49:2; v/v/v), mobile phase B: 50 mM NH4FA and 50 mM FA in ACN/MeOH/H2O (49:49:2; v/v/v); flow rate: 1.25 mL/min, gradient: 0-0.4 min 0 %B, 0.4-1.0 min 0-100 %B, 1.0-3.0 min 100 %B, 3.0-3.2 min 100-0 %B, 3.2-4.0 min 0 %B, column temperature: 50°C.

On the ZWIX(+) column, the guanidinium group of Arg experiences attractive electrostatic interactions with the sulfonate moiety of the ZWIX(+) selector, hence Arg enantiomers are well retained with large separation factor (suppl. Figure S5a). On contrary, the carboxylate groups of Asp experience a repulsive electrostatic effect on ZWIX(+) due to the sulfonate moiety of the chiral selector, and hence show less retention. The stereoselective urea-carbamate hydrogen bonding interaction gains relative importance affording a large separation factor (suppl. Figure S5b). On the ZWIX(+) column, Arg and Asp were favourably separated, however, only 14 of 24 enantiomer pairs yielded R_s >1.5 under the given conditions with insufficient resolution observed for the aliphatic, hydrophobic amino acids such as Leu isomers, Ala, and Val probably due to their weak retention with the employed polar organic elution mode (k^* < 1, Table S4, hydrophobic interactions do not play a major role under these highly organic elution conditions).

Based on this observation, a combination of the two columns in a tandem arrangement was evaluated. The separation factors achieved on the tandem column (QN-AX coupled in series with ZWIX(+) as the second column in the tandem approach; both with D-enantiomer eluting before the L-enantiomer except for Pro for which elution order is reversed on both columns) are due to a combined additive retention effect from both columns [44]: Arg and Asp benefitted from the enantioselectivity of the ZWIX(+) column (suppl. Figure S5a and S5b), while maintaining high resolution for the other amino acids, e.g. Asn like other amino acids was fully baseline separated on both columns (suppl. Figure S5c). Pro enantiomers were insufficiently retained and not resolved on ZWIX(+) under given conditions, however, QN-AX contributed sufficient enantioselectivity (see suppl. Figure S5d). With this arrangement, only the resolution for Glu was substantially reduced compared to the single QN-AX column (R_s = 1.92 vs. 1.27) and it was the only amino acid with R_s < 1.5 using the tandem column setup. While most AQC-derivatized enantiomers could be separated within 1 min using the tandem column approach, important constitutional isomers and diastereomers co-elute under such fast LC elution regime and therefore need specific attention, which was partly achieved by extending the separation to 3 min. In total 23 of 24 amino acid enantiomer pairs can be resolved with a resolution ≥ 1.5 while Glu is partially resolved (R_s = 1.27) within a 3 min analysis time plus re-equilibration (Figure 1).

3.4.4.2 LC separation of isomeric amino acids

In addition to the separation of enantiomers, the tandem column method was evaluated for separation of Leu isomers (Leu, Ile, *a*Ile, *t*Leu, *n*Leu) and Thr isomers (Thr, *a*Thr, Hse) of identical configurations. This is of critical importance since these isomers cannot be distinguished by MS due to their identical precursor ion *m/z* and lack of specific fragment ions in tandem MS experiments for AQC-amino acid derivatives.

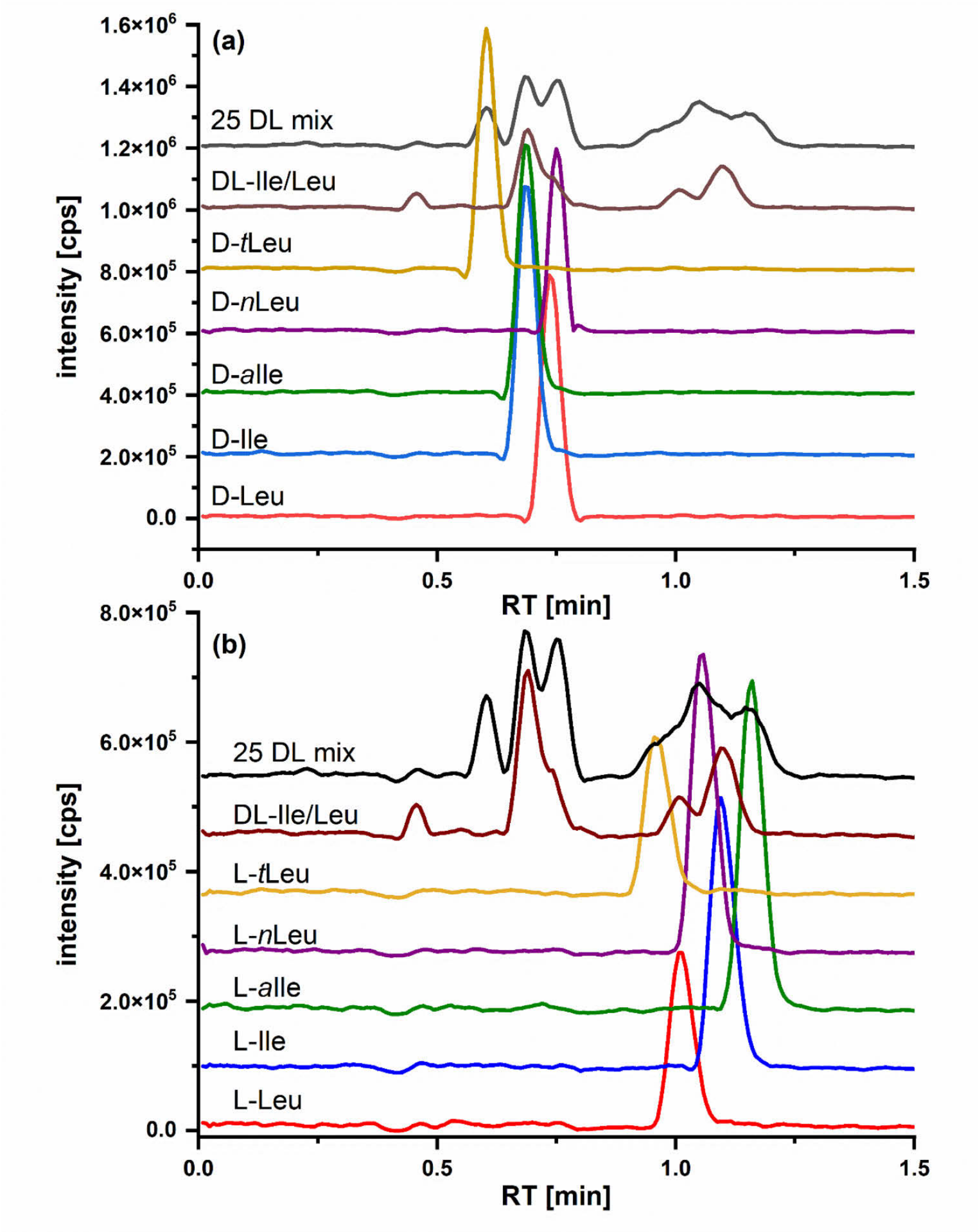

Figure 2. Extracted ion chromatograms (EIC) (intensity vs. LC retention times) of the leucine isomers. (a) D-leucine isomers and (b) L-leucine isomers. Experimental conditions are the same as described in Figure 1.

3.4.4.2.1 Leu isomers

Enantiomers of the investigated amino acids can be resolved within 1 min after AQC derivatization on the employed tandem column (Figure S6). However, under such fast elution regime constitutional isomers and diastereomers co-elute. They need specific attention, which was partly achieved by extending the analysis time. Using optimized conditions on the tandem column, D-*t*Leu elutes first and can be separated with a resolution of 1.18 from the co-eluting pair D-*a*Ile/D-Ile (Figure 2a and Table S5). Conversely, a partial separation between the biologically important isomer pair of D-Ile and D-Leu (R_s = 0.75) can be achieved. There was no separation between D-Leu and the non-canonical D-*n*Leu in the mixture even though a slight difference in the retention time was observed for the single standard injections. However, *n*Leu is usually not present in biological and pharmaceutical samples. The important pairs L-Leu and L-Ile (R_s= 0.79), and L-Ile and L-*a*Ile (R_s= 0.88) are partially separated, but only a minor degree of separation of L-*t*Leu from L-Leu (R_s = 0.42) is observed (Figure 2b). Nevertheless, this level of resolution of Leu isomers could be enough selectivity between the biologically relevant L-Ile and L-Leu while their D-enantiomers can be determined as their sum in initial screening approach.

3.4.4.2.2 Thr/*a*Thr/Hse

The separation of Thr isomers is shown in Figure 3. In the 25 DL-mixture, the D-enantiomers of Thr, *a*Thr and Hse co-elute as a single broad peak. L-Hse can be baseline separated from L-*a*Thr (R_s = 2.83, Table S6), but only partial separation between L-*a*Thr and L-Thr (R_s = 0.83) is observed. However, biological samples typically do not contain Hse and hence only the separation of a mixture of Thr/*a*Thr is relevant for the majority of cases whereby near-baseline separation is achieved (i.e. D-Thr and D-*a*Thr: R_s = 1.18; Table S7).

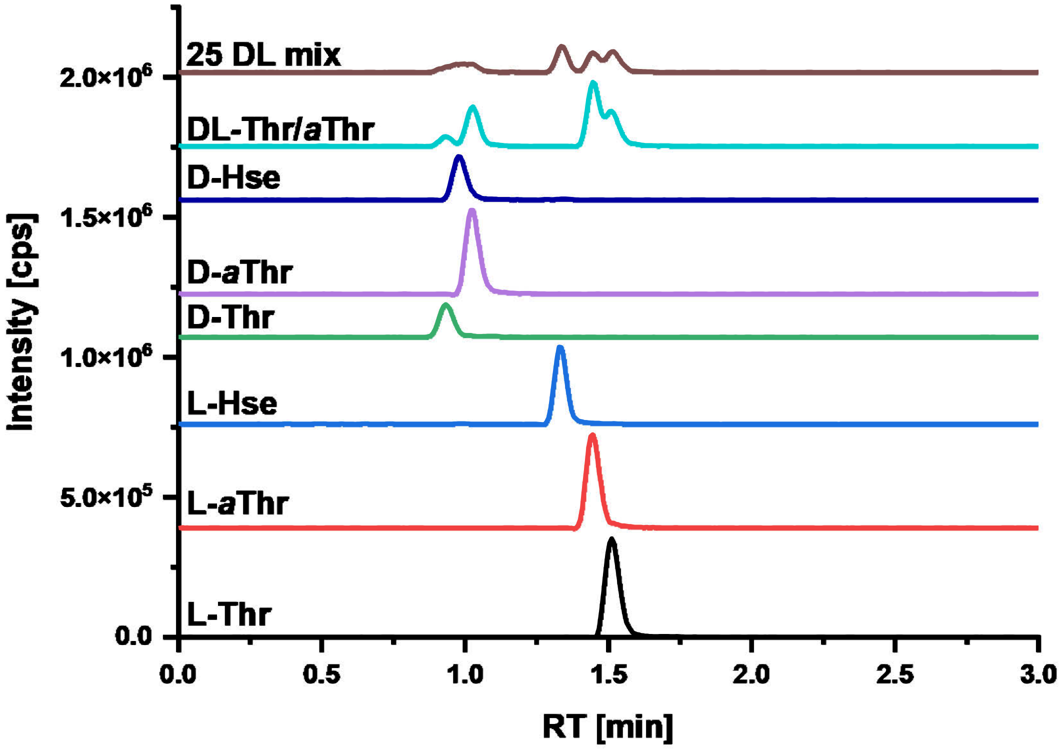

Figure 3. Extracted ion chromatograms (EIC) (intensity vs. LC retention times) of the threonine isomers. Tandem column: QN-AX + ZWIX(+) prototype core shell columns (3.0x50 mm, 2.7µm, respectively). Experimental conditions are the same as described in Figure 1.

3.4.4.3 Evaluation of IM-MS to improve the fast enantioselective method

The aforementioned shortcomings of enantioselective LC for separating constitutional isomers and diastereomers under fast elution conditions raised the question whether results could be improved using an additional IM separation dimension integrated without extending the total analysis time. First, the gain in resolving power between standard arrival time spectra showing very broad IM peaks (Figure S7a) and HRdm spectra (Figures S7b) showing much sharper peaks can be clearly demonstrated and was already shown for other analytes [40, 45]. Across the full set of amino acids evaluated in this work, the addition of the AQC derivatization led to a systematic increase in the observed $^{DT}CCS_{N2}$ values of the corresponding protonated molecular ions (Figure S8). This broad trend is unsurprising due to the consistent protonation site on the heteroatom of the aminoquinoline group and the structural rigidity of the AQC group itself, which is also in good agreement with observations from previous work focused on dansylation of amino acids [46]. However, some outliers within this trend were observed including Trp and Tyr, which exhibit a much smaller increase in $^{DT}CCS_{N2}$ due to π-π-interactions between the aromatic rings of the amino acid and the AQC, while Val has a large shift in comparison to the structurally similar Thr. Val and Thr have large differences in their $^{DT}CCS_{N2}$ values for the underivatized forms due to the contribution of the terminal OH group of Thr (see Figure S9). In the case of the key isomer sets, Leu, Ile and *a*Ile have almost identical $^{DT}CCS_{N2}$ values (180.9 Å²) while *n*Leu is slightly larger (182.1 Å²) with a $\Delta^{DT}CCS_{N2}$ of only 0.66 % (see Table 2, Figure S10, Table S8). An intermediate $^{DT}CCS_{N2}$ value was obtained for *t*Leu (181.6 Å²) leading to a $\Delta^{DT}CCS_{N2}$ of only 0.39 % compared to Leu, Ile, *a*Ile and 0.28 % compared to *n*Leu and unsatisfactory results with HRdm data processing (see Supporting Information Table S8, Figure S10). Comparing to the underivatized analogues (i.e., $[AA\text{-}AQC+H]^+$ vs. $[AA+H]^+$), the selectivity for *t*Leu vs. *n*Leu is reduced from 2.26% to 0.28% following AQC derivatization, while Leu vs. Ile selectivity is also substantially reduced almost to no selectivity from 0.61% to < 0.1%. These results can be rationalized by the almost uniform impact of the AQC on the size of the ions as well as the free rotation of alkyl chains leading to an averaged $^{DT}CCS_{N2}$. In contrast, the combination of IM separation and application of HRdm allows the separation of *a*Thr from Hse and Thr to be achieved (Figure 4). This is possible due to the larger differences of the $^{DT}CCS_{N2}$ values with $\Delta^{DT}CCS_{N2}$ (*a*Thr, Hse) = 0.58 %, $\Delta^{DT}CCS_{N2}$ (*a*Thr, Thr) = 1.34 %, and $\Delta^{DT}CCS_{N2}$ (Hse, Thr) = 0.75 %.

Table 2. Overview of the chromatographic, ion mobility and mass spectrometry results of the enantioselective analysis with the tandem column. Mobile phase A: 10 mM NH_4FA and 10 mM FA in ACN/MeOH/H_2O (49:49:2; v/v/v), mobile phase B: 50 mM NH_4FA and 50 mM FA in ACN/MeOH/H_2O (49:49:2; v/v/v); flow rate: 1.25 mL/min, gradient: 0-0.4 min 0 %B, 0.4-1.0 min 0-100 %B, 1.0-3.0 min 100 %B, 3.0-3.2 min 100-0 %B, 3.2-4.0 min 0 %B, column temperature: 50°C.

AA-AQC	**RT(D) [min]**	**RT(L) [min]**	**k*(D)[a]**	**k*(L)[a]**	**α**	**R**	**$^{DT}CCS_{N2}$ [Å²]**	**arrival time [ms]**	***m/z***
*a*Ile	0.68	1.15	0.55	1.61	2.96	4.27	180.9	24.19	302.150
Ala	0.94	1.15	1.14	1.61	1.42	2.75	164.7	21.89	260.103
Arg	1.39	2.30	2.16	4.23	1.96	7.67	188.3	25.31	345.167
Asn	1.31	1.97	1.98	3.48	1.76	7.08	174.3	23.32	303.109
Asp	2.19	2.44	3.98	4.55	1.14	2.11	175.2	23.44	304.093
*a*Thr	0.98	1.45	1.23	2.30	1.87	3.70	171.8	22.94	290.114
Cys-IAA	1.28	1.67	1.91	2.80	1.46	4.60	183.5	24.68	349.097
Gln	1.17	1.41	1.66	2.20	1.33	2.83	178.0	23.85	317.124
Glu	1.70	1.84	2.86	3.18	1.11	1.27	178.2	23.88	318.108
Gly[b]	1.32	n/a	2.00	n/a	n/a	n/a	159.5	21.15	246.087
His	1.28	1.91	1.91	3.34	1.75	5.72	181.1	24.29	326.125
Hse	0.98	1.34	1.23	2.05	1.67	2.83	172.8	23.07	290.114
Ile	0.68	1.06	0.55	1.41	2.58	4.08	180.9	24.19	302.150
Leu	0.75	1.06	0.70	1.41	2.00	2.29	180.9	24.19	302.150
Lys-bis-AQC	1.38	1.70	2.14	2.86	1.34	3.78	209.4	28.44	487.209
Met	1.07	1.34	1.43	2.05	1.43	3.98	182.0	24.39	320.106
*n*Leu	0.75	1.06	0.70	1.41	2.00	4.06	182.1	24.35	302.150
Phe	1.04	1.36	1.36	2.09	1.53	3.78	187.1	25.12	336.134
Pro	1.18	1.02	1.68	1.32	0.78	1.89	168.6	22.5	286.119
Ser	1.13	1.62	1.57	2.68	1.71	5.78	168.8	22.49	276.098
Thr	0.98	1.52	1.23	2.45	2.00	3.75	174.1	23.25	290.114
*t*Leu	0.60	1.01	0.36	1.30	3.56	4.03	181.6	24.28	302.150
Trp	1.27	2.19	1.89	3.98	2.11	9.87	191.4	25.8	375.145
Tyr	1.09	1.50	1.48	2.41	1.63	5.38	188.4	25.34	352.129
Val	0.71	1.15	0.61	1.61	2.63	5.77	175.6	23.44	288.134

[a] a void time of 0.44 min was determined and used for calculation of the retention factor

[b] Gly is an achiral amino acid

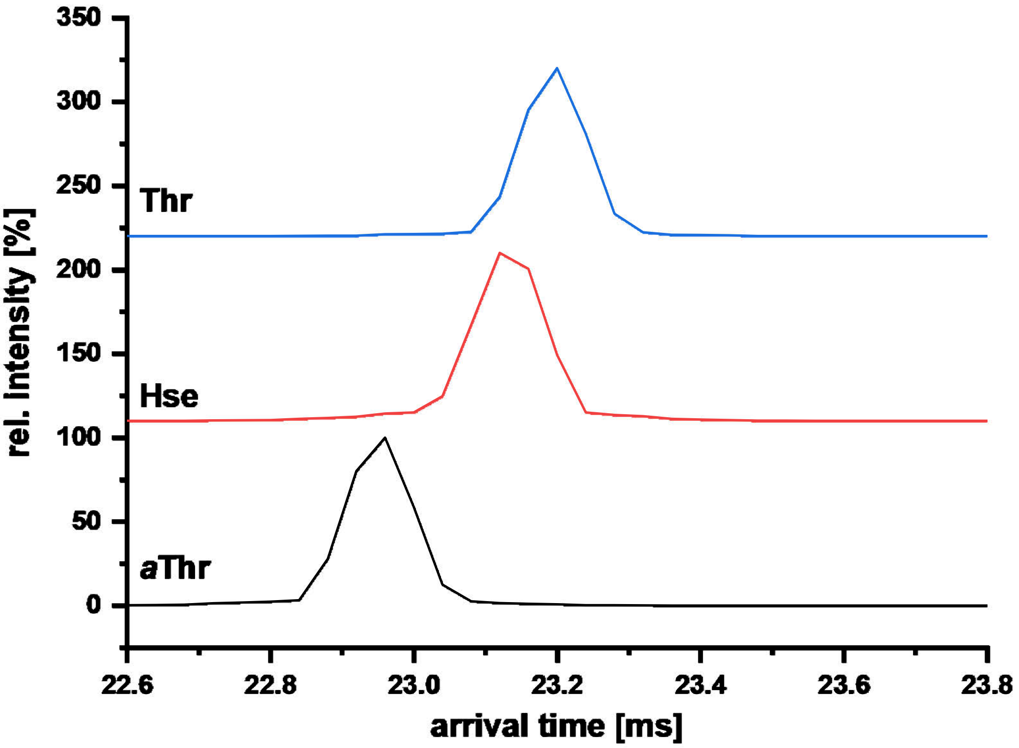

Figure 4. Arrival time spectra after high resolution demultiplexing of single threonine isomers. Extraction of the spectra at 302.150 *m/z* ± 15 mDa.

In this case, the higher degree of separation achieved is due to the impact of the OH group on the alkyl chain and the formation of a hydrogen bond with the HNCONH of AQC group preventing free rotation of the alkyl chain of the Thr isomers (see Supporting Information Figure S9, 11 and 12; Tables S9-11) therefore maintaining the ability to distinguish not only the L-enantiomers of the threonine isomers, but also D-*a*Thr from D-Hse and D-Thr in complex mixtures. Optimized structures of different conformers of Leu isomers in the gas phase and their calculated CCS_{N2} values can be found in Figure S13-15, Table S12-14. Corresponding information for some uncommon amino acids, sometimes present in non-ribosomal peptides ae summarized in Figure S16-18 and Table S15-20.

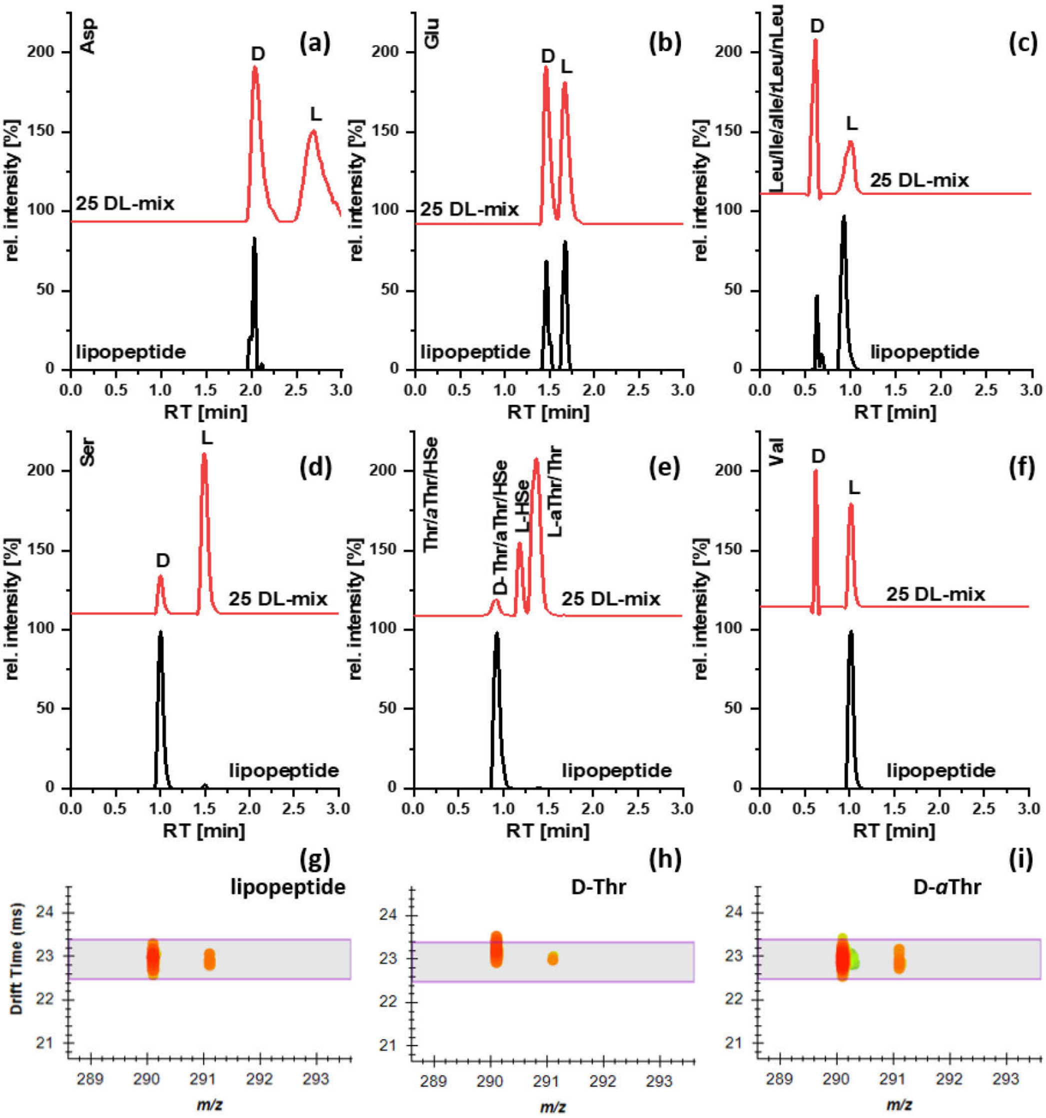

Figure 5. LC-IM-MS analysis of the lipopeptide hydrolysate THA 6.6 1367. (a-f) Extracted ion chromatograms (EICs) of the hydrolysate and 2D-contour plots of the (g) lipopeptide hydrolysate (h) D-Thr standard and (i) D-*a*Thr standard. The purple area indicates the IM-filtering range for D-*a*Thr. Tandem column: QN-AX + ZWIX(+) prototype core shell columns (3.0x50 mm, 2.7µm, respectively). Mobile phase A: 10 mM NH_4FA and 10 mM FA in ACN/MeOH/H_2O (49:49:2; v/v/v), mobile phase B: 50 mM NH_4FA and 50 mM FA in ACN/MeOH/H_2O (49:49:2; v/v/v); flow rate: 1.25 mL/min, gradient: 0-0.7 min 0-100 %B, 0.7-1.66 min 100 %B, 1.66-1.7 min 100-0 %B,1.7-3.0 min 0 %B, column temperature: 50°C

3.4.4.4 Application to natural lipopeptide samples

The LC-IM-MS method was subsequently employed to analyse a non-ribosomal lipopeptide, which often contain Thr or *a*Thr as well as any of Leu/Ile/*a*Ile following full hydrolysis to confirm the amino acid composition (known from MS sequencing and NMR of intact peptide) and determine absolute configurations of the individual amino acids. The results (Figure 5 and Table 3) demonstrate the capability of the method to assign the absolute configuration of the incorporated amino acids. It can be readily derived from the chromatograms that Asp and Ser (Figure 5a+d) are present in their D-configuration, Val as the L-enantiomer (Figure 5f), and Glu as a 1:1 mixture of D- and L-enantiomers (Figure 5b). While Glu appears only once in the lipopeptide sequence, the second equivalent originates from acidic hydrolysis of the side chain of Gln (deamidation). In the case of the investigated lipopeptide, the configuration could be assigned bioinformatically as L-Glu and D-Gln. In the case of the Thr isomers, the configuration could be assigned as the D-enantiomer. However, as LC-MS results alone could not elucidate which of D-Thr, D-*a*Thr or D-Hse isomers were present, the IM data were used as a second criteria for confirmation. Figure 5h+i shows results for individual standards of Thr and *a*Thr with different arrival times in the IM dimension (23.25 ms for Thr and 22.94 ms for *a*Thr). Comparison with the arrival times in the sample (22.94 ms, Figure 5g) confirms the identity as *a*Thr. With an excellent match to the LC retention time (0.92 min) and not to that of D-Thr (RT = 0.85 ± 0.012 min), we could assign this amino acid unequivocally as D-*a*Thr (Figure S19).

Table 3. Amino acid composition and determined configuration of the lipopeptide sample.

Amino acid	Asp	Thr	Ser	Leu	Gln	Val	Glu
Number	1	1	1	5	1	1	1
Configuration	D	D-*a*Thr	D	n/a[a]	D[b]	L	L[b]

[a] Multiple Leu present with both D- and L-configuration. [b] Gln is deamidated through the hydrolysis conditions, but L-Gln and D-Glu configuration was determined bioinformatically.

In attempts to assign the absolute configuration of the five Leu isomers in the lipopeptide sample, overlays of sample and reference standard LC chromatograms (Supporting Information Figure S20a and b for corresponding D- and L-amino acids) were used. Comparison of the retention time of the L-enantiomer peak in the sample with the individual L-amino acid standards of the other isomers reveals a good match with L-Leu, while there is a significant mismatch with the other isomers including L-Ile and L-*a*Ile (Figure S20b, Figure S21). Likewise, the comparison with D-enantiomer standards reveal best agreement with D-Leu, but this result has to be taken with care due to the very minor retention time differences to D-Ile and D-*a*Ile and the insignificant differences in IM arrival times for this suite of isomers. Confirmation of the absolute configuration would need further verification, e.g. enantioselective 2D-LC [23] or accepting longer run times with the current method. For this case, the correct assignment was made using NMR data, which suggested Leu as amino acid residue in the lipopeptide. An L:D-enantiomer ratio of 4:1 can be derived from the peak area ratio in Figure 5c. The position of the single D-Leu amino acid in the lipopeptide remains open and needs further complementary investigation. However, this is beyond the present study.

The somatostatin-mimicking therapeutic peptide octreotide (Figure S22a) was also analyzed with absolute configurations of the amino acids in this peptide agreeing with the results of the specifications (Figure S22b-g). In this case, for Cys-IAA-AQC (Figure S22b) and Lys-bis-AQC (Figure S20c) the L-enantiomer was found. Two equivalents of Phe were confirmed and could be assigned as one D- and one L-enantiomer (Figure S22d). In case of the Thr isomers, either L-*a*Thr or L-Thr were suggested based on LC retention time (Figure S22e). IMS data (Figure S22h-j) together with LC retention time allow unequivocal identification as L-Thr because RT and arrival time (1.38 min, 23.25 ms, respectively) in the octreotide hydrolysate sample match perfectly with the L-Thr reference (1.38 min, 23.25 ms), but not L-*a*Thr (1.33 min, 22.94 ms). It indicates that in critical cases, IM-MS may help to reliably determine absolute configurations in peptides.

3.4.4.5 Quantitative method performance

As the absolute concentrations of individual amino acids can vary greatly in real samples, the quantitative capabilities of enantioselective LC-IM-MS method was evaluated using an 8-level calibration (Table S3). To this end, an external calibration with stable isotope labelled internal standards (SIL-IS) was used. The molar concentrations of the SIL-IS mixture range from 12.1 mol% for L-Ala to only 0.4 mol% for L-His, respectively (Table S2). Due to the use of a racemisation procedure described elsewhere [21] the SIL-IS signal intensities for some isomers were too low and (in these cases) a surrogate IS strategy with normalization to the more intense L-U-$^{13}C^{15}N$-Val signal was used. The calibration functions together with their linearity (in terms of R²), limit of detection (LOD), limit of quantification (LOQ), linear range, the accuracy (as % recovery) and precision (% RSD) of a quality control sample (1 µM, n = 3) and the applied quantification method for D- and L-amino acids are summarized in Supporting Information Table S21 and Table S22. The majority of the D-amino acids meet the criteria for accuracy (85-115 %) and precision (≤ 15 %) as defined by the FDA [47]. Only D-Ala (16.1 %) and D-Thr (20.2 %) do not meet the precision criteria which might originate from insufficient correction by the surrogate IS (Table S21). Similarly, all L-amino acids meet both the accuracy and precision criteria except for L-His (accuracy of 83.2 %) which might also originate from insufficient correction by the surrogate IS (Table S22). As previously stated, the resolution between D-Leu and D-Ile as well as L-Leu and L-Ile with this rapid method is not sufficient for accurate quantification and only the sum of the corresponding constitutional Leu/Ile isomer pairs can be determined. Quantification of Cys was not possible as some sample preparation problems occurred and alkylation seem to be incomplete. The LOQ calculated according to ICH guideline Q2(R1) [48] ranges from 0.16 µM for L-Phe up to 0.72 µM for D-Asp, respectively. Overall, the performance appears adequate for application of relative quantification of the amino acid composition in synthetic and natural peptides.

3.4.5 Conclusions

The in-line coupled tandem column consisting of two prototype core shell chiral columns showed superior resolution compared to the single columns for a set of 24 amino acid enantiomer pairs, and diastereomers and constitutional isomers of leucine and threonine. New insights into the capabilities of IM for resolving derivatized amino acid enantiomers could be derived from experimental results and additional computational assessments. Generally, IM resolution between key amino acid isomers was either equal or reduced upon AQC-derivatization. While the combination of DTIM separation and HRdm (or another type of IM analyser with high native resolving power) can resolve Thr, *a*Thr and Hse in a rapid analysis method, the mobility differences for AQC-derivatized Leu isomers are too small to be addressed by different IM technologies given the simultaneous requirements of comprehensive sampling of the fast LC separation (i.e., LC FWHM of < 5 s) and high IM resolving powers of > 200 for ions across a wide mass range. Overall, the LC-IM-MS method demonstrates its capability to be used for high throughput quantitative analysis of amino acid enantiomers in pharmaceutical and nutritional products as well as food samples.

3.4.6 References

[1] C. Ollivaux, D. Soyez, J.-Y. Toullec, Biogenesis of d-amino acid containing peptides/proteins: where, when and how?, J. Pept. Sci., 20 (8) (2014) 595-612.

[2] G. Jahanshah, Q. Yan, H. Gerhardt, Z. Pataj, M. Lämmerhofer, I. Pianet, M. Josten, H.-G. Sahl, M.W. Silby, J.E. Loper, H. Gross, Discovery of the Cyclic Lipopeptide Gacamide A by Genome Mining and Repair of the Defective GacA Regulator in Pseudomonas fluorescens Pf0-1, J. Nat. Prod., 82 (2) (2019) 301-308.

[3] S. Kapil, V. Sharma, d-Amino acids in antimicrobial peptides: a potential approach to treat and combat antimicrobial resistance, Can. J. Microbiol., 67 (2) (2021) 119-137.

[4] L. Wang, N. Wang, W. Zhang, X. Cheng, Z. Yan, G. Shao, X. Wang, R. Wang, C. Fu, Therapeutic peptides: current applications and future directions, Signal Transduction and Targeted Therapy, 7 (1) (2022) 48.

[5] H.M. Werner, C.C. Cabalteja, W.S. Horne, Peptide Backbone Composition and Protease Susceptibility: Impact of Modification Type, Position, and Tandem Substitution, ChemBioChem, 17 (8) (2016) 712-718.

[6] L. Piubelli, G. Murtas, V. Rabattoni, L. Pollegioni, The Role of D-Amino Acids in Alzheimer's Disease, Journal of Alzheimer's Disease, 80 (2021) 475-492.

[7] J.J.A.J. Bastings, H.M. van Eijk, S.W. Olde Damink, S.S. Rensen, d-amino Acids in Health and Disease: A Focus on Cancer, Nutrients, 11 (9) (2019) 2205.

[8] C. Calderón, M. Lämmerhofer, Enantioselective metabolomics by liquid chromatography-mass spectrometry, J. Pharm. Biomed. Anal., 207 (2022) 114430.

[9] M. Danielsen, C. Nebel, T.K. Dalsgaard, Simultaneous Determination of L- and D-Amino Acids in Proteins: A Sensitive Method Using Hydrolysis in Deuterated Acid and Liquid Chromatography–Tandem Mass Spectrometry Analysis, Foods, 9 (3) (2020) 309.

[10] Y. Nakano, M. Taniguchi, Y. Umakoshi, D. Watai, E. Fukusaki, High-Throughput LC-MS/MS Method for Chiral Amino Acid Analysis Without Derivatization, in: M.A. Alterman (Ed.), Amino Acid Analysis: Methods and Protocols, Springer New York, New York, NY, 2019, pp. 253-261.

[11] J. Horak, M. Lämmerhofer, Stereoselective separation of underivatized and 6-aminoquinolyl-N-hydroxysuccinimidyl carbamate derivatized amino acids using zwitterionic quinine and quinidine type stationary phases by liquid chromatography–High resolution mass spectrometry, J. Chromatogr. A, 1596 (2019) 69-78.

[12] K. Petritis, A. Valleix, C. Elfakir, M. Dreux, Simultaneous analysis of underivatized chiral amino acids by liquid chromatography–ionspray tandem mass spectrometry using a teicoplanin chiral stationary phase, J. Chromatogr. A, 913 (1) (2001) 331-340.

[13] T.L. Xiao, E. Tesarova, J.L. Anderson, M. Egger, D.W. Armstrong, Evaluation and comparison of a methylated teicoplanin aglycone to teicoplanin aglycone and natural teicoplanin chiral stationary phases, J. Sep. Sci., 29 (3) (2006) 429-445.

[14] Z. Pataj, I. Ilisz, R. Berkecz, A. Misicka, D. Tymecka, F. Fülöp, D.W. Armstrong, A. Péter, Comparison of performance of Chirobiotic T, T2 and TAG columns in the separation of β2- and β3-homoamino acids, J. Sep. Sci., 31 (21) (2008) 3688-3697.

[15] L. Miller, L. Yue, Chiral separation of underivatized amino acids in supercritical fluid chromatography with chiral crown ether derived column, Chirality, 32 (7) (2020) 981-989.

[16] G. Mazzoccanti, S. Manetto, A. Ricci, W. Cabri, A. Orlandin, M. Catani, S. Felletti, A. Cavazzini, M. Ye, H. Ritchie, C. Villani, F. Gasparrini, High–throughput enantioseparation of Nα–fluorenylmethoxycarbonyl proteinogenic amino acids through fast chiral chromatography on zwitterionic-teicoplanin stationary phases, J. Chromatogr. A, 1624 (2020) 461235.

[17] F. Ianni, R. Sardella, A. Lisanti, A. Gioiello, B.T. Cenci Goga, W. Lindner, B. Natalini, Achiral–chiral two-dimensional chromatography of free amino acids in milk: A promising tool for detecting different levels of mastitis in cows, J. Pharm. Biomed. Anal., 116 (2015) 40-46.

[18] S. Ferré, V. González-Ruiz, J. Zangari, S. Girel, J.-C. Martinou, R. Sardella, S. Rudaz, Separation and determination of cysteine enantiomers in plasma after derivatization with 4-fluoro-7-nitrobenzofurazan, J. Pharm. Biomed. Anal., 209 (2022) 114539.

[19] C. Ishii, T. Akita, M. Mita, T. Ide, K. Hamase, Development of an online two-dimensional high-performance liquid chromatographic system in combination with tandem mass spectrometric detection for enantiomeric analysis of free amino acids in human physiological fluid, J. Chromatogr. A, 1570 (2018) 91-98.

[20] M. Oyaide, A. Furusho, C. Ishii, T. Akita, M. Mita, T. Ide, K. Hamase, Development of an off-line heart cutting two-dimensional HPLC system for enantioselective analysis of serine, threonine and allo-threonine in human physiological fluids, J. Pharm. Biomed. Anal., 217 (2022) 114807.

[21] J. Horak, M. Lämmerhofer, Derivatize, Racemize, and Analyze—an Easy and Simple Procedure for Chiral Amino Acid Standard Preparation for Enantioselective Metabolomics, Anal. Chem., 91 (12) (2019) 7679-7689.

[22] R. Karongo, J. Horak, M. Lämmerhofer, Comprehensive Online Reversed-Phase × Chiral Two-Dimensional Liquid Chromatography-Mass Spectrometry with Data-Independent Sequential Window Acquisition of All Theoretical Fragment-Ion Spectra-Acquisition for Untargeted Enantioselective Amino Acid Analysis, Anal. Chem., 94 (49) (2022) 17063-17072.

[23] R. Karongo, M. Ge, C. Geibel, J. Horak, M. Lämmerhofer, Enantioselective multiple heart cutting online two-dimensional liquid chromatography-mass spectrometry of all proteinogenic amino acids with second dimension chiral separations in one-minute time scales on a chiral tandem column, Anal. Chim. Acta, 1180 (2021) 338858.

[24] Y. Nagata, T. Akita, C. Ishii, M. Oyaide, M. Mita, T. Ide, K. Hamase, Development of an enantioselective three-dimensional HPLC system for the determination of alanine, valine, isoleucine, allo-isoleucine and leucine in human plasma and urine, Journal of Pharmaceutical and Biomedical Analysis Open, 2 (2023) 100013.

[25] Q. Wu, J.-Y. Wang, D.-Q. Han, Z.-P. Yao, Recent advances in differentiation of isomers by ion mobility mass spectrometry, TrAC, Trends Anal. Chem., 124 (2020) 115801.

[26] E. Zlibut, J.C. May, J.A. McLean, Enantiomer Differentiation of Amino Acid Stereoisomers by Structural Mass Spectrometry Using Noncovalent Trinuclear Copper Complexes, J. Am. Soc. Mass. Spectrom., 33 (6) (2022) 996-1002.

[27] L. Gu, F. Wu, S. Yang, F. Xu, X. Dai, Y. Jiang, X. Fang, S. Yu, C.-F. Ding, Direct distinction of ibuprofen and flurbiprofen enantiomers by ion mobility mass spectrometry of their ternary complexes with metal cations and cyclodextrins in the gas phase, J. Sep. Sci., 44 (12) (2021) 2474-2482.

[28] C. Xie, L. Gu, Q. Wu, L. Li, C. Wang, J. Yu, K. Tang, Effective Chiral Discrimination of Amino Acids through Oligosaccharide Incorporation by Trapped Ion Mobility Spectrometry, Anal. Chem., 93 (2) (2021) 859-867.

[29] R. Pérez-Míguez, B. Bruyneel, M. Castro-Puyana, M.L. Marina, G.W. Somsen, E. Domínguez-Vega, Chiral Discrimination of DL-Amino Acids by Trapped Ion Mobility Spectrometry after Derivatization with (+)-1-(9-Fluorenyl)ethyl Chloroformate, Anal. Chem., 91 (5) (2019) 3277-3285.

[30] J.M. Will, A. Behrens, M. Macke, C.D. Quarles, Jr., U. Karst, Automated Chiral Analysis of Amino Acids Based on Chiral Derivatization and Trapped Ion Mobility–Mass Spectrometry, Anal. Chem., 93 (2) (2021) 878-885.

[31] Y. Li, B. Zhou, K. Wang, J. Zhang, W. Sun, L. Zhang, Y. Guo, Powerful Steroid-Based Chiral Selector for High-Throughput Enantiomeric Separation of α-Amino Acids Utilizing Ion Mobility–Mass Spectrometry, Anal. Chem., 93 (40) (2021) 13589-13596.

[32] C. Xie, Y. Chen, X. Wang, Y. Song, Y. Shen, X. Diao, L. Zhu, J. Wang, Z. Cai, Chiral derivatization-enabled discrimination and on-tissue detection of proteinogenic amino acids by ion mobility mass spectrometry, Chemical Science, 13 (47) (2022) 14114-14123.

[33] J.N. Dodds, J.C. May, J.A. McLean, Investigation of the Complete Suite of the Leucine and Isoleucine Isomers: Toward Prediction of Ion Mobility Separation Capabilities, Anal. Chem., 89 (1) (2017) 952-959.

[34] D.C. Patel, Z.S. Breitbach, M.F. Wahab, C.L. Barhate, D.W. Armstrong, Gone in Seconds: Praxis, Performance, and Peculiarities of Ultrafast Chiral Liquid Chromatography with Superficially Porous Particles, Anal. Chem., 87 (18) (2015) 9137-9148.

[35] O.H. Ismail, A. Ciogli, C. Villani, M. De Martino, M. Pierini, A. Cavazzini, D.S. Bell, F. Gasparrini, Ultra-fast high-efficiency enantioseparations by means of a teicoplanin-based chiral stationary phase made on sub-2μm totally porous silica particles of narrow size distribution, J. Chromatogr. A, 1427 (2016) 55-68.

[36] G.L. Losacco, H. Wang, I.A. Haidar Ahmad, J. DaSilva, A.A. Makarov, I. Mangion, F. Gasparrini, M. Lämmerhofer, D.W. Armstrong, E.L. Regalado, Enantioselective UHPLC Screening Combined with In Silico Modeling for Streamlined Development of Ultrafast Enantiopurity Assays, Anal. Chem., 94 (3) (2022) 1804-1812.

[37] K. Schmitt, U. Woiwode, M. Kohout, T. Zhang, W. Lindner, M. Lämmerhofer, Comparison of small size fully porous particles and superficially porous particles of chiral anion-exchange type stationary phases in ultra-high performance liquid chromatography: effect of particle and pore size on chromatographic efficiency and kinetic performance, J. Chromatogr. A, 1569 (2018) 149-159.

[38] C. Geibel, K. Dittrich, U. Woiwode, M. Kohout, T. Zhang, W. Lindner, M. Lämmerhofer, Evaluation of superficially porous particle based zwitterionic chiral ion exchangers against fully porous particle benchmarks for enantioselective ultra-high performance liquid chromatography, J. Chromatogr. A, 1603 (2019) 130-140.

[39] S.M. Stow, T.J. Causon, X. Zheng, R.T. Kurulugama, T. Mairinger, J.C. May, E.E. Rennie, E.S. Baker, R.D. Smith, J.A. McLean, S. Hann, J.C. Fjeldsted, An Interlaboratory Evaluation of Drift Tube Ion Mobility–Mass Spectrometry Collision Cross Section Measurements, Anal. Chem., 89 (17) (2017) 9048-9055.

[40] J.C. May, R. Knochenmuss, J.C. Fjeldsted, J.A. McLean, Resolution of Isomeric Mixtures in Ion Mobility Using a Combined Demultiplexing and Peak Deconvolution Technique, Anal. Chem., 92 (14) (2020) 9482-9492.

[41] M. Frisch, G. Trucks, H.B. Schlegel, G. Scuseria, M. Robb, J. Cheeseman, G. Scalmani, V. Barone, G. Petersson, H. Nakatsuji, Gaussian 16, Gaussian, Inc. Wallingford, CT, 2016.

[42] C. Ieritano, J. Crouse, J.L. Campbell, W.S. Hopkins, A parallelized molecular collision cross section package with optimized accuracy and efficiency, Analyst, 144 (5) (2019) 1660-1670.

[43] R. Kimura, H. Tsujimura, M. Tsuchiya, S. Soga, N. Ota, A. Tanaka, H. Kim, Development of a cognitive function marker based on D-amino acid proportions using new chiral tandem LC-MS/MS systems, Scientific Reports, 10 (1) (2020) 804.

[44] I. D'Acquarica, F. Gasparrini, B. Giannoli, E. Badaloni, B. Galletti, F. Giorgi, M.O. Tinti, A. Vigevani, Enantio- and chemo-selective HPLC separations by chiral–achiral tandem-columns approach: the combination of CHIROBIOTIC TAG™ and SCX columns for the analysis of propionyl carnitine and related impurities, J. Chromatogr. A, 1061 (2) (2004) 167-173.

[45] K.E. Butler, J.N. Dodds, T. Flick, I.D.G. Campuzano, E.S. Baker, High-Resolution Demultiplexing (HRdm) Ion Mobility Spectrometry–Mass Spectrometry for Aspartic and Isoaspartic Acid Determination and Screening, Anal. Chem., 94 (16) (2022) 6191-6199.

[46] T. Mairinger, R. Kurulugama, T.J. Causon, G. Stafford, J. Fjeldsted, S. Hann, Rapid screening methods for yeast sub-metabolome analysis with a high-resolution ion mobility quadrupole time-of-flight mass spectrometer, Rapid Commun. Mass Spectrom., 33 (S2) (2019) 66-74.

[47] FDA, Bioanalytical Method Validation - Guidance for Industry, in: U.S.D.o.H.a.H. Services (Ed.) Food and Drug Administration, 2018.

[48] ICH, ICH Harmonised Tripartite Guideline - Validation of Analytical Procedures: Text and Methodology Q2(R1), 2005, pp. 1-13.

3.4.7 Supporting Information

Three-Minute Enantioselective Amino Acid Analysis by Ultra-High Performance Liquid Chromatography Drift Tube Ion Mobility-Mass Spectrometry Using a Chiral Core-Shell Tandem Column Approach

Simon Jaag[a], Younes Valadbeigi[b], Tim Causon[c,*], Harald Gross[d], Michael Lämmerhofer[a,*]

[a] Pharmaceutical (Bio-)Analysis, Institute of Pharmaceutical Sciences, University of Tuebingen, Auf der Morgenstelle 8, 72076 Tuebingen, Germany

[b] Department of Chemistry, Faculty of Science, Imam Khomeini International University, 3414896818 Qazvin, Iran

[c] University of Natural Resources and Life Sciences, Vienna Department of Chemistry, Institute of Analytical Chemistry, Muthgasse 18, 1190 Vienna, Austria

[d] Pharmaceutical Biology, Institute of Pharmaceutical Sciences, University of Tuebingen, 72076 Tuebingen, Germany

*Corresponding authors:

E-Mail address: michael.laemmerhofer@uni-tuebingen.de (M. Lämmerhofer)

E-Mail address: tim.causon@boku.ac.at (T. Causon)

Analytical Chemistry 2024

DOI: 10.1021/acs.analchem.3c05426

3.4.7.1 Experimental

3.4.7.1.1 Materials

Table S13. Amino acid reference standards with corresponding 3-letter and 1-letter code (if available) for the proteinogenic (1-20) and isobaric amino acids (21-25).

1. Aspartic acid (D, Asp)	10. Arginine (R, Arg)	19. Alanine (A, Ala)
2. Methionine (M, Met)	11. Histidine (H, His)	20. Threonine (T, Thr)
3. Asparagine (N, Asn)	12. Isoleucine (I, Ile)	21. *allo*-Threonine (*a*Thr)
4. Glutamine (Q, Gln)	13. Leucine (L, Leu)	22. Homoserine (Hse)
5. Tryptophan (W, Trp)	14. Cysteine (C, Cys)	23. *allo*-Isoleucine (*a*Ile)
6. Tyrosine (Y, Tyr)	15. Glycine (G, Gly)	24. *tert*-Leucine (*t*Leu)
7. Glutamic acid (E, Glu)	16. Valine (V, Val)	25. *nor*-Leucine (*n*Leu)
8. Lysine (K, Lys)	17. Serine (S, Ser)	
9. Proline (P, Pro)	18. Phenylalanine (F, Phe)	

Table S14. Composition of the "cell-free" amino acid mix L-U-^{13}C-^{15}N based on the certificate of analysis from Cambridge Isotope Laboratories.

amino acid	molar [%]	weight [%]
Ala	12.1	8.2
Arg	2.8	3.7
Asn	4.0	4.0
Asp	4.6	4.6
Cys	0.6	1.1
Gln	3.7	4.1
Glu	3.4	3.7
Gly	7.0	3.9
His	0.4	0.4
Ile	7.0	7.0
Leu	11.5	11.5
Lys	9.6	10.7
Met	1.1	1.3
Phe	5.9	7.4
Pro	2.7	2.4
Ser	3.2	2.5
Thr	2.8	2.5
Trp	5.5	8.6
Tyr	3.1	4.3
Val	9.0	8.0

3.4.7.1.2 Data Analysis with LC-IM-MS data pre-processing

Standard workflow

1. Using the PNNL Pre-processor, datafiles were subject to summing of adjacent frames and minimum pulse coverage set to 50% for de-multiplexing.
2. Datafiles were mass re-calibrated with purine and HP-921 used as reference masses.
3. Datafiles were *CCS* calibrated using vendor software (IM-MS Browser).
4. Peak-picking was performed using vendor software (IM-MS Browser).

High-resolution demultiplexing (HRdm) workflow

The application of high-resolution demultiplexing was already described by Butler et al. [1] and May et al. [2].

1. Using the PNNL Pre-processor, 3-point interpolation of arrival time spectra was applied in addition to the standard demultiplexing workflow settings. No summing of adjacent frames was used.
5. Peak-picking was performed using vendor software (IM-MS Browser).
2. Each feature list (per data file) was exported into the vendor *.CEF format and HRdm applied using the following settings: HR processing level – medium; m/z width multiplier – 6; IF multiplier – 0.95.
3. Datafiles were mass re-calibrated with purine and HP-921 used as reference masses.
4. HRdm datafiles were *CCS* calibrated using vendor software (IM-MS Browser).
5. Peak-picking for HRdm datafiles was performed using vendor software (IM-MS Browser).

3.4.7.1.3 Sample Preparation

Automatized sample preparation using the OT-2 pipette robot

An OT-2 pipette robot from Opentrons (New York City, NY, USA) was used and equipped with a P20 8-channel Gen 2 (20 µL), a P300 8-channel Gen 2 (300 µL) pipette and a temperature module Gen 2. The original Opentrons pipette tips for the 20 µL and 300 µL pipettes were used. A 12-well reservoir with 22 mL wells (Starlab, Hamburg, Germany), 96-well PCR plate with 200 µL wells (HSP9601) from Bio-Rad (Feldkirchen, Germany) and a PierceASeal Foil heat sealable seal (Sigma-Aldrich) were used.

Due to high consumption of pipette tips the protocol was divided into two steps: First the alkylation was performed and second the AQC-derivatization and SIL-IS spiking was performed. All mentioned transfer volumes are per well. Tips were changed before each aspiration step, tip position for aspiration was 1 mm above the bottom and for dispensing 0.5 mm above the bottom. The “blowout” function was used at the dispensing step at the destination well. For mixing of the solutions the mixing function was used which comprises of a specified number of aspiration and dispensing steps with a pre-defined mixing volume. After each heating step the well plate was centrifuged (Eppendorf Centrifuge 5415 R) at 3,000 rpm for 3 min to recover condensate from the sealing foil. A calibration series was prepared manually with the concentrations levels as describe in Table S15**.**

Alkylation

The starting deck configuration is shown in Figure S14. Samples and blanks (10 µL) were transferred from the sample plate to the reaction chamber plate, then 5 µL of the DTT solution and 70 µL borate buffer were added and a mixing step with 40 µL mix volume was done three times. The protocol was paused and the reaction chamber was sealed with an aluminium foil to prevent evaporation and the plate was put onto the heater block module (slot 10) and reduction was done for 10 min at 55°C. After alkylation the plate was cooled down, the foil was removed and the plate put back to its original slot 3. The protocol was continued with the transfer of 10 µL of IAA solution, then a mixing with 20 µL mixing volume and three replications was performed. The plate was sealed and transferred to the heater module and alkylation was done for 10 min at 55°C. After alkylation the plate was moved back to slot 3 and cooled down to room temperature. The foil was removed and 5 µL DTT was added and mixing with a 20 µL volume was performed in triplicate. The plate was sealed again and the alkylation quenched for 10 min at 55°C on the heater module. After quenching the plate was moved back, cooled down and the foil was removed. The final deck state configuration is shown in Figure S15.

AQC derivatization and SIL-IS spiking

The starting deck for AQC derivatization and SIL-IS spiking is shown in Figure S16. The alkylated sample plate from the previous protocol step was used and AQC-derivatized and racemised SIL-IS was added to column 12. In the first step the samples and blanks (11.1 µL) from the alkylated sample plate (slot 3) were transferred to the derivatization chamber plate (slot 2). Then 78.9 µL borate buffer and 10 µL AQC solution were transferred and mixed with 20 µL mixing volume three times. The plate was sealed and transferred to the temperature module and derivatization was done for 10 min at 55°C. After derivatization the plate was moved back to slot 3, cooled down and the foil was removed. The SIL-IS (8 µL) was transferred to two new well plates ("IS spiked sample" and "IS spiked sample 2") to obtain duplicate well plates (one for initial analysis the second for storage). The AQC-derivatized samples and blanks (72 µL) were transferred to the SIL-IS containing plates and mixing performed three times with 65 µL mixing volume. The final deck state configuration is shown in Figure S17. The sample plates can be directly analysed using the 96-well plates seal by a foil or submitted for lyophilisation for long-term storage.

Long term storage and reconstitution prior analysis

For long-term storage the samples can be transferred to 1.5 mL eppi tubes and lyophilised at 0.050 mbar overnight using a FreeZone Benchtop Freeze Dryer 4.5 L, -105°C from Labconco (Kansas City, MO, USA). Prior usage, the samples were reconstituted with 100 µL H2O/MeOH 1:1 (v/v), vortexed 60 s, centrifuged at 3,000 g for 60 s and finally transferred to an HPLC vial with micro insert. Lyophilised samples can be stored a -20°C.

The OT-2 protocols are attached to the supplementary protocols and can be viewed and adapted at https://designer.opentrons.com/

Table S15. Concentration levels before and after AQC-derivatization.

concentration level	c(prior derivat-ization) [µM]	c(final) [µM]
C8	1,000	10
C7	200	2
C6	150	1.5
C5	80	0.8
C4	60	0.6
C3	40	0.4
C2	20	0.2
C1	10	0.1

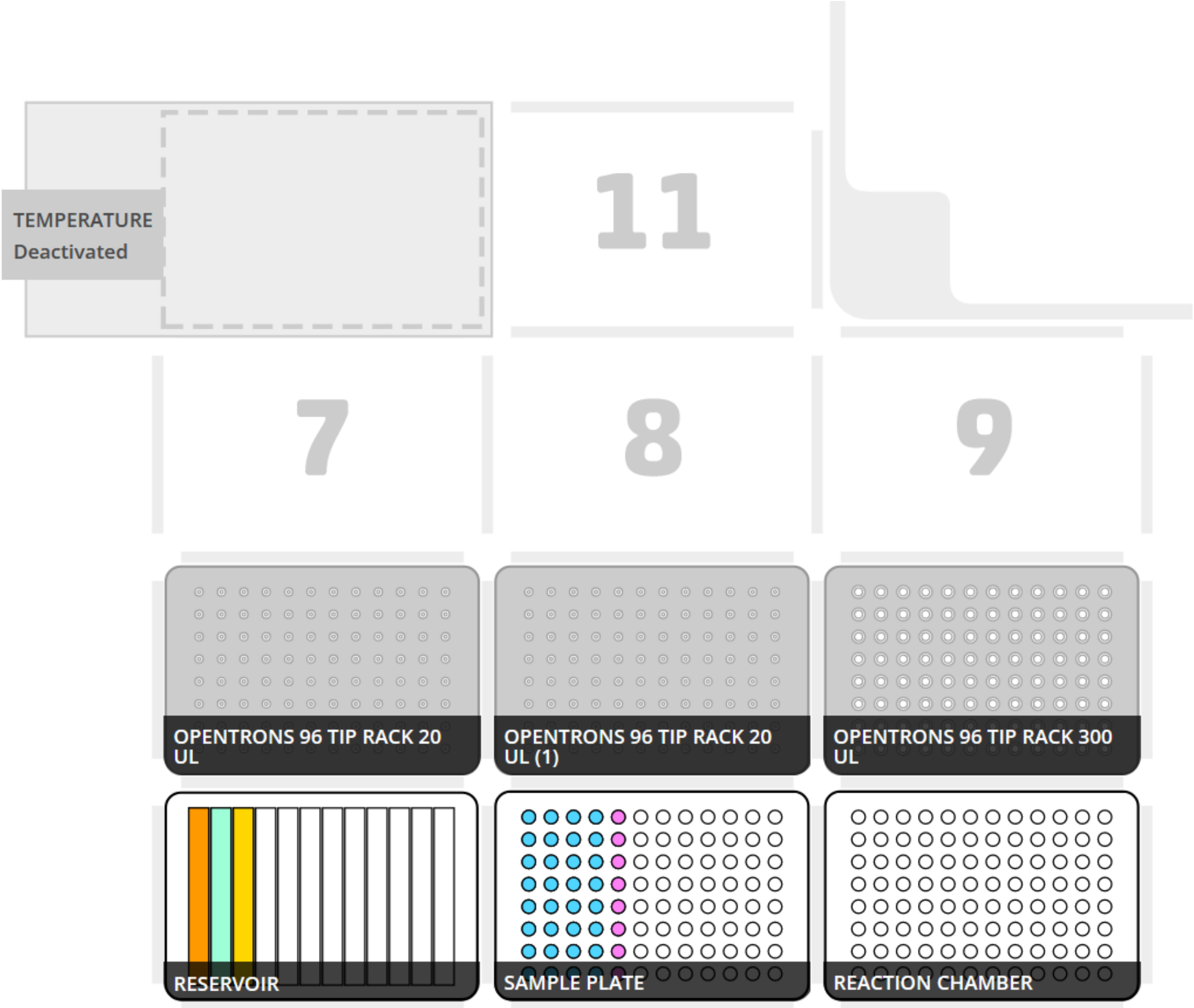

Figure S14. Starting deck configuration for the alkylation step of the amino acids. The reservoir (bottom left, slot 1) contains the 10 mL 0.4 M borate buffer pH 8.8 (well 1), 10 mL 10 mM IAA solution (well 2) and 10 mL 10 mM DTT solution (well 3). The sample plate (bottom centre, slot 1) contains the samples (calibrants, QCs, columns 1 to 4) and blanks (column 5).

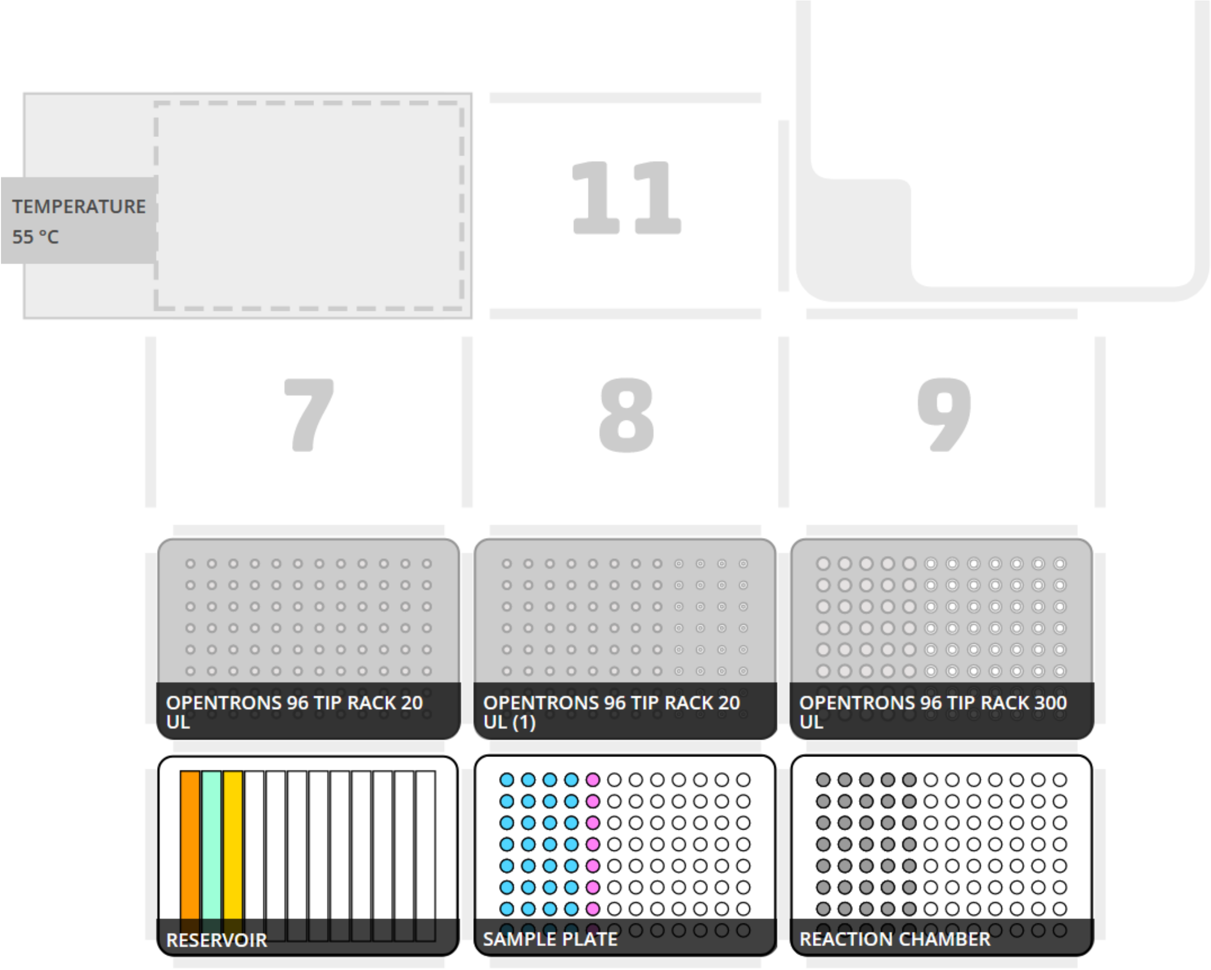

Figure S15. Final deck state after complete alkylation.

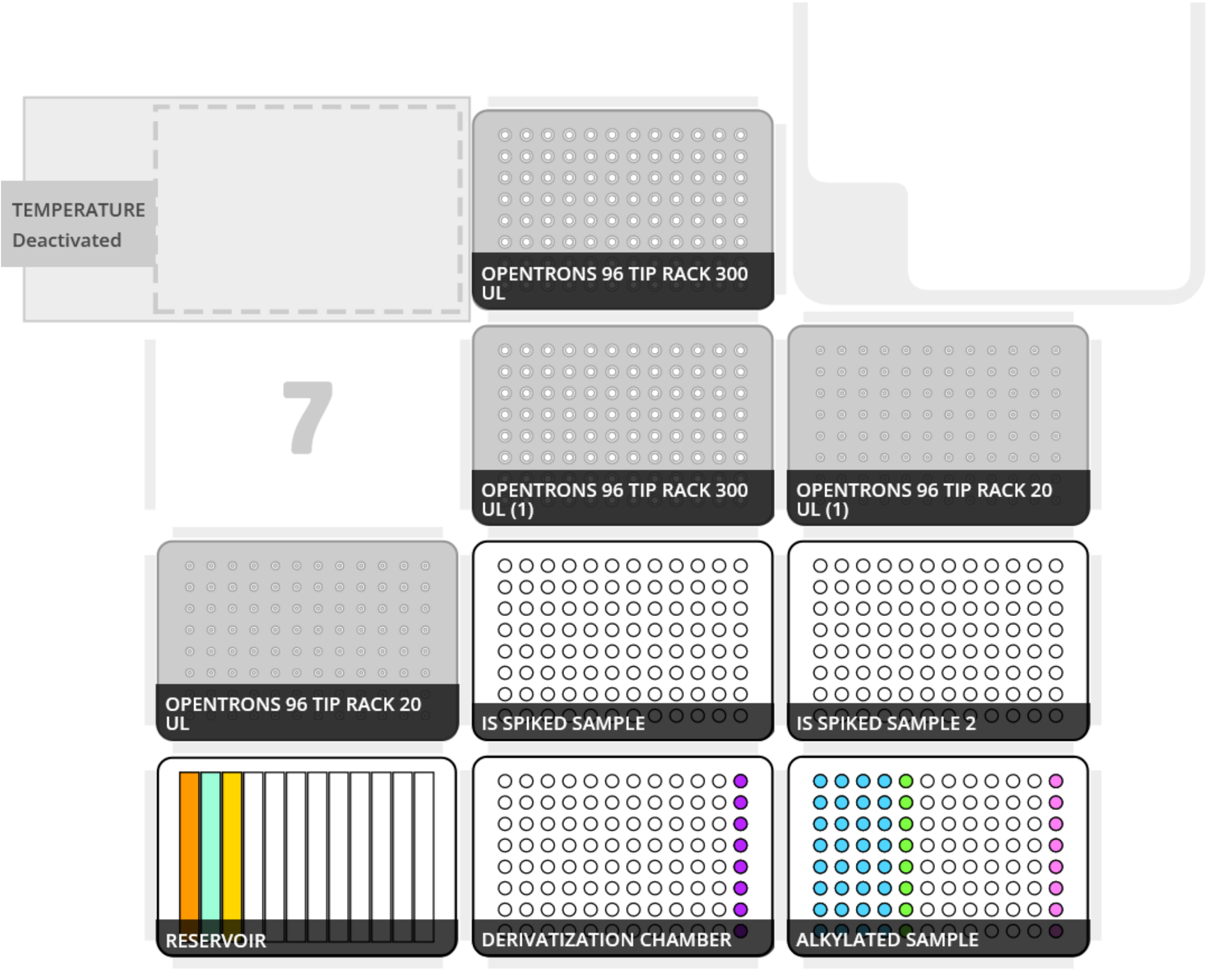

Figure S16. Start deck state of the AQC-derivatization step. The reservoir (bottom left, slot 1) contains the 10 mL 0.4 M borate buffer pH 8.8 (well 1), 10 mL 10 mM IAA solution (well 2) and 10 mL 10 mM DTT solution (well 3). The derivatization chamber (bottom centre, slot 2) contains 120 µL 14 mM AQC reagent (dissolved in ACN) in each well of column 12. The alkylated sample plate originates from the alkylation step 120 µL of the AQC-derivatized and racemised SIL-IS mix were added in column 12 prior running the protocol.

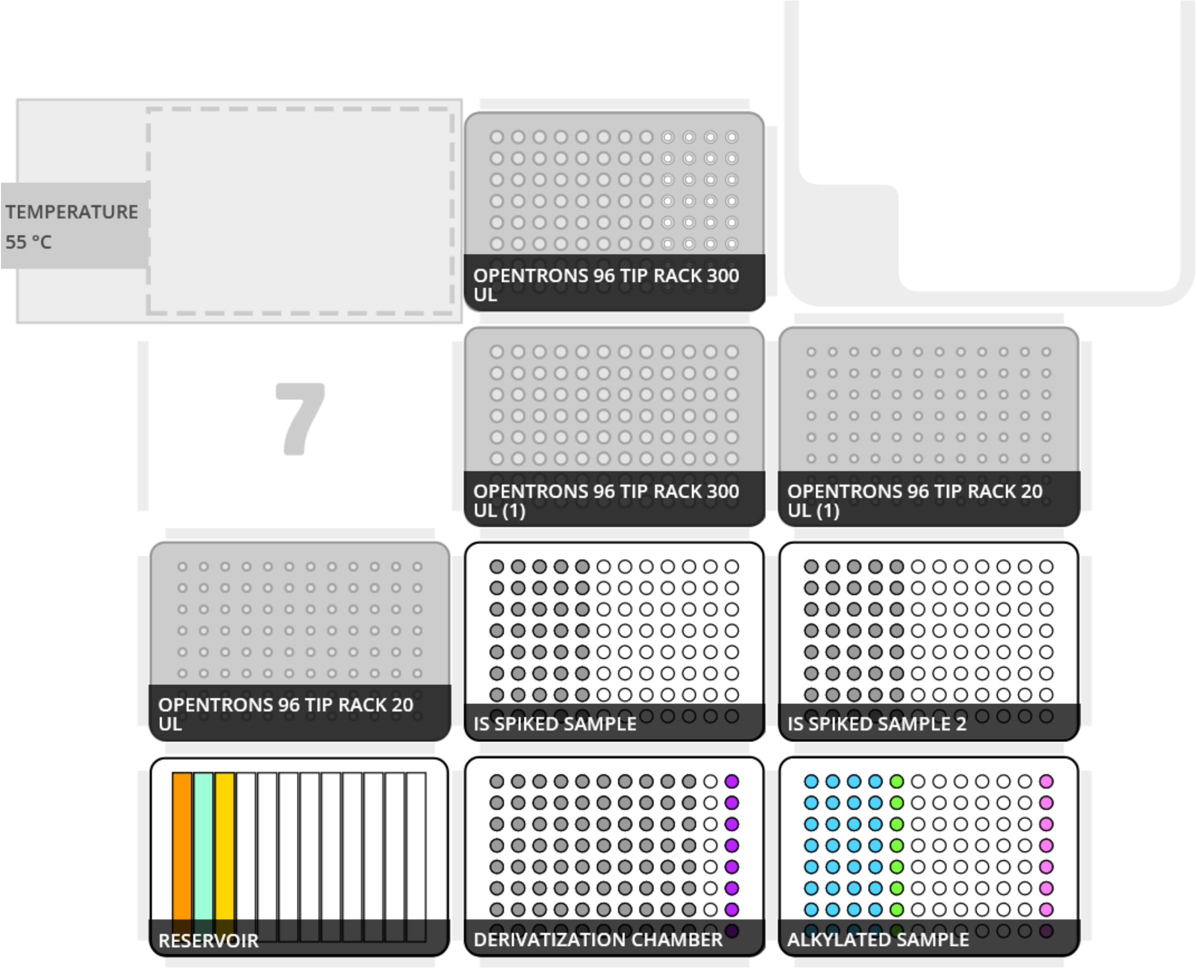

Figure S17. Final deck state after AQC-derivatization and IS spiking.

3.4.7.2 Results and discussion

3.4.7.2.1 Separation of enantiomers by single and tandem columns

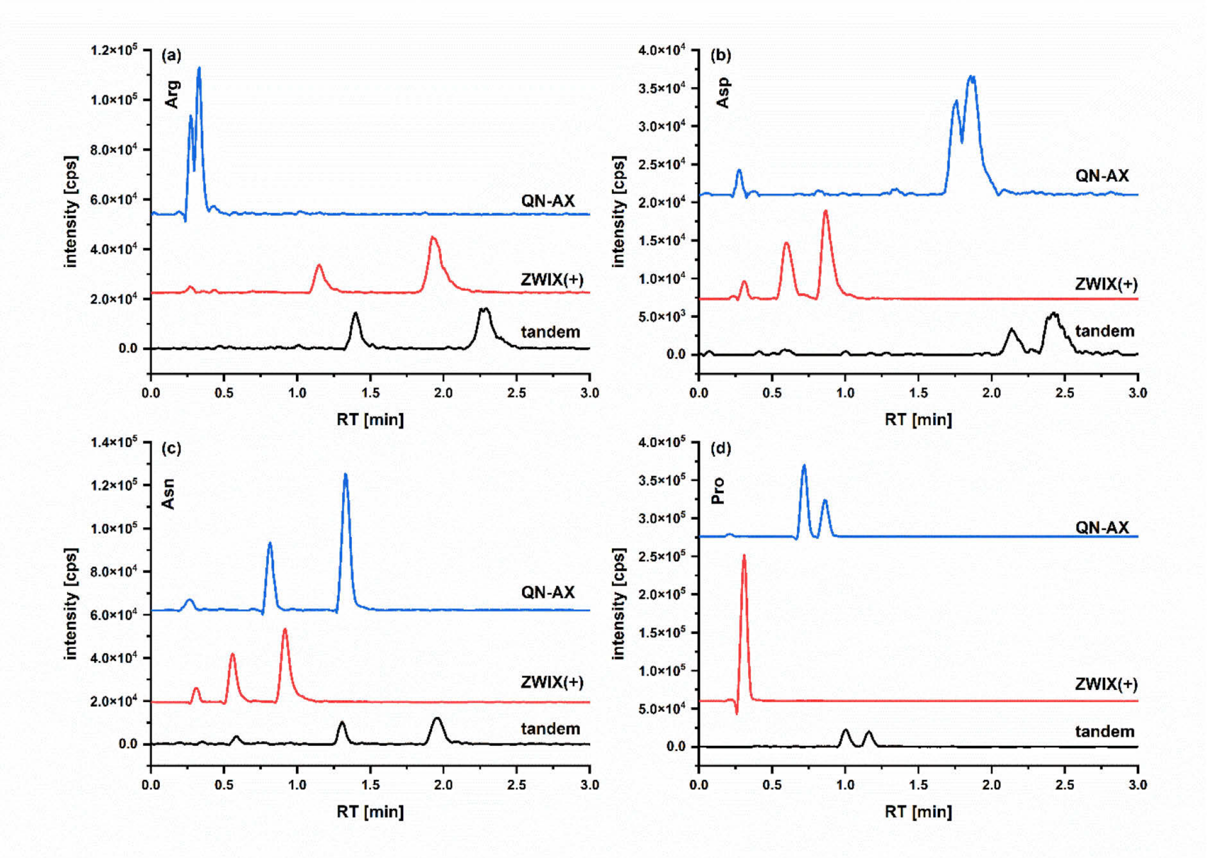

Figure S18. Extracted ion chromatograms (EIC) of the (a) arginine, (b) aspartic acid, (c) asparagine and (d) proline LC enantiomer separation using the single QN-AX, ZWIX(+) or the combined tandem column. Mobile phase A: ACN/MeOH/H_2O 49:49:2 (v/v/v) 10 mM NH_4FA + 10 mM FA, mobile phase B: ACN/MeOH/H_2O 49:49:2 (v/v/v) 50 mM NH_4FA + 50 mM FA; flow rate: 1.25 mL/min, gradient: 0-0.4 min 0 %B, 0.4-1.0 min 0-100 %B, 1.0-3.0 min 100 %B, 3.0-3.2 min 100-0 %B, 3.2-4.0 min 0 %B, column temperature: 50°C.

Table S16. Chromatographic performance parameters for the single QN-AX and ZWIX(+) column and the combined tandem column. Void times: tandem: 0.44 min, QN-AX and ZWIX(+): 0.22 min. Same experimental conditions as in Figure S5.

	tandem				QN-AX				ZWIX(+)			
AA-AQC	**k*(D)**	**k*(L)**	**α**	**R**	**k*(D)**	**k*(L)**	**α**	**R**	**k*(D)**	**k*(L)**	**α**	**R**
Ala	1.14	1.61	1.42	2.75	1.68	2.59	1.54	1.97	0.59	0.73	1.23	0.44
*a*Ile	0.55	1.61	2.96	4.27	1.05	2.95	2.83	3.30	0.41	0.41	1.00	0.00
Arg	2.16	4.23	1.96	7.67	0.23	0.45	2.00	0.98	4.27	7.77	1.82	6.49
Asn	1.98	3.48	1.76	7.08	2.73	5.18	1.90	7.08	1.59	3.23	2.03	3.86
Asp	3.98	4.55	1.14	2.11	6.95	7.41	1.07	0.79	1.77	2.95	1.67	2.36
*aT*hr	1.23	2.30	1.87	3.70	2.18	3.59	1.65	4.06	0.59	1.77	3.00	2.79
Cys-IAA	1.91	2.80	1.46	4.60	2.86	4.23	1.48	3.93	1.45	2.45	1.69	2.88
Gln	1.66	2.20	1.33	2.83	2.32	3.32	1.43	2.60	1.09	1.73	1.58	1.84
Glu	2.86	3.18	1.11	1.27	5.09	5.68	1.12	1.92	1.18	1.64	1.38	1.31
Gly	2.00	2.00	1.00	n/a	2.91	2.91	1.00	n/a	1.41	1.41	1.00	n/a
His	1.91	3.34	1.75	5.72	0.95	1.95	2.05	3.25	3.09	5.50	1.78	4.17
Hse	1.23	2.05	1.67	2.83	1.77	3.05	1.72	3.30	0.59	1.32	2.23	2.36
Ile	0.55	1.41	2.58	4.08	1.05	2.95	2.83	3.30	0.41	0.41	1.00	0.00
Leu	0.70	1.41	2.00	2.29	1.05	2.23	2.13	2.56	0.41	0.41	1.00	0.00
Lys-bis-AQC	2.14	2.86	1.34	3.78	2.50	3.77	1.51	4.13	2.32	3.14	1.35	1.93
Met	1.43	2.05	1.43	3.98	2.23	3.50	1.57	3.67	0.77	1.00	1.29	0.98
*n*Leu	0.70	1.41	2.00	4.06	1.05	2.23	2.13	3.41	0.41	0.41	1.00	0.00
Phe	1.36	2.09	1.53	3.78	2.14	3.68	1.72	5.02	0.59	0.95	1.62	1.57
Pro	1.68	1.32	1.28	1.89	2.91	2.32	0.80	1.70	0.41	0.41	1.00	0.00
Ser	1.57	2.68	1.71	5.78	2.27	3.77	1.66	4.33	1.00	2.77	2.77	4.60
Thr	1.23	2.45	2.00	3.75	1.77	3.77	2.13	5.19	0.59	1.77	3.00	2.79
*t*Leu	0.36	1.30	3.56	4.03	0.73	2.23	3.06	4.87	0.41	0.41	1.00	0.00
Trp	1.89	3.98	2.11	9.87	2.59	4.41	1.70	4.72	1.32	4.95	3.76	8.58
Tyr	1.48	2.41	1.63	5.38	2.23	3.95	1.78	4.98	0.86	1.59	1.84	2.70
Val	0.61	1.61	2.63	5.77	1.09	2.91	2.67	6.74	0.23	0.41	1.80	1.18

3.4.7.2.2 LC separation of isomeric amino acids

Leu isomers

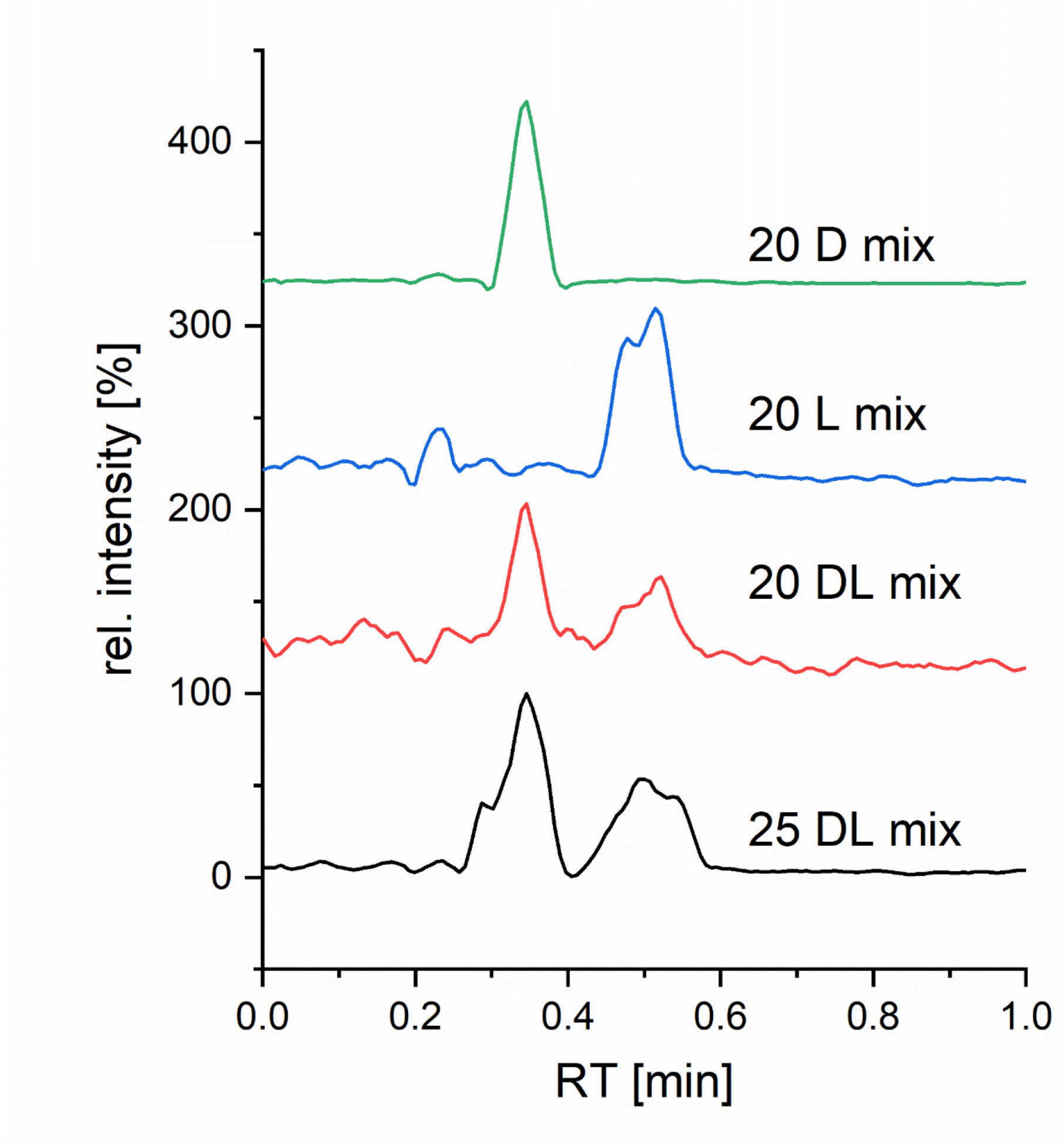

Figure S19. Extracted ion chromatograms (EIC) of leucine isomer separation using the combined tandem column. Mobile phase A: ACN/MeOH/H_2O 49:49:2 (v/v/v) 10 mM NH_4FA + 10 mM FA, mobile phase B: ACN/MeOH/H_2O 49:49:2 (v/v/v) 50 mM NH_4FA + 50 mM FA; flow rate: 2.5 mL/min, gradient: 0-0.2 min 0 %B, 0.2-0.5 min 0-100 %B, 0.5-1.5 min 100 %B, 1.5-1.6 min 100-0 %B, 1.6-2.0 min 0 %B, column temperature: 50°C.

Table S17. Evaluation of the chromatographic performance of the leucine isomer separation in the 25 DL-AA mix sample. Tandem column: QN-AX + ZWIX(+) prototype core shell columns (3.0x50 mm, 2.7µm, respectively). Same LC conditions as in Figure S18.

AA-AQC	RT [min]	$w_{1/2}$ [min]	t'R [min]	k*	α	R	$^{DT}CCS_{N2}$ [Å²]
D-*t*Leu	0.60	0.04	0.16	0.36	n/a	n/a	181.6
D-*a*Ile	0.68	0.04	0.24	0.55	1.50	1.18	180.9
D-Ile	0.68	0.05	0.24	0.55	1.00	0.00	180.9
D-Leu	0.75	0.06	0.31	0.70	1.29	0.75	180.9
D-*n*Leu	0.75	0.06	0.31	0.70	1.00	0.00	182.1
L-*t*Leu	1.01	0.08	0.57	1.30	1.84	2.19	181.6
L-Ile	1.06	0.06	0.62	1.41	1.09	0.42	180.9
L-Leu	1.06	0.10	0.62	1.41	1.00	0.00	180.9
L-*n*Leu	1.06	0.03	0.62	1.41	1.00	0.00	182.1
L-*a*Ile	1.15	0.09	0.71	1.61	1.15	0.88	180.9

Thr/*a*Thr/Hse

Table S18. Chromatographic performance evaluation of the threonine isomer mixture consisting of DL threonine (Thr), *allo*-threonine (*a*Thr) and homo-serine (Hse). Tandem column: QN-AX + ZWIX(+) prototype core shell columns (3.0x50 mm, 2.7µm, respectively). Same LC conditions as in Figure S18.

AA-AQC	RT [min]	$w_{1/2}$ [min]	t'R [min]	k*	α	R
D-*a*Thr	0.98	0.11	0.54	1.23	n/a	n/a
D-Hse	0.98	0.11	0.54	1.23	1.00	0.00
D-Thr	0.98	0.11	0.54	1.23	1.00	0.00
L-Hse	1.34	0.04	0.90	2.05	1.67	2.83
L-*a*Thr	1.45	0.04	1.01	2.30	1.12	1.62
L-Thr	1.52	0.06	1.08	2.45	1.07	0.83

Table S19. Chromatographic performance evaluation of the threonine isomer mixture consisting of DL-threonine (Thr) and *allo*-threonine (aThr). Tandem column: QN-AX + ZWIX(+) prototype core shell columns (3.0x50 mm, 2.7µm, respectively). Same LC conditions as in Figure S18.

AA-AQC	RT [min]	$w_{1/2}$ [min]	t'R [min]	k*	α	R
D-Thr	0.94	0.04	0.5	1.14	n/a	n/a
D-*a*Thr	1.03	0.05	0.59	1.34	1.18	1.18
L-*a*Thr	1.45	0.05	1.01	2.30	1.71	4.96
L-Thr	1.50	0.06	1.06	2.41	1.05	0.54

3.4.7.2.3 Evaluation of IM-MS to improve the fast enantioselective method

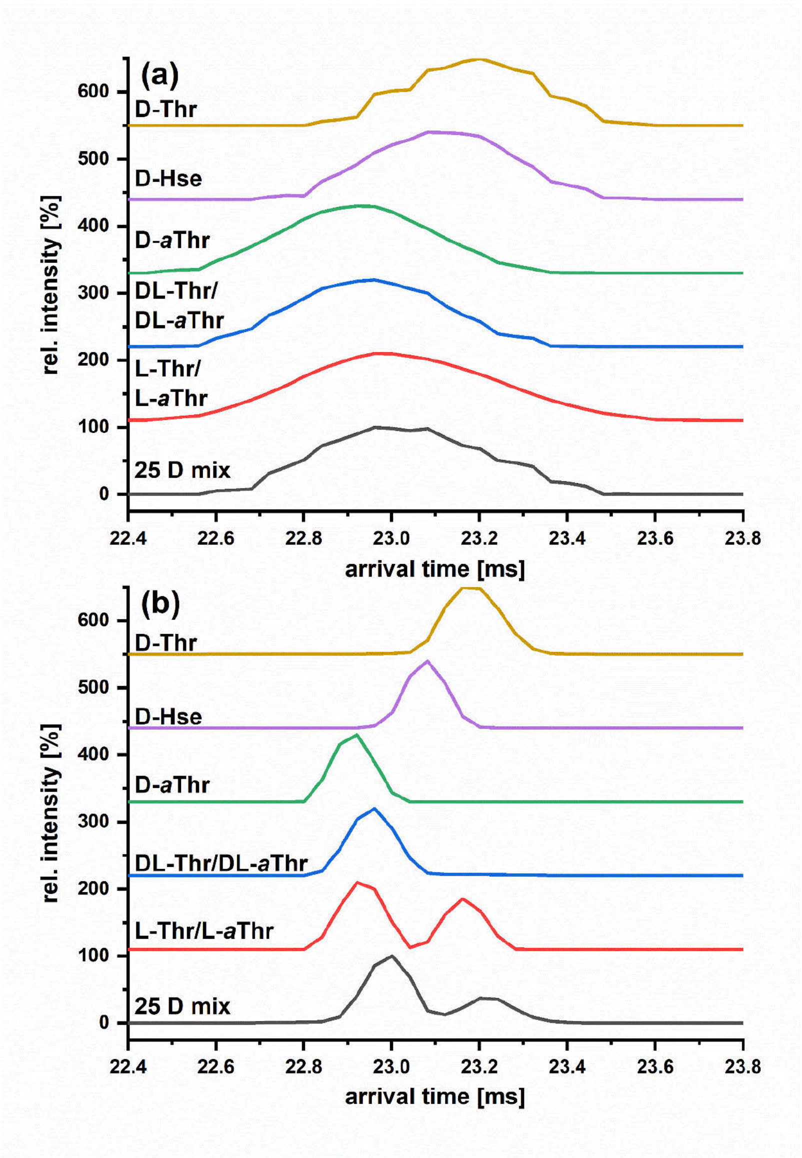

Figure S20. Standard arrival time spectra (a) and high-resolution demultiplexed arrival time (b).

Table S20. Calculation of the difference in the collisional cross section (CCS) of leucine and threonine isomers.

AA-AQC (A)	**$^{DT}CCS_{N2}$ (A) [Å^2]**	**AA-AQC (B)**	**$^{DT}CCS_{N2}$ (B) [Å^2]**	**$\Delta^{DT}CCS_{N2}$ (A,B) [%]**
Ile	180.9	Leu	180.9	0.00
Ile	180.9	*a*Ile	180.9	0.00
Ile	180.9	*t*Leu	181.6	0.39
Ile	180.9	*n*Leu	182.1	0.66
Leu	180.9	*a*Ile	180.9	0.00
Leu	180.9	*t*Leu	181.6	0.39
Leu	180.9	*n*Leu	182.1	0.66
*a*Ile	180.9	*t*Leu	181.6	0.39
*a*Ile	180.9	*n*Leu	182.1	0.66
*t*Leu	181.6	*n*Leu	182.1	0.28
*a*Thr	171.8	Hse	172.8	0.58
*a*Thr	171.8	Thr	174.1	1.34
Hse	172.8	Thr	174.1	0.75

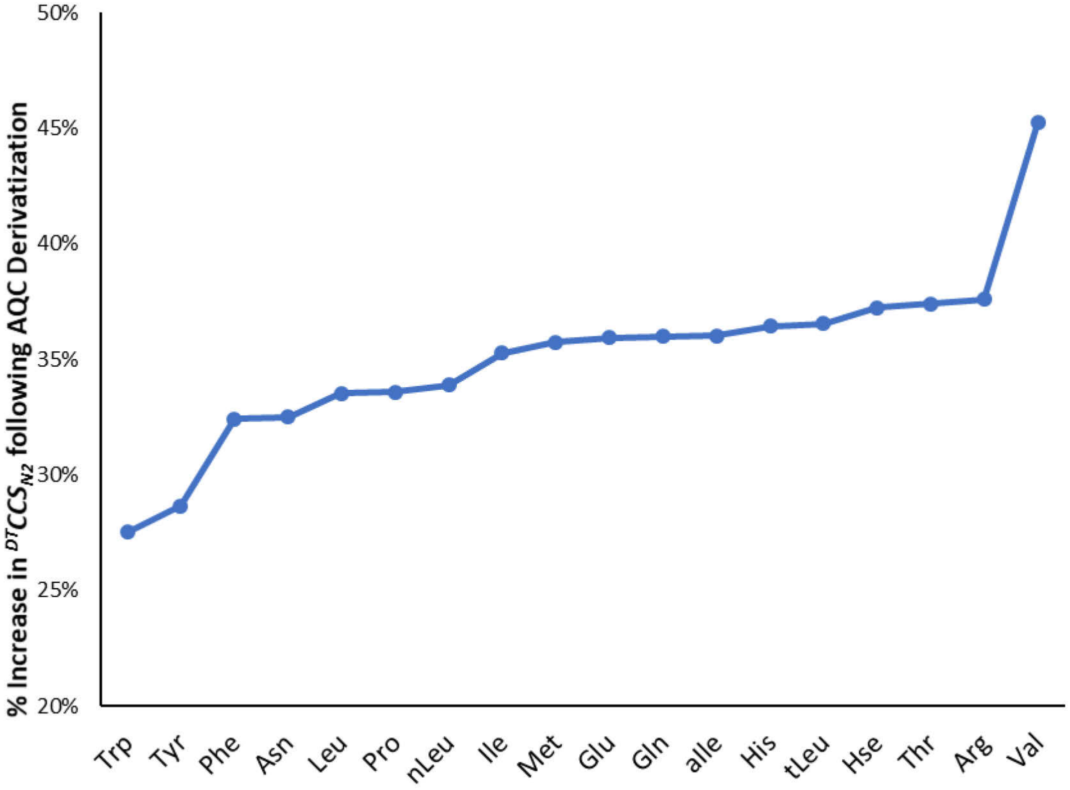

Figure S21. Impact of AQC derivatization on $^{DT}CCS_{N2}$ of corresponding protonated amino acids. Data for underivatized amino acids retrieved from the CCS Compendium (https://mcleanresearchgroup.shinyapps.io/CCS-Compendium/).

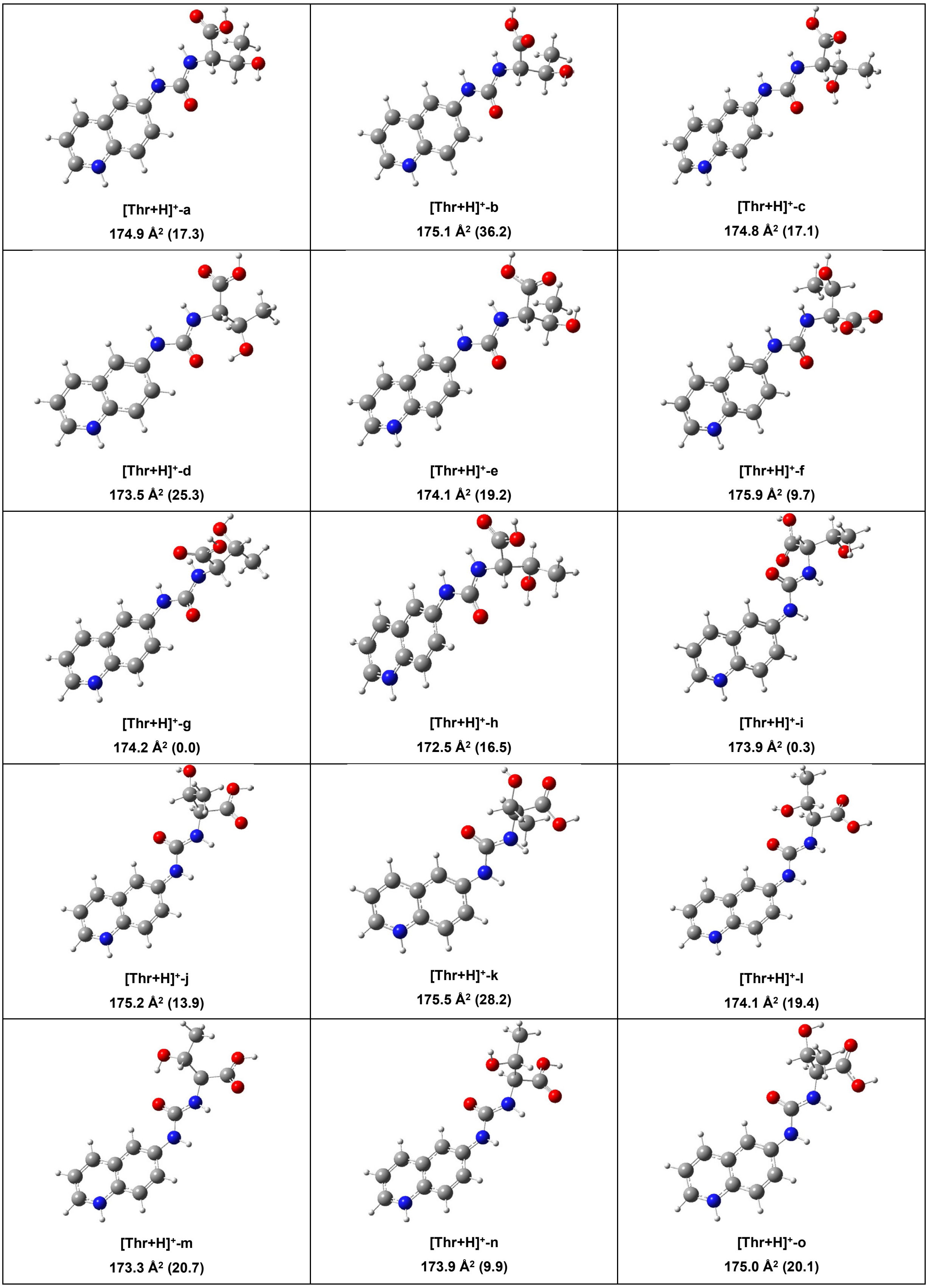

[Thr+H]$^+$-a
174.9 Å^2 (17.3)

[Thr+H]$^+$-b
175.1 Å^2 (36.2)

[Thr+H]$^+$-c
174.8 Å^2 (17.1)

[Thr+H]$^+$-d
173.5 Å^2 (25.3)

[Thr+H]$^+$-e
174.1 Å^2 (19.2)

[Thr+H]$^+$-f
175.9 Å^2 (9.7)

[Thr+H]$^+$-g
174.2 Å^2 (0.0)

[Thr+H]$^+$-h
172.5 Å^2 (16.5)

[Thr+H]$^+$-i
173.9 Å^2 (0.3)

[Thr+H]$^+$-j
175.2 Å^2 (13.9)

[Thr+H]$^+$-k
175.5 Å^2 (28.2)

[Thr+H]$^+$-l
174.1 Å^2 (19.4)

[Thr+H]$^+$-m
173.3 Å^2 (20.7)

[Thr+H]$^+$-n
173.9 Å^2 (9.9)

[Thr+H]$^+$-o
175.0 Å^2 (20.1)

Figure S22. Optimized structures of different conformers of [Thr+H]$^+$ in the gas phase and their calculated CCS_{N2} values. The numbers in parenthesis are the relative Gibbs free energies in kJ mol^{-1}.

Table S21. The calculated *CCS_{N2}* values and relative Gibbs free energies for the conformers of $[Thr+H]^+$. $^{DT}CCS_{N2}$ = 174.1 Å².

$[M+H]^+$	**ΔG (kJ mol^{-1})**	**CCS_{N2} ($Å^2$)**
$[Thr+H]^+$-a	17.3	174.9
$[Thr+H]^+$-b	36.2	175.1
$[Thr+H]^+$-c	17.1	174.8
$[Thr+H]^+$-d	25.3	173.5
$[Thr+H]^+$-e	19.2	174.1
$[Thr+H]^+$-f	9.7	175.9
$[Thr+H]^+$-g	**0.0**	**174.2**
$[Thr+H]^+$-h	16.5	172.5
$[Thr+H]^+$-i	0.3	173.9
$[Thr+H]^+$-j	13.9	175.2
$[Thr+H]^+$-k	28.2	175.5
$[Thr+H]^+$-l	19.4	174.1
$[Thr+H]^+$-m	20.7	173.3
$[Thr+H]^+$-n	9.9	173.9
$[Thr+H]^+$-o	20.1	175.0

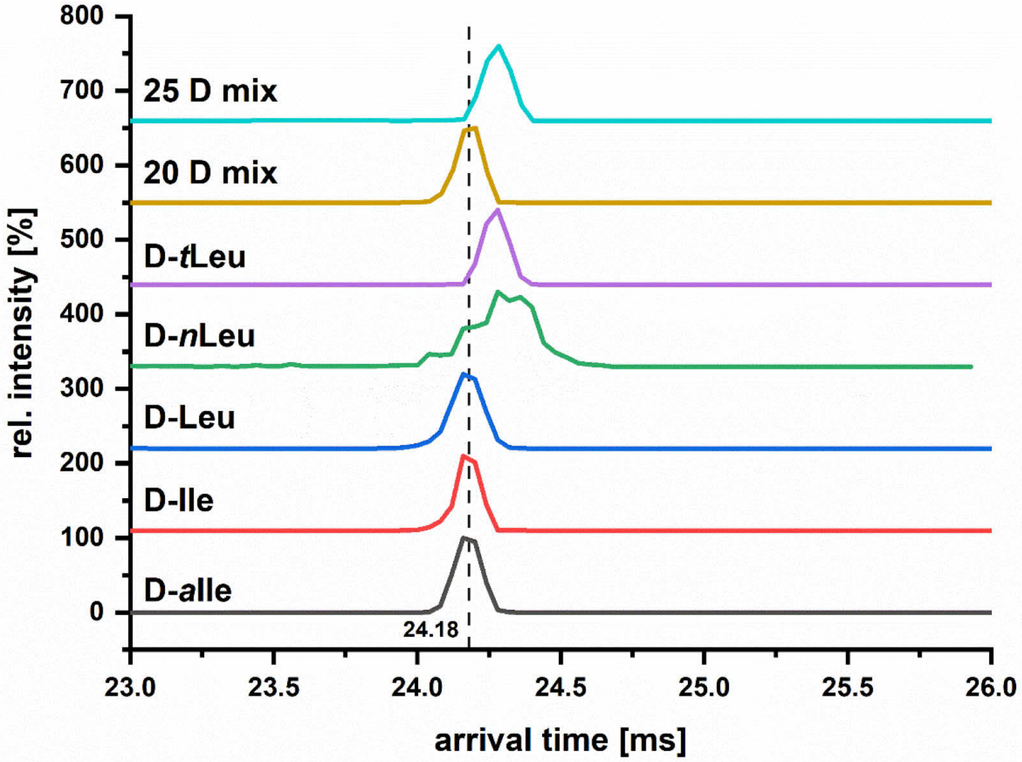

Figure S23. Arrival time spectra of single D-leucine isomers standards and a mixture of all 20 proteinogenic D-amino acids (including Leu and Ile) and a mixture of 25 D-amino acids (including Leu, Ile, *a*Ile, *n*Leu, *t*Leu) after application of high-resolution de-multiplexing.

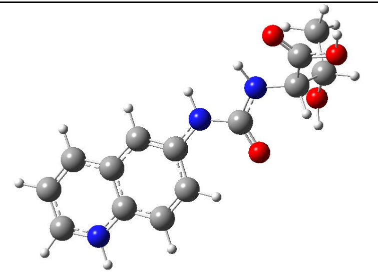 **[aThr+H]$^+$-a** **172.9 Å^2 (5.6)**	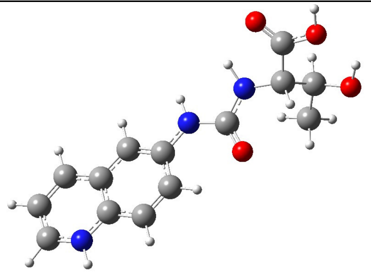 **[aThr+H]$^+$-b** **172.2 Å^2 (11.8)**	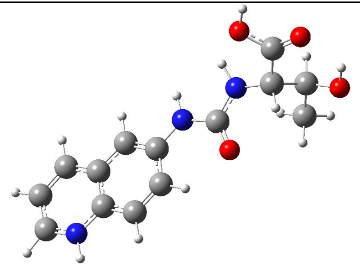 **[aThr+H]$^+$-c** **174.4 Å^2 (21.9)**
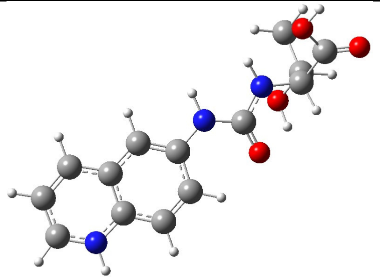 **[aThr+H]$^+$-d** **176.0 Å^2 (17.5)**	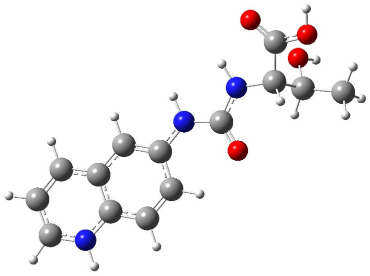 **[aThr+H]$^+$-e** **173.2 Å^2 (7.7)**	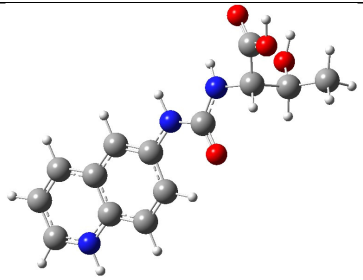 **[aThr+H]$^+$-f** **173.7 Å^2 (6.3)**
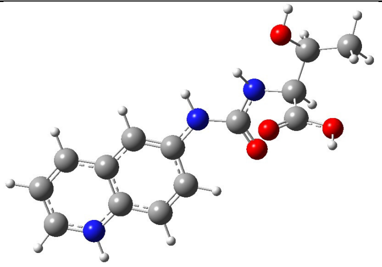 **[aThr+H]$^+$-g** **171.2 Å^2 (4.9)**	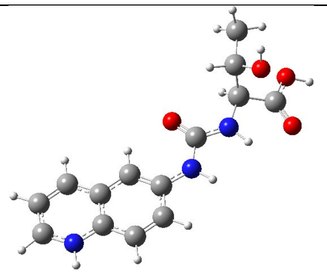 **[aThr+H]$^+$-h** **171.7 Å^2 (1.0)**	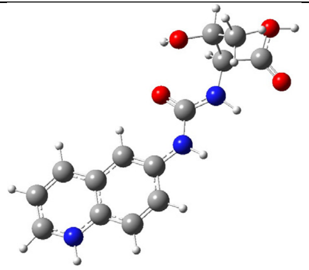 **[aThr+H]$^+$-i** **171.8 Å^2 (1.8)**
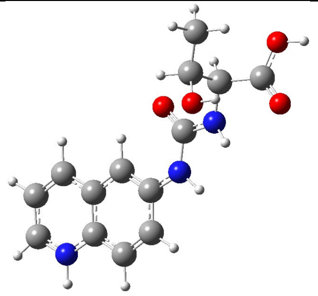 **[aThr+H]$^+$-j** **174.2 Å^2 (2.6)**	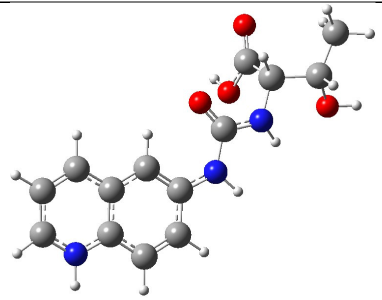 **[aThr+H]$^+$-k** **174.9 Å^2 (5.8)**	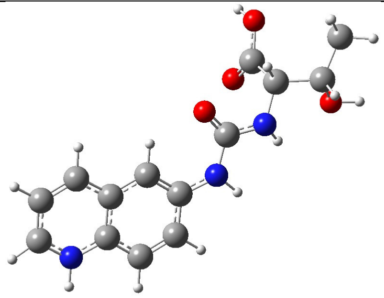 **[aThr+H]$^+$-l** **172.2 Å^2 (0.0)**

Figure S24. Optimized structures of different conformers of [aThr+H]$^+$ in the gas phase and their calculated CCS_{N2} values. The numbers in parenthesis are the relative Gibbs free energies in kJ mol^{-1}.

Table S22. The calculated *CCS_{N2}* values and relative Gibbs free energies for the conformers of $[aThr+H]^+$. Experimental *$^{DT}CCS_{N2}$* = 171.8 Å².

$[M+H]^+$	**ΔG (kJ mol^{-1})**	**CCS_{N2} (Å^2)**
$[aThr+H]^+$-a	5.6	172.9
$[aThr+H]^+$-b	11.8	172.2
$[aThr+H]^+$-c	21.9	174.4
$[aThr+H]^+$-d	17.5	176.0
$[aThr+H]^+$-e	7.7	173.2
$[aThr+H]^+$-f	6.3	173.7
$[aThr+H]^+$-g	4.9	171.2
$[aThr+H]^+$-h	1.0	171.7
$[aThr+H]^+$-i	1.8	171.8
$[aThr+H]^+$-j	2.6	174.2
$[aThr+H]^+$-k	5.8	174.9
$[aThr+H]^+$-l	**0.0**	**172.2**

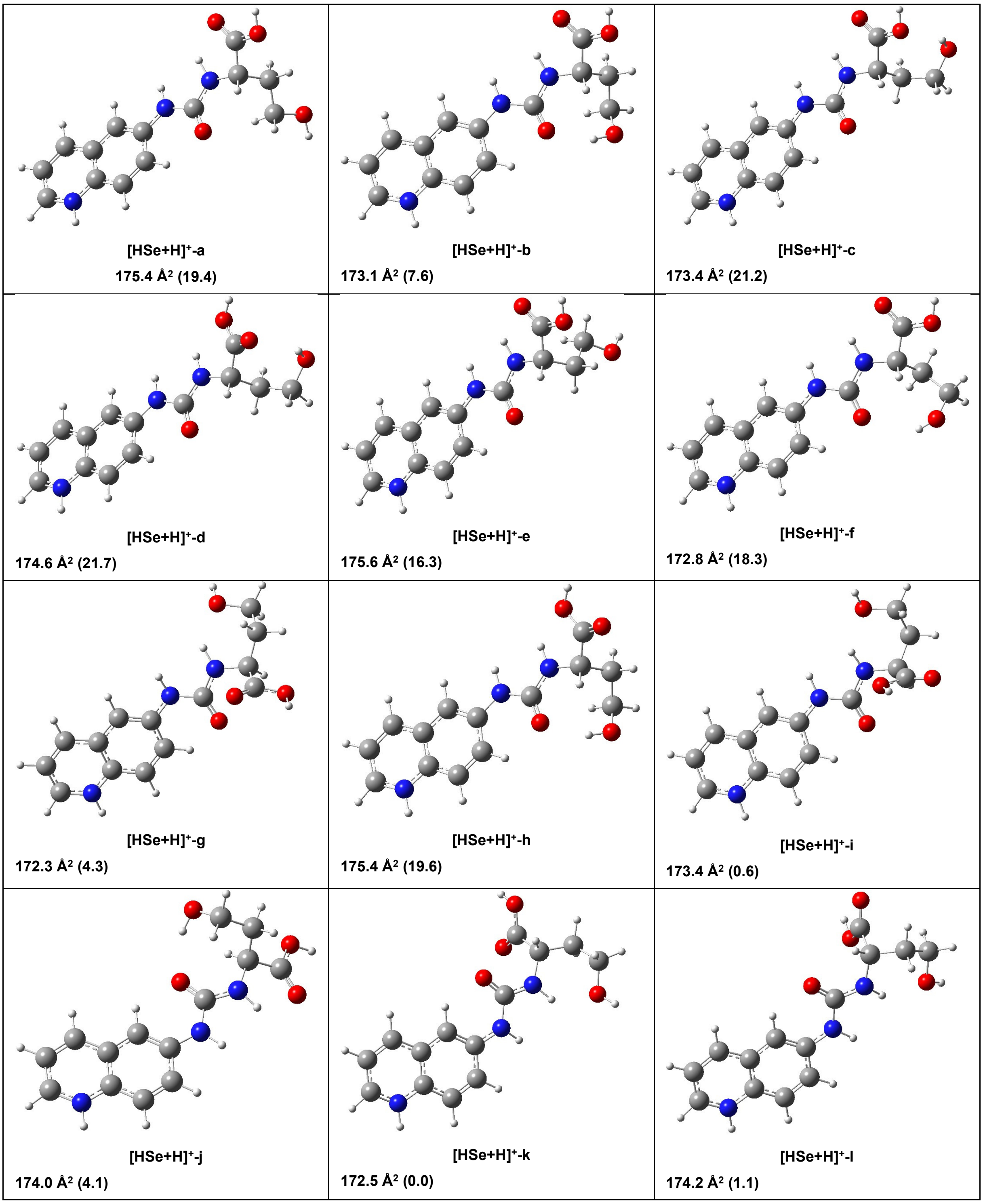

$[HSe+H]^+$-a
175.4 Å^2 (19.4)

$[HSe+H]^+$-b
173.1 Å^2 (7.6)

$[HSe+H]^+$-c
173.4 Å^2 (21.2)

$[HSe+H]^+$-d
174.6 Å^2 (21.7)

$[HSe+H]^+$-e
175.6 Å^2 (16.3)

$[HSe+H]^+$-f
172.8 Å^2 (18.3)

$[HSe+H]^+$-g
172.3 Å^2 (4.3)

$[HSe+H]^+$-h
175.4 Å^2 (19.6)

$[HSe+H]^+$-i
173.4 Å^2 (0.6)

$[HSe+H]^+$-j
174.0 Å^2 (4.1)

$[HSe+H]^+$-k
172.5 Å^2 (0.0)

$[HSe+H]^+$-l
174.2 Å^2 (1.1)

Figure S25. Optimized structures of different conformers of $[HSe+H]^+$ in the gas phase and their calculated CCS_{N2} values. The numbers in parenthesis are the relative Gibbs free energies in kJ mol^{-1}.

Table S23. The calculated CCS_{N2} values and relative Gibbs free energies for the conformers of $[HSe+H]^+$. Experimental $^{DT}CCS_{N2}$ = 172.8 Å².

$[M+H]^+$	**ΔG (kJ mol^{-1})**	**CCS_{N2} (Å^2)**
$[HSe+H]^+$-a	19.4	175.4
$[HSe+H]^+$-b	7.6	173.1
$[HSe+H]^+$-c	21.2	173.4
$[HSe+H]^+$-d	21.7	174.6
$[HSe+H]^+$-e	16.3	175.6
$[HSe+H]^+$-f	18.3	172.8
$[HSe+H]^+$-g	4.3	172.3
$[HSe+H]^+$-h	19.6	175.4
$[HSe+H]^+$-i	0.6	173.4
$[HSe+H]^+$-j	4.1	174.0
$[HSe+H]^+$-k	**0.0**	**172.5**
$[HSe+H]^+$-l	1.1	174.2

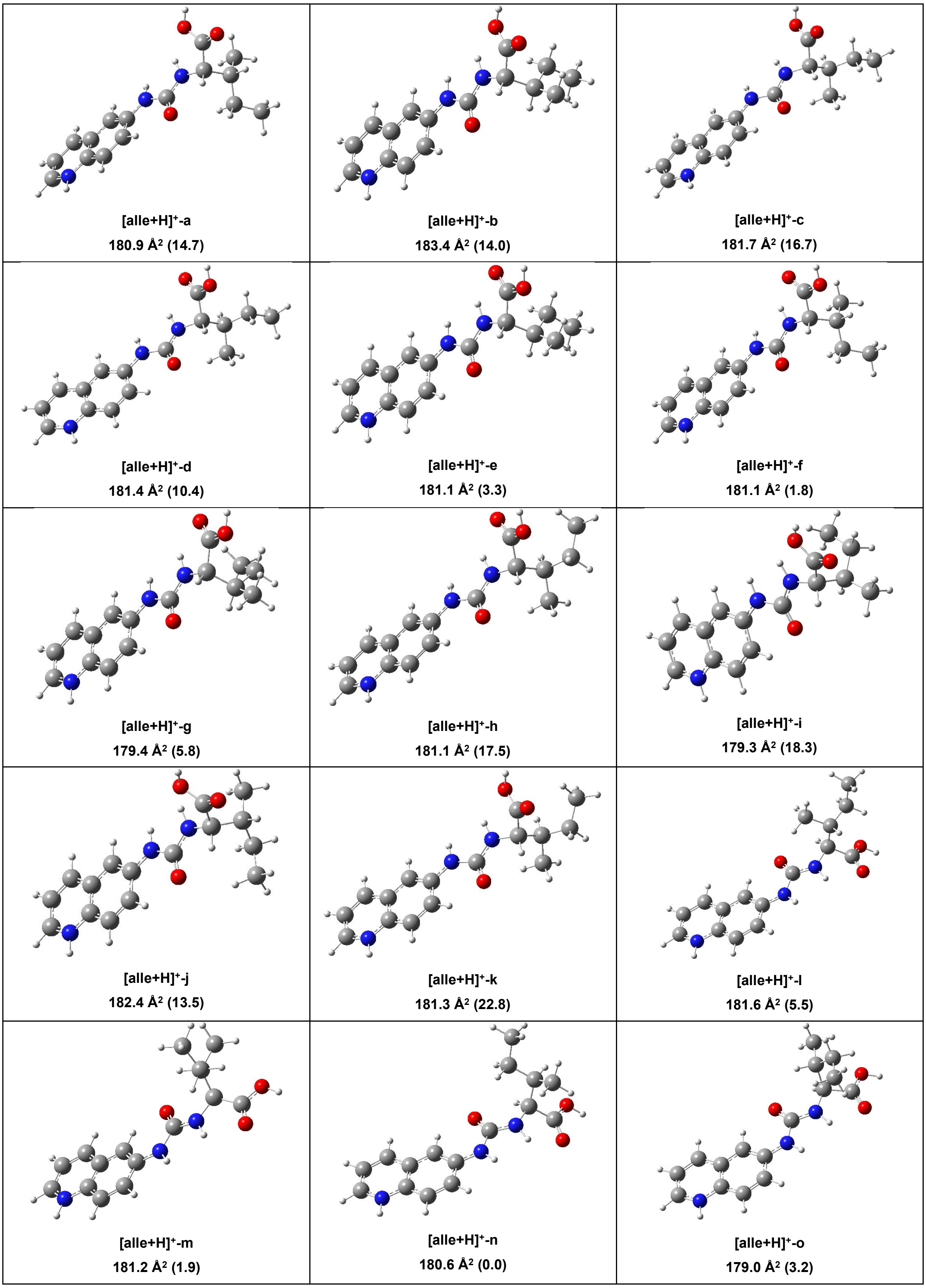

[alle+H]$^+$-a
180.9 Å^2 (14.7)

[alle+H]$^+$-b
183.4 Å^2 (14.0)

[alle+H]$^+$-c
181.7 Å^2 (16.7)

[alle+H]$^+$-d
181.4 Å^2 (10.4)

[alle+H]$^+$-e
181.1 Å^2 (3.3)

[alle+H]$^+$-f
181.1 Å^2 (1.8)

[alle+H]$^+$-g
179.4 Å^2 (5.8)

[alle+H]$^+$-h
181.1 Å^2 (17.5)

[alle+H]$^+$-i
179.3 Å^2 (18.3)

[alle+H]$^+$-j
182.4 Å^2 (13.5)

[alle+H]$^+$-k
181.3 Å^2 (22.8)

[alle+H]$^+$-l
181.6 Å^2 (5.5)

[alle+H]$^+$-m
181.2 Å^2 (1.9)

[alle+H]$^+$-n
180.6 Å^2 (0.0)

[alle+H]$^+$-o
179.0 Å^2 (3.2)

Figure S26. Optimized structures of different conformers of [alle+H]$^+$ in the gas phase and their calculated CCS_{N2} values. The numbers in parenthesis are the relative Gibbs free energies in kJ mol^{-1}.

Table S24. The calculated *CCS_{N2}* values and relative Gibbs free energies for the conformers of $[alle+H]^+$. Experimental $^{DT}CCS_{N2}$ = 180.9 Å².

$[M+H]^+$	**ΔG (kJ mol^{-1})**	**CCS_{N2} ($Å^2$)**
$[alle+H]^+$-a	14.7	180.9
$[alle+H]^+$-b	14.0	183.4
$[alle+H]^+$-c	16.7	181.7
$[alle+H]^+$-d	10.4	181.4
$[alle+H]^+$-e	3.3	181.1
$[alle+H]^+$-f	1.8	181.1
$[alle+H]^+$-g	5.8	179.4
$[alle+H]^+$-h	17.5	181.1
$[alle+H]^+$-i	18.3	179.3
$[alle+H]^+$-j	13.5	182.4
$[alle+H]^+$-k	22.8	181.3
$[alle+H]^+$-l	5.5	181.6
$[alle+H]^+$-m	1.9	181.2
$[alle+H]^+$-n	**0.0**	**180.6**
$[alle+H]^+$-o	3.2	179.0

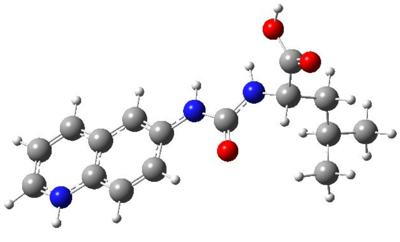 [Leu+H]$^+$-a 184.3 Å^2 (13.7)	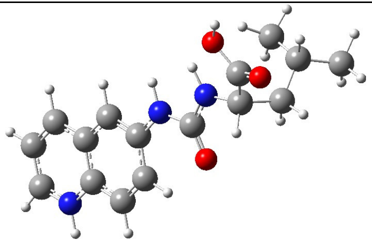 [Leu+H]$^+$-b 182.8 Å^2 (18.6)	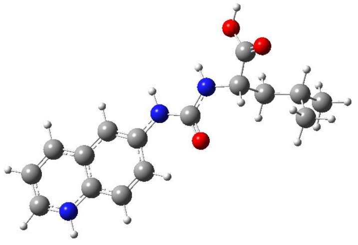 [Leu+H]$^+$-c 181.8 Å^2 (16.8)
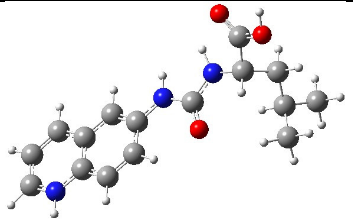 [Leu+H]$^+$-d 182.3 Å^2 (1.6)	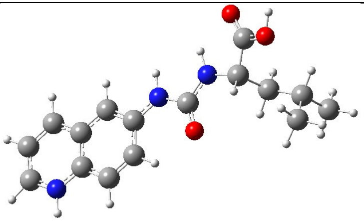 [Leu+H]$^+$-e 181.8 Å^2 (8.9)	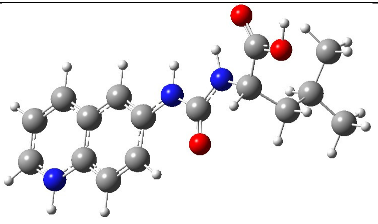 [Leu+H]$^+$-f 180.1 Å^2 (8.4)
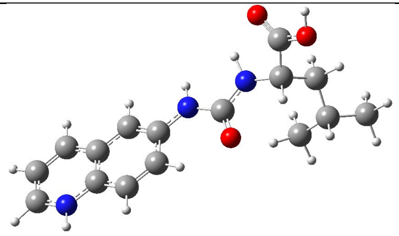 [Leu+H]$^+$-g 181.2 Å^2 (11.5)	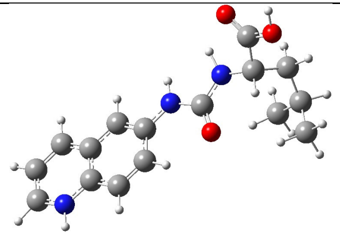 [Leu+H]$^+$-h 180.8 Å^2 (11.1)	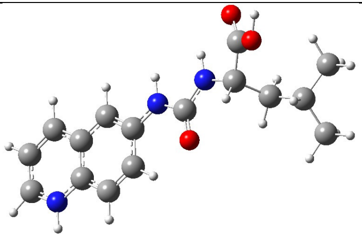 [Leu+H]$^+$-i 182.4 Å^2 (15.9)
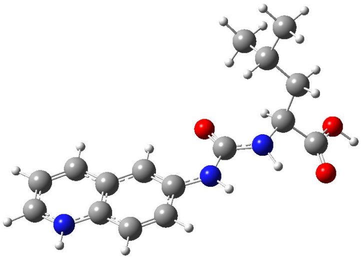 [Leu+H]$^+$-j 180.1 Å^2 (0.0)	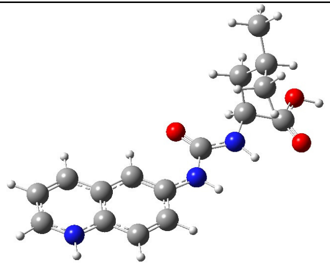 [Leu+H]$^+$-k 180.9 Å^2 (3.6)	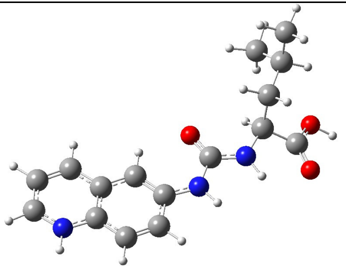 [Leu+H]$^+$-l 181.3 Å^2 (2.1)
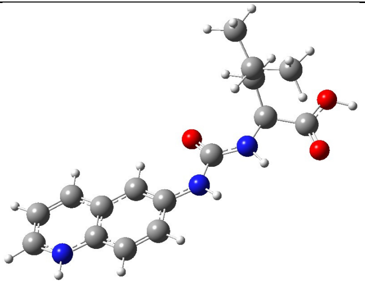 [Leu+H]$^+$-m 179.5 Å^2 (2.2)	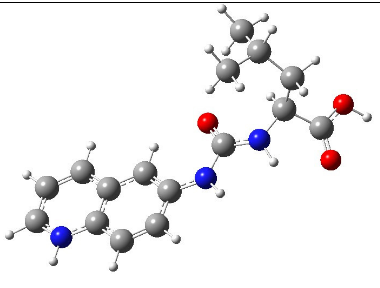 [Leu+H]$^+$-n 180.6 Å^2 (9.9)	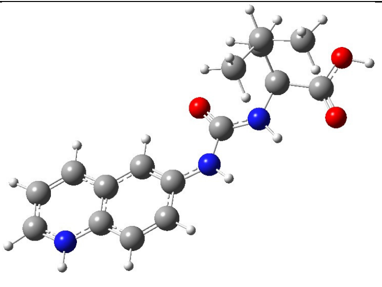 [Leu+H]$^+$-o 178.7 Å^2 (12.6)

Figure S27. Optimized structures of different conformers of [Leu+H]$^+$ in the gas phase and their calculated *CCS*$_{N2}$ values. The numbers in parenthesis are the relative Gibbs free energies in kJ mol^{-1}.

Table S25. The calculated *CCS_{N2}* values and relative Gibbs free energies for the conformers of $[Leu+H]^+$. Experimental $^{DT}CCS_{N2}$ = 180.9 Å².

$[M+H]^+$	**ΔG (kJ mol^{-1})**	**CCS_{N2} (Å^2)**
$[Leu+H]^+$-a	13.7	184.3
$[Leu+H]^+$-b	18.6	182.8
$[Leu+H]^+$-c	16.8	181.8
$[Leu+H]^+$-d	1.6	182.3
$[Leu+H]^+$-e	8.9	181.8
$[Leu+H]^+$-f	8.4	180.1
$[Leu+H]^+$-g	11.5	181.2
$[Leu+H]^+$-h	11.1	180.8
$[Leu+H]^+$-i	15.9	182.4
$[Leu+H]^+$-j	**0.0**	**180.1**
$[Leu+H]^+$-k	3.6	180.9
$[Leu+H]^+$-l	2.1	181.3
$[Leu+H]^+$-m	2.2	179.5
$[Leu+H]^+$-n	9.9	180.6
$[Leu+H]^+$-o	12.6	178.7

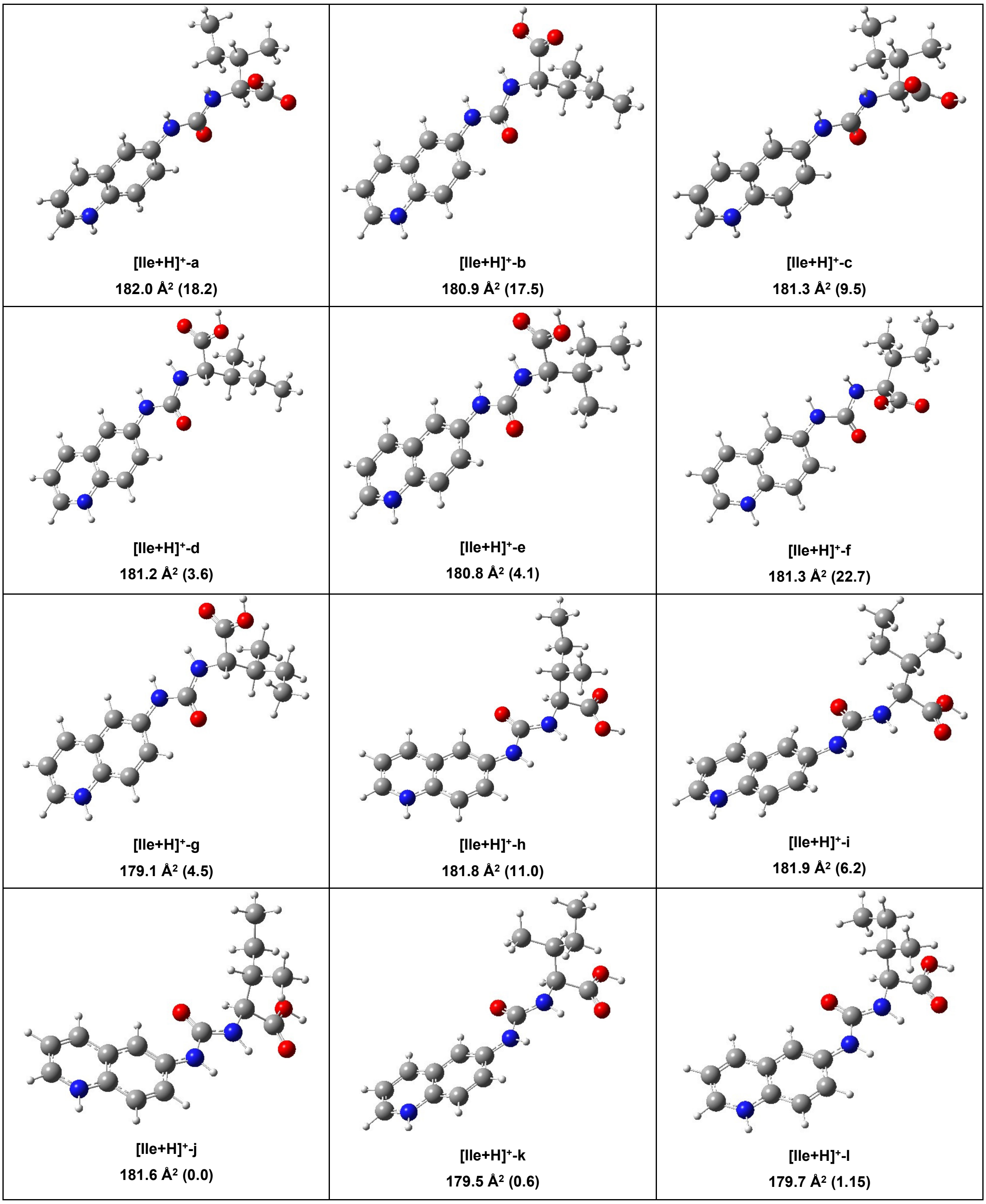

[Ile+H]$^+$-a
182.0 Å^2 (18.2)

[Ile+H]$^+$-b
180.9 Å^2 (17.5)

[Ile+H]$^+$-c
181.3 Å^2 (9.5)

[Ile+H]$^+$-d
181.2 Å^2 (3.6)

[Ile+H]$^+$-e
180.8 Å^2 (4.1)

[Ile+H]$^+$-f
181.3 Å^2 (22.7)

[Ile+H]$^+$-g
179.1 Å^2 (4.5)

[Ile+H]$^+$-h
181.8 Å^2 (11.0)

[Ile+H]$^+$-i
181.9 Å^2 (6.2)

[Ile+H]$^+$-j
181.6 Å^2 (0.0)

[Ile+H]$^+$-k
179.5 Å^2 (0.6)

[Ile+H]$^+$-l
179.7 Å^2 (1.15)

Figure S28. Optimized structures of different conformers of [Ile+H]$^+$ in the gas phase and their calculated CCS_{N2} values. The numbers in parenthesis are the relative Gibbs free energies in kJ mol^{-1}.

Table S26. The calculated *CCS*$_{N2}$ values and relative Gibbs free energies for the conformers of [Ile+H]$^+$. Experimental ^{DT}*CCS*$_{N2}$ = 180.9 Å².

[M+H]$^+$	**ΔG (kJ mol^{-1})**	**CCS$_{N2}$ (Å^2)**
[Ile+H]$^+$-a	18.2	182.0
[Ile+H]$^+$-b	17.5	180.9
[Ile+H]$^+$-c	9.5	181.3
[Ile+H]$^+$-d	3.6	181.2
[Ile+H]$^+$-e	4.1	180.8
[Ile+H]$^+$-f	22.7	181.3
[Ile+H]$^+$-g	4.5	179.1
[Ile+H]$^+$-h	11.0	181.8
[Ile+H]$^+$-i	6.2	181.9
[Ile+H]$^+$-j	**0.0**	**181.6**
[Ile+H]$^+$-k	0.6	179.5
[Ile+H]$^+$-l	1.5	179.7

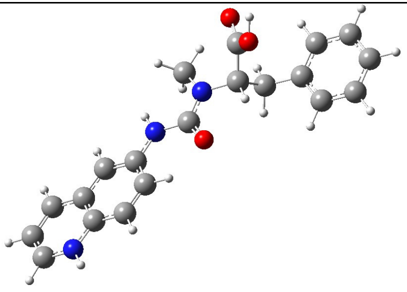 **[NMePh +H]$^+$-a** **196.4 Å^2 (19.5)**	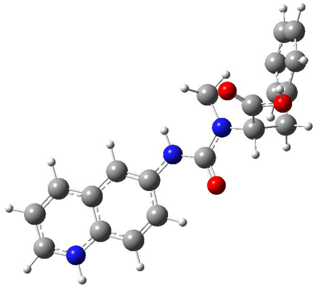 **[NMePh +H]$^+$-b** **193.6 Å^2 (11.4)**	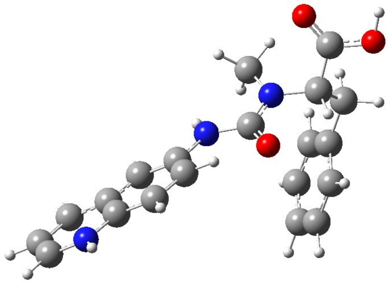 **[NMePh +H]$^+$-c** **189.6 Å^2 (0.0)**
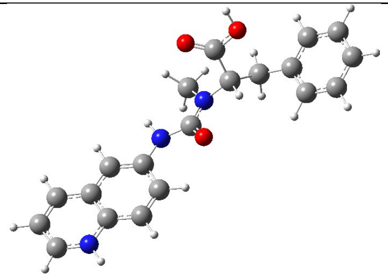 **[NMePh +H]$^+$-d** **197.2 Å^2 (19.9)**	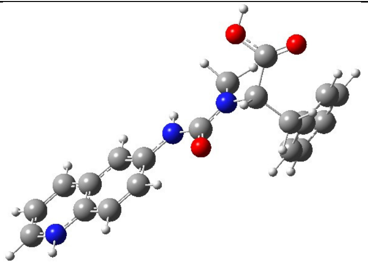 **[NMePh +H]$^+$-e** **192.5 Å^2 (10.9)**	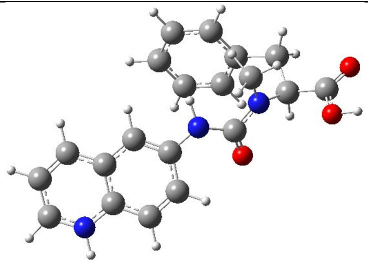 **[NMePh +H]$^+$-f** **185.6 Å^2 (10.3)**
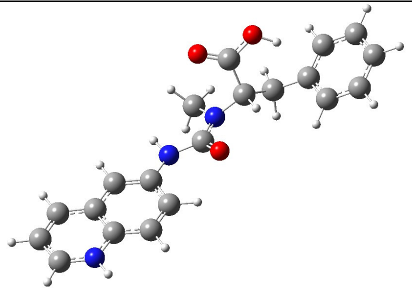 **[NMePh +H]$^+$-g** **197.1 Å^2 (23.8)**	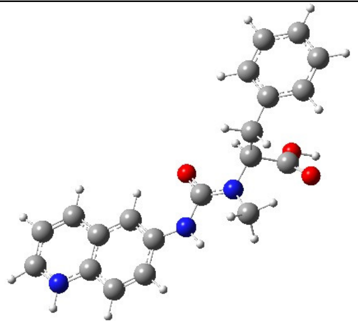 **[NMePh +H]$^+$-h** **197.3 Å^2 (10.7)**	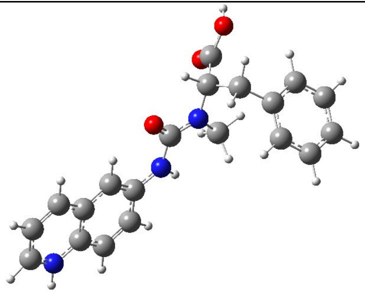 **[NMePh +H]$^+$-i** **192.7 Å^2 (7.8)**
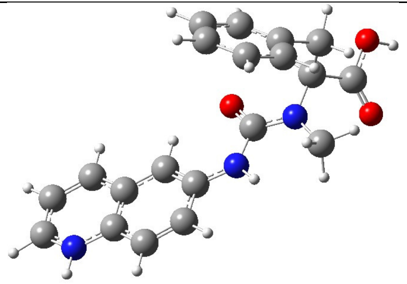 **[NMePh +H]$^+$-j** **190.2 Å^2 (2.8)**	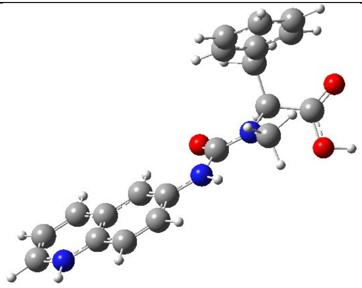 **[NMePh +H]$^+$-k** **189.7 Å^2 (12.0)**	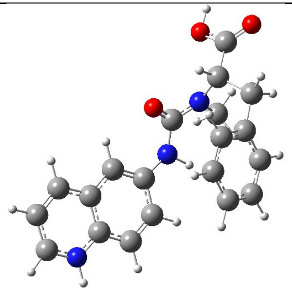 **[NMePh +H]$^+$-l** **186.2 Å^2 (14.9)**

Figure S29. Optimized structures of different conformers of [NMePh+H]$^+$ in the gas phase and their calculated CCS_{N2} values. The numbers in parenthesis are the relative Gibbs free energies in kJ mol^{-1}.

Table S27. The calculated CCS_{N2} values and relative Gibbs free energies for the conformers of $[NMePh+H]^+$.

$[M+H]^+$	**ΔG (kJ mol^{-1})**	**CCS_{N2} ($Å^2$)**
$[NMePh+H]^+$-a	19.5	196.4
$[NMePh+H]^+$-b	11.4	193.6
$[NMePh+H]^+$-c	**0.0**	**189.6**
$[NMePh+H]^+$-d	19.9	197.2
$[NMePh+H]^+$-e	10.9	192.5
$[NMePh+H]^+$-f	10.3	185.6
$[NMePh+H]^+$-g	23.8	197.1
$[NMePh+H]^+$-h	10.7	197.3
$[NMePh+H]^+$-i	7.8	192.7
$[NMePh+H]^+$-j	2.8	190.2
$[NMePh+H]^+$-k	12.0	189.7
$[NMePh+H]^+$-l	14.9	186.2

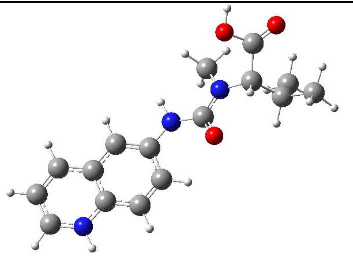

[NMeVal +H]$^+$-a

177.2 Å^2 (23.5)

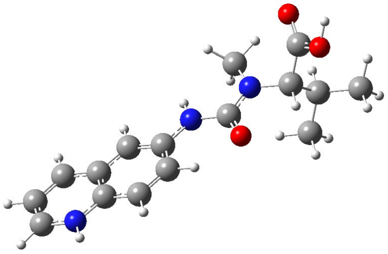

[NMeVal +H]$^+$-b

178.8 Å^2 (6.8)

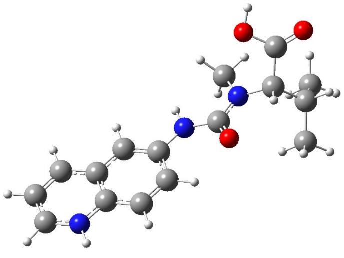

[NMeVal +H]$^+$-c

177.3 Å^2 (14.6)

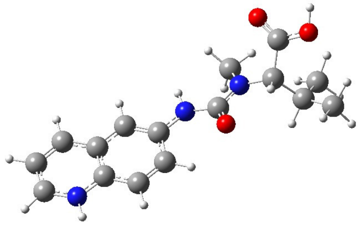

[NMeVal +H]$^+$-d

178.4 Å^2 (18.7)

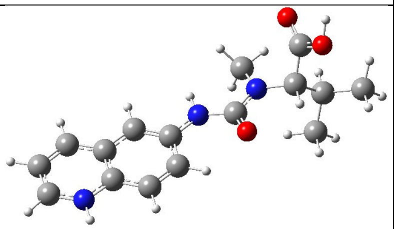

[NMeVal +H]$^+$-e

178.2 Å^2 (13.5)

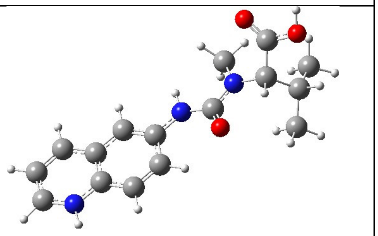

[NMeVal +H]$^+$-f

177.3 Å^2 (10.5)

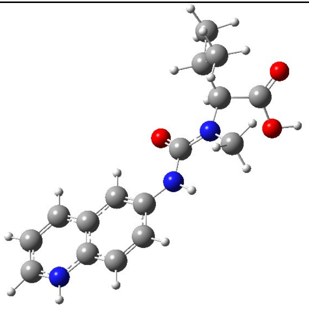

[NMeVal +H]$^+$-g

177.8 Å^2 (17.4)

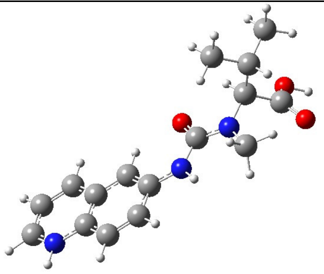

[NMeVal +H]$^+$-h

178.7 Å^2 (0.0)

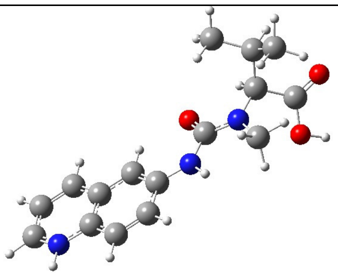

[NMeVal +H]$^+$-i

177.6 Å^2 (9.8)

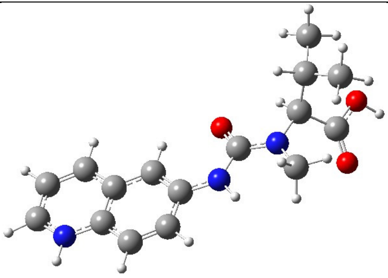

[NMeVal +H]$^+$-j

177.9 Å^2 (13.8)

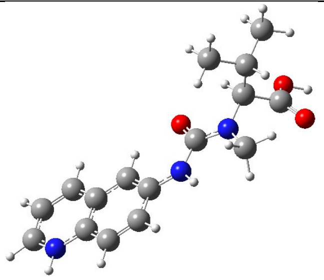

[NMeVal +H]$^+$-k

177.8 Å^2 (0.1)

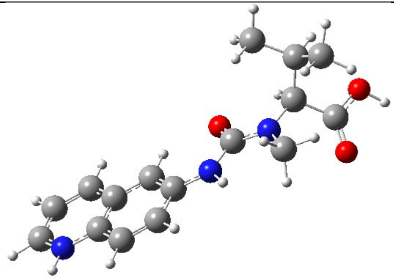

[NMeVal +H]$^+$-l

175.6 Å^2 (3.7)

Figure S30. Optimized structures of different conformers of [NMeVal+H]$^+$ in the gas phase and their calculated CCS_{N2} values. The numbers in parenthesis are the relative Gibbs free energies in kJ mol^{-1}.

Table S28. The calculated *CCS_{N2}* values and relative Gibbs free energies for the conformers of $[NMeVal+H]^+$.

$[M+H]^+$	**ΔG (kJ mol^{-1})**	**CCS_{N2} ($Å^2$)**
$[NMeVal+H]^+$-a	23.5	177.2
$[NMeVal+H]^+$-b	6.8	178.8
$[NMeVal+H]^+$-c	14.6	177.3
$[NMeVal+H]^+$-d	18.7	178.4
$[NMeVal+H]^+$-e	13.5	178.2
$[NMeVal+H]^+$-f	10.5	177.3
$[NMeVal+H]^+$-g	17.4	177.8
$[NMeVal+H]^+$-h	**0.0**	**178.7**
$[NMeVal+H]^+$-i	9.8	177.6
$[NMeVal+H]^+$-j	13.8	177.9
$[NMeVal+H]^+$-k	0.1	177.8
$[NMeVal+H]^+$-l	3.7	175.6

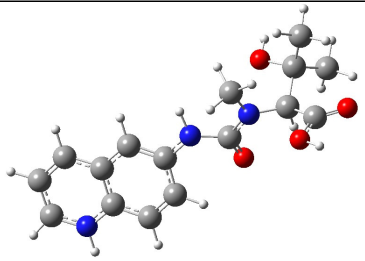 $[NMeValOH +H]^+$-a 178.4 Å^2 (14.0)	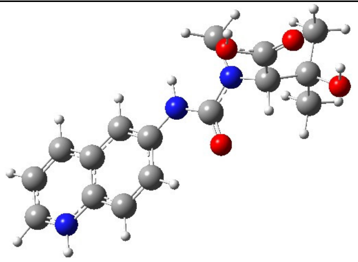 $[NMeValOH +H]^+$-b 182.2 Å^2 (17.6)	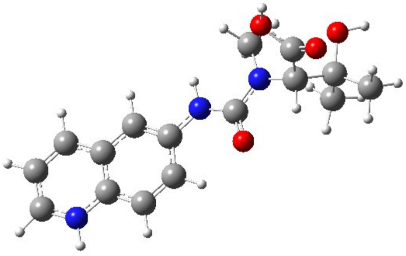 $[NMeValOH +H]^+$-c 181.3 Å^2 (12.8)
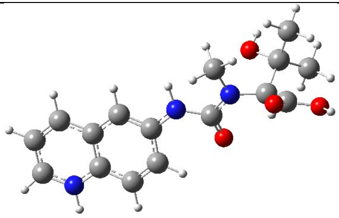 $[NMeValOH +H]^+$-d 180.5 Å^2 (10.0)	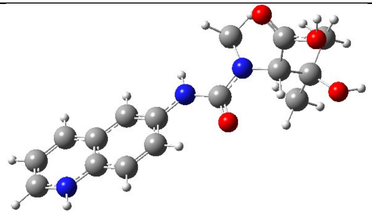 $[NMeValOH +H]^+$-e 181.6 Å^2 (25.1)	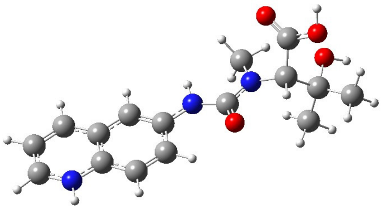 $[NMeValOH +H]^+$-f 180.3 Å^2 (0.6)
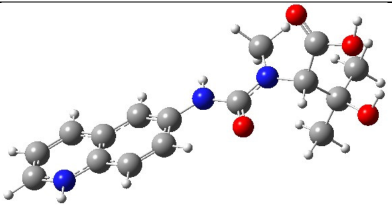 $[NMeValOH +H]^+$-g 181.9 Å^2 (14.8)	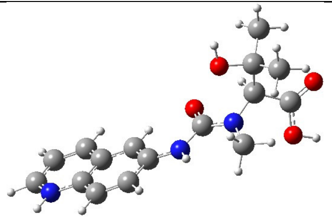 $[NMeValOH +H]^+$-h 179.7 Å^2 (11.2)	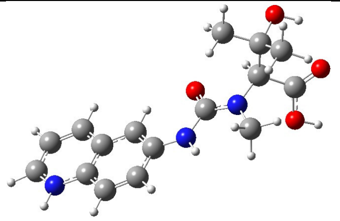 $[NMeValOH +H]^+$-i 179.7 Å^2 (4.8)
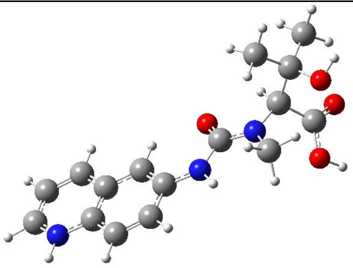 $[NMeValOH +H]^+$-j 181.5 Å^2 (2.6)	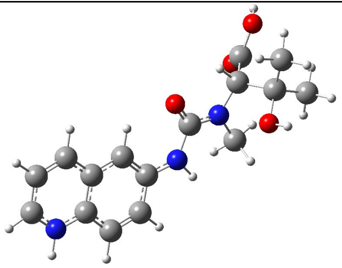 $[NMeValOH +H]^+$-k 178.4 Å^2 (8.9)	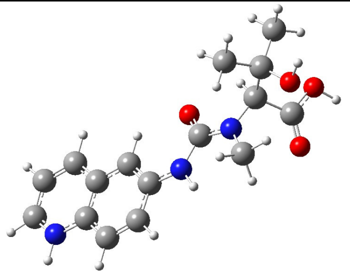 $[NMeValOH +H]^+$-l 178.8 Å^2 (0.0)

Figure S31. Optimized structures of different conformers of $[NMeValOH+H]^+$ in the gas phase and their calculated CCS_{N2} values. The numbers in parenthesis are the relative Gibbs free energies in kJ mol^{-1}.

Table S29 The calculated *CCS*$_{N2}$ values and relative Gibbs free energies for the conformers of [NMeValOH+H]$^+$.

[M+H]$^+$	**ΔG (kJ mol^{-1})**	**CCS$_{N2}$ (Å^2)**
[NMeValOH+H]$^+$-a	14.0	178.4
[NMeValOH+H]$^+$-b	17.6	182.2
[NMeValOH+H]$^+$-c	12.8	181.3
[NMeValOH+H]$^+$-d	10.0	180.5
[NMeValOH+H]$^+$-e	25.1	181.6
[NMeValOH+H]$^+$-f	0.6	180.3
[NMeValOH+H]$^+$-g	14.8	181.9
[NMeValOH+H]$^+$-h	11.2	179.7
[NMeValOH+H]$^+$-i	4.8	179.7
[NMeValOH+H]$^+$-j	2.6	181.5
[NMeValOH+H]$^+$-k	8.9	178.4
[NMeValOH+H]$^+$-l	**0.0**	**178.8**

Table S30. Comparison of experimentally obtained and theoretically calculated CCS-values from octreotide sample hydrolysate.

AA-AQC	**RT [min]**	**exp. $^{DT}CCS_{N2}$ [Å²]**	**calc. $^{DT}CCS_{N2}$ [Å²]**	**$\Delta^{DT}CCS_{N2}$ [%]**	***m/z***	**conformer with lowest energy**
D-Phe	1.04	187.1	n/a	n/a	336.134	n/a
L-Cys-IAA	1.67	183.5	n/a	n/a	349.097	n/a
L-Phe	1.36	187.1	n/a	n/a	336.134	n/a
D-Trp	1.27	191.4	n/a	n/a	375.145	n/a
L-Lys-bis-AQC	1.38	209.4	n/a	n/a	487.209	n/a
L-Thr	0.98	174.1	174.2	0.06	290.114	g
L-Thr-ol	0.47	169.9	n/a	n/a	276.134	n/a

Table S31. Comparison of the experimentally obtained and theoretically calculated CCS-values from the lipopeptide sample hydrolysate.

AA-AQC	**RT [min]**	**exp. $^{DT}CCS_{N2}$ [Å²]**	**calc. $^{DT}CCS_{N2}$ [Å²]**	**$\Delta^{DT}CCS_{N2}$ [%]**	***m/z***	**conformer with lowest energy**
D-Asp	2.19	175.2	n/a	n/a	304.093	n/a
D-Glu	1.7	178.2	n/a	n/a	318.108	n/a
L-Glu	1.84	178.2	n/a	n/a	318.108	n/a
D-Ser	1.13	168.8	n/a	n/a	276.098	n/a
D-Thr	0.98	174.1	174.2	0.06	290.114	g
L-Val	1.15	175.6	n/a	n/a	288.134	n/a

Table S32. Comparison of the experimentally obtained and theoretically calculated CCS-values from the aureobasidin A sample hydrolysate.

AA-AQC	**RT [min]**	**exp. $^{DT}CCS_{N2}$ [Å²]**	**calc. $^{DT}CCS_{N2}$ [Å²]**	**$\Delta^{DT}CCS_{N2}$ [%]**	***m/z***	**conformer with lowest energy**
L-Leu	0.92	180.9	180.1	-0.44	302.15	j
L-NMeValOH	n/a	n/a	178.8	n/a	318.1241	l
D-OIle	n/a	n/a	n/a	n/a	n/a	n/a
L-MeVal[a]	1.03	181	178.7	-1.29	302.1500	h
L-Phe	1.20	187.1	n/a	n/a	286.119	n/a
L-MePhe	0.86	186.4	189.6	1.69	350.1497	c
L-Pro	0.91	168.6	n/a	n/a	286.119	n/a
L-*a*Ile	1.03	180.9	180.6	-0.17	302.15	n

[a]: isobaric to Leu

3.4.7.2.4 Application to natural lipopeptide samples

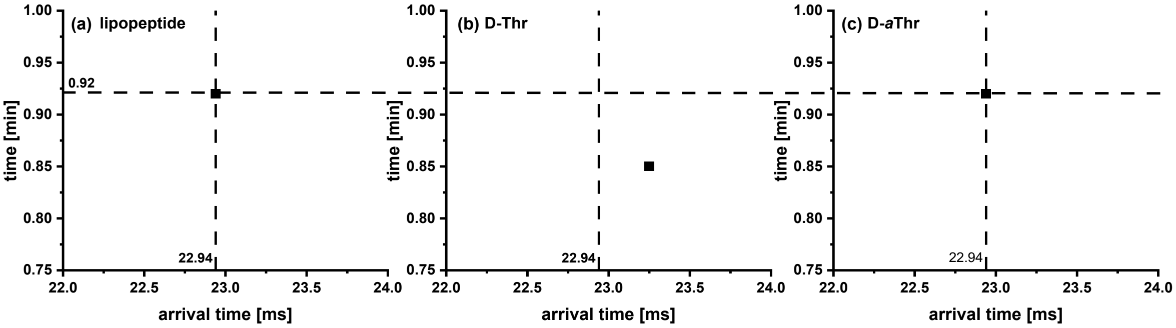

Figure S32. Retention time vs. arrival time plot for the (a) lipopeptide hydolysate, (b) D-Thr and (c) D-*a*Thr standards. Same conditions as in Figure 5.

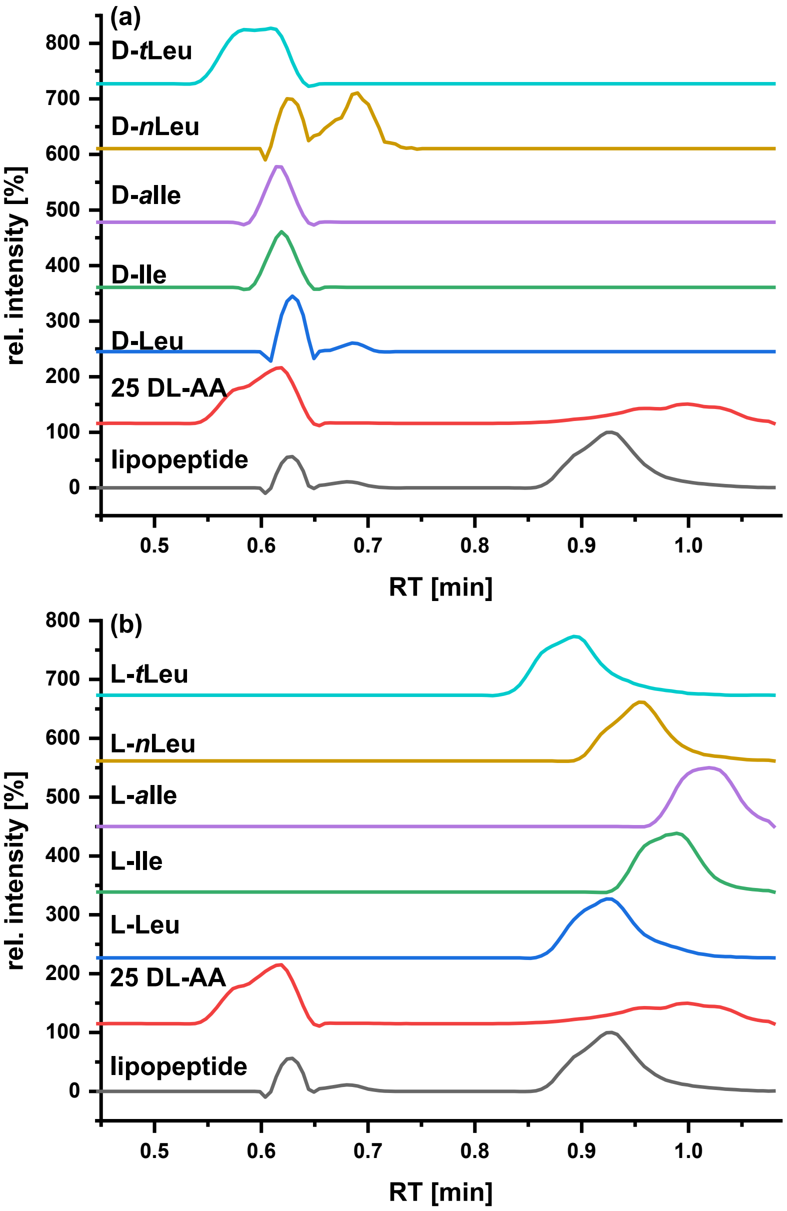

Figure S33. EICs of leucine isomers for the lipopeptide hydrolysate sample, 25 DL AA mix and single (a) D-AA and single (b) L-AA reference standard injections. Same experimental conditions as in Figure 5.

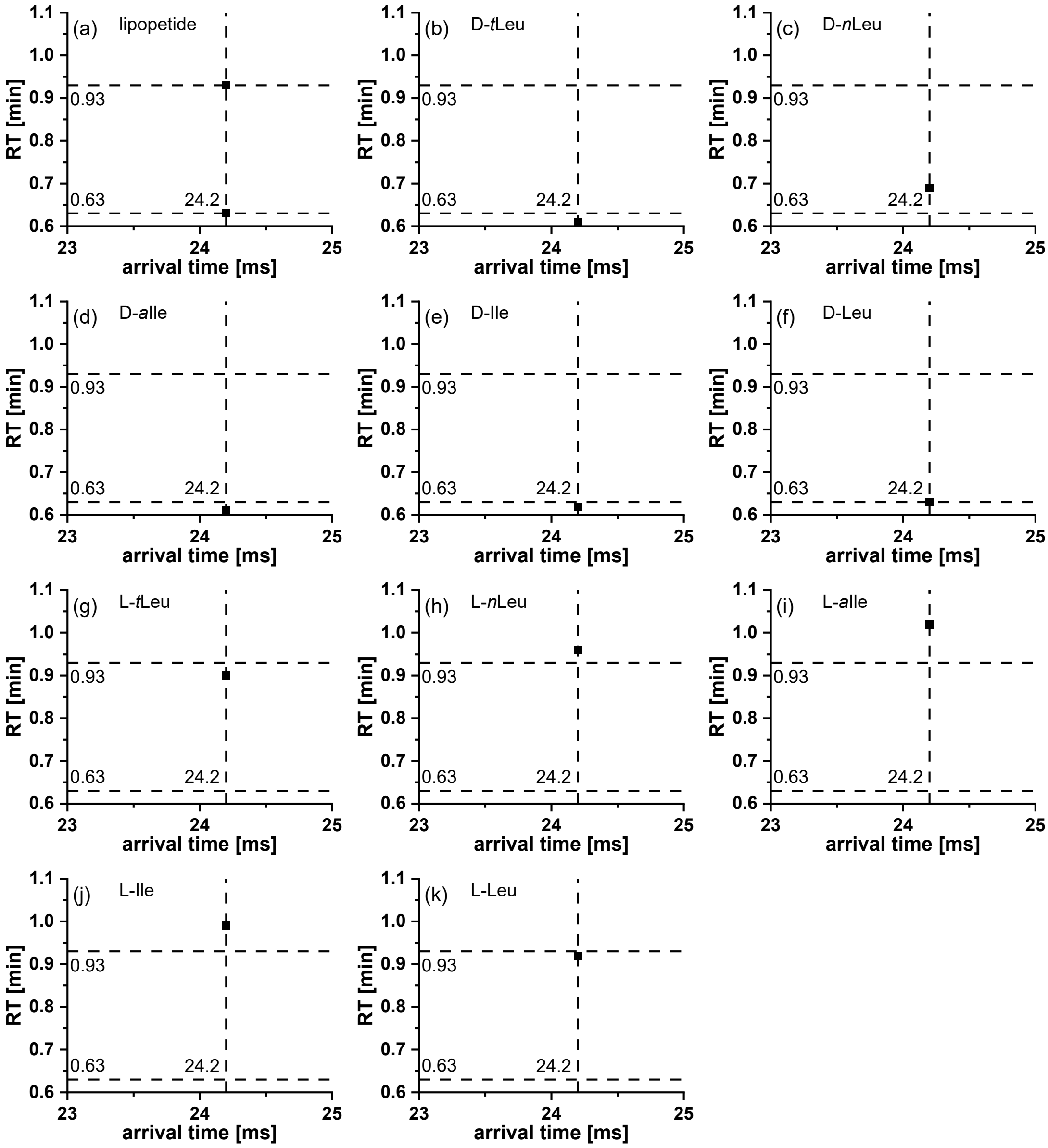

Figure S34. Retention time vs. drift time plot for the (a) lipopeptide hydrolysate, (b) D-*t*Leu, (c) D-*n*Leu, (d) D-*a*Ile, (e) D-Ile, (f) D-Leu, (g) L-*t*Leu, (h) L-*n*Leu, (i) L-*a*Ile, (j) L-Ile and (k) L-Leu. Same conditions as in Figure S33.

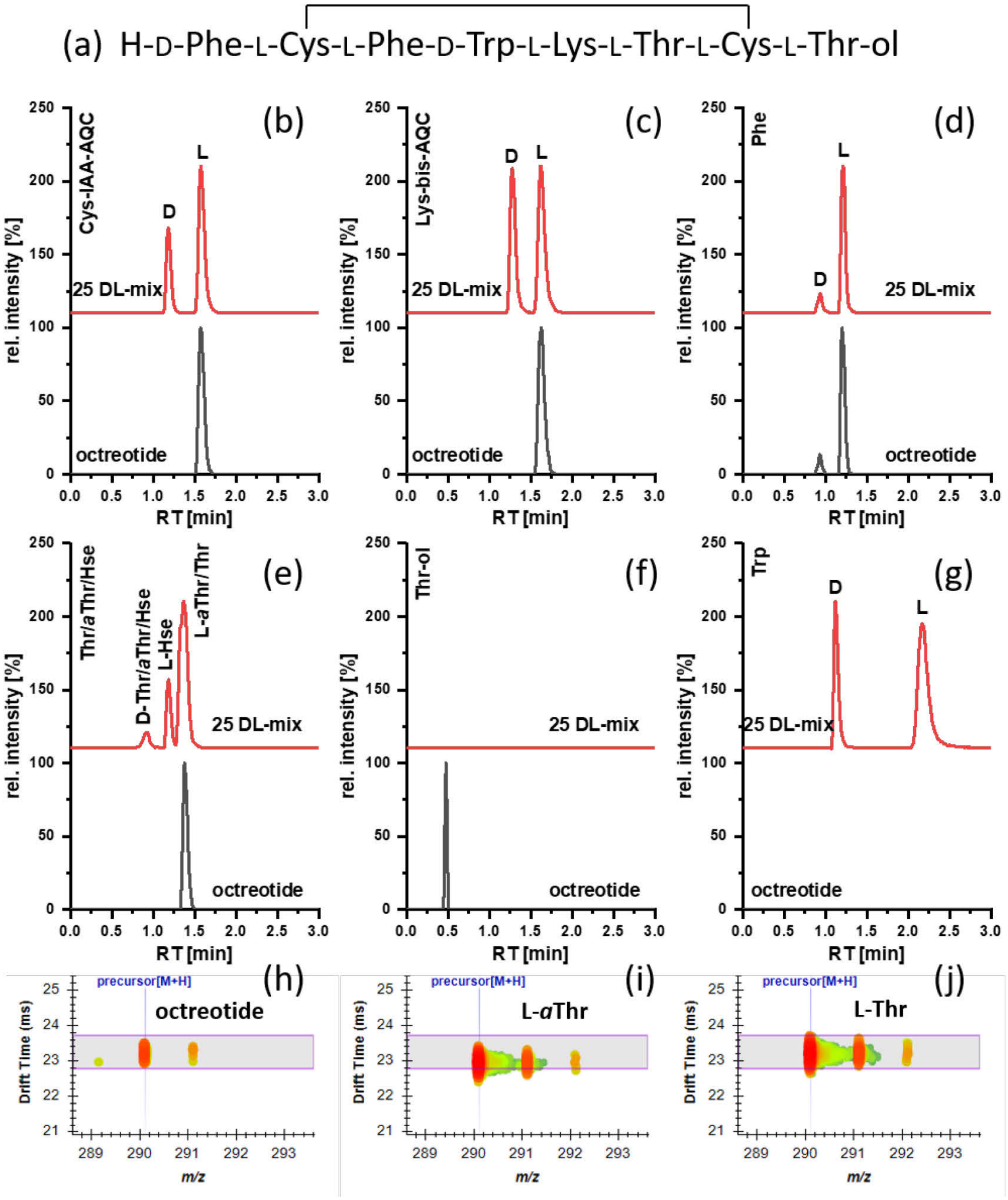

Figure S35. Enantioselective analysis of the peptide octreotide after its full hydrolysis**.** (a) Structure of octreotide. (b-g), EICs of the respective amino acids and drift time vs. *m/z* contour plots from threonine isomers of (h) octreotide hydrolysate, (i) L-*a*Thr and L-Thr single standards. Same experimental conditions as in Figure 5.

3.4.7.2.5 Quantitative method performance

Determination of limit of detection (LOD) was based on the slope *S’* and standard error of the y-intercept (σ) of calibration curve according to the ICH guidline Q2(R1) [3]:

$$LOD = \frac{3.3\sigma}{S\prime} \qquad \text{(Eq. S1)}$$

The limit of quantification (LOQ) was calculated analogously:

$$LOQ = \frac{10\sigma}{S\prime} \qquad \text{(Eq. S2)}$$

Table S33. Calibration functions of the D-amino acids including the linearity (R^2) the limit of detection (LOD), the limit of quantification (LOQ), the concentration range used for calibration, the accuracy and precision of a quality control sample and the applied quantification method. Either quantification based on light-to-heavy peak area ratios (L/H) or surrogate calibration with normalization of the peak areas by peak area of L-U-^{13}C^{15}N-Val (surrog.) was used depending on the signal intensity of the SIL-IS peak.

AA-AQC	slope	intercept	R^2	LOD [µM]	LOQ [µM]	range [µM]	av. accuracy	precision	quant. Method
D-Ala	3.69E-02	-6.36E-05	0.999	0.14	0.42	0.2-10	90.6%	16.1%	surrog.
D-Arg	3.63E+00	3.17E-01	0.971	0.19	0.57	0.1-2	89.2%	8.7%	L/H
D-Asn	3.56E+00	-5.91E-02	0.993	0.14	0.41	0.1-10	104.7%	2.9%	L/H
D-Asp	1.40E+00	-3.02E-02	0.989	0.24	0.72	0.1-10	92.6%	5.1%	L/H
D-Gln	3.65E-01	-9.83E-03	0.960	0.08	0.25	0.1-2	96.3%	10.7%	surrog.
D-Glu	2.21E+00	-1.35E-02	0.976	0.19	0.56	0.1-2	104.4%	13.1%	L/H
D-Gly	9.78E-01	1.11E-02	0.994	0.12	0.35	0.1-10	94.6%	3.5%	L/H
D-His	4.33E-01	2.05E-02	0.983	0.17	0.51	0.1-2	90.7%	12.8%	surrog.
D-Ile	7.41E-01	-1.32E-02	0.998	0.07	0.22	0.1-10	95.1%	8.1%	L/H
D-Leu	7.63E-01	-2.26E-02	0.994	0.08	0.25	0.1-10	95.6%	7.4%	L/H
D-Lys-bis-AQC	6.10E-01	1.70E-03	0.931	0.19	0.56	0.1-2	93.8%	9.3%	surrog.
D-Met	2.55E-01	-1.53E-02	0.975	0.08	0.25	0.1-2	95.8%	8.1%	surrog.
D-Phe	2.06E-01	-7.60E-03	0.976	0.13	0.38	0.1-2	104.8%	11.7%	surrog.
D-Pro	2.81E+01	-1.93E-01	0.985	0.15	0.46	0.1-2	92.8%	5.1%	L/H
D-Ser	1.87E-01	-3.58E-03	0.993	0.09	0.28	0.1-2	91.1%	3.9%	surrog.
D-Thr	3.47E-02	-4.54E-03	0.992	0.13	0.39	0.1-2	102.3%	20.2%	surrog.
D-Trp	9.35E-01	-1.65E-02	0.950	0.10	0.30	0.1-2	96.3%	9.7%	surrog.
D-Tyr	5.05E+00	-1.83E-01	0.993	0.14	0.44	0.1-2	100.1%	9.1%	L/H
D-Val	6.77E-01	-1.15E-02	0.991	0.12	0.35	0.1-2	94.3%	6.5%	L/H

Table S34. Calibration functions of the L-amino acids including the linearity (R²) the limit of detection (LOD), the limit of quantification (LOQ), the concentration range used for calibration, the accuracy and precision of a quality control sample and the applied quantification method. Either quantification based on light-to-heavy peak area ratios (L/H), surrogate calibration with normalization of the peak areas by peak area of L-U-$^{13}C^{15}N$-Val (surrog.) or calibration by normalization by total ion current (TIC) was used depending on most appropriate conditions.

AA-AQC	slope	intercept	R²	LOD [µM]	LOQ [µM]	range [µM]	av. accuracy	precision	quant. Method
L-Ala	3.31E-01	2.34E-02	0.985	0.12	0.35	0.1-2	88.0%	8.9%	surrog.
L-Arg	1.06E+00	2.97E-02	0.988	0.08	0.24	0.1-2	92.3%	6.5%	surrog.
L-Asn	1.50E+00	1.31E-01	0.991	0.09	0.27	0.1-2	99.1%	9.2%	L/H
L-Asp	2.65E-01	1.90E-02	0.976	0.15	0.45	0.1-2	87.6%	10.2%	surrog.
L-Gln	1.27E+00	4.68E-02	0.959	0.18	0.54	0.1-2	90.6%	12.2%	L/H
L-Glu	1.18E+00	1.38E-01	0.959	0.20	0.59	0.1-2	102.3%	8.0%	L/H
L-Gly	9.78E-01	1.08E-02	0.994	0.11	0.35	0.1-10	94.5%	3.3%	L/H
L-His	5.08E-01	9.86E-03	0.993	0.13	0.39	0.1-2	83.2%	9.4%	surrog.
L-Ile	5.37E-01	3.04E-02	0.993	0.07	0.23	0.1-2	92.9%	5.7%	L/H
L-Leu	5.37E-01	3.02E-02	0.992	0.08	0.24	0.1-2	92.9%	5.0%	L/H
L-Lys-bis-AQC	3.63E+05	2.72E+04	0.950	0.16	0.48	0.1-2	92.0%	14.8%	TIC
L-Met	8.58E-01	4.52E-02	0.978	0.07	0.22	0.1-2	93.1%	5.4%	surrog.
L-Phe	1.44E+00	7.85E-02	0.996	0.05	0.16	0.1-2	96.9%	5.1%	L/H
L-Pro	2.97E+00	2.93E-02	0.987	0.17	0.51	0.1-2	98.5%	11.2%	L/H
L-Ser	1.99E+00	1.03E-01	0.967	0.15	0.47	0.1-2	91.5%	8.6%	L/H
L-Thr	2.24E+00	9.10E-02	0.994	0.08	0.23	0.1-2	91.4%	3.5%	L/H
L-Trp	1.45E+00	4.08E-02	0.991	0.07	0.21	0.1-2	97.0%	3.9%	surrog.
L-Tyr	2.91E+00	6.80E-02	0.994	0.08	0.24	0.1-10	95.7%	2.1%	L/H
L-Val	4.70E-01	2.15E-02	0.994	0.16	0.49	0.1-2	94.4%	8.0%	L/H

3.4.7.3 References

[1] K.E. Butler, J.N. Dodds, T. Flick, I.D.G. Campuzano, E.S. Baker, High-Resolution Demultiplexing (HRdm) Ion Mobility Spectrometry–Mass Spectrometry for Aspartic and Isoaspartic Acid Determination and Screening, Anal. Chem., 94 (16) (2022) 6191-6199.

[2] J.C. May, R. Knochenmuss, J.C. Fjeldsted, J.A. McLean, Resolution of Isomeric Mixtures in Ion Mobility Using a Combined Demultiplexing and Peak Deconvolution Technique, Anal. Chem., 92 (14) (2020) 9482-9492.

[3] ICH, ICH Harmonised Tripartite Guideline - Validation of Analytical Procedures: Text and Methodology Q2(R1), 2005, pp. 1-13.

3.5 HPLC stereoisomer separation of a tetrapeptide fragment of the natural product epifadin and annotation of the absolute configurations

3.5.1 Introduction

The full structure elucidation of natural compounds is important to understand their biological activity and pinpoint the correct identity. The sum formula of a compound can be obtained using high resolution mass spectrometry (HR-MS) and tandem MS (MS/MS) is a useful tool to reduce the number of possible structures based on specific fragments [1]. In case of a peptide, MS/MS can be used to determine the amino acid sequence but the presence of isomeric amino acids like threonine or leucine isomers needs complementary techniques for differentiation like liquid chromatography (LC) or nuclear magnetic resonance spectroscopy (NMR) [2]. For natural compounds with chiral elements, identity is unequivocally clarified only after the annotation of their absolute configurations. Moreover, the use of genome mining approaches like the antiSMASH tool can be used to identify and analyse biosynthetic gene clusters, which complements the classical analytical chemistry-based approaches by prediction of molecule structures [3]. Classical chemistry-based methods include chromatographic separation modes like RP-LC or HILIC, which can be used to discriminate between diastereomeric peptides [4]. The separation of enantiomer pairs of a peptide can be done using chiral chromatography of the free or the derivatized peptide [5]. Furthermore, the absolute configuration of the peptide can be elucidated on the amino acid level using full hydrolysis followed by enantioselective chromatography [6].

In the current work, the absolute configuration of a natural tetrapeptide was elucidated. The amino acid sequence was determined in pre-experiments using LC-MS/MS. The number of all theoretical isomers can be calculated by 2^n where n is the number of chiral centres. A tetrapeptide can have $2^4 = 16$ stereoisomers with eight enantiomer pairs (not considering chiral centers in the side chain). Genome mining was used to predict the absolute configuration of the tetrapeptide, however, for an unambiguous identification chiral LC-MS was deemed necessary. The absolute configuration of the natural peptide could be confirmed successfully. Later the chromatographic separation was extended to the complete set of all 16 stereoisomers without the need to rely on the genome mining approach.

3.5.2 Experimental

3.5.2.1 Sample preparation

The tetrapeptide stereoisomers were synthesised by stereoselective solid-phase peptide synthesis (SPPS). The reaction and washing steps were carried out in a peptide synthesis reactor (5 mL, 25 µm polypropylene frit, Carl Roth). The LDLD tetrapeptide was synthesised starting with swelling of the Fmoc-D-Asn(Trt) resin (TG S RAM, Rapp Polymere, loading: 0.23 mmol/g, 150 mg, 34.5 µmol scale) in 2 mL DMF for 30 min. First the Fmoc protection group was cleaved by alkaline treatment with a solution of 2 % DBU/10% morpholine in DMF (v/v) for three min and an additional second treatment for 12 min. The resin-bound residue was then submitted to iterative peptide assembly using a solution of the respective Fmoc-D/L-AAx-OH (Fmoc-L-Asp(O*t*Bu)-OH, Fmoc-D-Phe-OH, Fmoc-L-Phe-OH) (6 equivalents), HOBt and HATU (both 6 equiv.) and NMM (8 equiv.) in 2 mL DMF to couple the next amino acid in a 45 min reaction. Subsequently the Fmoc-deprotection was performed using 2 % DBU/10% morpholine in DMF (v/v) for three min and an additional second treatment for 12 min. After full assembly and final Fmoc-deprotection of the tetrapeptide amide on the solid support, the resin was washed with 3x 2 mL DMF, 3x 2 mL DCM, 3x 2 mL toluene, 3x 2 mL IPA, 3x2 mL diethylether (Et_2O) and then dried under reduced pressure for three hours. The dried peptide was cleaved from the resin by acidic treatment with TFA/TIPS/H_2O (95:2.5:2.5 v/v, 2 mL) for one hour and for a total of three times. A final cleavage step with 2 mL pure TFA for 10 min was performed. The cleavage solvents were removed under reduced pressure and the residue washed three times with 2 mL Et_2O. The precipitate was dissolved in 10 mL *tert*-butanol/H_2O (1:1 v/v) and lyophilised. All other stereoisomers were synthesised in the same fashion using the respective Fmoc-D/L-Asn(Trt) resins and Fmoc-D/L-AAx-OH amino acids.

Lyophilised samples were initially dissolved in water/MeOH/FA (0.4995:0.4995:0.001 v/v/v) to a concentration of 1 mg/mL. Two series of samples with different diluents were prepared for RP separation and chiral separation, respectively, to ensure samples are in a weak elution strength solvent mitigating potential breakthrough issues. Chiral LC samples were dissolved in ACN/MeOH/H_2O (49:49:2 v/v/v) while RP-LC samples were dissolved in ACN/water (1:9 v/v). For both sample series a sample mixture of all 16 stereoisomers was prepared at a final concentration of 100 µM (54.1 µg/mL) and samples containing the enantiomer pairs were prepared in a 1:3 ratio to enable peak assignment based on the peak area as shown in Tab. 1.

Tab. 1: Preparation of the enantiomer pair sample mixtures.

enantiomer pair	label enantiomer pair	label enantiomer 1	label enantiomer 2	c [µM]
DLDL_LDLD	A	A1	A2	40:120
DDDD_LLLL	B	B1	B2	40:120
DDDL_LLLD	C	C1	C2	40:120
DDLD_LLDL	D	D1	D2	40:120
DDLL_LLDD	E	E1	E2	40:120
DLDD_LDLL	F	F1	F2	40:120
DLLD_LDDL	G	G1	G2	40:120
DLLL_LDDD	H	H1	H2	40:120

3.5.2.2 Instrumentation and Software

The optimization of the chromatographic separation was performed on an Agilent 1290 Infinity UHPLC system (Agilent, Waldbronn, Germany) equipped with a binary pump (G4220A), a thermostated column compartment (G1316A), and a PAL HTC-xt autosampler (CTC Analytics AG, Zwingen, Switzerland). Mass spectrometric detection was performed using a Sciex 5600+ QTOF system (Sciex, Ontario, Canada) equipped with a DuoSpray ion source which was operated in ESI(+) mode. The ion source was operated at a temperature of 600°C, curtain gas (CUR) was at 35 psi, nebulizer gas (GS1) at 50 psi, heater gas (GS2) at 40 psi and the ion spray voltage floating was at 5,000 V. Data was acquired in SWATH mode with a total of 25 MS experiments (cycle time 2382 ms) including one survey scan and 24 MS/MS scans. The TOF survey scan had the collision energy (CE) at 10 V, declustering potential was at 100 V and the accumulation time was 50 ms. Each SWATH MS/MS experiment had an accumulation time of 95.1 ms, the DP was 100 V, the rolling collision energy option was used with a collision energy spread (CES) of 15 V. The first SWATH window was from 50-200 Da, SWATH windows 2 to 21 were 20 Da wide with a one Da overlap to the adjacent windows. SWATH window 23 was from 800-1,000.5 Da and the last SWATH window 24 was from 1,000-1,250 Da. The TOF scan range for both the survey scan and the

MS/MS scans was from 100-2,000 Da, respectively. Data was acquired with Analyst TF 1.8.1 Software (Sciex).

Pre-experiments of the enantiomer separation were carried out on an Agilent Infinity II instrument with an autosampler (G7167B), binary pump (G7120A), thermostated column compartment (G7116B) and a diode array detector (DAD, G7117A).

Data processing and visualization was done with Microsoft Excel 2019 (Microsoft, Redmond, WA, USA), Skyline 22.2 (MacCoss Lab, Seattle, WA, USA), DryLab 4.3.5 (Molnár-Institute, Berlin, Germany) and OriginPro 2022 (OriginLab, Northapton, MA, US).

The enantiomer separation was performed on a ZWIX(+) column from Daicel Chiral Technologies Europe SAS (Illkirch Cedex, France) (3.0x150 mm, 3 µm) using ACN/MeOH/H_2O (49:49:2 v/v/v) with 50 mM FA/25 mM NH_3 as mobile phase in an isocratic method at 0.5 mL/min and 25°C. Samples were dissolved in mobile phase to a concentration of 0.1 mg/mL and 2 µL were injected onto the column.

Diastereomer separation was done with an Acquity UPLC BEH C18 column (Waters Corporation, Milford, MA, USA), 1.0x150mm, 1.7 µm, with: H_2O + 0.1 % FA as mobile phase A, ACN + 0.1 % FA as mobile phase B, a flow rate of 100 µL/min and a column temperature of 40°C.

3.5.2.3 Calculations

The retention factor *k* can be calculated using the retention time t_R and the dead-time t_0 of an unretained compound using equation (1)

$$k = \frac{t_R - t_0}{t_0} \tag{1}$$

The selectivity α can be calculated based on the retention factors of two peaks:

$$\alpha = \frac{k_2}{k_1} \tag{2}$$

The resolution *R* of two peaks can be calculated based on their retention times and their peak widths at half height $W_{1/2}$:

$$R_S = 1.18 \cdot \frac{t_{R_2} - t_{R_1}}{W_{1/2_1} + W_{1/2_2}} \tag{3}$$

The plate number *N* is a measure of column performance:

$$N = 5.54 \cdot \left(\frac{t_R}{W_{1/2}}\right)^2 \tag{4}$$

3.5.3 Results and Discussion

The predicted structure based on antiSMASH analysis of the natural peptide was L-Phe-D-Phe-L-Asp-D-Asn (LDLD, Fig. 1a) and the corresponding enantiomer has the opposite configuration (Fig. 1b).

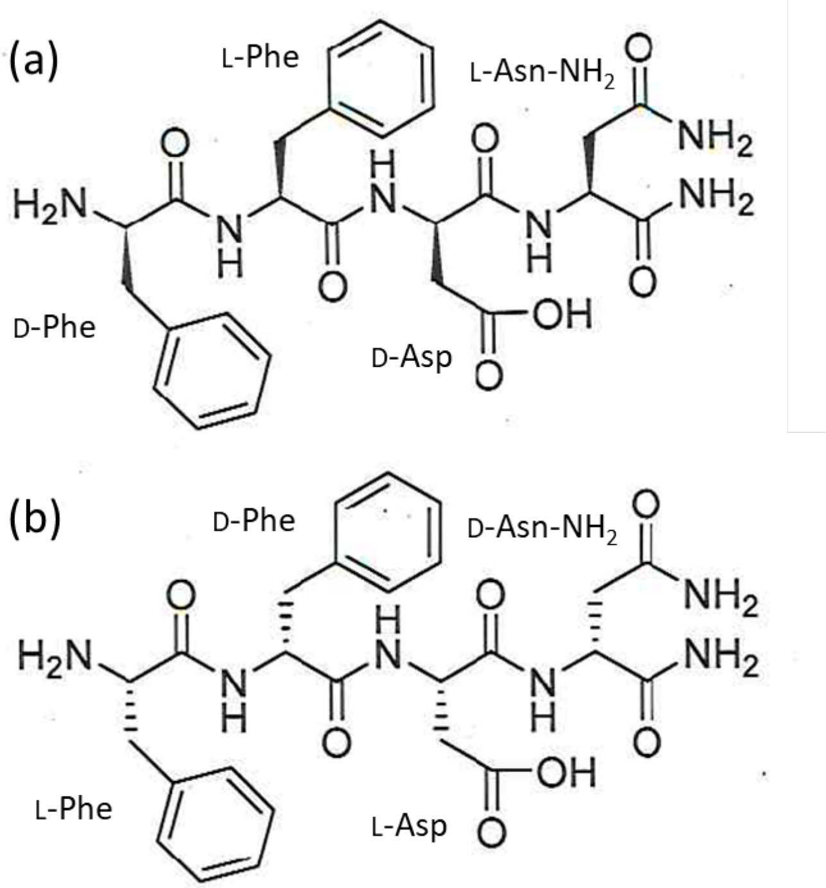

Fig. 1: Structures of the two possible enantiomers of the tetrapeptide. (a) DLDL enantiomer of the tetrapeptide and (b) LDLD enantiomer of the tetrapeptide.

The total number of stereoisomers of a tetrapeptide is 16 with eight enantiomer pairs, respectively. Thus, in an achiral separation, e.g. RP-LC, 8 peaks are expected which are diastereomeric to each other and each consist of two coeluting enantiomers.

3.5.3.1 Optimization of the Enantiomer Separation

The influence of the buffer concentration of the mobile phase on the enantioselective separation was investigated (Fig. 2). The higher the buffer concentration, the lower the retention (smaller *k*, refer Tab. 2) on the stationary phase. Furthermore, the separation efficiency in terms of the plate number *N* decreases with decreasing buffer concentration due to stronger peak broadening. The highest resolution of the LDLD/DLDL peak pair was obtained at a concentration of 25/12.5 mM FA/NH_3 (R_s = 5.62) but at the highest buffer concentration the resolution was only slightly lower (R_s = 5.36) and the overall analysis time is two minutes shorter. At buffer concentrations below 50/25 mM an impurity peak was observed which eluted at the dead time (1.48 min) at the highest buffer concentrations. Therefore, the buffer concentration of 50/25 mM FA/NH_3 was selected to be optimal for the enantiomer separation of the LDLD/DLDL peak pair and baseline separation could be achieved.

The optimized enantiomer separation conditions were then applied for the separation of all 16 stereoisomers. For six out of eight enantiomer pairs baseline separation (R_s > 1.5, Tab. 3) was achieved while the DDDD_LLLL and DLLL_LDDD enantiomer pairs had resolutions of 0.81 and 0.88, respectively. Still this resolution is sufficient to differentiate the enantiomers. Unfortunately, the mixture of all 16 stereoisomers has several co-eluting diastereomers. Therefore, chiral LC alone is not sufficient to separate all stereoisomers and the separation of the diastereomers requires an orthogonal method. In addition to the tetrapeptide peak, peaks from the respective aspartate succinimide impurities could be detected (see

Fig. 3b) in different relative amounts. The mechanism of the aspartate succinimide formation and isomerization of aspartate to *iso*-aspartate will be covered in the following chapter.

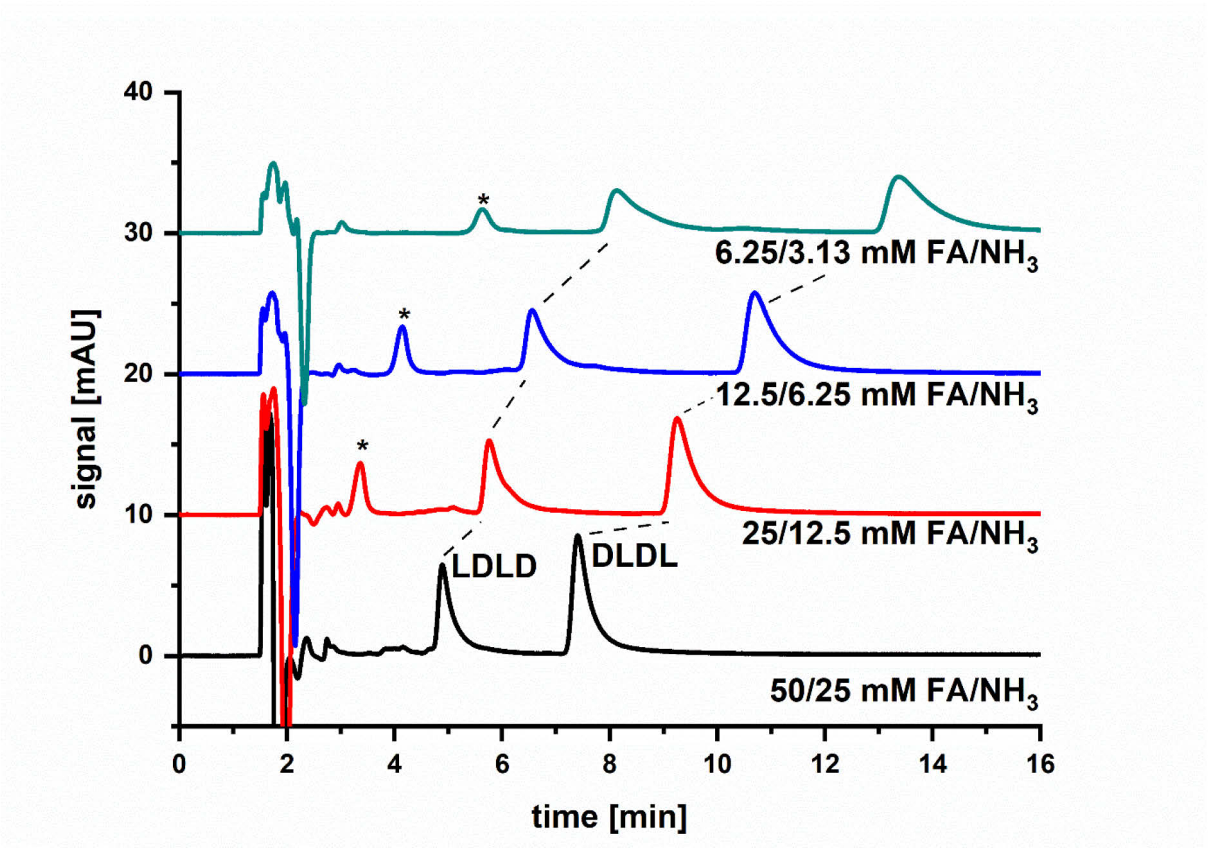

Fig. 2: Evaluation of the influence of the mobile phase buffer concentration on the enantiomer separation. The dashed lines highlight how the LDLD and DLDL peaks change their retention times at different buffer concentrations. The asterisk (*) highlights an impurity peak. Column: ZWIX(+) 3.0x150 mm, 3 µm, flow rate: 0.5 mL/min isocratic at 25°C, mobile phase: ACN/MeOH/H_2O (49:49:2 v/v) with buffer composition described in the figure, detection: 230 nm.

Tab. 2: Performance evaluation of different mobile phase buffer concentrations. The void-time t_0 is 1.48 min.

c (buffer FA/NH_3)[mM]	peak	t_R [min]	$w_{1/2}$ [min]	t'_R [min]	k	α	R_s	N
50/25	LDLD	4.887	0.244	2.949	2.3	n/a	n/a	2,224
	DLDL	7.403	0.31	2.846	4.0	1.74	5.36	3,162
25/12.5	LDLD	5.756	0.313	3.343	2.9	n/a	n/a	1,875
	DLDL	9.252	0.421	2.842	5.3	1.82	5.62	2,678
12.5/6.25	LDLD	6.56	0.379	2.848	3.4	n/a	n/a	1,661
	DLDL	10.688	0.539	2.995	6.2	1.81	5.31	2,180
6.25/3.13	LDLD	8.129	0.624	3.213	4.5	n/a	n/a	941
	DLDL	13.372	0.812	3.198	8.0	1.79	4.31	1,504

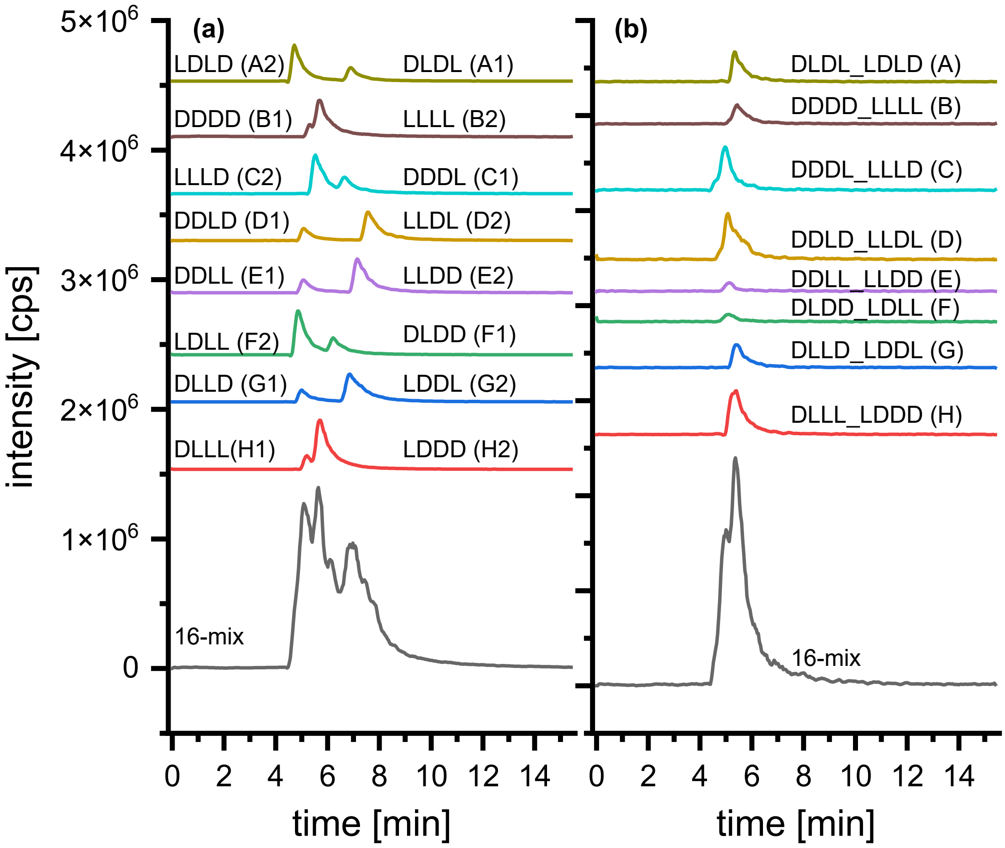

Fig. 3: Extracted ion chromatograms (EICs) of the optimized enantiomer separation on the chiral ZWIX(+) column. Separation of the (a) tetrapeptide amide enantiomers (*m/z* = 541.2405) and (b) the tetrapeptide Asp-succinimide impurity (*m/z* = 523.2300). Column: ZWIX(+) (3.0x150 mm, 3 µm) using ACN/MeOH/H_2O (49:49:2 v/v) with 50 mM FA/25 mM NH_3 as mobile phase in an isocratic method at 0.5 mL/min and 25°C.

Tab. 3: Chromatographic performance evaluation of the enantiomer separation. The void-time t_0 is 1.48 min.

peak	t_R [min]	$w_{1/2}$ [min]	t'_R [min]	k	α	R_s	N
DDDD	5.32	0.25	3.84	2.6	n/a	n/a	2,511
LLLL	5.73	0.35	4.25	2.9	1.11	0.81	1,486
LLLD	5.49	0.43	4.01	2.7	n/a	n/a	904
DDDL	6.66	0.40	5.18	3.5	1.29	1.66	1,537
DDLD	5.04	0.37	3.56	2.4	n/a	n/a	1,029
LLDL	7.54	0.47	6.06	4.1	1.70	3.51	1,427
DDLL	5.08	0.38	3.60	2.4	n/a	n/a	991
LLDD	7.14	0.46	5.66	3.8	1.57	2.89	1,336
LDLL	4.84	0.37	3.36	2.3	n/a	n/a	949
DLDD	6.25	0.42	4.77	3.2	1.42	2.11	1,228
LDLD	4.68	0.35	3.20	2.2	n/a	n/a	991
DLDL	6.94	0.38	5.46	3.7	1.71	3.65	1,849
DLLD	4.96	0.39	3.48	2.4	n/a	n/a	897
LDDL	6.82	0.48	5.34	3.6	1.53	2.52	1,119
DLLL	5.20	0.29	3.72	2.5	n/a	n/a	1,783
LDDD	5.69	0.37	4.21	2.8	1.13	0.88	1,311

3.5.3.2 Development of the Diastereomer Separation

The optimized enantiomer separation could still not separate the diastereomers in the mixture of all 16-stereoisomers (Fig. 3a), therefore, an orthogonal RP-LC method was developed. In a first screening experiment a C18 column and a water-acetonitrile gradient was tested using the full gradient range from 5 to 100 % ACN and a gradient time of 30 min (Fig. 4). Two more gradient times (60 and 90 min) were used as well to use the design of experiment (DoE) software DryLab to optimize the gradient design.

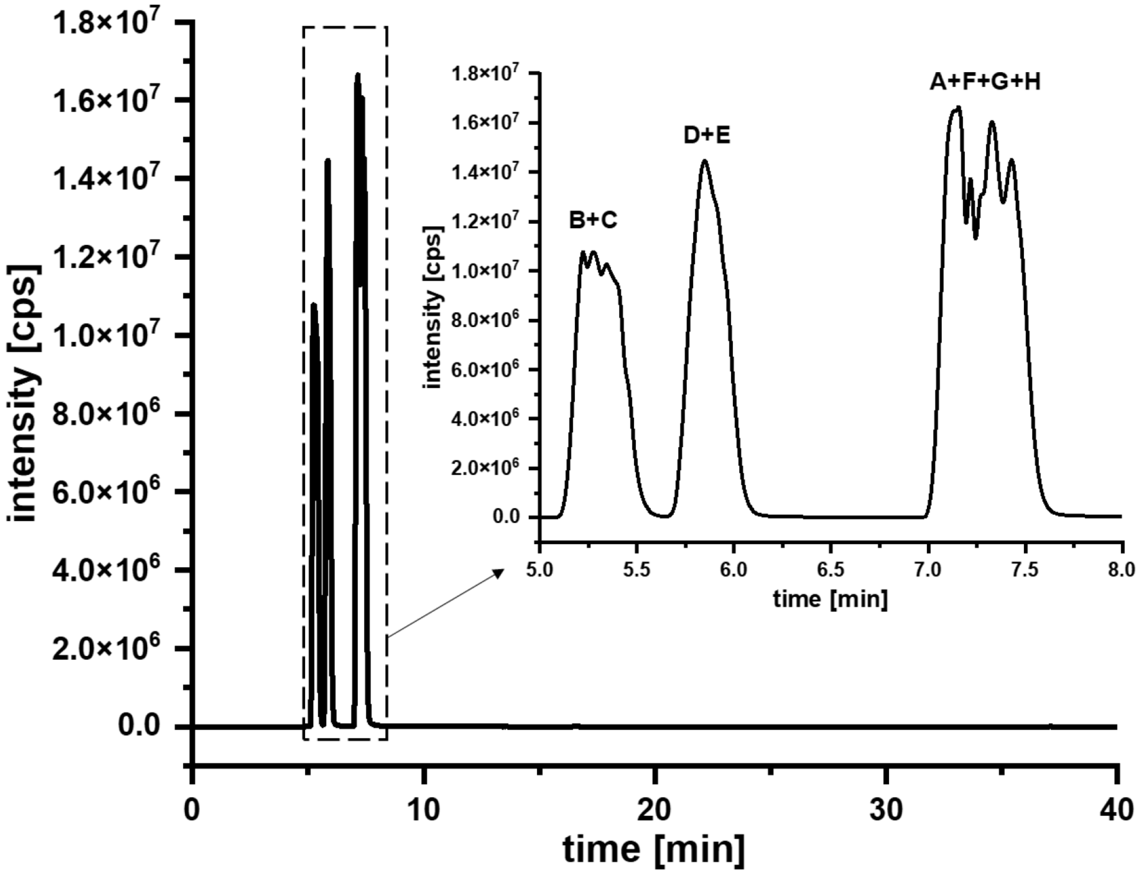

Fig. 4: EIC of the full acetonitrile gradient RP-LC separation of the diastereomers. Column: Waters Acquity UPLC BEH C18, 1.0x150mm, 1.7 µm, mobile phase A: H_2O + 0.1 % FA, mobile phase B: ACN + 0.1 % FA, gradient: 0-30 min 5-100 % B, 30-35 min 100 % B, 35-45 min 5 % B. Flow rate 100 µL/min, column temperature: 40°C.

The DryLab optimized gradient design for a gradient time of 30 min is shown in Fig. 5. The diastereomers B, C, D and E could be resolved partially while the diastereomers H and G, and the diastereomers A and F co-elute, respectively.

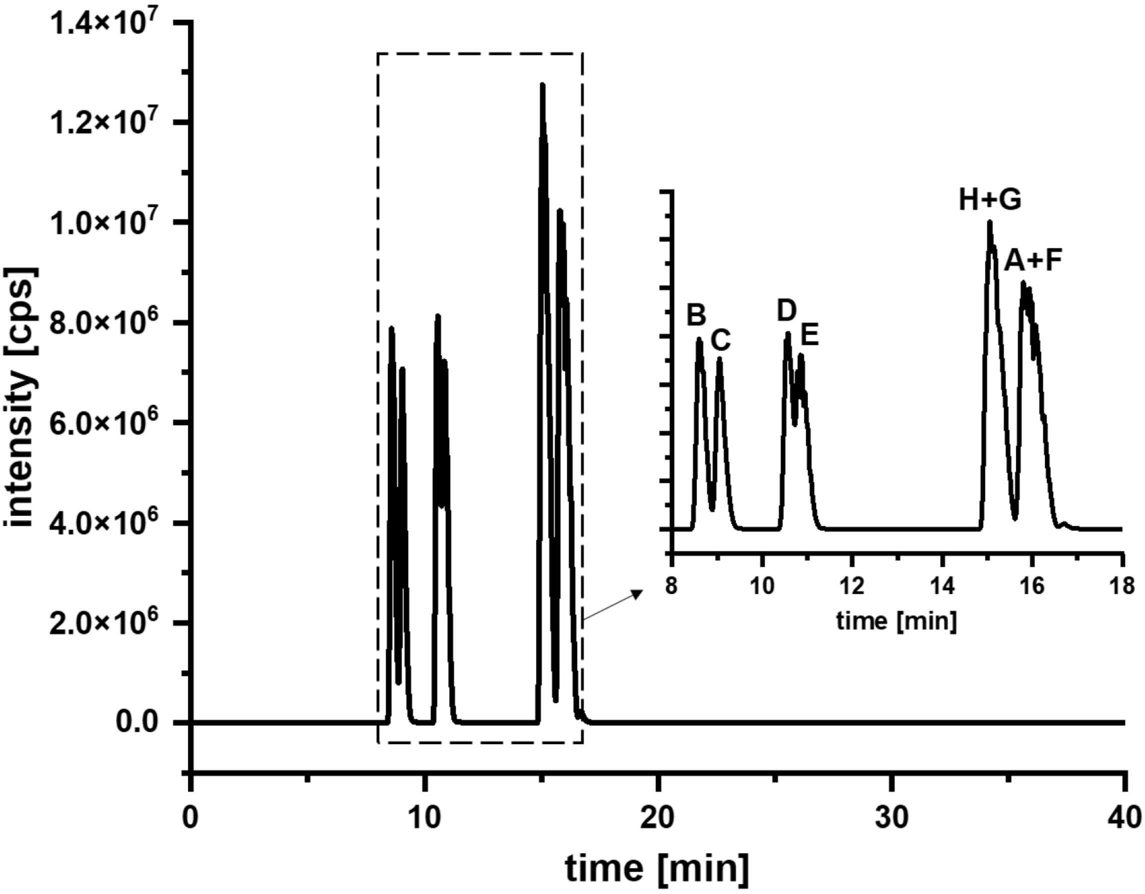

Fig. 5: EIC of the optimized conditions of the diastereomer separation on RP-LC. Column: Waters Acquity UPLC BEH C18, 1.0x150mm, 1.7 µm, mobile phase A: H_2O + 0.1 % FA, mobile phase B: ACN + 0.1 % FA, gradient: 0-30 min 5-30 % B, 30-35 min 30-100 % B, 35-45 min 5 % B. Flow rate 100 µL/min, column temperature: 40°C.

After increasing the gradient time to 90 min (Fig. 6) the diastereomers A and F can be resolved partially, while H and G still co-elute.

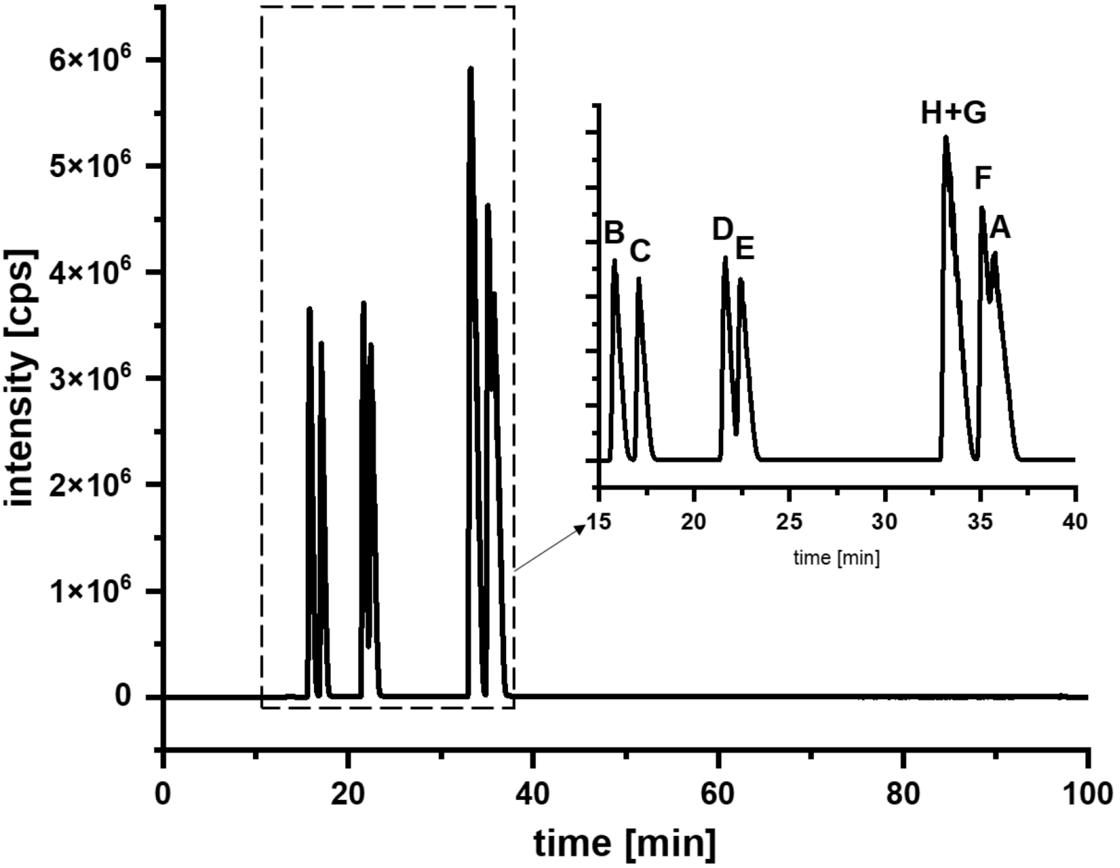

Fig. 6: EIC of the optimized conditions of the diastereomer separation on RP-LC at 90 min gradient time. Column: Waters Acquity UPLC BEH C18, 1.0x150mm, 1.7 µm, mobile phase A: H_2O + 0.1 % FA, mobile phase B: ACN + 0.1 % FA, gradient: 0-90 min 5-30 % B, 90-95 min 30-100 % B, 95-105 min 5 % B. Flow rate 100 µL/min, column temperature: 40°C.

The separation conditions shown in Fig. 6 were the best found so far, but still a more extensive method development is needed to obtain a separation of the H and G diastereomers. The assignment of the diastereomers to the respective peaks was done by the injection of the single enantiomer pairs (Fig. 7).

The samples H (DLLL_LDDD) and G (DLLD_LDDL) showed an additional peak in the extracted ion chromatograms which might be an *iso*-aspartate (*iso*Asp) impurity which is isomeric and thus has the same *m/z* value as the original tetrapeptide. Isomerization of Asp to *iso*Asp is a known issue and can occur during synthesis [7]. Some stereoisomers might be more prone to isomerization compared to others. On the other hand, the diastereomer separation conditions might not be sufficient to separate all tetrapeptide stereoisomers from their respective *iso*Asp impurities. During the development of the enantiomer separation no *iso*Asp peaks were observed indicating insufficient selectivity in the chiral LC separations.

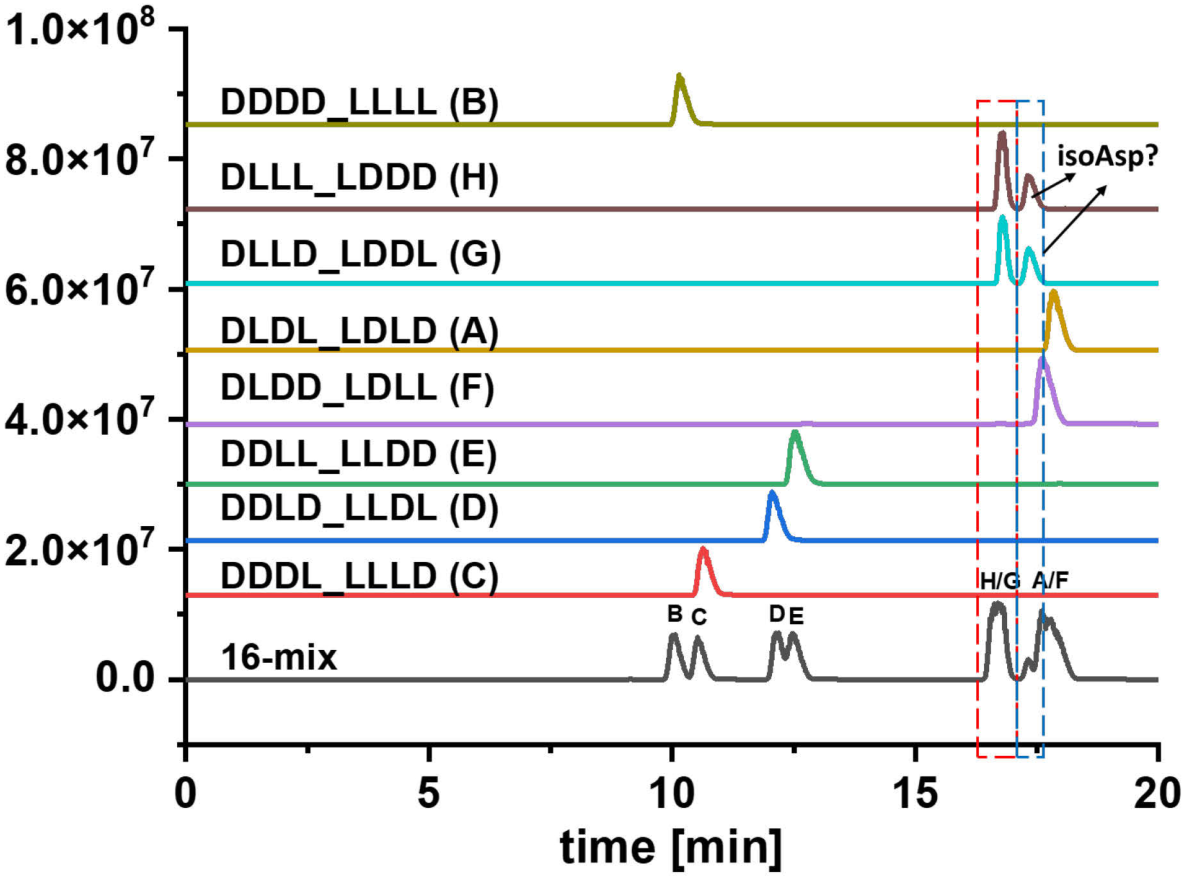

Fig. 7: EICs for the assignment of the diastereomer peaks in the tetrapeptide mixture. The red box highlights the co-elution of the two enantiomer pairs DLLL_LDDD (H) and DLLD_LDDL (G). The blue box might contain an *iso*-aspartic acid (*iso*Asp) impurity peak. Column: Waters Acquity UPLC BEH C18, 1.0x150mm, 1.7 µm, mobile phase A: H_2O + 0.1 % FA, mobile phase B: ACN + 0.1 % FA, gradient: 0-90 min 5-30 % B, 90-95 min 30-100 % B, 95-105 min 5 % B. Flow rate 100 µL/min, column temperature: 40°C.

Aspartic acid can be subject to a multistep equilibration reaction including isomerization and racemization steps as shown in Fig. 8. Starting from L-α-aspartate containing tetrapeptide, L-succinimide can be formed through (Fig. 8a). This L-succinimide peptide can subsequently form either the L-*iso*-aspartate (Fig. 8b) or racemise to the D-succinimide peptide (Fig. 8c). The D-succinimide ring open either to the D-aspartate peptide (Fig. 8d) or to the respective D-*iso*-aspartate peptide (Fig. 8e).

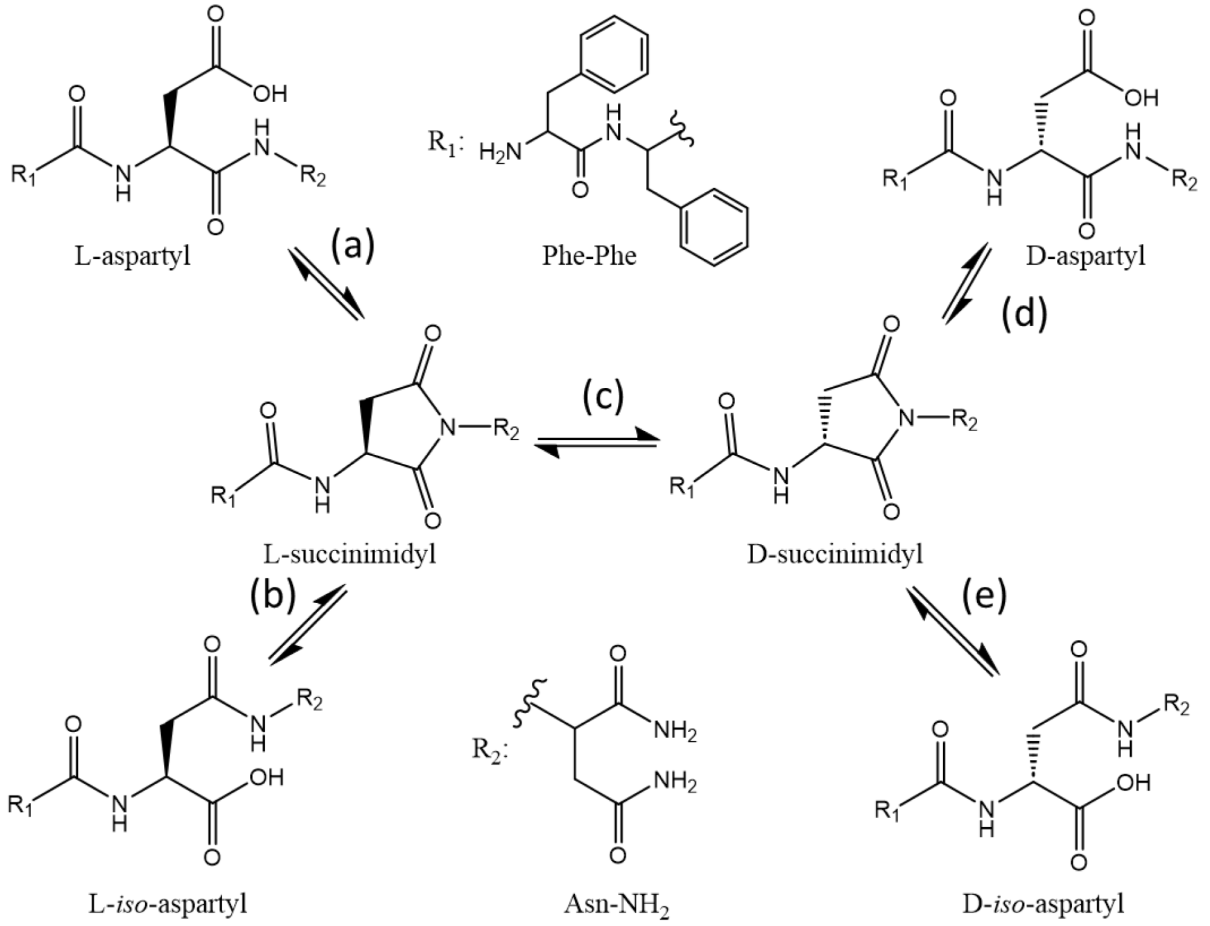

Fig. 8: Aspartate isomerization of the tetrapeptide. (a) L-Succinimide formation, (b) formation of L-*iso*-aspartate (c) racemization of L-succinimide to D-succinimide, (d) formation of D-aspartic acid and (e) formation of D-*iso*-aspartic acid.

Indeed, the aspartate succinimide impurity was found in all samples but at quite different amounts indicating the stereoselectivity of the isomerization reaction (Fig. 9). The enantioselective analysis of the *iso*Asp impurity was beyond the scope of the presented work.

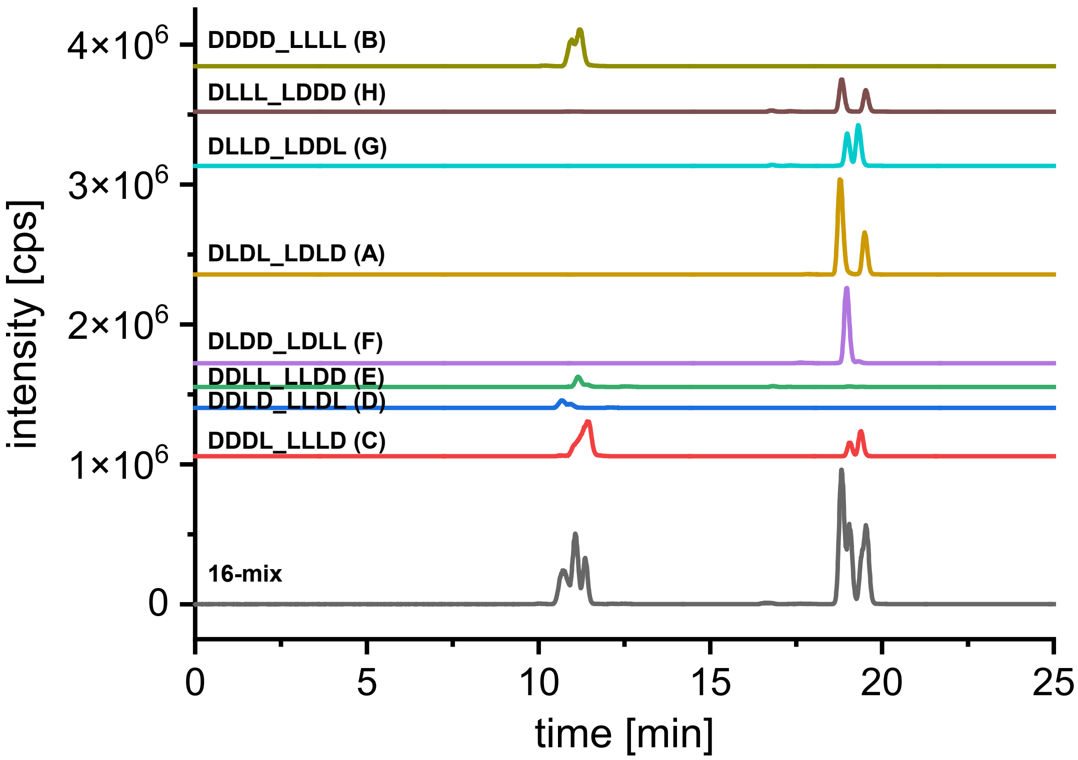

Fig. 9: Extracted ion chromatograms (EIC) of the aspartate succinimide impurity containing tetrapeptide. Waters Acquity UPLC BEH C18, 1.0x150mm, 1.7 µm, mobile phase A: H_2O + 0.1 % FA, mobile phase B: ACN + 0.1 % FA, gradient: 0-90 min 5-30 % B, 90-95 min 30-100 % B, 95-105 min 5 % B. Flow rate 100 µL/min, column temperature: 40°C.

The next method development steps should include a column and mobile phase screening to find suitable conditions to separate all eight diastereomers. Furthermore, the method should be capable to separate the aspartate and *iso*-aspartate forms of the tetrapeptide. After optimization of the diastereomer separation a 2D-LC method should be established combining the diastereomer and enantiomer separation. This should finally result in a method which can separate all 16 stereoisomers within a single 2D-LC-MS experiment.

3.5.3.3 Analysis of the Natural Tetrapeptide

The optimized enantiomer method was applied to a natural tetrapeptide sample. Based on genome mining the absolute configuration was expected to be LDLD. The chiral LC-MS results (Fig. 10) and the peak area ratios (Tab. 4) show clearly the absolute configuration of the natural peptide is indeed LDLD. In a next step the natural peptide sample should be analysed again with a diastereomer selective LC method and finally with a 2D-LC method to verify the absolute configuration based only on the chromatographic results without the need to rely on the genome mining information.

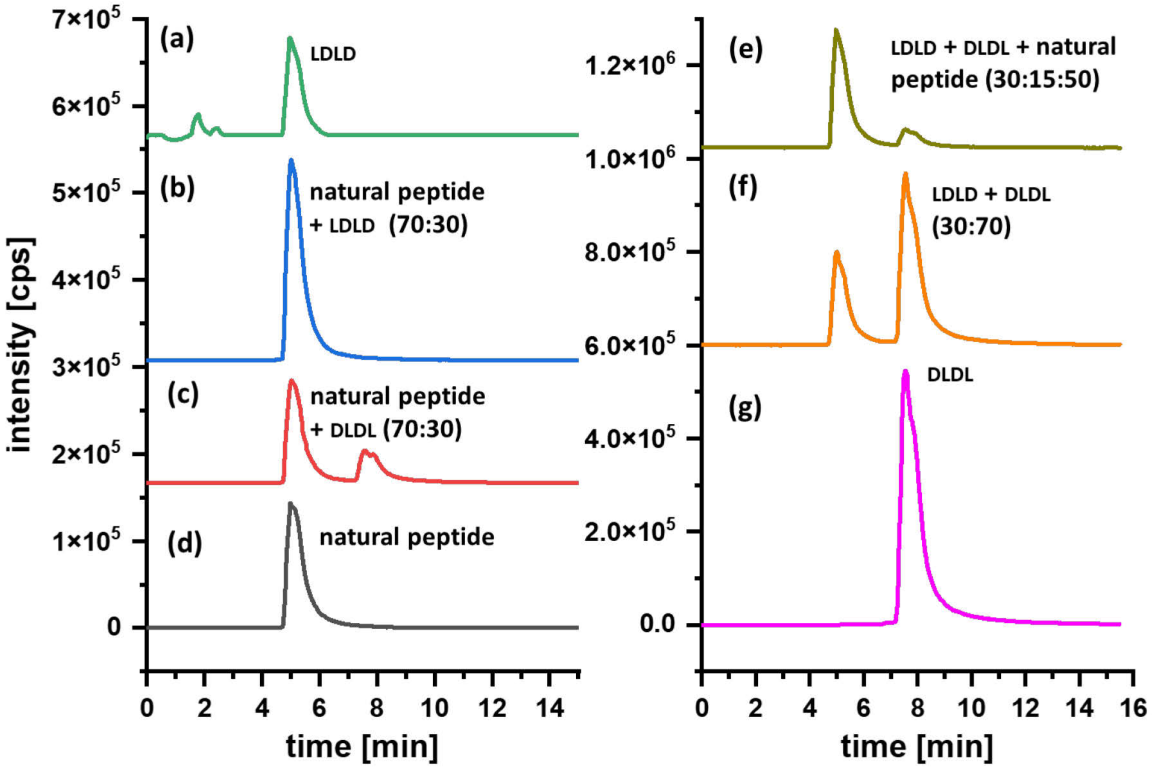

Fig. 10: Extracted ion chromatograms (EICs, m/z = 541.2405 ± 0.05) of the analyses of the peptide amides were recorded with a HPLC-ESI-QTOF-MS. All pure samples had a concentration of 0.1 mg/mL. (a) The EIC of the synthetic LDLD peptide (green). (b) The EIC (blue) shows a mixture (70:30) of the isolated natural peptide and the synthetic LDLD peptide. (c) A mixture (70:30) of the isolated natural peptide and the synthetic DLDL peptide is shown (EIC, red). (d) The EIC of the natural peptide purified from culture extract is shown (black). (e) The olive EIC shows a ternary mixture (30:15:50) of the synthetic LDLD peptide, synthetic DLDL peptide and the isolated natural peptide. (f) The mixture (30:70) of the synthetic LDLD peptide and synthetic DLDL peptide shows the given EIC (orange). (g) The EIC of the synthetic DLDL peptide is presented (purple). The enantiomer separation was performed on a ZWIX(+) column (150x3.00 mm, 3 µm) using ACN/MeOH/H_2O (49:49:2 v/v) with 50 mM FA/25 mM NH_3 as mobile phase in an isocratic method at 0.5 mL/min and 25°C. Sample was dissolved in mobile phase to a concentration of 0.1 mg/mL and 2 µL were injected onto the column.

Tab. 4: Sample composition with theoretical and experimental peak area ratios from Fig. 10. It was assumed the natural peptide has the LDLD configuration for the calculation of the theoretical peak area ratio of the samples containing the natural peptide.

sample	**LDLD [%]**	**DLDL [%]**	**theor. ratio (LDLD/DLDL)**	**Area (LDLD) [/]**	**Area (DLDL) [/]**	**exp. ratio (LDLD/DLDL)**
natural peptide + DLDL	70	30	2.33	4,611,127	1,901,269	2.43
LDLD + DLDL + natural peptide	80	15	5.33	9,688,335	2,062,175	4.70
LDLD + DLDL	30	70	0.43	7,542,081	15,710,150	0.48

3.5.4 Conclusion

An enantioselective chiral LC-MS method was developed which enables baseline separation of six out of eight enantiomer pairs and partial resolution of the remaining two enantiomer pairs. The initial method development of the diastereomer separation was performed and six out of eight expected diastereomer peaks could be resolved partially while two diastereomer peaks still co-eluted. A natural tetrapeptide as real sample was analysed with the enantioselective method and the absolute configuration could be confirmed based on the chiral separation in conjunction with genome mining analysis. The diastereomer separation still needs further optimization in form of an extended column and mobile phase screening. The enantiomer and diastereomer separation then can be combined in a 2D-LC separation which should then be capable to separate all 16 stereoisomers in a single analysis run.

3.5.5 References

[1] Z. Tian, F. Liu, D. Li, A.R. Fernie, W. Chen, Strategies for structure elucidation of small molecules based on LC–MS/MS data from complex biological samples, Computational and Structural Biotechnology Journal, 20 (2022) 5085-5097.

[2] Z.J. Anderson, C. Hobson, R. Needley, L. Song, M.S. Perryman, P. Kerby, D.J. Fox, NMR-based assignment of isoleucine vs. allo-isoleucine stereochemistry, Organic & Biomolecular Chemistry, 15 (44) (2017) 9372-9378.

[3] K. Blin, S. Shaw, K. Steinke, R. Villebro, N. Ziemert, S.Y. Lee, M.H. Medema, T. Weber, antiSMASH 5.0: updates to the secondary metabolite genome mining pipeline, Nucleic Acids Res., 47 (W1) (2019) W81-W87.

[4] C. Czerwenka, W. Lindner, Stereoselective peptide analysis, Analytical and Bioanalytical Chemistry, 382 (3) (2005) 599-638.

[5] M. Morvan, I. Mikšík, Recent Advances in Chiral Analysis of Proteins and Peptides, Separations, 8 (8) (2021) 112.

[6] M. Danielsen, C. Nebel, T.K. Dalsgaard, Simultaneous Determination of L- and D-Amino Acids in Proteins: A Sensitive Method Using Hydrolysis in Deuterated Acid and Liquid Chromatography–Tandem Mass Spectrometry Analysis, Foods, 9 (3) (2020) 309.

[7] J. Kuang, Y. Tao, Y. Song, L. Chemmalil, N. Mussa, J. Ding, Z.J. Li, Understanding the pathway and kinetics of aspartic acid isomerization in peptide mapping methods for monoclonal antibodies, Analytical and Bioanalytical Chemistry, 413 (8) (2021) 2113-2123.

4 Acknowledgements

I would like to thank all people who contributed to this thesis in several different ways.

First, I would like to thank Prof. Dr. Michael Lämmerhofer for the opportunity to do my PhD in his research group. He helped a lot through his guidance, mentoring and scientific discussions. I appreciate the opportunity to do advanced training, visit scientific conferences and have valuable co-operations with other research groups and industry partners.

Second, I thank my second supervisor Jun.-Prof. Dr. Matthias Gehringer for his evaluation of this dissertation.

I want to thank Benjamin Peters, Jason Stahlecker, Theresa Klett, Larissa Ernst, Younes Valadbeigi, Taulant Dema, Prof. Dr. Frank. M. Böckler, Prof. Dr. H. Groß, Prof. Dr. S. Grond, and Assoc. Prof. Dr. Tim Causon for their fruitful scientific collaborations.

Many thanks to Chunmei Wen who was my master thesis student and helped me a lot with kinetic performance evaluation study.

I would like to thank my former colleagues Dr. Jeannie Horak, Dr. Siyao Liu, Dr. Stefan Neubauer, Dr. Bernhard Drotleff, Dr. Jörg Schlotterbeck, Dr. Malgorzata Cebo, Dr. Carlos Caldéron, Dr. Stefanie Bäurer, Dr. Ryan Karongo, Dr. Christian Geibel, Dr. Kristina Dittrich Ece Aydin and Marc Wolter for welcoming me and introducing me to proper scientific working.

Many thanks to my current colleagues Dr. Xiaoqing Fu, Dr. Adrain Sievers-Engler, Feiyang Li, Adrian Brun, Franz Fießinger, Tamara Janker, Cornelius Knappe, Mirna Maalouf, Matthias Olfert, Kristian Serafimov and Min Su for having a lot of memorable moments and fun in the laboratory. They helped me a lot by sharing their experience, having scientific discussions and practical help in the laboratory.

My special thanks go to my girlfriend Bianka for her endless support, motivation, and patience. Without you it would have been a much tougher time.

Finally, I thank my family for their endless support and motivation throughout my PhD time. In particular, I want to thank my mother Sabine, my father Werner and my older brothers Daniel and Lukas.